

LEWIS GRANT
1N-34-CR
75749
P-248

MICHIGAN TECHNOLOGICAL UNIVERSITY
COLLEGE OF ENGINEERING
MECHANICAL ENGINEERING - ENGINEERING MECHANICS DEPARTMENT
HOUGHTON, MI 49931

**FILM CONDENSATION IN A HORIZONTAL
RECTANGULAR DUCT**

QING LU

N.V. SURYANARAYANA
(PRINCIPAL INVESTIGATOR)

PROJECT E24744

**FINAL REPORT ON THE EXPERIMENTAL PART OF THE PROJECT ON
FILM CONDENSATION UNDER MICROGRAVITY CONDITIONS**

WITH A GRANT FROM
NATIONAL AERONAUTICS AND SPACE ADMINISTRATION
NASA-LEWIS RESEARCH CENTER
GRANT NO. NAG 3-711
CLEVELAND, OHIO

February 20, 1992

(NASA-CR-190044) FILM CONDENSATION IN A
HORIZONTAL RECTANGULAR DUCT Final Report
(Michigan Technological Univ.) 248 p

N92-19249

CSCL 20D

Unclas

G3/34 0075749

**MICHIGAN TECHNOLOGICAL UNIVERSITY
COLLEGE OF ENGINEERING
MECHANICAL ENGINEERING - ENGINEERING MECHANICS DEPARTMENT
HOUGHTON, MI 49931**

**FILM CONDENSATION IN A HORIZONTAL
RECTANGULAR DUCT**

QING LU

**N.V. SURYANARAYANA
(PRINCIPAL INVESTIGATOR)**

PROJECT E24744

**FINAL REPORT ON THE EXPERIMENTAL PART OF THE PROJECT ON
FILM CONDENSATION UNDER MICROGRAVITY CONDITIONS**

**WITH A GRANT FROM
NATIONAL AERONAUTICS AND SPACE ADMINISTRATION
NASA-LEWIS RESEARCH CENTER
GRANT NO. NAG 3-711
CLEVELAND, OHIO**

February 20, 1992

ABSTRACT

Condensation heat transfer in a horizontal rectangular duct was experimentally and analytically investigated. To prevent the dripping of condensate on the film, the experiment was conducted inside a horizontal rectangular duct with vapor condensing only on the bottom cooled plate of the duct. R-113 and FC-72 (Fluorinert Electronic Fluid developed by the 3M Company) were used as the condensing fluids.

The experimental program included measurements of film thickness, local and average heat transfer coefficients, wave length, wave speed, and a study of wave initiation. The measured film thickness was used to obtain the local heat transfer coefficient. The wave initiation was studied both with condensation and with an adiabatic air-liquid flow. The test sections used in both experiments were identical.

Experimental results showed that the average heat transfer coefficient increased with increasing inlet vapor velocity. There was a significant increase in the heat transfer after the appearance of interfacial waves (when the inlet Reynolds number was approximately greater than 1,000,000). The local heat transfer coefficient decreased with axial distance of the condensing surface. The local heat transfer coefficient decreased rapidly with axial distance near the leading edge of the condensing surface but was nearly constant towards the trailing edge.

It was observed that the condensate flow along the condensing surface experienced a smooth flow, a two-dimensional wavy flow, and a three-dimensional wavy flow. The change in the flow pattern depended on the vapor velocity and the difference between the saturation temperature of the vapor and the condensing surface temperature. The wave length decreased with axial distance and the inlet vapor velocity, while the wave speed increased with vapor velocity.

An analytical model simulating the condensation process was formulated by

employing the universal conservation laws. The resulting equations were solved numerically. The heat transfer coefficients predicted from the model are within $\pm 20\%$ of the measured values.

Using the present experimental data and analysis, correlations for the average heat transfer coefficients in the annular flow regime were developed. The average deviation between the predictions and the experimental values is within $\pm 18\%$. Also, predictions from some correlations selected from the literature for the heat transfer coefficients of condensation in the annular flow regime were compared with the experimental data. It is found that the correlations of Shah (1979) and Soliman et al. (1968) yielded satisfactory predictions. (The average is within $\pm 21\%$ for Shah's correlation and $\pm 22\%$ for Soliman's correlation.)

The effects of air velocity, liquid flow rate, and the liquid viscosity on the initiation of interfacial waves were studied with an adiabatic air-liquid flow. The liquid viscosity was varied by varying the mass fraction of glycerine in the water-glycerine mixture. It was observed that the interfacial waves were initiated closer to the leading edge when the air velocity or the liquid flow rate was increased.

It was found that with condensation, the flow appeared more stable in the adiabatic liquid flow; condensation appears to have a damping effect on the initiation of interfacial waves.

Several criteria for the instability in two-phase flow were examined and compared with each other. It is found that none of them can be confidently used in the present experiment. With the modification of one of the investigated criteria and the use of the present experimental data of the air-liquid flow, a criterion for predicting the instability of the two phase flow is tentatively given. This criterion provides a reasonable prediction for the initiation of interfacial waves with air-liquid flow, as well as with condensation.

CONTENTS

ABSTRACT	i
LIST OF FIGURES	vii
LIST OF TABLES	xii
NOMENCLATURE	xiii
1. INTRODUCTION	1.1
2. LITERATURE REVIEW	2.1
2.1. Introduction	2.1
2.2. Condensation	2.2
2.2.1. Analytical Studies of Condensation over a Flat Plate	2.2
2.2.2. Analytical Studies of Condensation inside Tubes	2.4
2.2.3. Studies of Interfacial Shear Stress	2.10
2.2.4. Experimental Studies of Condensation inside a Duct	2.11
2.3. Wave Initiation in Two Phase Flows	2.15
2.4. Concluding Comments	2.18
3. OBJECTIVES	3.1
4. DESCRIPTION OF EXPERIMENT	4.1
4.1. Introduction	4.1
4.2. Experimental Set-up of Condensation	4.1
4.2.1. Test Section	4.4
4.2.2. Converging Unit	4.8
4.2.3. Boiler	4.9
4.2.4. Auxiliary Condenser	4.10
4.2.5. Temperature Controller and Gravity Tank for Condensation	4.10
4.3. Experimental Set-up of Air-liquid Flow	4.12
4.4. Measurements in Condensation Experiment	4.14

4.4.1.	Measurement of Vapor Flow Rates	4.15
4.4.2.	Measurement of Condensate Flow Rate	4.15
4.4.3.	Measurement of Cooling Water Flow Rate	4.17
4.4.4.	Measurement of Temperatures	4.17
4.4.5.	Measurement of Vapor Pressure	4.21
4.4.6.	Measurement of Film Thickness	4.22
4.4.7.	Measurements of Wave Length and Wave Speed	4.23
4.5.	Measurements in Air-liquid Flow Experiment	4.25
4.5.1.	Measurement of Mass Flow Rate of Air	4.25
4.5.2.	Measurement of Mass Flow Rate of Liquid	4.25
4.5.3.	Measurement of Density of Liquid	4.25
4.5.4.	Measurement of Viscosity of Liquid	4.25
4.6.	Data Acquisition System	4.26
4.7.	Liquids	4.27
4.7.1.	Liquids in Condensation Experiments	4.27
4.7.2.	Liquids in Air-liquid Flow Experiments	4.27
4.8.	Experimental Procedures	4.27
4.8.1.	Procedure of Condensation Experiments	4.27
4.8.2.	Procedure of Air-Liquid Flow Experiments	4.31
4.9.	Data Processing	4.32
4.9.1.	Condensate Film Thickness	4.32
4.9.2.	Heat Transfer Rate and Heat Transfer Coefficients	4.33
4.9.3.	Liquid Velocity	4.38
4.9.4.	Vapor and Air Velocities	4.40
5.	ANALYTICAL MODEL FOR CONDENSATION	5.1
5.1.	Introduction	5.1
5.2.	Physical Description of the Problem	5.1
5.3.	Formulation	5.2
5.3.1.	Assumptions	5.2

5.3.2.	Mass Conservation	5.2
5.3.3.	Energy Conservation	5.5
5.3.4.	Condensation Velocity	5.6
5.3.5.	Interfacial Velocity	5.8
5.3.6.	Differential Equation for Condensation Film Thickness	5.9
5.3.7.	Heat Transfer Rate and Heat Transfer Coefficients	5.11
5.4.	Solution Procedure	5.13
6.	RESULTS AND DISCUSSION	6.1
6.1.	Introduction	6.1
6.2.	Ranges of Experimental Variables	6.1
6.2.1.	Condensation Heat Transfer	6.1
6.2.2.	Wave Initiation	6.2
6.3.	Observation of Flow Patterns	6.3
6.4.	Temperature Distributions in Test Section	6.6
6.5.	Condensate Film Thickness	6.8
6.6.	Heat Transfer Rates and Heat Transfer Coefficients	6.8
6.6.1.	Total Heat Transfer Rates and Average Heat Transfer Coefficients	6.8
6.6.2.	Sectional Heat Transfer Rates and Sectional Heat Transfer Rates	6.17
6.6.3.	Local Heat Transfer Coefficients	6.21
6.7.	Dimensionless Parameters	6.25
6.7.1.	Derivation of Dimensionless Parameters	6.25
6.7.2.	Average Nusselt Numbers and Stanton Numbers	6.28
6.8.	Comparison with Correlations Data in Literature	6.30
6.8.1.	Comparison of Heat Transfer Correlations	6.30
6.8.2.	Comparison with Experimental Data in the Literature	6.44
6.9.	Predictions by Analysis	6.44
6.10.	Heat Transfer Correlations	6.67

6.10.1. Semi-empirical Heat Transfer Correlation	6.67
6.10.2. Empirical Heat Transfer Correlation	6.70
6.10.3. Comparison between Heat Transfer Correlations	6.72
6.11 Interfacial Waves	6.73
6.11.1. Observation of the Interfacial Wave Initiation	6.73
6.11.2. Criteria Predicting the Instability of Liquid Flow	6.82
6.11.3. Interfacial Wave Length and Speed	6.88
7. CONCLUSIONS AND RECOMMENDATIONS	7.1
7.1 Conclusions	7.1
7.2 Recommendations for Further Study	7.3
APPENDIX A: UNCERTAINTY ANALYSES	A.1
A.1. Total Average Heat Transfer Coefficient	A.1
A.2. Inlet Vapor Reynolds Number	A.11
A.3. Total Average Nusselt Number	A.13
A.4. Total Average Stanton Number	A.14
APPENDIX B: TEST OF CONVERGING UNIT	B.1
APPENDIX C: CALIBRATION OF FLOW METERS	C.1
APPENDIX D: CALIBRATION OF THERMOCOUPLES	D.1
APPENDIX E: CALIBRATION OF ULTRASONIC TRANSDUCER	E.1
APPENDIX F: COMPARISON BETWEEN EQ. 4-6 AND EQ. 4-7	F.1
APPENDIX G: EXPERIMENTAL DATA	G.1
BIBLIOGRAPHY	H.1

LIST OF FIGURES

2.1	Illustration of flow regimes of condensation in horizontal tubes	2.2
2.2	Condensate flow models	2.5
4.1	Schematic of experimental set-up of condensation	4.2
4.2	Photograph of experimental set-up of condensation	4.3
4.3	Schematic of test section of condensation	4.5
4.4	Cross section of test section of condensation	4.6
4.5	Details of mixing chamber	4.7
4.6	Details of converging unit	4.8
4.7	Details of boiler	4.9
4.8	Details of auxiliary condenser	4.11
4.9	Schematic of experimental set-up of air-liquid flow	4.13
4.10	Photograph of experimental set-up of air-liquid flow	4.13
4.11	Details of inlet section	4.14
4.12	Details of gauge glass	4.16
4.13	Details of condensing surface	4.18
4.14	Arrangement of thermocouples for measuring vapor temperature	4.19
4.15	Arrangement of different thermocouples	4.20
4.16	Illustration of film thickness measuring system	4.22
4.17	Typical pulse trace	4.23
4.18	Photograph of wave length	4.24
4.19	Schematic of wave-speed measuring device	4.24
4.20	Schematic of viscosity meter	4.26
4.21	Condensate film	4.32

4.22	Illustration of heat balance in the vapor duct of the test section	4.34
5.1	Physical model and coordinate system	5.1
5.2	Control volume of condensate	5.3
5.3	Control volume of vapor	5.4
5.4	Control volume of energy conservation	5.5
5.5	Illustration of L_i and L_{i+1}	5.12
5.6	Arrangement of grids	5.13
5.7	Flow chart of computing program	5.14
6.1	Photographs of 2-D waves and 3-D waves	6.4
6.2	Photograph of condensate flow patterns along condensing surface	6.5
6.3	Various temperature distributions in the test section	6.7
6.4	Distributions of condensate film thickness along the condensing surface	6.9
6.5	Total heat transfer rates	6.10
6.6	Variation of average heat transfer coefficients with v_{gi}	6.12
6.7	Comparison of heat transfer coefficients measured from the heat balance method with values obtained from the film thickness data	6.13
6.8	Typical examples of film thickness correlations	6.15
6.9	Total average heat transfer coefficients as a function of vapor mass velocity to the inlet of the test section	6.16
6.10	Sectional heat transfer rates	6.18
6.11	Sectional heat transfer coefficients	6.19
6.12	Comparison of sectional heat transfer coefficients of R-113 with that of FC-72	6.20
6.13	Effect of condensing fluids on condensate film thickness	6.22
6.14	Comparison of sectional heat transfer coefficients measured from heat balance method with values obtained from film thickness data	6.23
6.15	Variations of local heat transfer coefficients along the condensing surface	6.24
6.16	Variations of average Nusselt number with Re_{gL}	6.29
6.17	Variations of Stanton number with Re_{gL}	6.31

6.18	Typical variation of quality along the condensing surface	6.36
6.19	Comparison of predictions of local heat transfer coefficients from the correlations of Azer, Soliman, and Traviss with experiment data	6.36
6.20	Predictions of sectional heat transfer coefficients from other researchers' correlations	6.38
6.21	Predictions of total average heat transfer coefficients from other researchers' correlations	6.42
6.22	Comparison of the present experimental data with that of Akers and Rosson (1960)	6.45
6.23	Comparisons of predicted film thickness with measured values ($c_f = 0.0592$)	6.47
6.24	Comparisons of predicted sectional heat transfer coefficients with measured values ($c_f = 0.0592$)	6.50
6.25	Predicted sectional heat transfer coefficients at higher Re_{gL}	6.52
6.26	Predicted total average heat transfer coefficients ($c_f = 0.0592$)	6.53
6.27	Comparison of adiabatic shear stress with momentum shear stress ($c_f = 0.0592$)	6.55
6.28	Predicted total average heat transfer coefficients using Jensen and Yuen's friction equation	6.56
6.29	Predicted film thickness using Jensen and Yuen's friction equation	6.57
6.30	Predicted sectional heat transfer coefficients using Jensen and Yuen's friction equation	6.58
6.31	Effect of c_f on S	6.59
6.32	Predicted total average heat transfer coefficients ($c_f = 0.245$)	6.61
6.33	Predicted film thickness ($c_f = 0.245$)	6.62
6.34	Predicted sectional heat transfer coefficients ($c_f = 0.245$)	6.63
6.35	Predicted sectional heat transfer coefficients at higher Re_{gL} ($c_f = 0.245$)	6.64
6.36	Comparison between the present model and Narain's model	6.65
6.37	Distributions of vapor and liquid velocities along the test section	6.66

6.38	Distributions of the interfacial shear stress along the test section	6.66
6.39	Comparison of the heat transfer correlation (Eq. 6-20) with the experiment	6.69
6.40	Comparison of the heat transfer correlation (Eq. 6-22) with the experiment	6.71
6.41	Comparison of different heat transfer correlations	6.73
6.42	Photograph of interfacial wave initiation in condensation	6.74
6.43	Relationship between Re_{gL} causing the interfacial wave initiation and ΔT	6.74
6.44	Photographs of interfacial wave initiation in air-liquid flow	6.75
6.45	Illustration of onset length	6.76
6.46	Variation of onset length with liquid flow rate	6.77
6.47	Variation of liquid film thickness along the test section of air-liquid flow	6.78
6.48	Variation of v_g for wave initiation with v_l in air-liquid flow	6.80
6.49	Variation of v_g for wave initiation with \dot{m}_l in air-liquid flow	6.80
6.50	Effect of liquid viscosity on wave initiation	6.81
6.51	Variation of v_{gi} for wave initiation with \dot{m}_l in condensation	6.81
6.52	Damping effect of condensation on wave initiation	6.82
6.53	Validity of the instability criterion (Eq. 6-31)	6.87
6.54	Distributions of local wave length along the condensing surface	6.89
6.55	Variation of average wave length with inlet vapor velocity	6.90
6.56	Variation of average wave length with Reynolds number of condensate	6.90
6.57	Variation of wave speed with inlet vapor velocity	6.92
6.58	Comparison of wave length and wave speed of R-113 with those of FC-72	6.93
A.1	Illustration of heat transfer through the vapor duct	A.5
A.2	Heat Transfer through the sides and the bottom of the cooling channel	A.6
A.3	Heat Transfer through the front side of the cooling channel	A.6
A.4	Heat Transfer through the rear side of the cooling channel	A.6

A.5	Illustration of the surface thermocouple	A.10
B.1	Schematic of the selected deflector	B.1
B.2	Air velocity profile at the outlet of the converging unit	B.2
C.1	Rotameter calibration	C.1
C.2	Comparison between the present calibration results of the vapor rotameter and the manufacturer data	C.2
C.3	Venturi meter calibration	C.3
C.4	Repeatability of the calibration of venturi meter	C.4
D.1	Thermocouple calibration	D.1
D.2	Differential thermocouple calibration	D.2
E.1	Schematic of calibration device of ultrasonic transducer	E.1
E.2	Sonic velocities of condensing liquids (R-113 and FC-72)	E.2

LIST OF TABLES

4.1	Selected thermodynamics properties of R-113 and FC-72	4.28
6.1	Rangers of variables in the experiment of condensation heat transfer	6.2
6.2	Ranger of variables in the experiment of interfacial wave initiation	6.2
6.3	Inlet vapor Reynolds number at which interfacial waves appear — condensation	6.3
6.4	Conditions of 3-D waves covering the whole condensing surface	6.6
6.5	Average deviations in comparison of the sectional heat transfer coefficients	6.40
6.6	Average deviations in comparison of the total average heat transfer coefficients	6.41
6.7	Rangers of experimental data used in correlating Eq. 6-20	6.68
6.8	Comparison of the predictions from Eq.s 6-23, 6-24, and 6-27 with the experimental results of air-liquid flow	6.86
6.9	Comparison of the predictions from Eq. 6-23, 6-24, and 6-27 with the experimental results of condensation	6.87
C.1	Calibration data of vapor rotameter	C.3
C.2	Calibration data of venturi meters	C.5
C.3	Calibration data of coolant rotameters	C.6
D.1	Sample results of the thermocouple calibrations	D.2
D.2	Results of calibration of differential thermocouples	D.3
E.1	Comparison of measured and reported sonic velocities	E.2
G.1	Heat transfer coefficients	G.1
G.2	Film thickness	G.13
G.3	Interfacial wave initiation in air-liquid flow	G.16
G.4	Interfacial wave initiation in condensation	G.18
G.5	Interfacial wave speed and length	G.19

NOMENCLATURE

ALPHABETICAL SYMBOLS

a_r	sonic velocity
A	total area of condensing surface
A_s	sectional area of condensing surface
C_{pl}	specific heat of condensate
C_{pg}	specific heat of vapor
C_{pw}	specific heat of water
f	friction factor
G	mass velocity of vapor
D_H	hydraulic diameter of test section
g	gravity
\bar{h}_1	average heat transfer coefficient over section 1
\bar{h}_2	average heat transfer coefficient over section 1 and 2
h_{gi}	enthalpy of vapor at the inlet of the test section
h_g	enthalpy of vapor
h_l	enthalpy of liquid
h_{fg}	enthalpy difference, $(h_g - h_l)$
h_x	local heat transfer coefficient
\bar{h}_s	sectional heat transfer coefficient
\bar{h}_t	average heat transfer coefficient over the entire condensing surface
$\bar{h}_{t(pred)}$	predicted total average heat transfer coefficient
H	height of the test section
k_l	thermal conductivity of liquid
L	total length of condensing surface

Nomenclature

L_{on}	onset length
L_w	wave length
\dot{m}_g	vapor or air flow rate
\dot{m}_l	liquid flow rate
\dot{m}_{Lt}	total flow rate of condensate
\dot{m}_i	total mass flow rate of vapor at the inlet of the test section
\dot{m}_w	coolant flow rate
\dot{m}_x	condensate rate per unit area of the condensing surface
P	saturation pressure
q''	heat flux
q	total heat transfer rate
t_f	time for the ultrasonic signal to pass through the film of condensate
T_g	temperature of vapor in the test section
T_{sat}	saturation temperature
T_s	condensing surface temperature
T_l	condensate temperature
T_w	coolant temperature
ΔT	temperature difference, $(T_{sat} - T_s)$
ΔT_w	temperature difference of coolant across cooling channel
v	difference between vapor velocity and interfacial liquid velocity
v_g	vapor (or air) velocity
v_{gi}	inlet vapor velocity
v_l	liquid velocity
v_{li}	interfacial liquid velocity
v_w	wave speed
W	width of test section
x	distance of condensing surface from the leading edge
X	quality

GREEK SYMBOLS

δ	film thickness of liquid
Δ	average film thickness
μ_g	dynamic viscosity of vapor (or air)
μ_l	dynamic viscosity of liquid
ν_g	kinematic viscosity of vapor (or air)
ν_l	kinematic viscosity of liquid
ρ_g	density of vapor (or air)
ρ_l	density of liquid
σ	surface tension of liquid
τ_a	adiabatic shear stress
τ_i	interfacial shear stress
τ_m	equivalent shear stress due to momentum
τ_w	wall shear stress

DIMENSIONLESS GROUPS

Ja	Jacob number, $C_{pl}\Delta T/h_{fg}$
Nu_1	Nusselt number for section 1, $\bar{h}_1 L/k_l$
Nu_2	Nusselt number for sections 1 and 2, $\bar{h}_2 L/k_l$
Nu_t	Nusselt number for the whole condensing surface, $\bar{h}_t L/k_l$
Pr_l	Prandtl number of liquid, $C_{pl}\mu_l/k_l$
Re_g	vapor or (air) Reynolds number, $v_g L/\nu_g$
Re_{gi}	inlet vapor Reynolds number, $v_{gi} L/\nu_g$
Re_l	Reynolds number of liquid, $v_l \delta/\nu_l$
Re_x	local vapor Reynolds number, $v_g x/\nu_l$
St_1	Stanton number for section 1, $\bar{h}_1/(\rho_l C_{pl} v_{gi})$

Nomenclature

St_2	Stanton number for sections 1 and 2, $\overline{h}_2/(\rho_1 C_{pl} v_{gi})$
St_t	Stanton number for the whole condensing surface, $\overline{h}_t/(\rho_1 C_{pl} v_{gi})$

1. INTRODUCTION

In applications involving condensation of a vapor, the condensate is drained by the gravitational forces in external condensation or by the shear force if condensation is inside horizontal tubes. In space applications under microgravity conditions, for draining the condensate mechanisms that do not depend on gravity are needed. One possibility is condensation inside tubes. All the characteristics of condensation inside horizontal tubes are not fully understood, and those that are understood under 1-g conditions may occur differently under microgravity conditions.

With condensation inside horizontal tubes it has been established that the major part of the heat transfer occurs in the annular and annular-wavy regimes. The results of an experimental and analytical study of condensation in the two regimes are presented in this thesis. The results can be used as a base for comparison with results of condensation under reduced gravity conditions.

With condensation inside horizontal tubes interfacial instabilities lead to the annular-wavy regime. Amplification of the waves may lead to undesirable flow instabilities. Thus, there is a need to study the role of various parameters that affect the stability of the condensate film, and the effect of the interfacial waves on the heat transfer rate.

In the annular flow regime in horizontal tubes under 1-g conditions there is the possibility of the condensate from the upper half of the tube dripping on the lower half leading to waves in the condensate. To avoid the effect of such dripping condensation, a rectangular horizontal duct with vapor condensing on the bottom cooled surface of the horizontal duct was chosen for the experimental and analytical study. This report presents the results of condensation heat transfer in the annular and annular-wavy flow regimes with the condensate drained by the vapor shear, and

1. Introduction

predictions from a simple analytical model. Refrigerant 113 (R-113) and a fluorinert electronic fluid (FC-72 developed by the 3M company) were selected as the condensing fluids. The experiments yielded the condensate film thickness at several axial locations, the local and average heat transfer rates, and the wave length and wave speed of interfacial waves when they appeared. Observed conditions for the incipience of interfacial waves are also reported.

To better identify the parameters relevant to the initiation of the interfacial waves, and to relate the effect of condensation on the initiation of such waves another series of experiments with an adiabatic air-liquid flow were performed. These experiments were conducted in a test section which was identical to the test section used in the experiments.

The condensation was simulated by an analytical model. The resulting equations were solved numerically yielding the condensate film thickness, The interfacial shear stress, and the local and average heat transfer coefficients. The validity of the model is examined by comparing the predictions with the experimental results. There is considerable differences between the predictions and the experimental results. The difference is attributed to the lack of a proven model for the interfacial shear stress.

2. LITERATURE REVIEW

2.1. Introduction

Condensation heat transfer (with condensation inside ducts) is influenced by the flow regimes and usually by the orientations of the condensing surface, if the vapor shear stress is not high enough for the gravity force to be negligible. Fig. 2.1 illustrates the flow regimes occurring during condensation inside a horizontal tube. As the condensation proceeds along the tube, the liquid flow rate increases and the vapor flow rate decreases; the flow regime changes along the tube. Unless the vapor velocity is very low, the flow begins as an annular flow and is followed by wavy, slug, and plug flows (or stratified flow when the inlet vapor mass flow rate is low). The annular flow regime is known to be the dominant flow regime, existing over most of the condensing length both inside a horizontal tube and a vertical tube [Soliman et al, (1968)]. In the annular flow regime, condensate film forms on the periphery of the tube; the flow of the liquid film is driven mainly by the momentum and the shear stress of the vapor flow in the core of the tube. With increasing vapor velocity, waves appear on the surface of the liquid film. The annular flow regime with interfacial waves is termed annular wavy flow regime.

In this review, emphasis is on a survey of the analytical and experimental studies of condensation inside a horizontal tube. A brief review of condensation of vapor flowing parallel to a cooled surface is also included as there are some similarities between the two.

The annular flow regime also includes the annular wavy flow regime. As the interfacial waves have a significant effect on the heat transfer rate, a survey of the literature of the interfacial instability is also given.

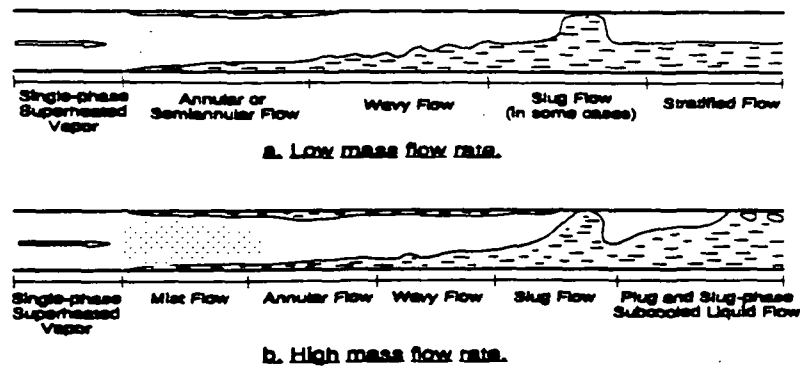


Fig. 2.1 Illustration of flow regimes of condensation in horizontal tubes
[This figure is reproduced from Sardesai et al. (1981)]

2.2. Condensation

2.2.1. Analytical Studies of Condensation over a Flat Plate

Nusselt (1916) first analyzed the film condensation of a quiescent vapor on an inclined plate. In his analysis, he assumed the following: the condensate film is laminar; all the properties of vapor and liquid are constant; the subcooling, momentum change, and interfacial shear stress are negligible; the temperature profile in the condensate is linear.

Jakob (1949) was among the first to point out a high deviation of the Nusselt analysis with the experimental results involving a turbulent condensate film flow. Akers and Rosson (1960) also showed that the Nusselt analysis may not be applicable when the effects of the liquid subcooling or the vapor shear are significant or when the liquid film is turbulent.

For condensation of vapor flow over a flat plate, Koh (1962) presented numerical

2. Literature Review

solution to a system of differential equations of mass, momentum, and energy balance. The equations included inertia and convective terms. The results of his analysis showed that for a thin condensate layer and for Prandtl number less than 10, the condensate velocity and temperature profiles are essentially linear. Koh showed that for higher Prandtl numbers, neglecting the convective terms in the energy equation considerably underestimated the heat transfer rates.

Shekrilasze and Gomelaui (1966) expressed some skepticism about Koh's result regarding the effect of the inertia forces and the convective terms on the condensation heat transfer rate. They developed a model of condensation on a flat plate, based on the assumptions that the temperature profile is linear and the inertia forces are negligible. They assumed that at high vapor velocities, the interfacial shear stress is equal to the momentum associated with the condensing vapor. Approximate solutions for predicting the heat transfer coefficients were given for condensation both with a uniform surface temperature and a constant heat flux. From the results of the model, they found that the assumption of negligible inertia forces is appropriate for the condensation of non-metallic liquids and that the subcooling of the liquid was insignificant for $N \leq 1$ ($N = k_f \Delta T / h_{fg} \mu_l$). They also reported a good agreement when comparing their model predictions with the experimental data of Jakob (1935).

Sparrow et al. (1967) studied forced convection condensation on a horizontal flat plate. Their model included the effect of a non-condensable gas, but neglected the inertia and the convective terms. They used similarity analysis and numerical methods to solve the equations. They showed that in forced convection condensation, the effect of non-condensable gases was insignificant. They also indicated that the interfacial thermal resistance due to the effect of the transport of the molecules from the condensed vapor and the molecules evaporating from the surface was negligible for the forced convection condensation of steam.

Uehara et al. (1984) analyzed the turbulent film condensation of a saturated vapor in forced flow over a flat plate. They assumed a turbulent liquid layer and a turbulent

2. Literature Review

vapor boundary layer above the liquid. The temperature and the velocity profiles in the liquid layer and the vapor boundary layer were assumed. In the analysis, they found that the thickness of the sublayer within the vapor boundary layer influenced the heat transfer, and, therefore, was included in the equation for the heat transfer coefficients. For their predictions to completely agree with experimentally determined correlations for heat transfer coefficients, the value of the sublayer thickness was adjusted.

Narain and Kizilyalli (1991) developed a set of scaled mass, momentum, and energy differential equations to model the condensation of pure saturated vapor flow between two horizontal, parallel plates. In their study, the vapor flow was considered to be a pressure driven laminar flow. It was also assumed that condensation occurred only on the cooled bottom plate with the upper plate adiabatic, and that the temperature profile of the condensate was linear. Narain (1991) further simplified the model by dropping the gravity, inertia, and convection terms in the liquid phase. Comparison of the predicted heat transfer coefficients with the present experimental data showed agreement within $\pm 40\%$. Using the data from the present experiments, Narain and Kamath (1991) refined the friction factor model of the interface for both laminar and turbulent flows of vapor. The resulting agreement between the theory and some of the experiments with regard to film thickness was within $\pm 10\%$.

2.2.2. Analytical Studies of Condensation inside Tubes

Low Mass Flow Rate of Vapor

For condensation of vapor inside a horizontal tube at low inlet mass flow rates, condensation occurs on the inside wall of the tube and the condensate drains to the bottom of the tube in the same vertical plane, similar to the external condensation of quiescent vapor on a horizontal cylinder. The condensate at the bottom of the tube is a thick liquid layer, while the condensate on the rest of the wall is a thin liquid film

(Fig. 2.2) .

Chaddock (1957) studied condensation of vapor in a horizontal duct at low vapor velocities. He postulated that the condensate was driven by the hydraulic gradient of the condensate (Fig. 2.2 a). The surface profile of the bottom condensate was estimated on this assumption, and defined the area covered by the

condensate film. It was further assumed that condensation occurred only on the surface above the bottom condensate layer and that the condensation heat transfer rate was given by the Nusselt analysis on a horizontal cylinder.

Chato (1957) adopted the Chaddock model to estimate the surface profile of the bottom condensate in a horizontal tube. The heat transfer to the bottom condensate was neglected, while the heat transfer to the condensate film on the upper part of the inside tube wall was derived from an analytical model involving the integral momentum and energy equations. The predicted heat transfer coefficient agreed with his experimental data when the vapor Reynolds number was less than 35,000. Comparing his analytical model with the Nusselt analysis, Chato concluded that the Nusselt analysis was applicable when the liquid Prandtl number is of order 1 or greater, but when the liquid Prandtl number was less than 1, using the Nusselt analysis would underestimate the heat transfer coefficients.

Rufer and Kezios (1966) regarded the condensate flow model assumed by Chaddock (1957) and Chato (1961) as unrealistic. They assumed that the condensate

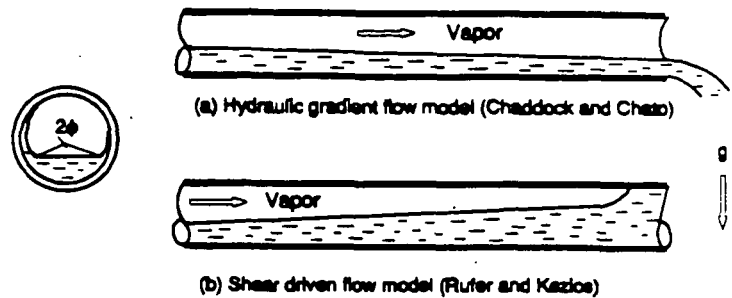


Fig. 2.2 Condensate flow models

2. Literature Review

depth at the bottom of an inclined or a horizontal circular tube increased in the direction of vapor flow (Fig. 2.2 b). They also assumed that the flow of the bottom condensate was mainly by the pressure gradient. An equation predicting the depth of the bottom condensate was derived from the mass, momentum, and energy balance equations of the bottom condensate. Rufer and Kezios also included the heat transfer to the bottom condensate. The average heat transfer coefficient was evaluated from the Nusselt analysis. In the momentum equation, they neglected the interfacial shear stress between the vapor flow and the bottom condensate on the basis of the assumption that the bottom flow of the condensate was stratified. The predicted condensation depth at the bottom was compared with the experimental data in terms of the flow angle of the bottom condensate wetted on the inside tube surface. They found that the predicted value was in good agreement with the experimental data.

Comparing the equation of Rufer and Kezios (1966) for the condensate depth with that of Chato (1962), Khabenskiy et al. (1981) concluded that both equations were basically the same. However, those two equations would give contradicting results due to the different initial conditions assumed for each equation (Chato assumed that the condensate depth increased along the condensing tube, while Rufer and Kezios assumed that the condensate depth decreased with increasing the length of the tube). Using an example for a condensing system including an horizontal or inclined condensing tube, Khabenskiy et al. indicated that the condensate flow patterns assumed by both Chato (1962) and Rufer and Kezios (1966) existed in practice. They considered that the flow model of Chato described the case of an incomplete condensation of vapor inside a horizontal or an inclined tube, while that of Rufer and Kezios simulated the situation of complete condensation inside the tube.

Rosson and Myer (1965) found that their experimentally determined heat transfer rates across the bottom condensate inside a horizontal condensing tube (using methanol and acetone as condensing fluids) was about 23 % of the heat transfer rates across condensate film covering the upper part of the inside surface of the tube. They

2. Literature Review

therefore concluded that the heat transfer to the bottom condensate should not be neglected. The heat transfer to the bottom condensate was evaluated using the von Kármán analogy between heat and momentum transfers. The heat transfer to the condensate film was determined using the Nusselt analysis. To include the effect of the interfacial shear stress in the Nusselt analysis, they used an experimentally determined function of vapor Reynolds number to replace an original constant in the Nusselt equation. A comparison of the model predictions with the experimental data showed that the predicted values were on the low side if the liquid Reynolds number was low and were on the high side if the liquid Reynolds number was high. They assumed that the deviation was caused by the use of the Lockhart-Martinelli (1949) correlation, which might not have been suitable for condensation.

Moalem and Sideman (1976) analyzed the simultaneous process of condensation of a vapor flow inside a horizontal tube and the evaporation of a fluid on the outer surface of the tube. Neglecting the effect of the interfacial shear stress on the condensate film, which was considered to be appropriate for vapor velocities of less than 15.2 m/s, they solved the momentum and energy equations using integral methods. They predicted the variation of the local heat transfer coefficient with the periphery of the tube. Similar to the experimental results of Rosson and Myer (1965), they showed that the heat transfer coefficient at the bottom of the tube was about 20 % of the highest heat transfer coefficient. Comparison of the predicted overall average heat transfer coefficient of condensate and evaporation with one source of experimental data showed that the predicted values were generally 30 - 40 % lower than the experimental data. The predicted low heat transfer coefficients might have been due to the neglect of the interfacial shear stress in the analysis.

High Mass Flow Rate of Vapor

High mass flow rate of vapor at the inlet to a horizontal tube leads to a thin

2. Literature Review

condensate film around the periphery of the tube. The condensate film flows in the axial direction of the tube, resulting in the annular condensation regime.

Soliman et al. (1968) developed an annular condensation model by modifying the energy equation (for condensation inside a tube) given by Carpenter and Colburn (1951). The main modification was in the expressions for the friction force including interfacial shear stress and the momentum change of condensate and vapor. In calculating the friction force, Soliman et al. neglected the effect of condensation of vapor (on the condensate) in the total interfacial shear stress and determined the friction force using the Lockhart and Martinelli method applied to an adiabatic two-phase flow. In evaluating the momentum change, they considered the condensate film as a turbulent liquid layer and assumed the ratio of the interfacial velocity to the average condensate velocity to be 1.25. By substituting the equations for the friction force and the momentum change into the Carpenter and Colburn expression, an equation predicting the heat transfer coefficient in an annular condensation was given. Two constants in the equation were determined based on a regression analysis with nine different sources of experimental data for condensation in both horizontal and vertical tubes. However, no comparison of the equation with other experimental data that were not used for determining the constants in the equation was reported.

The model of Soliman et al. (1968) was modified by Bae et al. (1971). In the modification, the von Kármán momentum-heat transfer analogy was used to determine the heat transfer coefficient, where the ratio of the eddy conductivity to the eddy viscosity was assumed to be 1 and the von Kármán universal velocity distribution was used to determine the condensate velocity. Also, the ratio of the interfacial velocity to the average liquid velocity, which varied approximately between 2 and 1.1, was assumed to be a unique function of δ^* ($\delta^* = \delta / v_l \sqrt{g \tau_w / \rho}$). With increasing δ^* , the velocity ratio decreased. From the analysis, an expression for predicting the heat transfer coefficient was derived, but the calculation of the heat transfer coefficient required considerable iteration. Subsequently, Traviss et al. (1973) simplified the

2. Literature Review

expression for heat transfer coefficients by neglecting a term representing the correction due to the difference between the wall and interfacial shear stresses. They claimed that neglecting the term was valid when the gradient of the quality of the mixture was not large. The predicted heat transfer coefficients were compared with their experimental data and the data of Bae et al. (1969). They found that the predicted values were generally lower than the experimental data. They considered that the deviation resulted from model not taking into account the effect of the entrainment of the condensing liquid; some of the experimental data was taken when entrainment occurred, which reduced the thickness of the condensate and increased the heat transfer coefficient.

Analyzing a heat transfer model similar to the one given by Bae et al. (1971), Cavallini and Zecchin (1974) determined the major non-dimensional parameters affecting the average Nusselt number in an annular condensation. Based on the regression analysis of their experimental data, an equation for the Nusselt number is given.

Jaster and Kosky (1976) studied condensation heat transfer in a mixed flow regime between an annular flow and a stratified flow (Fig. 2-1 a). First, they derived a criterion in terms of the ratio of the axial shear force and the gravitational body force to determine the annular and the stratified flow regimes. Based on this criterion, a heat transfer correlation for the mixed flow regime was given simply by using a linear interpolation from the known heat transfer correlation specified for an annular flow and from the available heat transfer correlation for a stratified flow. Comparison of the calculated heat transfer coefficient with the experimental data in the mixed regime showed an average deviation of $\pm 34\%$.

Shah (1979) developed a correlation for condensation inside tubes. This correlation was obtained from a modification of the single phase heat transfer correlation of Dittus and Boelter (1930) for a turbulent flow of a single phase fluid. The Dittus and Boelter correlation was multiplied by a term involving the quality.

2. Literature Review

The modification was derived by an examination of correlations for film boiling based on the assumption of similarity between the mechanisms of heat transfer during film condensation and film boiling inside tubes. Shah compared his heat transfer correlation with 474 different sets of experimental data from 21 independent sources for condensation inside both horizontal tubes and vertical tubes. The mean deviation is reported to be within $\pm 15.4\%$.

Kutsuna et al (1985) derived a system of ordinary differential equations for the film condensation inside a horizontal rectangular duct. In the derivation, they assumed that the temperature profile in the condensate film was linear and the interfacial shear stress was calculated using the Shekriladze approximation ($\tau_i = \dot{m}_x v_g$). The predicted heat transfer coefficient was in good agreement with their own experimental data.

2.2.3. Studies of Interfacial Shear Stress

The interfacial shear stress in condensation plays an important role in influencing the heat transfer rates. However, because of the difficulty in measuring the interfacial shear stress, different models have been proposed, but none has been validated.

Rohsenow et al. (1956) used a force balance on an element of condensate flowing along a vertical condensing surface to derive the interfacial shear stress. In their derivation, the momentum changes through the element (including the momentum effect due to the condensation of the vapor were assumed to be small and negligible.

A number of researchers [for example, Rosson and Myer (1965), Soliman et al. (1968), and Bae et al. (1971)] assumed that the interfacial shear stress in condensation is similar to that in an adiabatic two-phase flow. Therefore, some correlations normally applicable to adiabatic two-phase flows were used to determine the interfacial shear stress in condensation. In doing so, the effect of the momentum transfer caused by the mass transportation of the vapor condensed into liquid was neglected.

However, the aforementioned treatment on the interfacial shear stress was

2. Literature Review

regarded as inappropriate by Shekriladze and Gomelaury (1966). They suggested that the interfacial shear stress depended mainly on the effect of the momentum transfer due to the condensation of vapor into condensate. For high condensate rates, the interfacial shear stress is presumably approximately equal to the value of this momentum transfer.

Linehan et al (1969) suggested that the interfacial shear stress in the presence of condensation should be expressed as the sum of the adiabatic shear stress plus the product of the condensation rate and an average vapor velocity. This theory was tested in their experiments involving steam condensation inside a rectangular test section. The calculated local surface temperature and mean film thickness based on this theory was found to be close to the experimental results.

Jensen and Yuen (1982) used an expression of the interfacial shear stress of a two-phase flow without phase change to represent the term of the adiabatic shear stress in the Linehan model. Expression for the interfacial shear stress was given for the case of a smooth interface as well as for a wavy interface. For high condensation rates, the value of the momentum due to the condensation of the vapor was found to be the dominant factor in the expression of the interfacial shear stress, supporting the assumption of Shekriladze and Gomelaury (1966).

2.2.4. Experimental Studies of Condensation Inside a Duct

Akers et al. (1958) measured heat transfer coefficients with R-12 and propane inside a horizontal tube. The results showed that increasing the vapor velocity enhanced the average heat transfer coefficient. When the vapor velocity increased beyond a certain value, the average heat transfer coefficient exhibited a nearly linear relationship with the velocity. The experimental data at high vapor velocities were plotted on the basis of the parameters derived from a single phase heat transfer correlation proposed by Eckert (1950). The data with high vapor velocities correlated with Eckert equation. Akers et al. also investigated the effect of the differences

2. Literature Review

between the saturated vapor temperature and the condensing surface temperature (ΔT) on the condensation. It was found that effect of ΔT on the average heat transfer coefficient was not clear.

Chato (1962) conducted experiments with condensation of R-113 vapor flowing inside a 0.72 m long horizontal tube with 14.5 mm mean I.D. The condensate angle (Fig. 2.2) at the end of the test section was measured by visual observation and photography. The results of the experiment showed that increasing the slope of the test section to about 0.01 can lead to an increase in heat transfer rates. Further increasing the inclination did not increase the heat transfer rates appreciably. The experiment also showed that the orientation of the tube was not important at high vapor velocities.

Rossen and Myers (1965) measured the peripheral variation of local condensation heat transfer coefficients with methanol and acetone inside a horizontal tube using a heat meter. The tube was divided into a number of small areas. The heat flux measured from each area was defined as the local heat flux. The local heat transfer coefficient was then found from the measured local heat flux.

Goodykoontz et al (1966, 1967a, and 1967b) described a method for measuring the local heat transfer coefficient with R-113 and steam condensing inside a vertical tube. The axial temperature gradient of the coolant in the cooling jacket was measured using thermocouples. Neglecting axial conduction in the tube, the local heat transfer rate was determined by computing the product of the temperature gradient, the coolant flow rate, and the specific heat of coolant. The local heat transfer coefficient was calculated from the local heat transfer rate and the temperature difference between the saturation temperature of the vapor and the inner wall temperature.

Abis (1969) measured local heat transfer rate for forced convection condensation of R-12 inside a 2.44 m long, 12.7 mm I.D. horizontal tube. The vapor velocity was considered sufficiently high (refrigerant mass velocity, 135.62-446.20 kg/m² s) to produce an annular flow pattern throughout the entire length of the tube. The local

2. Literature Review

heat transfer coefficient was determined using a method similar to that of Goodykoontz et al (1966). The results showed that the local heat transfer coefficient decreased along the tube and increased when the vapor mass velocity increased. The effect of ΔT on the heat transfer coefficient was also studied, but no conclusion was drawn due to some conflicting results.

Using R-12 and R-22, Bae et al. (1971) measured the condensation heat transfer coefficients in the annular regime. The test section of nickel tube was 5.5 m long and had a 12.5 mm I.D. They compared their experimental data with those of Akers and Rosson (1960), Altman et al. (1959), and Chen (1962) using the coordinates suggested by Akers and Rosson (1960). Bae et al. found that their heat transfer coefficients were generally higher than those of the other researchers. They concluded that this was because the coordinates used in the comparison did not include the parameter of quality; since the quality was related to the thickness of condensate film (a major resistance to the heat transfer), any difference in the quality would lead to different heat transfer coefficients even when the vapor velocity was the same.

Sardesai et. al. (1981) reported measurements of the peripheral local heat transfer coefficients inside a 2.92 m long, 24.4 mm I.D. horizontal stainless steel tube, using R-113, steam, propanol, methanol, and n-pentane as the condensing fluids. Using thermocouples embedded in the tube wall, the local heat transfer coefficient was measured. The measured peripheral local heat transfer coefficient was used to determine the flow regimes. If the distribution of the local heat transfer coefficient was about uniform around the periphery of the tube, the flow regime was considered to be an annular flow; if the local heat transfer coefficient at the top of the tube was much higher than that at the bottom of the tube, the flow regime was considered to be a stratified flow. From the analysis of the experimental data, they found that the transition between the annular flow and the stratified flow regimes was determined by a parameter which was a function of the Martinelli number and the Froude number.

Kutsuna et al. (1985) reported experimental results of condensation of vapor flow

2. Literature Review

inside a horizontal rectangular duct. The test section was 100 mm wide, 30 mm high, and 500 mm long. The bottom plate of the duct was the condensing surface. The local heat flux was determined from a measurement of the temperature distribution in the condensing surface. The average heat flux was measured from the enthalpy of the condensate in the test section. The experimental results of the local heat transfer coefficient for pure steam showed a rapid decrease of the local heat transfer coefficient along the duct.

Christodoulou (1987) experimentally investigated the film condensation of a vapor flow inside a horizontal rectangular duct with R-113 condensing on the bottom plate of the duct. The duct was 40 mm wide, 25 mm high, and 1 m long. The condensing surface was made of a copper block, which was hollowed out into three separate, equal sections. Cooling water was circulated in a channel formed by those three sections. In the experiment, Christodoulou measured the film thickness of condensate using an ultrasonic technique, the sectional heat transfer coefficients, and the total average heat transfer coefficient. The results showed that the thickness of the condensate film increased with increasing distance from the entrance of the duct and decreased with increasing vapor velocity; the sectional heat transfer coefficients decreased with increasing distance from the entrance. However, the effect of vapor velocity on the total average heat transfer coefficient was not clear. Since the experiment was conducted within a limited range of inlet vapor velocity (0.15—0.45 m/s), no interfacial instabilities (interfacial waves) were observed in the experiment.

Barry and Corradini (1988) experimentally studied film condensation of a steam-air mixture in the presence of interfacial waves. The test section was a horizontal square duct of 102 mm wide, 102 mm high, and 1.83 m long. The bottom plate of aluminum in the test section was used as the condensing plate. To develop a technique for measuring the wave parameters, an isothermal experiment using air-water flow through the duct was carried out before the condensation experiment. The wave frequency, celerity, length, amplitude, and film thickness were measured using

2. Literature Review

hot-wire anemometry and probabilistic analysis. The local heat transfer coefficient along the length of the condensing surface was determined at four locations by measuring the temperature gradient along the condensing wall. The results of the condensation experiment showed that the local heat transfer coefficient decreased along the condensing surface and increased with increasing vapor velocity. Comparing the results of the condensation experiment and the isothermal experiment, they concluded that condensation may have a damping effect on wave initiation. However, the effects of interfacial waves on condensation heat transfer are not shown in the study.

2.3. Wave Initiation in Two Phase Flows

It has been observed that condensation heat transfer is considerably influenced by the flow regimes. Bell et al. (1970) compared the results from various correlations for condensation inside horizontal tubes and found that the difference between the various correlations was fairly large, varying by a factor of 10 or more for a given set of conditions. For condensation in the annular flow regime, the condensate film may be smooth or wavy, depending on the magnitude of the vapor velocity. According to Dukler (1977), the interfacial waves in the annular wavy flow regime substantially increased the transport of energy and momentum in both the vapor and liquid phases. This indicates that the condensation heat transfer rate in the annular flow regime with a smooth condensate film may be different from that with interfacial waves. Therefore, a study of the instability causing the initiation of the interfacial waves is important.

The instability of a liquid flowing horizontally adjacent to a gas flowing parallel to the liquid but with a different velocity was recognized by Helmholtz over a hundred years ago. Later, Kelvin also studied this instability. In their studies, the domain of each of the fluids was semi-infinite and viscous effects were ignored. Chandrasekhar

2. Literature Review

(1961) proposed a criterion to predict the instability. It is shown that both surface tension and gravity are stabilizing, but if either of them is neglected, the configuration is unconditionally unstable.

When the fluids, instead of being semi-infinite, are flowing between two parallel plates, the condition of instability, including surface tension (but neglecting viscous effects), is given by Milne-Thomson (1969). It is shown that the surface tension is significant only for short wave lengths corresponding to high wave numbers.

Feldman (1957) analyzed the stability of a liquid film with a very small thickness, in which the shear stress distribution was assumed to be linear, with a semi-infinite fluid on top of it; the two fluids flow with different velocities. He included the effect of the shear stress at the interface and gave the conditions for stability. From the results of his analysis, Feldman concluded that (in the following, subscripts 1 and 2 represent the lower fluid and the upper fluid)

a. If gravity and surface tension are ignored:

1. for very small ratios of ρ_2/ρ_1 , the flow is completely stable
2. for a given value of μ_1/μ_2 , there is always a value of ρ_2/ρ_1 for which the flow is unstable
3. as $\rho_2/\rho_1 \rightarrow 0$, the ratio of the wave speed to interfacial velocity approaches approximately 0.1
4. the critical conditions depend only on the liquid flow rate and not on the gas flow rate except for the change in the interfacial shear stress
5. all waves travel at speeds less than the velocity of the liquid—gas interface

b. If gravity and surface tension are significant, they are destabilizing.

Conclusions 2 and 3 seem to contradict conclusion 1. For air flowing over water

2. Literature Review

at 100 °C, Feldman quoted a critical liquid Reynolds number ($\rho_1 h_1 u_1 / \mu_1$) of 60,000 which appears to be much greater than the observed values. The physical conditions of 100 °C water in contact with air at atmospheric pressure is not realistic as vaporization may become significant. Conclusion b is in direct contradiction with the results given by Chandrasekhar (1961) and Milne-Thomson (1969).

The effect of viscosity stratification in two fluids was studied by Yih (1967). He pointed out that in both Couette and Poiseuille flows, the interface was always unstable, no matter how small the Reynolds number was. He also indicated that because, in practice, the upper fluid is lighter than the lower fluid and due to the stabilizing effect of gravity, such instabilities caused by viscosity stratification alone may not be discernible. His main point is that, when considering instabilities in such flows, viscosity stratification should be considered and that one of the parameters defining instabilities should be the Reynolds number.

The only study that takes into account phase changes in the flow appears to be that made by Kocamustafaogullari (1985). From a simplified equation for the stability, he derived a criterion for stability, which included the effects of gravity, surface tension, viscosity, and phase change. For condensation on a horizontal plate, the criterion predicted unconditional stability, (which contradicts experimental observations).

On the experimental side, Hanratty (1982) summarized the results of experiments conducted in a horizontal, enclosed channel with air and water as the fluids. For very low velocities of air, the interface was smooth. As the air velocity increased, long crested two-dimensional waves with wave lengths of 2.2-3.0 cm and with wave velocities greater than the liquid velocity appeared. Kao and Park (1972) reported results of experiments directed towards determining the effect of the presence of a layer of fluid in laminar flow (at low Reynolds numbers) on top of another fluid at much higher Reynolds numbers. They observed that the shear instability in the lower fluid occurred at a Reynolds number of 2300 and the disturbance at the interface

appeared when the liquid became turbulent. From their studies on condensation inside tubes, Soliman and Berenson (1970) reported that film instabilities were observed to originate very close to the inlet of the condenser tube and the instabilities appeared as irregularly shaped wave trains. They speculated the waves to be a combination of Kelvin-Helmholtz and Tollmein-Schlichting types.

2.4. Concluding Comments

From the survey of the available literature, it is found that a detailed study of condensation in the annular flow regime, especially condensation in the annular wavy flow regime, has not been done. Nearly all the analytical studies are based on the assumption of smooth film condensation. Several models also include constants which have to be determined from experimental results. Some models are based upon the analogies between heat and the momentum transports, depending upon the available pressure drop correlations for adiabatic two-phase flow. None of the analytical equations is supported by broad experimental verifications.

In addition to inadequate analytical work, the experimental work on condensation in a horizontal tube has also not been sufficient. Some researchers report only the average heat transfer coefficients, due to the relative ease of measuring them. Even though some researchers report experimental results of local heat transfer coefficient, in reality, the local value is actually an average value over a finite area of the condensing surface. Also, the experimental results about the effects of the interfacial waves on the heat transfer of condensation have not been reported.

3. OBJECTIVES

A survey of the literature reveals that the study on condensation in an annular flow regime is limited; more work is required in both the analytical modeling and the experimental investigation to understand and predict heat transfer in condensation.

The objectives of the research are as follows:

- to measure film thickness, local heat transfer coefficient, average heat transfer coefficient, wave length, and wave speed of condensation of a vapor flow inside horizontal rectangular duct
- to identify the dimensionless parameters that are significant in the condensation heat transfer
- to study the initiation of interfacial waves with phase change (condensation) and without phase change (air-liquid flow with liquid viscosity variation)
- to develop a simple analytical model for condensation of a vapor flow inside a horizontal rectangular duct

4. DESCRIPTION OF EXPERIMENTS

4.1. Introduction

The two main purposes of the experiment were to measure the heat transfer coefficients during condensation of a vapor flowing inside a horizontal rectangular duct (with the vapor condensing only on the bottom plate of the duct), and to study the effect of the interfacial waves on the heat transfer coefficient. Two separate experimental set-ups were used in the experiments. One was a condensation set-up for measuring the heat transfer with a smooth thin condensate film or with interfacial waves. To assist in the study of interfacial wave initiation, experiments were also conducted in an adiabatic air-liquid flow set-up. Since the geometric shapes and dimensions of the test sections in both experimental set-ups were identical, it is possible to compare the results of the interfacial wave initiation in the condensation experiment with those in the adiabatic air-liquid flow.

The experimental set-ups and procedures are separately described for condensation, and wave initiation in an adiabatic air-liquid flow.

4.2. Experimental Set-up of Condensation

The experimental set-up of condensation was a modification of a previous work by Christodoulou (1987) and is schematically shown in Figs. 4.1 and 4.2. The set-up included a condensation loop and a coolant loop. In the condensation loop, vapor was generated from a boiler and admitted to the rectangular duct of the test section through a converging unit. Part of the vapor was condensed on the bottom condensing plate

4. Description of Experiment

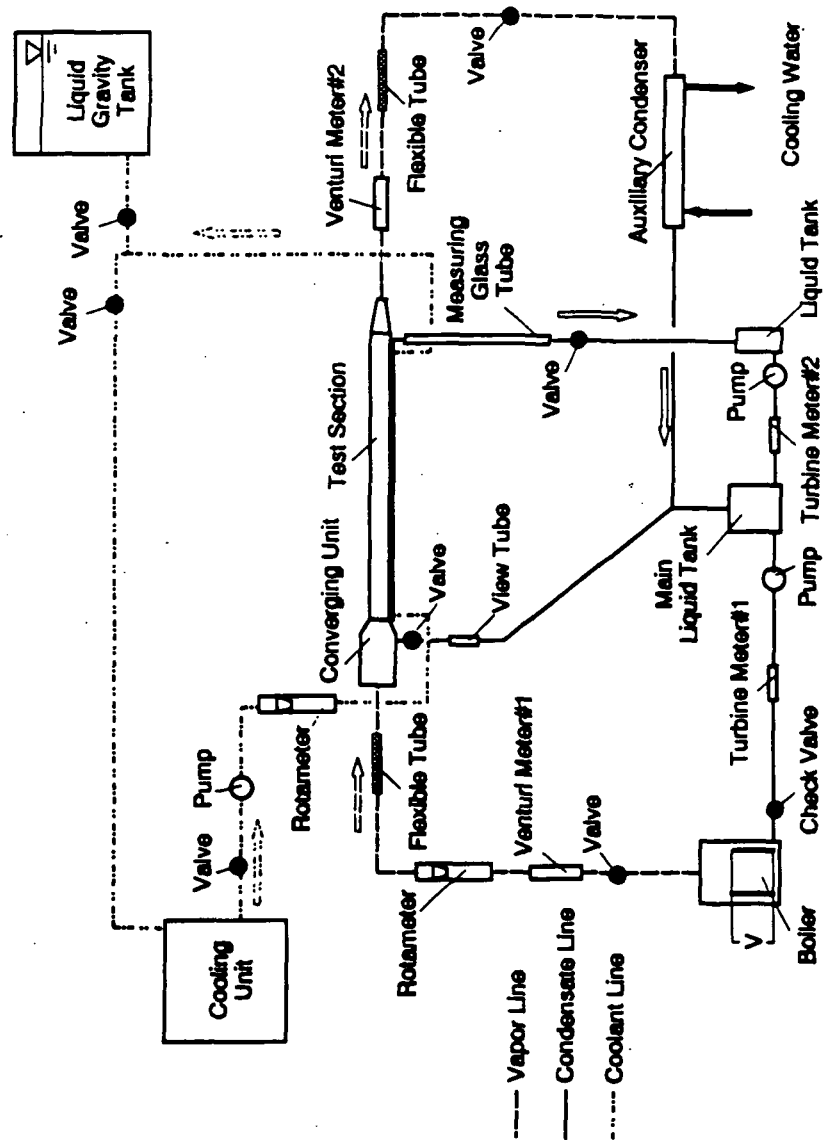


Fig. 4.1 Schematic of experimental set-up of condensation

4. Description of Experiment

ORIGINAL PAGE
BLACK AND WHITE PHOTOGRAPH

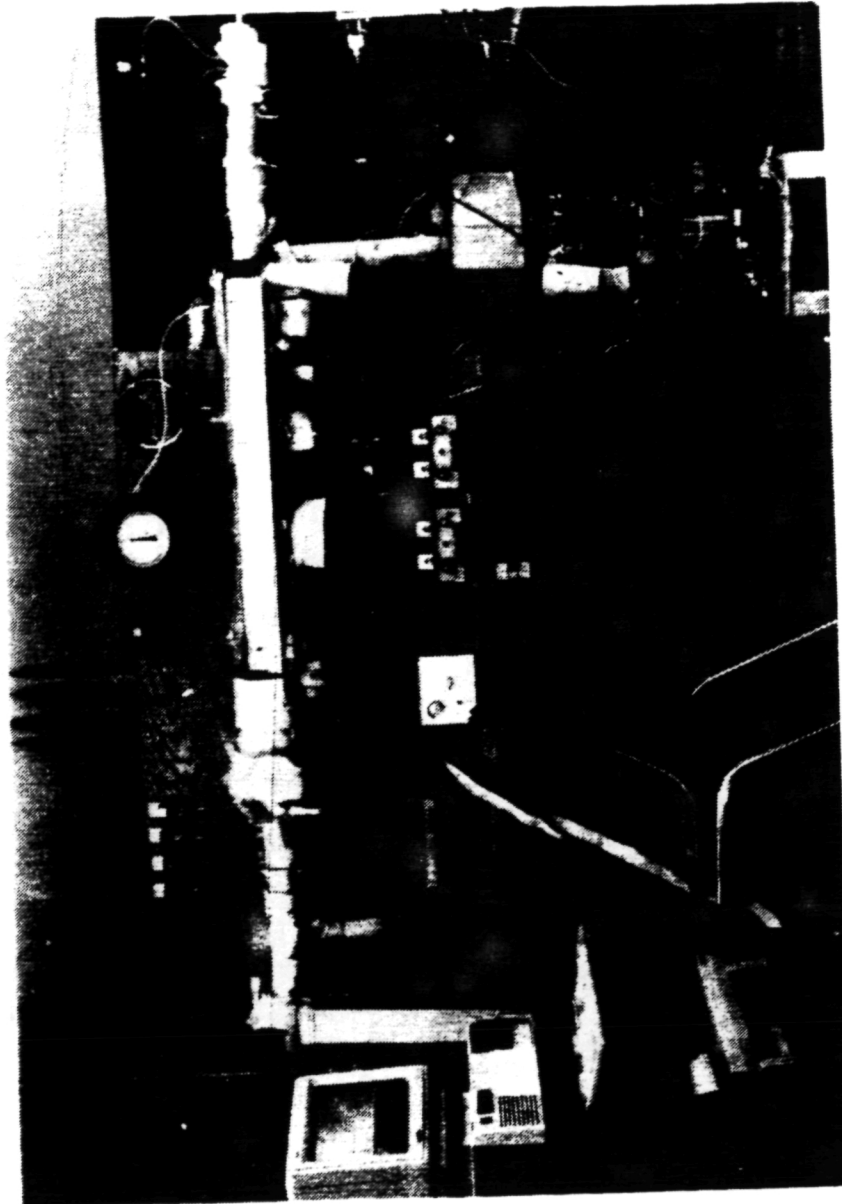


Fig. 4.2 Photograph of experimental set-up of condensation

4. Description of Experiments

inside the test section, while the rest of the vapor was discharged from the test section and was completely condensed in an auxiliary condenser. The condensates from the auxiliary condenser and the test section were gathered in a main liquid tank, from which the condensate was pumped back to the boiler. In the coolant loop, cooling water, which was provided by a temperature controller, flowed into the cooling channel of the test section via a set of rotameters. After passing through the cooling channel, the cooling water returned to the temperature controller.

The experimental set-up was assembled and frequently checked for leakage.

The following sections describe the apparatus used in the condensation set-up.

4.2.1. Test Section

The schematic of the test section is shown in Fig. 4.3. Details of the cross section of the test section are presented in Fig. 4.4.

The test section consisted of a rectangular duct and a cooling channel. The inside dimensions of the rectangular duct were 0.04 m wide, 0.025 m high, and 1 m long. The bottom condensing surface was of 0.914 m long, 0.04 m wide, and 6.4 mm thick copper plate. The side and top plates of the duct were of transparent polycarbonate sheets, which permitted visual observation of the flow patterns of the condensate. The condensate metering tube at the exit of the test section, which was also used as a drain for all the condensate in the test section, had an inside diameter of 6.4 mm and was connected to a small piece of a stainless steel plate attached to the end of the copper condensing plate. The top of the stainless steel plate was flush with the surface of the copper plate.

The cooling channel was underneath the condensing surface. The side plates of the channel were of brass; the bottom plate of the channel was of polycarbonate. The channel was divided into three equal sections by 3.2 mm thick plexiglass separators. Each section was 305 mm long and 17.5 mm deep. A mixing chamber (Fig. 4.5) was placed at the outlet of each section. The purpose of the mixing chamber was to assure

4. Description of Experiment

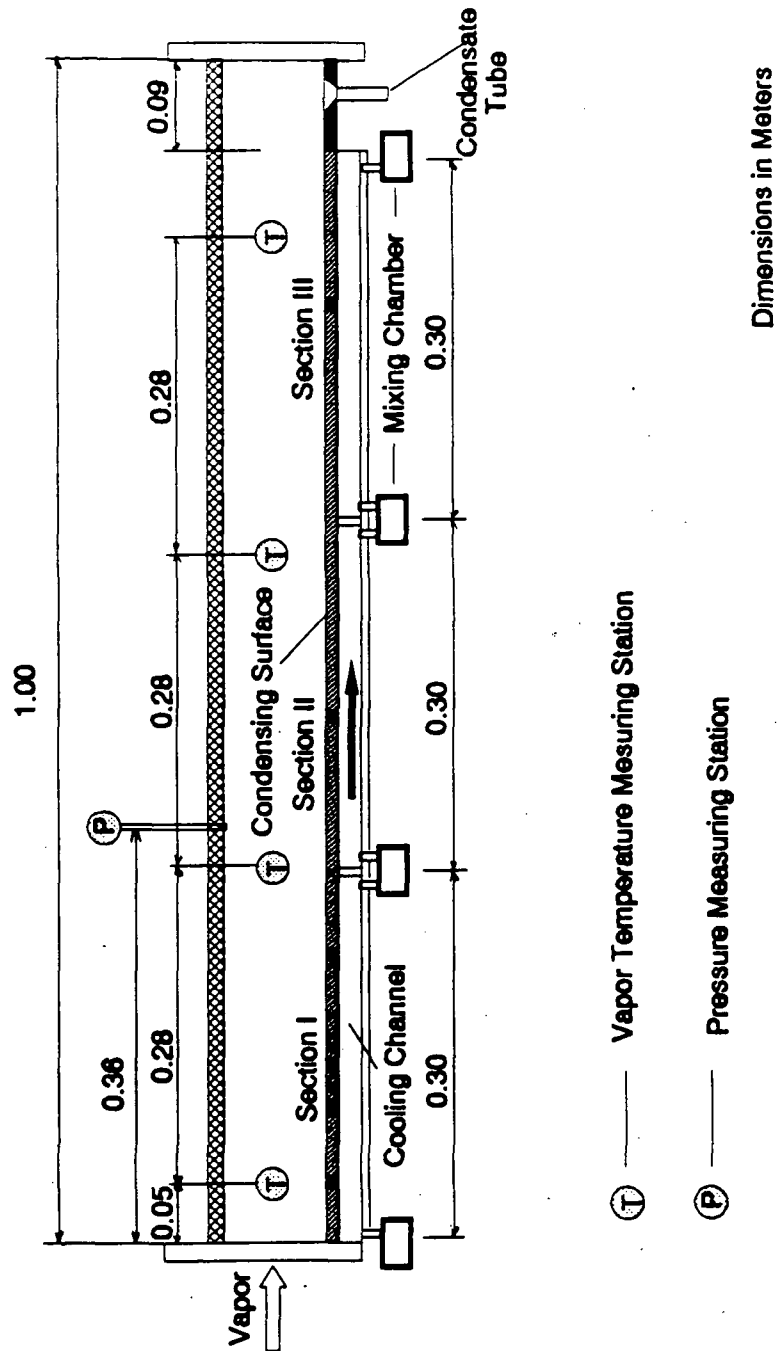


Fig. 4.3 Schematic of test section of condensation

4. Description of Experiment

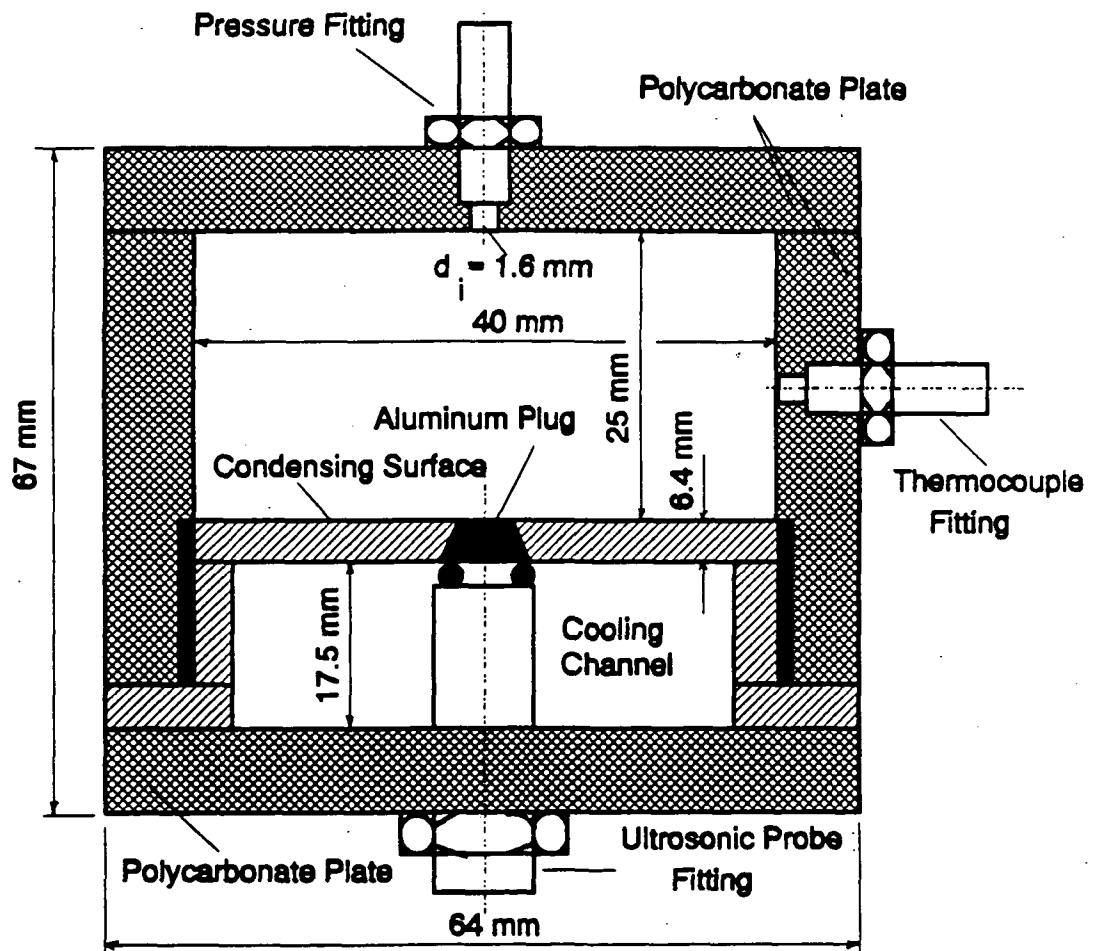


Fig. 4.4 Cross section of test section of condensation

4. Description of Experiments

the measurement of the correct mean coolant temperature by mixing the coolant in the chamber.

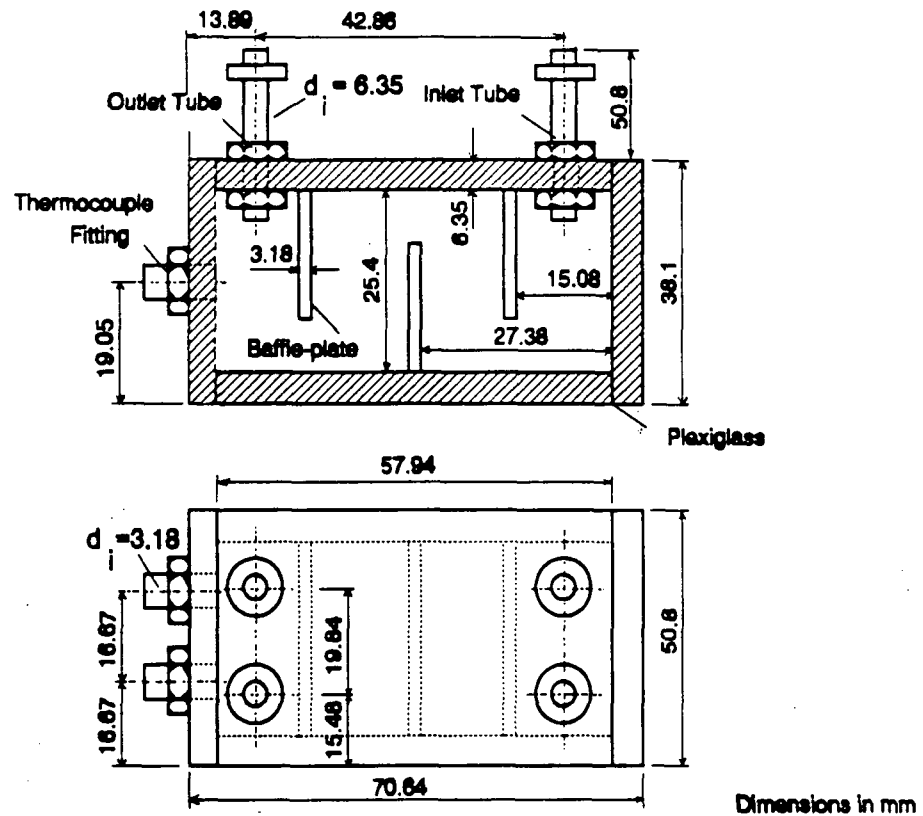


Fig. 4.5 Details of mixing chamber

The test section was mounted horizontally. A liquid level was used to ensure that the test section was horizontal. To allow for the thermal expansion of the tubes connected to the test section, flexible tubes were installed at the inlet and outlet of the test section. The test section was insulated with fiber glass and styrofoam sheets.

4. Description of Experiments

4.2.2. Converging Unit

To provide a uniform velocity distribution of vapor, a converging unit was installed at the inlet of the test section (Fig. 4.6). The converging unit consisted of a rectangular section and a reducer section. The walls of the two sections were of 3.18 mm thick brass plates. The inside dimensions of the rectangular section were 101.6 mm wide, 101.6 mm high, and 200.02 mm long. The length of the reducer section was 50.8 mm. The inside dimensions of the outlet of the reducer section were 40 mm wide and 25 mm high, which were identical to those of the test section. To assist in a uniform flow, a flow deflector was installed in the converging unit near its inlet and thin glass tubes were packed in the rectangular section. To assist in a uniform flow, a flow deflector was installed in the converging unit near its inlet and thin glass tubes were packed in the rectangular section.

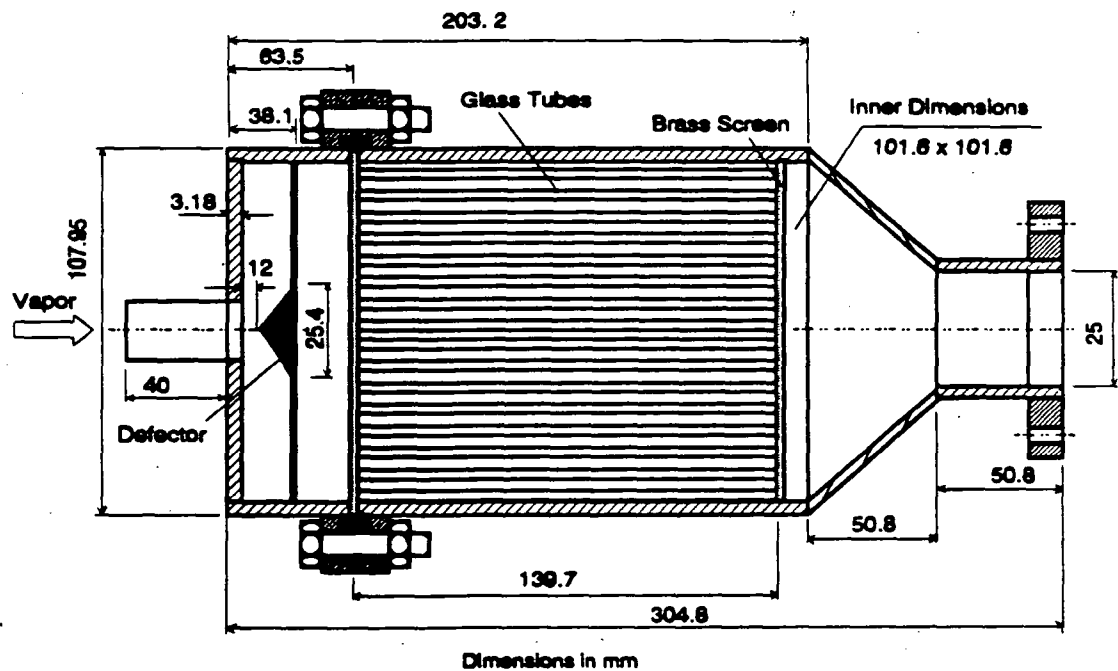


Fig. 4.6 Details of converging unit

4. Description of Experiments

The effectiveness of the converging unit was tested with air. The testing procedure and results are detailed in Appendix B, where it is shown that the velocity profile at the outlet of the converging unit was mostly uniform except near the side plates of the outlet where the velocities were lower than the average velocity due to the wall friction. In the test, the average deviation of the measured velocity at the outlet of the unit was $\pm 9.10\%$.

4.2.3. Boiler

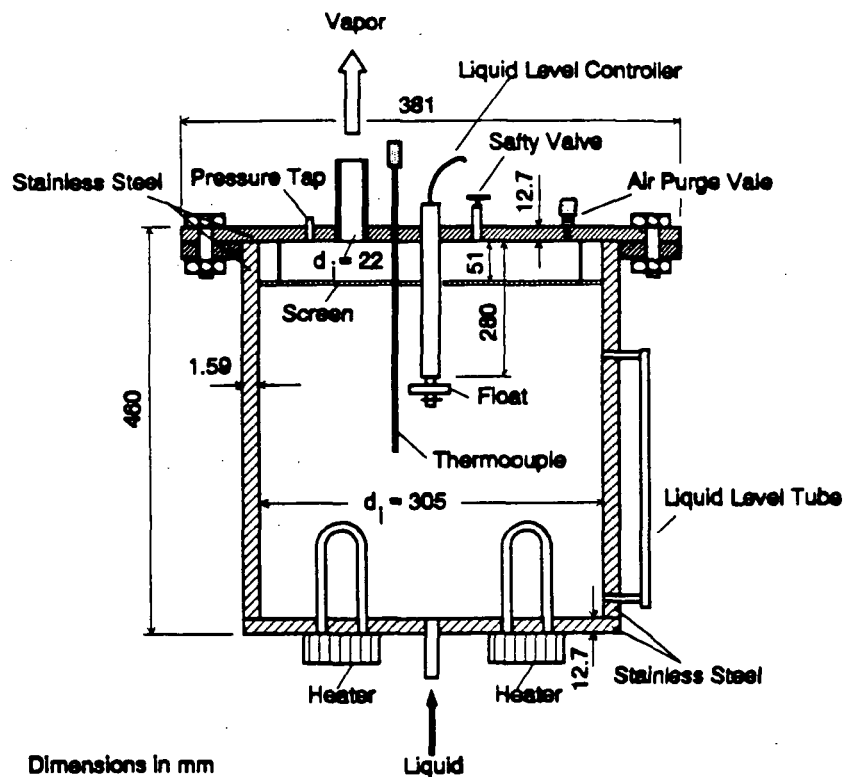


Fig. 4.7 Details of boiler

Details of the boiler are shown in Fig. 4.7. The 129 liter capacity boiler was fabricated from stainless steel. The maximum designed working pressure of the boiler

4. Description of Experiments

was 30 psi. The boiler usually contained about 23 liters of liquid. The liquid was heated by two 3 kw electrical heating elements mounted at the bottom of the boiler. A brass mesh screen covering the upper cross section of the boiler was used to reduce the liquid carryover. The mesh screen was located about 50 mm below the top of the boiler and was approximately 80 mm above the normal level of liquid in the boiler.

The temperature of the boiler was measured by a copper-constantan thermocouple. The pressure of the boiler was measured by a Bourdon Type Gauge through a pressure tap mounted on the top of the boiler. The level of the liquid in the boiler was observed through a view glass tube installed vertically on the side of the tank. This level was also automatically monitored by a level controller with a float on the surface of the liquid. If the liquid height was lower than 155 mm, the controller shut off the power supply to the heating elements until the normal level of fluid was restored. If the pressure of boiler was more than 70 kPa above the atmosphere pressure, a safety valve installed on the top of the boiler opened to relieve the pressure. Prior to its operation, the boiler was hydraulically tested at a pressure of 414 kPa.

4.2.4. Auxiliary Condenser

Details of the auxiliary condenser are shown in Fig. 4.8. The shell of the condenser was of stainless steel; the tubes inside the condenser were of copper. The vapor flowing in the shell side was cooled by building water supply flowing inside the tubes. The total heat transfer surface of the condenser was 0.24 m².

4.2.5. Temperature Controller and Gravity Tank for Coolant

A temperature controlling unit was used to supply cooling water to the test section. This unit included a heating circuit and cooling circuit. The controller had a capacity of delivering the cooling water to the test section at a rate of 0 to 7.6 liters per minute with an operating range from -30 °C to +70 °C. The temperature controller also served as a large coolant storage tank (= 46 liters) during experiment.

4. Description of Experiment

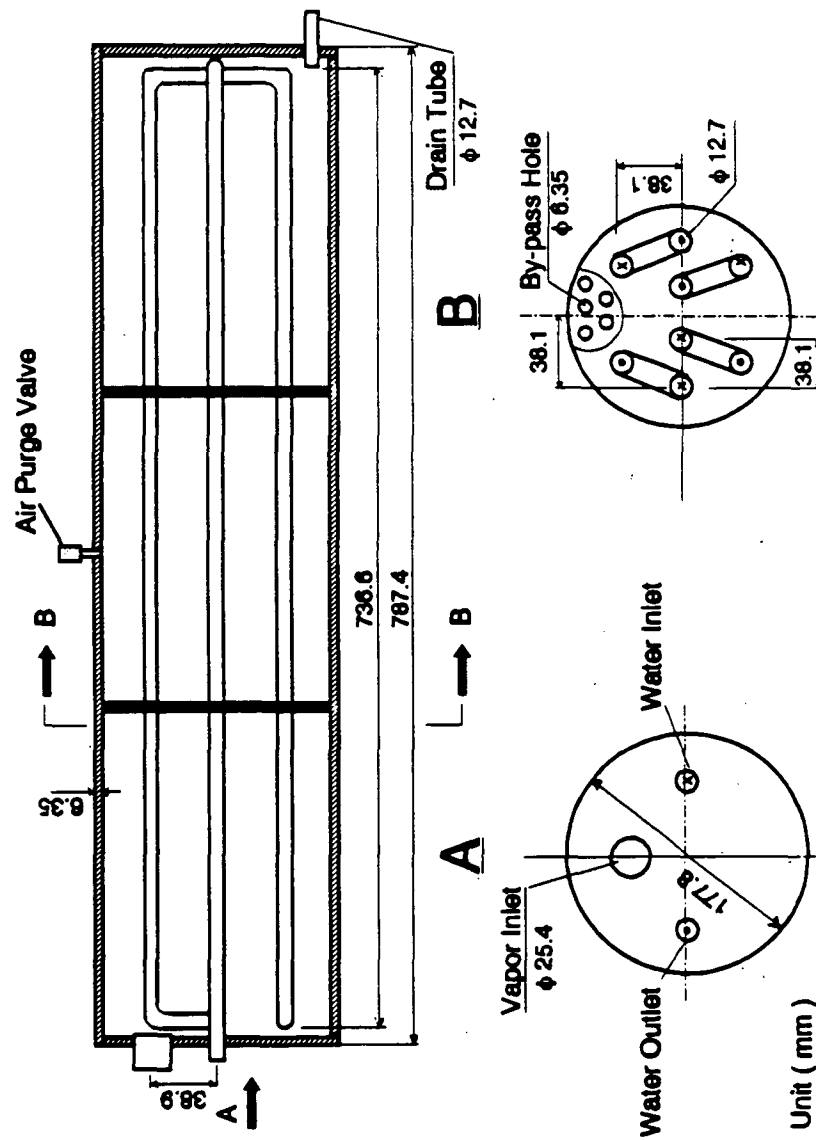


Fig. 4.8 Details of auxilliary condenser

4. Description of Experiments

The gravity tank was a 0.5 m high and 0.36 m in I.D. container filled with water and connected to the temperature controller through a valve. When the experiments were completed for the day and the temperature controller was shut off, the valve connecting the gravity tank and the cooling loop was opened. Since the tank was placed approximately 1 m above the test section, the tank provided positive water pressure to the cooling channel in the test section to prevent any air leak into the channel from the environment.

4.3. Experimental Set-up of Adiabatic Air-liquid Flow

The shape and the dimensions of the test section in the experimental set-up of the adiabatic air-liquid flow were identical to those of the test section for condensation. Therefore, it is expected that a comparison of the result of the wave initiation with the air-liquid flow with the results of the wave initiation with condensation will lead to a better understanding of the effect of condensation on wave initiation.

Fig. 4.9 is a schematic of the experimental set-up. A photograph of the set-up is provided in Fig. 4.10. The set-up consisted of an air passage connecting to the building compressed air line, and a liquid loop. During experiments, the air from the building supply passed through a compressed air reservoir, a converging unit, and an inlet section into the test section. The air flow rate was controlled by adjusting the pressure regulators at the inlet and the outlet of the reservoir and was measured by a venturimeter. In the liquid loop, the liquid from a gravity tank entered the test section. The liquid from the test section drained to a collecting tank, from where the liquid was pumped back to the gravity tank. When the gravity tank was full, the liquid overflowed to the collecting tank.

Fig. 4.11 illustrates the inlet section. The inside dimensions of the inlet section were same as those of the test section (40 mm wide and 25 mm high). The inlet section was divided into two parts (an air channel and a liquid channel) by a H shaped

4. Description of Experiment

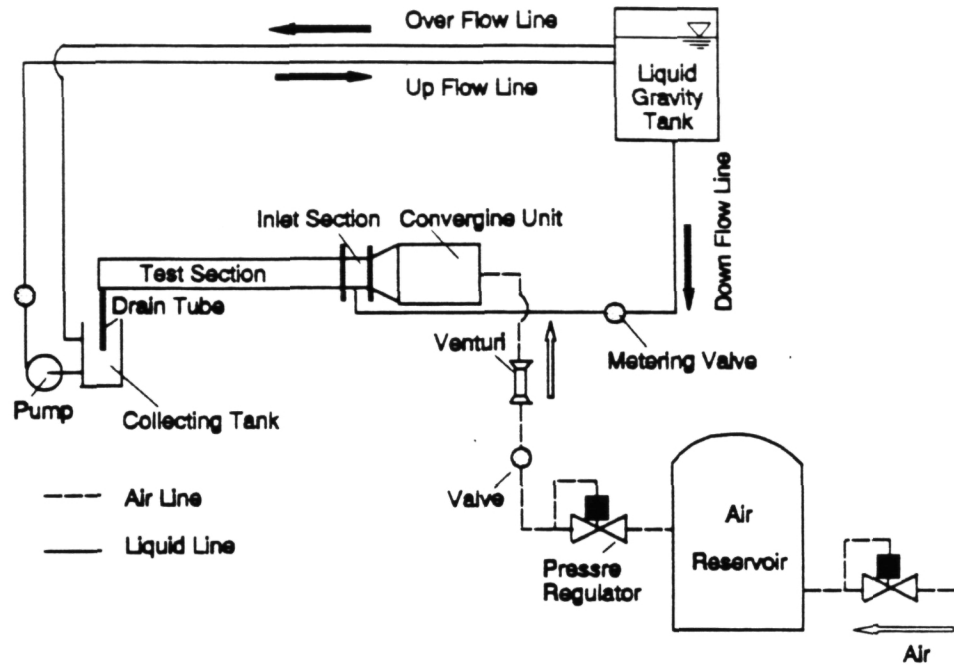


Fig. 4.9 Schematic of experimental set-up of air-liquid flow

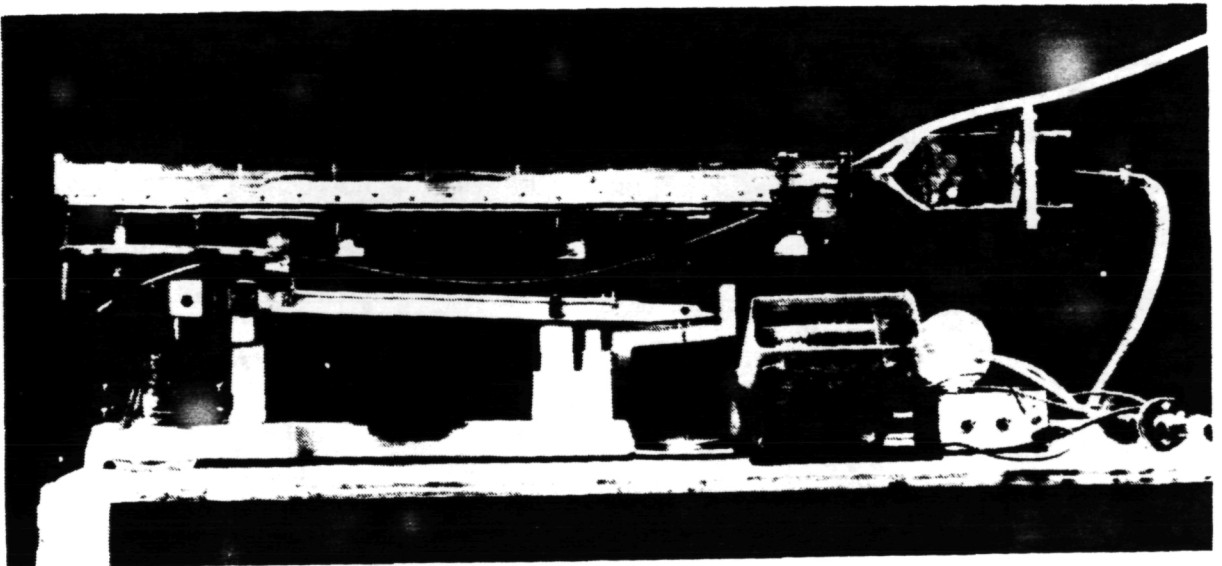


Fig. 4.10 Photograph of experimental set-up of air-liquid flow

4. Description of Experiments

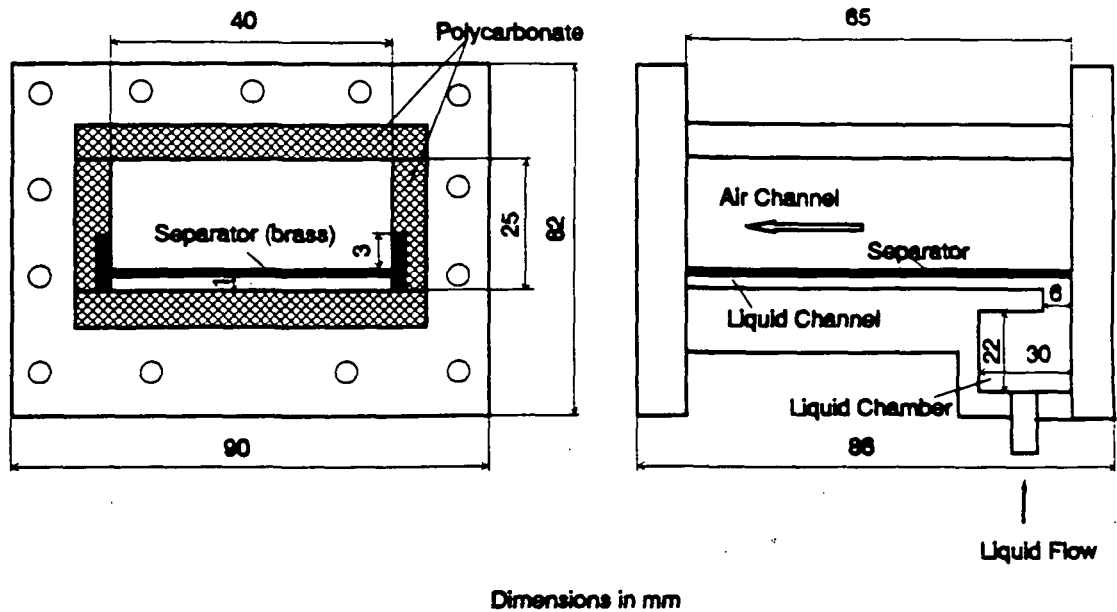


Fig. 4.11 Details of Inlet section

horizontal separator inserted inside the section (Fig. 4-11). Based on the way of installing the separator, the height of the liquid channel was changed to either 1 mm or 3 mm.

4.4. Measurements in Condensation Experiment

The measured variables in the condensation experiment were

- volumetric flow rate of vapor
- volumetric flow rate of condensate
- volumetric flow rate of coolant

4. Description of Experiments

- temperatures of the condensing surface at different locations, vapor, and coolant at the inlet and the outlet of each section
- vapor pressure in the test section
- thickness of condensate film at five locations along the condensing surface
- wave length and the wave speed in the condensate

The various instruments used in the experiments are described in the following sections

4.4.1. Measurement of Vapor Flow Rates

The vapor flow rates at the inlet of the test section was measured by a venturi meter and a rotameter. A turbine flow meter (turbine meter #1 in Fig. 4.1) was used to measure the condensate flow rate to the boiler. The rotameter and the venturi meter (venturi#1) were installed in the vapor line between the boiler and the inlet of the test section; the turbine flow meter (turbine#1) was installed in the condensate line between the inlet of the boiler and the outlet of the main liquid tank.

The rotameter and the venturi meter were calibrated in the laboratory using a laminar flow meter with air as the fluid. The turbine flow meter was calibrated by the manufacturer. The procedures and results of the laboratory calibrations of the rotameter and the venturimeter are given in Appendix C.

In the experiment, the vapor flow rate measured by the rotameter was used in the data analysis, while the measurements from the venturimeter and the turbine flow meter were only used as a check on the measurements with the rotameter. The differences were usually in the range of ± 5 -10 %.

4.4.2. Measurement of Condensate Flow Rate

The condensate flow rate from the test section was measured by a gauge glass installed at the outlet of the test section (Fig. 4.1); details of the gauge glass are shown

4. Description of Experiments

in Fig. 4.12. The gauge glass was provided with a quick shutoff valve at its bottom. The glass tube was 455 mm long with 13 mm I.D. When the quick shutoff valve was closed, the time required for the condensate to fill the gauge glass from the lower marker to the upper marker (Fig. 4.12) was measured; the temperature at the outlet of the gauge glass was measured by a thermocouple. From those measurements, the flow rate of the condensate was determined.

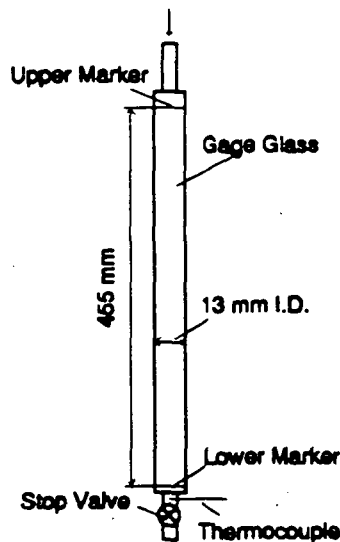


Fig. 4.12 Details of gauge glass

The flow rate of the condensate was also determined as the difference in the vapor flow rate into and out of the test section as measured by the venturimeters. A turbine flow meter (turbine meter#2 in Fig. 4.1) was installed at the outlet of the liquid tank collecting the condensate from the test section. It also measured the condensate flow rate from the test section.

The difference between the condensate measured by the gauge glass and that measured by the venturimeter varied from $\pm 5\%$ to $\pm 15\%$; the difference between the

4. Description of Experiments

gauge glass and the turbine flow meter was $\pm 5\%$ to $\pm 20\%$. The difference from the turbine flow meter was due to the variation of the liquid level in the liquid tank connecting the inlet of the turbine flow meter. Since the liquid level was influenced by the pressure in the test section, the vacuum in the auxiliary condenser, and the speed of the micro-pump in the condensate line, it was somewhat difficult to maintain a constant liquid level. Rate of condensation as measured by the gauge glass was used in the data analysis.

4.4.3. Measurement of Cooling Water Flow Rate

Cooling water flow rate was measured with a set of four rotameters in parallel. The rotameters were calibrated in the laboratory by weighing the water collected in a measured time interval. Results of the calibration are given in Appendix C. During experiments, the measurements from the rotameters was checked at regular intervals by weighing the coolant collected in a measured time.

4.4.4. Measurement of Temperatures

The following temperatures were measured in the experiment

- condensing surface
- vapor in the test section
- condensate
- cooling water in the cooling channel
- vapor through the flow meters
- surface of vapor tube, converging unit, and test section
- boiler and environment

Temperatures of Condensing Surface

The temperature of the condensing surface was measured by eight thermocouples embedded in the surface of the condensing plate. The layout of the thermocouples is

4. Description of Experiment

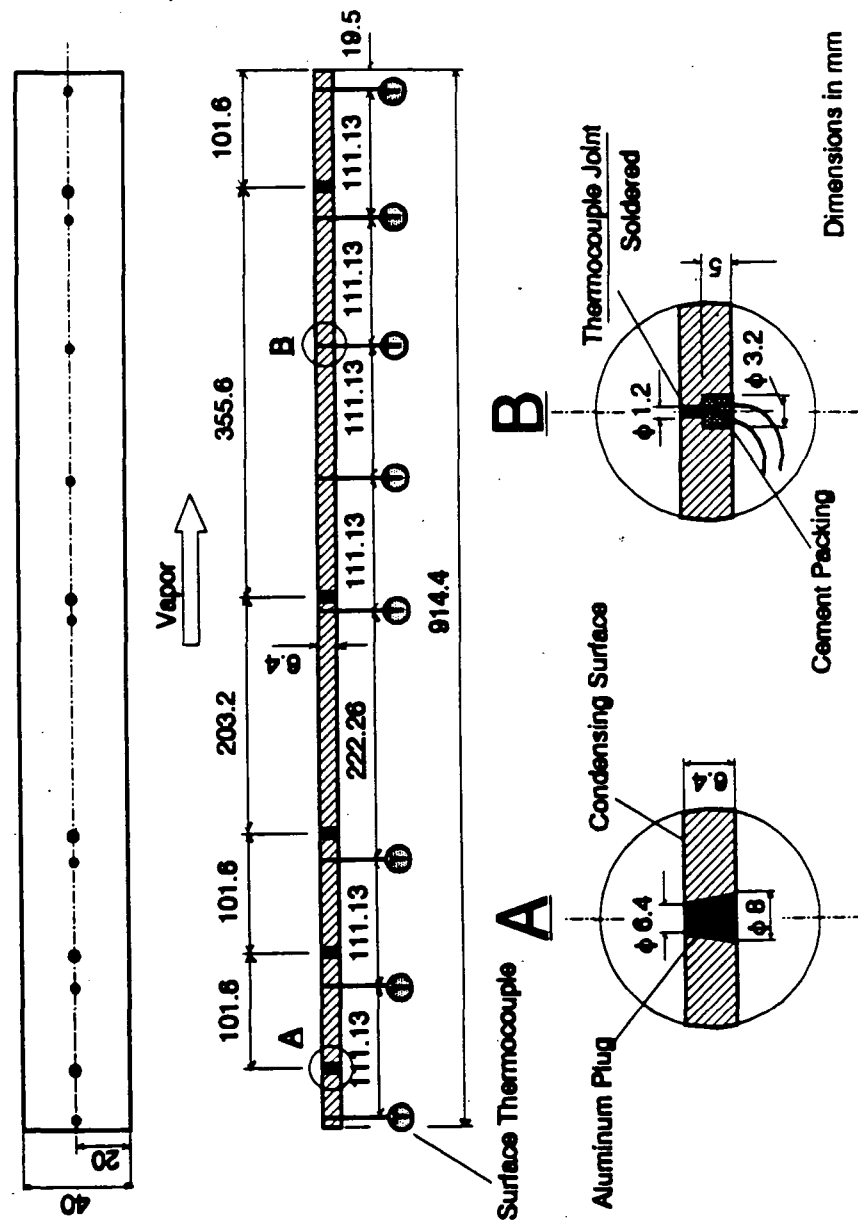


Fig. 4.13 Details of condensing surface

4. Description of Experiments

shown in Fig. 4.13. Each thermocouple junction was placed near the condensing surface through a 1.2 mm I.D. hole in the copper plate and soldered to the condensing surface. The residues of the soldering material on the surface were cleaned by using fine sand paper and Brasso (a metal polish solution). The space between the wire and the hole (3.2 mm I.D) in the plate was filled with electrical cement.

Temperatures of Vapor in the Test Section

The temperature of vapor in the test section was measured by four equally spaced thermocouples placed along the center line of the test section (Fig.4.3). The distance between two consecutive thermocouples was 280 mm. The distance from the entrance of the test section to its nearest thermocouple was 50 mm. The distance between the thermocouple hot junction and the side wall was 10 mm (Fig. 4.14).

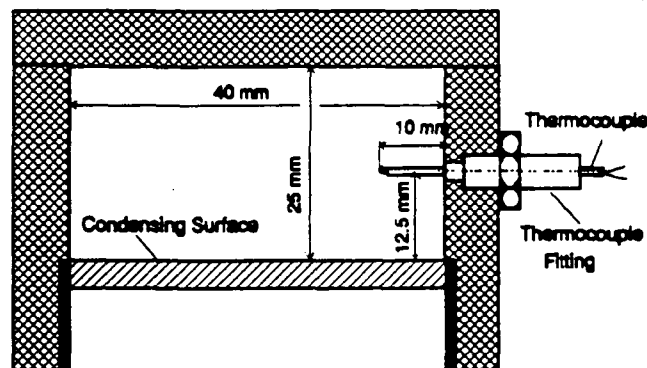


Fig. 4-14 Arrangement of thermocouples for measuring vapor temperature

Temperature of Condensate

The temperature of the condensate in the gauge measuring glass was measured by

4. Description of Experiments

a thermocouple. The location of the thermocouple is shown in Fig. 4.12.

Temperatures of Cooling Water

The temperatures of cooling water were measured using thermocouples installed inside the inlet and the outlet of the mixing chambers. The temperature difference of cooling water across each section of the cooling channel was measured using three pairs of differential thermocouples placed inside each mixing chamber. The total temperature change of the cooling water across the whole cooling channel was also measured by a pair of differential thermocouples placed at the inlet and the outlet of the channel. This total temperature change was compared with the value of the sum of the three temperature changes measured at each section of the cooling channel. The difference was usually within $\pm 2\%$. The arrangement of the differential thermocouples is shown in Fig. 4.15.

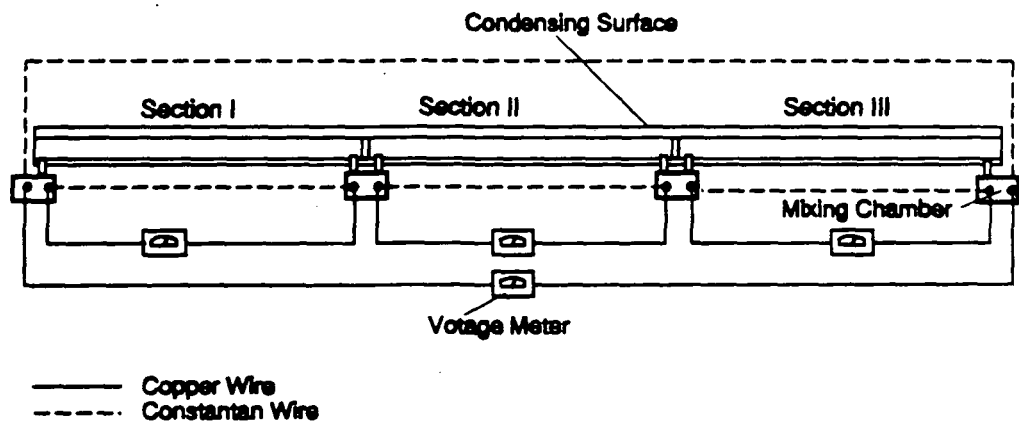


Fig. 4.15 Arrangement of differential thermocouples

4. Description of Experiments

Temperatures of Vapor at the Outlet of Rotameter and Venturi Meters

For determining the vapor mass flow rate using the rotameter and venturi meters, the temperatures of vapor at the outlet of the flow meters were needed. The temperatures of vapor at the outlet of the flow meters were measured using thermocouples.

Surface Temperatures of Vapor Tubes, Converging Unit, and Test Section

To prevent condensation of the vapor on the walls of the vapor tubes, the converging unit, and the test section, the surface temperatures of these parts were maintained at a slightly higher temperature than the saturation temperature of the vapor using additional heating elements. The heating elements were either wrapped around the tubes and the converging unit or placed on the top of the test section. The power to the heating elements was adjusted, so that the vapor was superheated by 3-5 °C. The surface temperatures of the vapor tubes, the converging unit, and the test section were measured using thermocouples.

All thermocouples used in the experiment were made of 28 gauge copper-constantan wires and were calibrated. A description of the calibration is given in Appendix D.

4.4.5. Measurement of Vapor Pressure

The vapor pressure in the test section was measured using a bourdon tube pressure gauge. The position of the pressure tap is shown in Figs. 4.3 and 4.4. The inside diameter of the pressure tap was 1.6 mm. The tube (made of transparent teflon) connecting the pressure gauge with the pressure tap was installed vertically and was heated slightly by an auxiliary heating element. If any vapor condensed in the tube, the condensate flowed down into the test section without blocking the tube.

The boiler pressure was measured by a bourdon tube pressure gauge. The atmospheric pressure was measured by a barometer in the laboratory. The vacuum in

4. Description of Experiments

the auxiliary condenser was observed through a vacuum meter.

4.4.6. Measurement of Film Thickness

An ultrasonic transducer was used to measure the condensate film thickness at five locations along the condensing surface. During the initial test of the transducer, it was found that with a copper plate, the attenuation of the reflected signal was significant. The signal strength was improved by using an aluminum plug. As a result, aluminum plugs were inserted in the copper plate at each location where the film thickness was to be measured. The aluminum plugs were made flush with the copper plate. The locations of the aluminum plugs are shown in Fig. 4.13.

Fig. 4.16 illustrates the ultrasonic measurement equipment. The ultrasonic transducer sent a 20 MHZ signal to the condensate film through the aluminum plug. The signal was first reflected at the interface of the transducer and the aluminum plug, next at the interface of the condensate film and the condensing surface, and then at the interface of condensate and vapor. In Fig. 4.16, the peak numbered 1 represented the

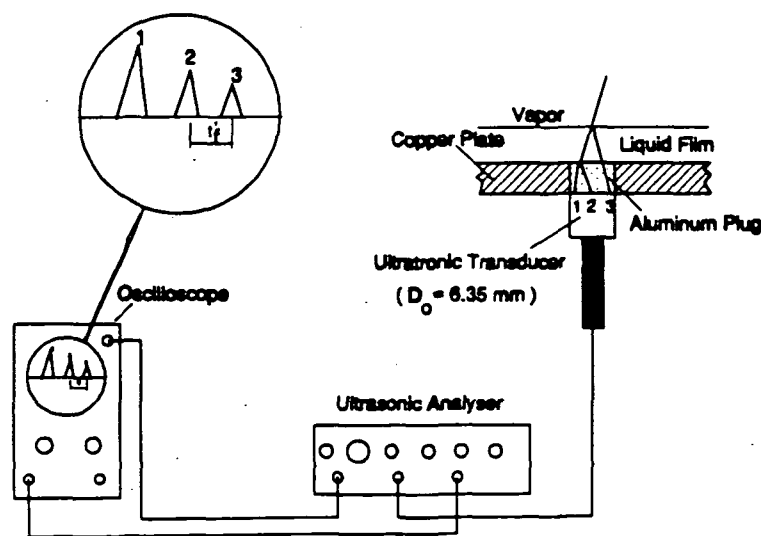


Fig. 4.16 Illustration of film thickness measuring system

4. Description of Experiments

reflection at the interface of the transducer with the bottom surface of the aluminum plug; peak number 2 was the signal reflected from the aluminum plug-condensate interface; peak number 3 was the reflection of the signal at the condensate-vapor interface. The interval (t_r') between number 2 and 3 was the time for the signal to pass through the film to reach the vapor-liquid interface and then reflected from there. Having t_r' and a_r (sonic velocity of liquid), the film thickness was determined. The procedure of using t_r' and a_r to find the film thickness is described later in Section 4.9.1.

A typical trace of the ultrasonic signal displayed on the oscilloscope screen is shown on Fig. 4.17. A description of calibration of the ultrasonic transducer (for obtaining the sonic velocity of the condensing fluid) is given in Appendix E.

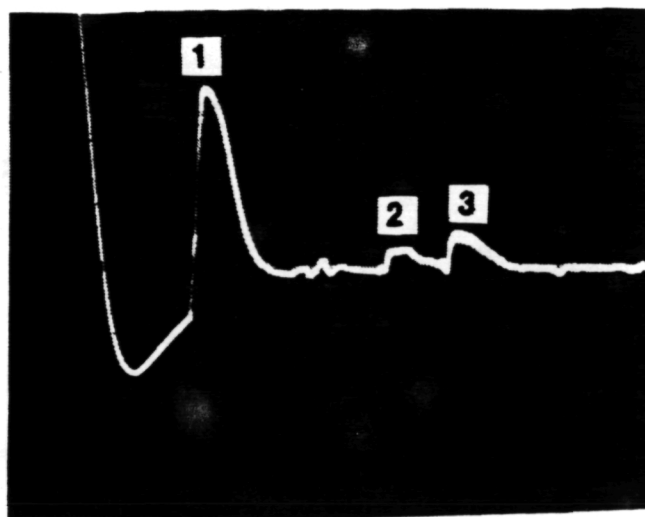


Fig. 4.17 Typical pulse trace

4.4.7. Measurements of Wave Length and Wave Speed

Wave Length

The wave length was determined by measuring the distance between two

4. Description of Experiments

consecutive crests. In the experiment, photographs of interfacial waves were taken with a ruler placed along the side of the test section. From the photographs, the wave length was measured (Fig. 4.18).

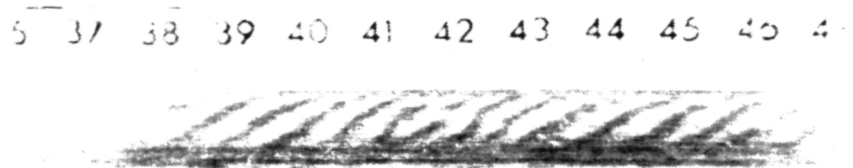


Fig. 4.18 Photograph of wave length (The unit of the scale in the picture is mm.)

Wave Speed

The wave speed was measured using a mechanical device shown in Fig. 4.19. The device was a moving belt driven by a variable speed motor. The top surface of the belt was marked with parallel white strips. During the measurement, the device was placed next to one of the sides of the test section, the speed of the motor was adjusted so that the strips on the belt moved at the speed of the waves. The speed of the belt was determined by measuring the rotational speed of the motor.

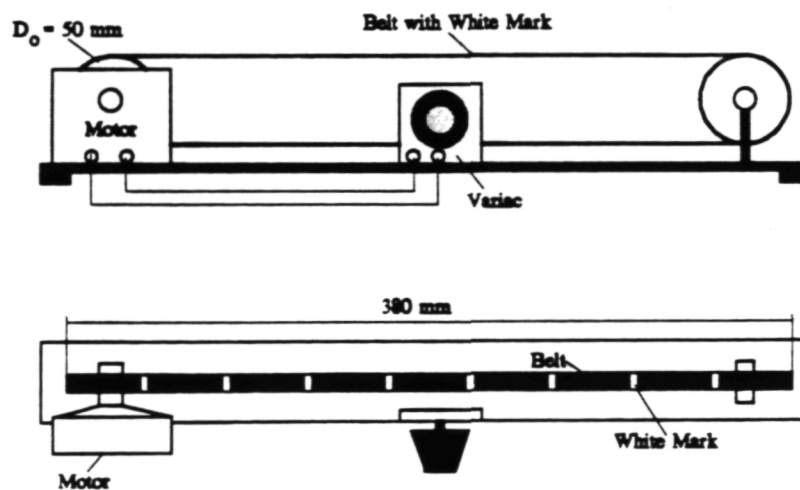


Fig. 4.19 Schematic of wave-speed measuring device

4.5. Measurements in Air-liquid Flow Experiment

The measured variables in the experiment of air-liquid flow were

- volumetric flow rate of air;
- mass flow rate of liquid;
- density of liquid;
- viscosity of liquid;
- thickness of liquid film.

The procedure of measuring these variables is described in the following sections.

4.5.1. Measurement of Mass Flow Rate of Air

The mass flow rate of air was measured using a venturimeter. The venturimeter was calibrated in the laboratory. The calibration results are given in Appendix C.

4.5.2. Measurement of Mass Flow Rate of Liquid

The mass flow rate of liquid was measured by weighing the liquid collected in a known time. The liquid was collected at the outlet of the test section.

4.5.3. Measurement of Density of Liquid

The density of liquid was measured using a volumetric method. The volume of the measuring flask was 500 ml.

4.5.4. Measurement of Viscosity of Liquid

In the experiment of air-liquid flow, the liquid viscosity was varied by mixing glycerin with water. The viscosity of liquid was measured using a Falling Ball Viscometer. As shown in Fig. 4.20, the main components of the instrument are a glass tube inclined at 10° with respect to the vertical and a set of calibrated balls for

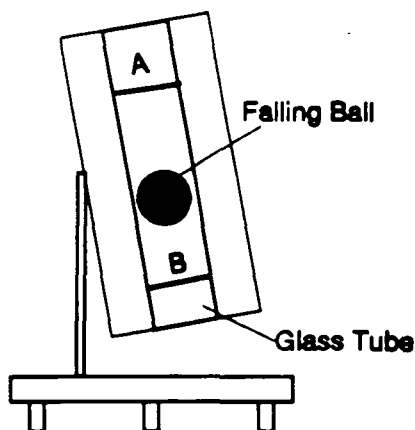


Fig. 4.20 Schematic of viscosity meter

different viscosity ranges. Two ring marks (A and B) on the tube are spaced 100 mm apart. During the measurement, a selected ball was placed inside the tube. The time for the ball to fall from marks A to B along the tube was recorded. Based on the falling time, the density of the liquid, and the ball and its drag coefficient (both provided by the manufacture), the viscosity of the liquid was determined.

The Falling Ball Viscometer was calibrated in the laboratory using distilled water and different standard liquids provided by the manufacturer. A comparison was made between the measured viscosity of the liquid (mixture of glycerin and water) and the value reported by Leffingwell (1945). The average difference of the comparison was within $\pm 7\%$.

4.6. Data Acquisition System

A data acquisition system was used in the condensation experiment to obtain the signals from the pressure transducers and most of the thermocouples. The system

4. Description of Experiments

consisted of a DT-100 data taker (made by Data Electronics Pty Ltd) and a P.C. The data taker had 23 differential channels or 46 single channels. The maximum sample rate of the data taker was 30 samples/second. The accuracy of the data taker was within $\pm 0.15\%$.

4.7. Liquids

4.7.1. Liquids in Condensation Experiments

R-113 (trichlorotrifluoroethane) and FC-72 (one of fluorinertTM electronic liquids developed by the 3M company) were used as the condensing liquids. The liquids were selected because of their low saturation temperature at atmospheric pressure ($T_{sat} \approx 47^\circ\text{C}$), wetting properties, and moderate toxicity. The properties of R-113 were taken from the ASHRAE Handbook (1985); the properties of FC-72 were obtained from the 3M Product Manual for FluorinertTM Electronic Liquids (1989). The thermodynamic properties of R-113 and FC-72 in the range of saturation temperatures employed in the experiments are given in Table 4.1.

4.7.2. Liquid in Air-liquid Flow Experiments

The liquid in the experiments of air-liquid flow was mixtures of distilled water and glycerin mixture. The glycerin was 99.9% chemically pure. The viscosity of the water- glycerin varied from $1 \times 10^{-6} \text{ kg/m s}$ at 0 % weight concentration to $7.6 \times 10^{-6} \text{ kg/m s}$ at 60 % weight concentration.

4.8. Experimental Procedures

4.8.1. Procedure for Condensation Experiments

The procedure of the experiments had 3 major steps: (1) preparation of experiments; (2) initial stage of experiments; (3) measurements.

4. Description of Experiment

Table 4.1 Selected thermodynamic properties of R-113 and FC-72

R-113							
T_{sat} °C	P KPa	ρ_g kg/m ³	ρ_l kg/m ³	h_{lg} kJ/kg	k_l mw/k m	c_{pl} J/kg k	Pr _l
40	78.0	5.8	1526.1	146.3	72.0	975	7.7
50	109.3	8.0	1501.7	142.8	70.1	986	7.1
60	149.8	10.8	1476.8	139.7	68.0	994	6.6
70	218.1	14.3	1451.2	136.2	65.8	1004	6.2
FC-72							
T_{sat} °C	P kPa	ρ_g kg/m ³	ρ_l kg/m ³	h_{lg} kJ/kg	k_l mw/k m	c_{pl} J/kg k	Pr _l
40	54.8	7.6	1640.0	89.7	55.6	1064	6.5
50	79.5	10.6	1621.9	86.9	54.5	1089	6.0
60	112.4	14.7	1604.2	84.1	54.4	1101	5.4
70	154.9	20.0	1583.9	81.1	52.3	1122	4.9

4. Description of Experiments

Preparation of Experiments

The preparation steps included removing air from the condensation loop, warming the test section and vapor tube, and heating the liquid in the boiler.

Some air would leak into the condensation loop during the period between experiments when the loop was under high vacuum. The air was removed from the condensation loop using a vacuum pump. To prevent vapor condensation on the wall of the test section and the vapor tubes, the test section and the vapor tubes from the boiler to the test section were heated to about 5 °C above the expected vapor saturation temperature in the test section using the heating elements placed on the top of the test section, and wrapped around the vapor tubes and the converging unit. The condensing liquid was heated in the boiler. When a slightly positive pressure was established in the boiler, a purge valve was slowly opened to discharge any air that might have leaked into the boiler.

Initial Stage of Experiments

The initial stage included adjusting the vapor flow rate to the inlet of the test section, the condensate flow rate to the boiler, the cooling water flow rate, and reaching a steady state. The vapor flow rate was gradually increased to a predetermined value by slowly opening a valve at the outlet of the boiler when the gauge pressure of the boiler reached about 14 kPa. The vapor from the boiler passed through the flow meters and the converging unit into the test section where a part of the vapor was condensed. In the test section, the temperature of the vapor was maintained approximately 3 °C above the vapor saturation temperature by adjusting the power to the heating elements around the vapor tubes and the converging unit. The remaining vapor from the test section was condensed in the auxiliary condenser. The condensate from both the test section and the auxiliary condenser was continuously pumped back into the boiler by a variable speed micro-pump. The steady vapor flow rate was maintained by adjusting the power supply to the heating

4. Description of Experiments

elements in the boiler.

A desired average condensing surface temperature was achieved by adjusting the flow rate and the temperature of cooling water to the cooling channel. After this adjustment, the surface temperature along the test section was with a ± 1.25 °C of the average value and the total temperature difference of the coolant across the whole cooling channel was maintained at about 5 °C. The minimum temperature difference of coolant across the whole cooling channel was 1.5 °C to reduce the uncertainty in measuring the temperature difference of the coolant.

The test section was visually inspected at regular intervals. Much attention was given to the inlet of the test section to ensure that there was no condensate entering the test section from the vapor inlet line. However, it was possible that some portion of vapor condensed in the inlet vapor line during the initial warming period of the system. If this occurred, such condensate was drained directly to the main liquid tank from the bottom of the converging unit through a valve in the tube connecting the tank and unit.

Steady state of the experiments was assumed when the changes in the vapor flow rate, the condensate flow rate from the test section, the condensing surface temperature, and the total temperature difference of cooling water across the whole cooling channel were within ± 1.5 %. Generally, it required 1 to 1½ hours to reach steady state.

Measurements

The experimental measurements were made after steady state was reached in a test run. The time for recording the data usually took about 15 minutes. During this time, the data from the venturi meters, the turbine meters, and the vapor thermocouples were taken repeatedly by the data acquisition system at 1 minute intervals and the measurements of the rotameter and the gauge glass for the condensate were repeated three times. The data was discarded if there was a large discrepancy between the

4. Description of Experiments

measurements collected at different times during the test run. Measurements were re-conducted one more time after 10 — 15 minutes.

To check for repeatability of the results, experiment was repeated for the same values of the variable on a different days. Due to the nature of the experiment, the inlet vapor velocities were within $\pm 1\%$ and ΔT within $\pm 1\%$; the heat transfer rates were within $\pm 4\%$.

4.8.2. Procedure of Air-liquid Flow Experiments

Water-glycerin mixture with a desired viscosity was prepared by mixing distilled water with glycerin in the liquid loop. The density and the viscosity of the liquid were measured.

The liquid flow to the test section was started by opening a metering valve in the liquid tube. By adjusting the valve, a smooth liquid flow with an even distribution of a liquid film along the bottom plate of the test section was obtained. After a certain amount of liquid was accumulated in the collecting tank (Fig. 4.10), the liquid pump was turned on to pump the liquid back to the gravity tank. The flow rate of the liquid to the gravity tank was adjusted by regulating a valve at the outlet of the liquid pump. The adjustment of this liquid flow was to maintain a constant liquid level in the gravity tank, ensuring a constant liquid flow to the test section. The air flow into the test section was started by opening on the valve in the air line. The air flow rate was slowly increased until interfacial waves appeared on the liquid surface in the test section. Then the air flow rate, the liquid flow rate, and the thickness of the liquid film on the bottom plate in the test section were measured. Those measurements including the measurement of the viscosity and the density of the liquid were repeated twice to check the repeatability of the measurements.

4.9. Data Processing

4.9.1. Condensate Film Thickness

The condensate film thickness was determined by measuring the time for the ultrasonic signal to pass through the liquid film and relating it to the sonic velocity of the liquid. The sonic velocity of the liquid is density dependent and was determined from an equation suggested by Reid and Sherwood (1958)

$$a_r = c_m \rho_l^3 \quad (4-1)$$

where c_m is a constant involving the molecular weight of the fluid. The values of c_m for R-113 and FC-72 were found during calibration of the ultrasonic transducer (Appendix D). For R-113, $c_m = 1.97 \times 10^{-7} \text{ m}^{10}/\text{kg}^3 \text{ s}$ and for FC-72, $c_m = 1.077 \times 10^{-7} \text{ m}^{10}/\text{kg}^3 \text{ s}$.

Referring to Fig. 4.21, an infinitesimal film thickness (dy) of the condensate film, is expressed as

$$dy = a_r d\tau \quad (4-2)$$

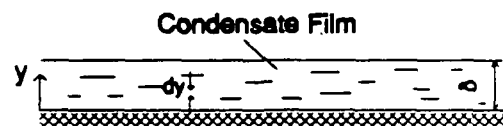


Fig. 4.21 Condensate film

Substituting Eq. 4-1 into Eq.4-2 yields

$$dy = c_m \rho_l^3 d\tau \quad (4-3)$$

If the liquid density (ρ_l), is assumed to be a linear function of the liquid temperature (T_l),

$$\rho_l = \rho_0(1 + \alpha T_l) \quad (4-4)$$

Substituting Eq. 4-4 into Eq. 4-3 and assuming a linear temperature profile in the

4. Description of Experiments

condensate film

$$T_l = a + by$$

$$dy = c_m \rho_0^3 (1 + a\alpha + b\alpha y)^3 dt \quad (4-5)$$

The condensate film thickness is found by integrating Eq. 4-5

$$\int_0^\delta \frac{dy}{(1 + a\alpha + b\alpha y)^3} = c_m \rho_0^3 \int_0^{t_r} dt$$

which gives

$$\delta = \frac{2c_m(1+\beta)^2(1+\alpha T_s)^3 \rho_0^3}{2+\beta} t_r \quad (4-6)$$

where

$$\beta = \frac{\alpha \Delta T}{1 + \alpha T_s}$$

An alternate way to determine the film thickness is to use a mean liquid density ($\bar{\rho}_l$), in Eq. 4-3 to yield

$$\delta = c_m \bar{\rho}_l^3 t_r \quad (4-7)$$

It was found that the difference between the film thickness evaluated from Eq. 4-7 and that from Eq. 4-6 was less than ± 0.1 % (See sample calculations in Appendix F). Eq. 4-7 was used in the data processing.

4.9.2. Heat Transfer Rates and Heat Transfer Coefficients

Total Heat Transfer Rate and Average Heat Transfer Coefficients

The total heat transfer rate from the vapor to the whole condensing surface was measured using two different methods: (1) heat balance in the cooling channel;

4. Description of Experiments

(2) heat balance in the vapor duct of the test section.

(1) Heat Balance in the Cooling Channel

The total heat transfer rate (q) of cooling water through the whole cooling channel is given by

$$q = \dot{m}_w c_{pw} \Delta T_w \quad (4-8)$$

(2) Heat Balance in the Vapor Duct of the Test Section

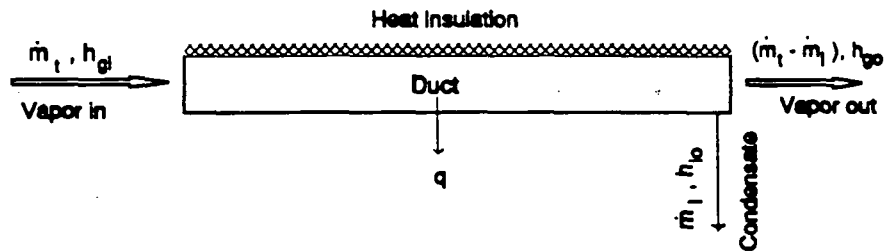


Fig. 4.22 Illustration of heat balance in the vapor duct of the test section

If the test section is taken as the control volume (Fig. 4.22), the total enthalpy of the vapor flowing into the control volume is $\dot{m}_t h_{gi}$ and the enthalpies of the vapor and the condensate flowing out of the control volume is $[(\dot{m}_t - \dot{m}_l) h_{go} + \dot{m}_l h_{lo}]$.

Applying the First Law of the thermodynamics to the control volume

$$\dot{m}_t h_{gi} = q + (\dot{m}_t - \dot{m}_l) h_{go} + \dot{m}_l h_{lo} \quad (4-9)$$

where

h_{gi} — specific enthalpy of the vapor at the inlet of the test section;

h_{go} — specific enthalpy of the vapor at the outlet of the test section;

4. Description of Experiments

h_{lo} — specific enthalpy of the condensate at the outlet of the test section;

\dot{m}_t — mass flow rate of the vapor at the inlet of the test section;

\dot{m}_{lt} — mass flow rate of the condensate at the outlet of the test section.

The specific enthalpies of the vapor and the condensate were evaluated as

$$h_{gi} = h_g + c_{pg}(T_{gi} - T_{sat})$$

$$h_{go} = h_g + c_{pg}(T_{go} - T_{sat})$$

$$h_{lo} = h_l + c_{pl}(T_{lo} - T_{sat})$$

where

T_{gi} — vapor temperature at the inlet of the test section;

T_{go} — vapor temperature at the outlet of the test section;

T_{lo} — condensate temperature at the outlet of the test section.

Rearranging Eq. 4-9

$$q = \dot{m}_t(h_{gi} - h_{go}) + \dot{m}_{lt}(h_{go} - h_{lo}) \quad (4-10)$$

The heat transfer rate computed by the two methods were usually within $\pm 5\%$. If the difference exceeded $\pm 10\%$, the data were discarded and the experiment repeated.

As the sectional heat transfer rate could be computed only by Eq. 4-8, therefore for consistency, Eq. 4-8 was used to compute the total heat transfer also with Eq. 4-10 providing a check on the results given by Eq. 4-8.

Based on the areas of the condensing surface, three average heat transfer coefficients were determined

$$\bar{h}_1 = \frac{q_1}{A_s(T_{sat} - T_{s1})} \quad (4-11)$$

4. Description of Experiments

$$\bar{h}_2 = \frac{q_2}{2A_s(T_{sat} - T_{s2})} \quad (4-12)$$

$$\bar{h}_1 = \frac{q}{A\Delta T} \quad (4-13)$$

where

- q_1 — total heat transfer rate on section 1 ($q_1 = \dot{m}_w c_{pw} \Delta T_{w1}$)
- q_2 — total heat transfer rate on sections 1 and 2 ($q_2 = \dot{m}_w c_{pw} \Delta T_{w2}$)
- q — total heat transfer rate on the entire test section ($q = \dot{m}_w c_{pw} \Delta T_w$)
- T_{s1} — arithmetic mean condensing surface temperature of section 1;
- T_{s2} — arithmetic mean condensing surface temperature of sections 1 and 2;
- ΔT_{w1} — temperature difference of the coolant through section 1;
- ΔT_{w2} — temperature difference of the coolant through sections 1 and 2.

Sectional Heat Transfer Rates and Heat Transfer Coefficients

The sectional heat transfer rate (q_{si} , $i=1,2,3$) was calculated from

$$q_{si} = \dot{m}_w c_{pw} \Delta T_{wi} \quad (4-14)$$

where ΔT_{wi} was the temperature difference of the coolant through section i

Knowing q_{si} , the sectional heat transfer coefficient (h_{si} , $i=1,2,3$) was evaluated

$$\bar{h}_{si} = \frac{q_{si}}{A_s \Delta T_{si}} \quad (4-15)$$

Local Heat Transfer Rate and Heat Transfer Coefficient

As in most analyses on film condensation, when the condensate film thickness is small ($\delta < 1$ mm), the temperature distribution within the condensate film is assumed to be linear. Based on this assumption, the local heat transfer rate is determined from

4. Description of Experiments

$$q'' = \frac{k_l \Delta T_x}{\delta} \quad (4-16)$$

where ΔT_x is the difference between the saturation temperature and the condensing surface temperature at x (distance from the leading edge).

Assuming a power law relation between δ and x

$$\delta = c_1 x^{c_2} \quad (4-17)$$

where c_1 and c_2 are the constants determined by a regression analysis on the measured values of the film thickness. Substituting Eq. 4-17 into Eq. 4-16

$$q'' = \frac{k_l \Delta T_x}{c_1} x^{-c_2} \quad (4-18)$$

The local heat transfer coefficient is defined as

$$h_x = \frac{q''}{\Delta T_x}$$

Substitution of Eq. 4-18 into the above equation

$$h_x = \frac{k_l}{c_1} x^{-c_2} \quad (4-19)$$

Using the expression for the local heat transfer rate (Eq. 4-18), the total average heat transfer coefficient and the sectional heat transfer coefficients were deduced.

For the total average heat transfer coefficient

$$h_t = \frac{W \int_0^L q'' dx}{A \Delta T} \quad (4-20)$$

4. Description of Experiments

Substitution of Eq. 4-18 into Eq. 4-20 (assuming $\Delta T_x = \text{constant}$)

$$\bar{h}_i = \frac{k_1 L^{1-c_2}}{c_1(1-c_2)} \quad (4-21)$$

For the sectional heat transfer coefficients

$$\bar{h}_{si} = \frac{1}{\Delta T_{si}(L_i - L_{i-1})} \int_{L_{i-1}}^{L_i} q'' dx$$

Substitution of Eq. 4-18 into the above equation (assuming $\Delta T_x = \Delta T_{si}$)

$$\bar{h}_{si} = \frac{k_1(L_i^{1-c_2} - L_{i-1}^{1-c_2})}{c_1(1-c_2)(L_i - L_{i-1})} \quad (4-22)$$

where

L_i —length from the leading edge of the condensing surface to the end of section i ;

L_{i-1} —length from the leading edge of the condensing surface to the beginning of section i .

The total average heat transfer coefficient and the sectional heat transfer coefficients calculated by Eqs. 4-20 and 4-21 were used to compare the values determined from (Eqs. 4-13 and 4-15) the method of heat balance in the cooling channel. From these comparisons, the technique using the film thickness measurement to obtain the local heat transfer coefficient (Eq. 4-19) was validated.

4.9.3. Liquid Velocity

In studying the interfacial wave initiation, a knowledge of the variation of the local, average liquid velocity along the test section was needed. The local, average liquid velocities are found from

4. Description of Experiments

$$v_l(x) = \frac{\dot{m}_l}{\delta W} \quad (4-23)$$

In the adiabatic air-liquid flow, the liquid flow rate (\dot{m}_l) was a constant, while in the condensation, \dot{m}_l was a function of x due to the condensation of vapor along the condensing surface

$$\dot{m}_l = W \int_0^x \dot{m}_x dx$$

where \dot{m}_x was the condensate rate per unit area at x . From a heat balance,

$$\int_0^x \dot{m}_x dx = \frac{\int_0^x q'' dx}{h_{fg}}$$

or

$$\dot{m}_l = \frac{W \int_0^x q'' dx}{h_{fg}} \quad (4-24)$$

Substitution of Eq. 4-24 into Eq. 4-23

$$v_l(x) = \frac{\int_0^x q'' dx}{\delta h_{fg}} \quad (4-25)$$

Substitution of Eqs. 4-17 for δ and 4-18 for q'' into Eq. 4-24

$$v_l(x) = \frac{k_l}{c_1^2 x c_2 h_{fg}} \int_0^x \Delta T_x x^{-c_2} dx$$

After integration of the above equation, and assuming $\Delta T_x \approx \Delta T$

4. Description of Experiments

$$v_l(x) = \frac{k_l \Delta T}{c_1^2 (1 - c_2) h_{fg}} x^{1-2c_2} \quad (4-26)$$

4.9.4. Vapor and Air Velocities

Similar to the liquid velocity, the variation of the local, average velocities of the vapor and the air (in the air-liquid experiment) along the test section was accounted for in studying the interfacial wave initiation. The velocities of both the vapor and the air are defined as

$$v_g(x) = \frac{\dot{m}_g}{(H - \delta)W} \quad (4-27)$$

where \dot{m}_g was the mass flow rate of the vapor or the air at x . For the air, \dot{m}_g was constant, while for the vapor, \dot{m}_g varied along the condensing surface and it was evaluated from

$$\dot{m}_g = \dot{m}_t - \dot{m}_l$$

Substituting Eq. 4-24 into the above equation

$$\dot{m}_g = \dot{m}_t - \frac{W \int_0^x q'' dx}{h_{fg}} \quad (4-28)$$

If $H \geq \delta$, Eq. 4-27 simplifies to

$$v_g(x) = \frac{\dot{m}_g}{HW} \quad (4-29)$$

5. ANALYTICAL MODEL FOR CONDENSATION

5.1. Introduction

An analytical model for condensation of a vapor flowing parallel to a bottom condensing surface in a horizontal rectangular duct was formulated by employing the conservation laws. Mass and energy balance equations were obtained using the integral method. The resulting equations were numerically solved to predict condensate film thickness, condensate velocity, interfacial shear stress, and heat transfer coefficients.

5.2. Physical Description of the Problem

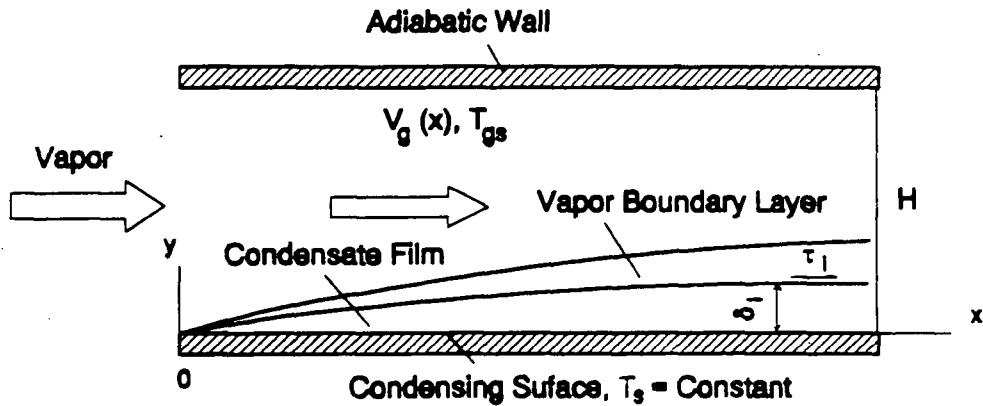


Fig. 5.1 Physical model and coordinate system

The physical situation considered in the analysis is illustrated in Fig. 5.1. Pure vapor flows into a horizontal rectangular duct along the x direction with uniform inlet

5. Analytical Model for Condensation

velocity (v_{gi}) and saturation temperature (T_{sat}). The bottom plate of the duct is maintained at a uniform temperature (T_s) while the other three sides of the duct are perfectly insulated. Since $T_{sat} > T_s$, vapor condenses on the bottom plate. The condensate film on the plate flows in the x-direction due to the action of the shear stress at the vapor-condensate interface and the momentum of the vapor. The flow of vapor is turbulent throughout the duct.

5.3. Formulation

5.3.1. Assumptions

1. Vapor enters the duct with a uniform velocity
2. Vapor flows as a boundary layer flow over the condensate
3. The interfacial thermal resistance is negligible, so that the condensate temperature at the interface is same as the saturation temperature
4. The change in the static pressure of vapor along the duct is small, so that the saturation temperature along the duct is uniform
5. The condensate film thickness is very thin and the temperature profile in the film layer is linear
6. The height of the duct is much greater than the condensate film thickness
7. The width of the duct is much greater than the condensate film thickness, so that the condensate flow is two-dimensional
8. The properties are constant
9. No non-condensable gases exist in the duct

5.3.2. Mass Conservation

Mass Conservation of Condensate Film

Mass conservation to the control volume of condensate film (Fig. 5.2) yields

5. Analytical Model for Condensation

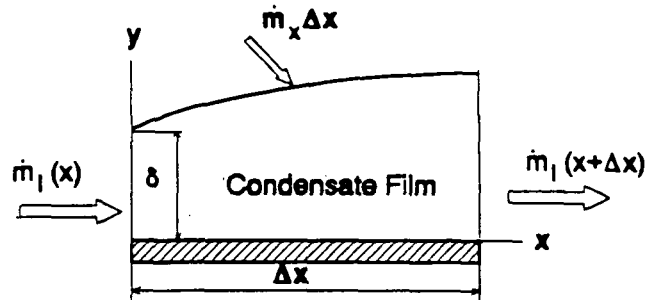


Fig. 5.2 Control volume of condensate

$$\dot{m}_l(x+\Delta x) - \dot{m}_l(x) - \dot{m}_x W \Delta x = 0$$

Rearranging the equation and letting $\Delta x \rightarrow 0$,

$$\dot{m}_x = \frac{1}{W} \frac{d\dot{m}_l(x)}{dx} \quad (5-1)$$

\dot{m}_l is expressed as

$$\dot{m}_l = W \rho_l \int_0^\delta v_l(x, y) dy \quad (5-2)$$

Substituting Eq. 5-2 into Eq. 5-1, an expression for the condensate rate is given

$$\dot{m}_x = \rho_l \frac{d}{dx} \left[\int_0^\delta v_l(x, y) dy \right] \quad (5-3)$$

Mass Conservation of Vapor

Fig. 5.3 shows a control volume of vapor in the duct. Mass conservation to the control volume gives

5. Analytical Model for Condensation

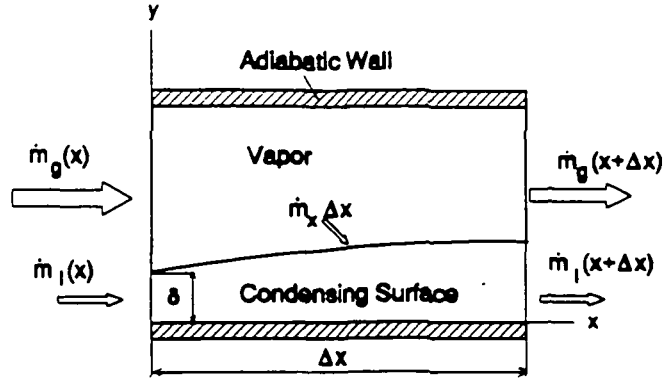


Fig. 5.3 Control volume of vapor

$$\dot{m}_g(x+\Delta x) + \dot{m}_x W \Delta x - \dot{m}_g(x) = 0$$

Rearranging the equation and letting $\Delta x \rightarrow 0$,

$$\frac{d\dot{m}_g}{dx} = -\dot{m}_x \cdot W \quad (5-4)$$

The mass flow of vapor, \dot{m}_g , at x is expressed as

$$\dot{m}_g = \rho_g (H - \delta) W v_g(x)$$

Since $H \gg \delta$ (assumption 6), the above equation is simplified as

$$\dot{m}_g = \rho_g H W v_g(x) \quad (5-5)$$

Substitution of Eq. 5-5 into Eq. 5-4 yields

$$v_g(x) = v_{gi} - \frac{1}{H\rho_g} \int_0^x \dot{m}_x dx \quad (5-6)$$

5. Analytical Model for Condensation

5.3.3. Energy Conservation

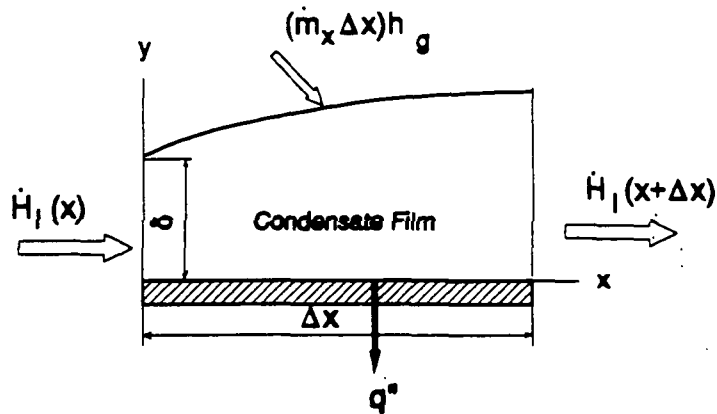


Fig. 5.4 Control volume for energy conservation

Neglecting changes in kinetic and potential energies of the condensate and viscous dissipation, the energy balance applied to the control volume shown in Fig. 5.4 is

$$\dot{H}_1(x) + [\dot{m}_x W \Delta x] h_g = q'' W \Delta x + \dot{H}_1(x + \Delta x) \quad (5-7)$$

where

\dot{H}_1 — rate of enthalpy flow across the condensate film;

q'' — rate of heat transfer per unit area of the condensing surface.

Rearranging Eq. 5-7 and letting $\Delta x \rightarrow 0$ yields

$$q''(x) = -\frac{1}{W} \frac{d}{dx} \dot{H}_1 + \dot{m}_x h_g \quad (5-8)$$

\dot{H}_1 is expressed as

5. Analytical Model for Condensation

$$\dot{H}_1(x) = \rho_1 W \int_0^\delta v_1(x,y) h_1 dy \quad (5-9)$$

Substitution of Eqs. 5-9 and 5-3 into Eq. 5-8 yields

$$q''(x) = \rho_1 h_{fg} \frac{d}{dx} \int_0^\delta v_1(x,y) dy \quad (5-10)$$

Based on the assumption of a linear temperature profile in the condensate, q'' is given by

$$q''(x) = \frac{k_1(T_{sat} - T_s)}{\delta} \quad (5-11)$$

Substitution of Eq. 5-11 into Eq. 5-10 yields

$$\frac{d}{dx} \left[\int_0^\delta v_1(x,y) dy \right] = \frac{A_1}{\delta} \quad (5-12)$$

where

$$A_1 = \frac{k_1 \Delta T}{\rho_1 h_{fg}} \quad (5-13)$$

5.3.4. Condensate Velocity

It has been well established that if the condensate film is thin the condensate velocity (v_1) in the film can be assumed to be linear

$$v_1(x,y) = c(x)y \quad (5-14)$$

The condition that $\tau_1 = \mu_1 (\partial v_1 / \partial y)$ at $y = \delta$ leads to $c(x) = \tau_1 / \mu_1$. Thus

5. Analytical Model for Condensation

$$v_1(x,y) = \frac{\tau_i}{\mu_1} y \quad (5-15)$$

where τ_i is the interfacial shear stress varying in the x direction.

Different hypotheses have been proposed for computing τ_i . Some researchers [for example, Rosson and Myer (1965), Soliman et al. (1968), and Bae et al. (1971)] assumed that τ_i in condensation was same as that in an adiabatic two-phase flow; therefore, the method applied in an adiabatic flow was used to determine the τ_i in condensation. Some other researchers [for example, Shekriladze and Gomelaury (1966), Linehan et al. (1969), Jensen and Yuen (1982)] assumed that τ_i in condensation resulted from a combination of an adiabatic shear stress exerted on the interface (without condensation) and a momentum shear stress due to the mass of vapor condensing on the film layer; when the condensate rate was high, the influence of the momentum was possibly the dominant contribution to the total value of τ_i . It appears that the latter assumption is more appropriate to the situation of condensation and is thus used in this analysis. Accordingly, τ_i is expressed as

$$\tau_i = f_c \frac{\rho_g v^2}{2} + \dot{m}_x v \quad (5-16)$$

where v is the average vapor velocity relative to the interfacial velocity (v_{li}), i.e.

$$v = v_g - v_{li} \quad (5-17)$$

and f_c is a local adiabatic friction factor and assumed to be a function of Re_x (v_x/v_g)

$$f_c = c_f Re_x^{n_f} \quad (5-18)$$

A discussion of the choice of the constants (c_f and n_f) is presented in Chapter 6.

5. Analytical Model for Condensation

5.3.5. Interfacial Velocity

The mass rate of flow of the condensate at x is given by

$$\dot{m}_l = \rho_l \bar{v}_l(x) W \delta = \rho_l W \int_0^\delta v_l(x, y) dy \quad (5-19)$$

where \bar{v}_l is the average liquid velocity varying only in the direction of x . After rearrangement of Eq. 5-19,

$$\bar{v}_l = \frac{1}{\delta} \int_0^\delta v_l(x, y) dy \quad (5-20)$$

Employing Eq. 5-14

$$v_{li} = 2\bar{v}_l(x) \quad (5-21)$$

Using Eq. 5-1 and 5-19, it is found that

$$\bar{v}_l = \frac{\int_0^x \dot{m}_x(x) dx}{\rho_l \delta} \quad (5-22)$$

Since

$$\int_0^x \dot{m}_x dx = \frac{k_l \Delta T}{h_{fg}} \int_0^x \frac{1}{\delta} dx \quad (5-23)$$

Employing Eq. 5-23, substituting Eq. 5-22 into 5-21, the expression for the interfacial velocity is

$$v_{li} = \frac{2A_1}{\delta} \int_0^x \frac{dx}{\delta} \quad (5-24)$$

where A_1 is defined by Eq. 5-13.

5. Analytical Model for Condensation

5.3.6. Differential Equation for Condensate Film Thickness

Substitution of Eq. 5-15 into Eq. 5-12 leads to

$$\frac{d}{dx}[\tau_i \delta^2] = \frac{2A_1 \mu_l}{\delta}$$

or

$$\delta \frac{d\tau_i}{dx} + 2\tau_i \frac{d\delta}{dx} = \frac{2A_1 \mu_l}{\delta^2} \quad (5-25)$$

Substituting Eq. 5-18 into Eq. 5-16 (with considering $Re_x = vx/v_g$)

$$\tau_i = \frac{c_f \rho_g v^{2+n_r} x^{n_r}}{2v_g^{n_r}} + \dot{m}_x v \quad (5-26)$$

Using Eqs. 5-3 and 5-12, \dot{m}_x is expressed as

$$\dot{m}_x = \frac{A_1 \rho_l}{\delta} \quad (5-27)$$

Substituting Eq. 5-27 into Eq. 5-26

$$\tau_i = \frac{c_f \rho_g v^{2+n_r} x^{n_r}}{2v_g^{n_r}} + \frac{A_1 \rho_l}{\delta} v \quad (5-28)$$

Differentiating τ_i with respect to x

$$\begin{aligned} \frac{d\tau_i}{dx} &= [(2 + n_r) A_2 x^{n_r-1} v^{1+n_r} + \frac{A_1 \rho_l}{\delta}] \frac{dv}{dx} \\ &\quad - \frac{A_1 \rho_l v}{\delta^2} \frac{d\delta}{dx} + n_r A_2 x^{n_r-1} v^{2+n_r} \end{aligned} \quad (5-29)$$

where

5. Analytical Model for Condensation

$$A_2 = \frac{c_p \rho_g}{2v_g^{n_1}} \quad (5-30)$$

Substituting Eqs. 5-6 and 5-24 into Eq. 5-17 for v and using Eq. 5-27

$$v = v_{gi} - \frac{A_1 \rho_l}{H \rho_g} \int_0^x \frac{dx}{\delta} - \frac{2A_1}{\delta} \int_0^x \frac{dx}{\delta} \quad (5-31)$$

Differentiation of v with respect to x yields

$$\frac{dv}{dx} = \left(\frac{2A_1}{\delta^2} \int_0^x \frac{dx}{\delta} \right) \frac{d\delta}{dx} - \left(\frac{A_1 \rho_l}{H \rho_g} + \frac{2A_1}{\delta} \right) \frac{1}{\delta} \quad (5-32)$$

Combining Eqs. 5-25, 5-26, 5-29, and 5-31, an ordinary differential equation for δ is obtained

$$\frac{d\delta}{dx} = \frac{\kappa + [\alpha(x)\delta + A_1 \rho_l](\xi\delta + \eta) - \gamma(x)\delta^3}{\epsilon[\alpha(x)\delta + A_1 \rho_l] + 2\delta[\theta(x)\delta + \beta(x)] - \beta(x)\delta} \quad (5-33)$$

where

$$\alpha(x) = (2 + n_1)A_2 x^{n_1-1} v^{1-n_1}, \quad \beta(x) = \rho_l A_1 v$$

$$\gamma(x) = n_1 A_2 x^{n_1-1} v^{2-n_1}, \quad \epsilon(x) = 2A_1 \rho_l \int_0^x \frac{dx}{\delta}$$

$$\xi = \frac{A_1 \rho_l}{H \rho_g}, \quad \eta = 2A_1$$

$$\theta(x) = A_2 v^{2-n_1} x^{n_1}, \quad \kappa = 2A_1 \mu_1$$

5. Analytical Model for Condensation

Define dimensionless variables

$$\delta = \delta^* L, \quad x = x^* L \quad (5-34)$$

Substituting Eq. 5-34 into Eq. 5-33, a non-dimensional differential equation for condensate film thickness is given by

$$\frac{d\delta^*}{dx^*} = \frac{\kappa + [\alpha(x^*)L\delta^* + A_1\rho_l](\xi L\delta^* + \eta) - \gamma(x^*)L^3\delta^{*3}}{\varepsilon[\alpha(x^*)L\delta^* + A_1\rho_l] + 2L\delta^*[\theta(x^*)L\delta^* + \beta(x^*)] - \beta(x^*)L\delta^*} \quad (5-35)$$

5.3.7. Heat Transfer Rate and Heat Transfer Coefficients

Total Heat Transfer Rate and Average Heat Transfer Coefficients

With ΔT constant, the total heat transfer rate from vapor to the entire condensing surface is given by

$$q = Wk_f\Delta T \int_0^L \frac{dx}{\delta} \quad (5-36)$$

The average heat transfer coefficient, \bar{h}_{si} , over a certain area of condensing surface, A_s , is defined as

$$\bar{h}_{si} = \frac{q_{si}}{A_s\Delta T} \quad (5-37)$$

where

$$q_{si} = Wk_f\Delta T \int_{L_{i-1}}^{L_i} \frac{dx}{\delta}$$

and

$$A_s = W(L_i - L_{i-1})$$

where the meanings of L_i and L_{i-1} is illustrated in Fig. 5.5.

5. Analytical Model for Condensation

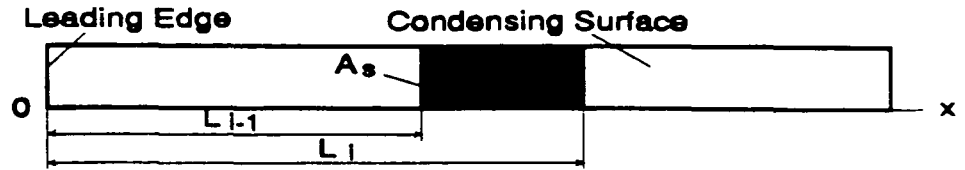


Fig. 5.5 Illustration of L_i and L_{i-1}

Rearranging Eq. 5-37

$$\bar{h}_{si} = \frac{k_l}{L_i - L_{i-1}} \int_{L_{i-1}}^{L_i} \frac{dx}{\delta} \quad (5-38)$$

If $L_{i-1} = 0$ and $L_i = L$, the expression for the total heat transfer coefficient (\bar{h}_i) over the entire condensing surface is given by

$$\bar{h}_i = \frac{k_l}{L} \int_0^L \frac{dx}{\delta} \quad (5-39)$$

Local Heat Transfer Coefficient

The local heat transfer coefficient at x is defined as

$$h_x = \frac{q''}{(T_{sat} - T_s)}$$

Substituting Eq. 5-11 into the above equation yields

$$h_x = \frac{k_l}{\delta} \quad (5-40)$$

5.4. Solution Procedure

Eq. 5-35 was solved numerically. The grid arrangement for the numerical computation is shown in Fig. 5.6. The dimensionless length of the condensing surface is taken as one ($L^*=1$). The total number of the grids was 600, of which 300 grids were evenly spaced in the leading section of the condensing surface (from $x^* = 0$ to $x^* = 0.2$) as δ increases rapidly at the leading edge of the condensing surface; the rest of grids were evenly distributed along the remaining length of the condensing surface. The total number of grids (600) was determined from a pre-computation of Eq. 5-35. It was found that when the total grid number was greater than 600, the relative change in δ was less than 0.05 %.

In the calculations, the vapor properties were evaluated at T_{sat} ; the liquid properties were determined at the arithmetic average of the saturation temperature and the surface temperature $[(T_{sat} + T_s)/2]$. The effect of subcooling was considered by modifying h_{lg} using the following equation (Rohsenow, 1970)

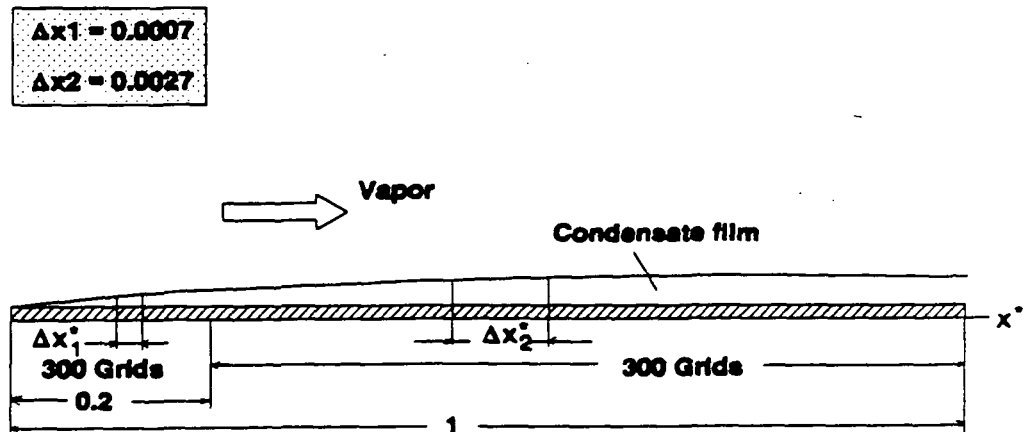


Fig. 5.6 Arrangement of grids

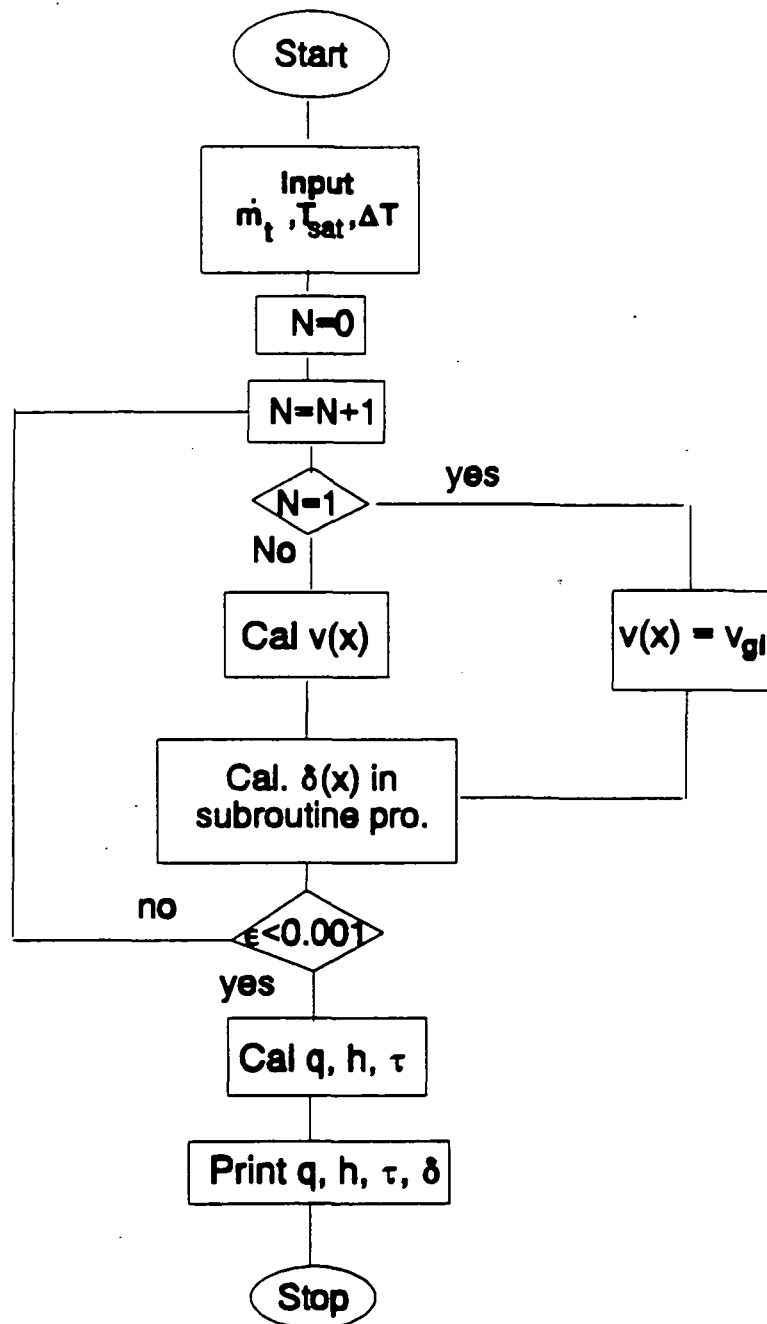


Fig. 5.7 Flow chart of computing program

5. Analytical Model for Condensation

$$h'_{fg} = h_{fg} + 0.68c_{pl}(T_{sat} - T_s)$$

Eq. 5-35 was first solved to obtain δ . Then, v_{li} , \bar{v}_l , v_g , τ_i , h_x , \bar{h}_{si} , \bar{h}_t were computed. In the computations, the values of c_t and n_t in Eq. 5-18 were determined based on a modified Schlichting friction equation (details are described in Chapter 6). The computational procedure (illustrated in Fig. 5.7) is as follows.

1. Input \dot{m}_i , T_{sat} , ΔT
2. Find the necessary thermodynamic properties from the subroutine program for the properties
3. Calculate A_1 (Eq. 5-13), A_2 (Eq. 5-30), and v_{gi}
4. In the initial calculation of iteration, assume that v_{li} is 0 and v is constant (assuming $v = v_{gi}$)
5. Solve Eq. 5-35 for δ^* using the 4th order Runge Kutta method
6. Use Eq. 5-31 to calculate v including v_g and v_{li} , employing the values of δ obtained in step 5
7. Repeat step 5 until $x^* = 1$
8. Calculate the total heat transfer rate using Eq. 5-36
9. Repeat steps 5 \rightarrow 8 once
10. If the relative difference of the newly calculated heat transfer rate with the previously obtained value is less than 10^{-3} ($\epsilon = |q_{new} - q_{old}|/q_{new} < 0.001$), halt the iteration; otherwise repeat steps 5 \rightarrow 8
11. Calculate \dot{m}_x , v_{li} , \bar{v}_l , v_g , τ_i using Eqs. 5-27, 5-24, 5-20, 5-6, and 5-28
12. Calculate \bar{h}_l , \bar{h}_{si} , h_x using Eqs. 5-39, 5-38, and 5-40

6. RESULTS AND DISCUSSION

6.1. Introduction

Condensation heat transfer with a vapor flow inside a horizontal rectangular duct, with condensation only on the bottom plate, was experimentally studied. Measurements were obtained both with a smooth condensate flow and a wavy condensate flow. The initiation of interfacial waves was investigated with condensation and with an adiabatic air-liquid flow. An analytical model was developed to simulate the condensation process. Typical results of the experimental measurements of the heat transfer coefficients, predictions of the analytical model, and the correlations relating the average heat transfer coefficient to the variables of significance, are discussed in this chapter. All the experimental results are given in Appendix G.

6.2. Ranges of Experimental Variables

6.2.1. Condensation Heat Transfer

There were 118 valid runs of experimental data with R-113 and 75 runs with FC-72; interfacial waves were observed in 76 runs with R-113 and 56 runs with FC-72. The two main variables in the experiment were the inlet vapor velocity to the test section (v_{gi}) and the difference between the saturation vapor temperature and the condensing surface temperature (ΔT). In the test section, since the vapor pressure changed in the range approximately from 2 Pa to 10 Pa, the saturation temperature of vapor (T_{sat}), is assumed constant. Table 6.1 lists the ranges of the values of the inlet vapor velocity, (v_{gi}), the temperature difference (ΔT), and the inlet vapor Reynolds

6. Results and Discussion

number ($Re_{gL} = v_{gi}L/v_g$).

Table 6.1 Ranges of variables in the experiment of condensation heat transfer

Condensing Fluids	v_{gi} , m/s	ΔT °C	Re_{gL}
R-113	0.31 - 4.39	10 - 40	210,000 - 2,700,000
FC-72	0.36 - 3.10	10 - 50	380,000 - 3,322,000

6.2.2. Wave Initiation

There were 46 runs of data with the adiabatic air-liquid flow and 8 runs of data with the condensation (R-113 and FC-72). For wave initiation with the air-liquid flow, the main variables were: air velocity (v_{gi}), mass flow rate of liquid (\dot{m}_l), and viscosity of liquid (μ_l); for wave initiation with condensation, the main variables were the inlet vapor velocity (v_{gi}) and the temperature difference (ΔT). The ranges of the variables in the experiments are given in Table 6.2.

Table 6.2 Ranges of variables in the experiment of interfacial wave initiation

Fluids	$\mu_l \times 10^6$ kg/m s	$\dot{m}_l \times 10^2$ kg/s	$\mu_g \times 10^6$ kg/m s	v_{gi} m/s
R-113 (condensation)	509 — 517	—	11	1.3-1.6
FC-72 (condensation)	439 — 461	—	12	0.9-1.1
Glycerine-water (adiabatic)	1000 — 7550	0.1 — 1.2	18	0.5-6.0

Since the experiments with the adiabatic air-liquid flow were performed at atmospheric pressure and room temperature (≈ 20 °C), the viscosity of air was assumed constant. Also, due to the insignificant change of the saturation temperature of vapor

6. Results and Discussion

in the experiment with condensation, the viscosity of vapor was approximately constant. However, the viscosity of the liquid (especially, the liquid viscosity of glycerine-water) varied in the experiments (Table 6.2).

6.3. Observation of Flow Patterns

The condensate flow patterns along the condensing surface were observed visually. The condensate Reynolds number (Re_l) was less than 450 so that the flow of condensate is assumed to be laminar. It was observed that the vapor-condensate interface was either smooth or wavy, depending on the magnitude of the inlet vapor Reynolds number (Re_{gL}) and the temperature difference (ΔT). Table 6.3 lists the value of Re_{gL} (critical Reynolds number) at which the transition of smooth interface to a wavy interface occurred (wave initiation).

Table 6.3 Inlet vapor Reynolds number at which interfacial waves appear—condensation

ΔT °C	R-113		FC-72	
	Re_{gL}	v_{gi} m/s	Re_{gL}	v_{gi} m/s
10	1,007,093	1.59	1,225,835	1.13
20	886,762	1.4	1,108,890	1.09
30	804,421	1.27	918,545	0.90
40	802,312	1.27	883,375	0.84
50	—	—	851,826	0.81

In the wavy flow regime, both two dimensional (2-D) and three dimensional (3-D) waves can appear. Fig. 6.1 shows photographs of typical 2-D waves and 3-D waves. It is seen that the 2-D waves have a clear wave length, while the 3-D waves are rather randomly shaped (a pebbled appearance). The 3-D waves appeared after the 2-D

5 37 38 39 40 41 42 43 44 45 46 4



a. 2-D waves

37 38 39 40 41 42 43 44 45 46 47



b. 3-D waves

Fig. 6.1 Photographs of 2-D waves and 3-D waves

a. $\Delta T = 11.1\text{ }^{\circ}\text{C}$; $v_{gi} = 1.85\text{ m/s}$; $Re_{gL} = 1,166,472$; R-113

b. $\Delta T = 10.2\text{ }^{\circ}\text{C}$; $v_{gi} = 2.95\text{ m/s}$; $Re_{gL} = 1,593,353$; R-113

6. Results and Discussion

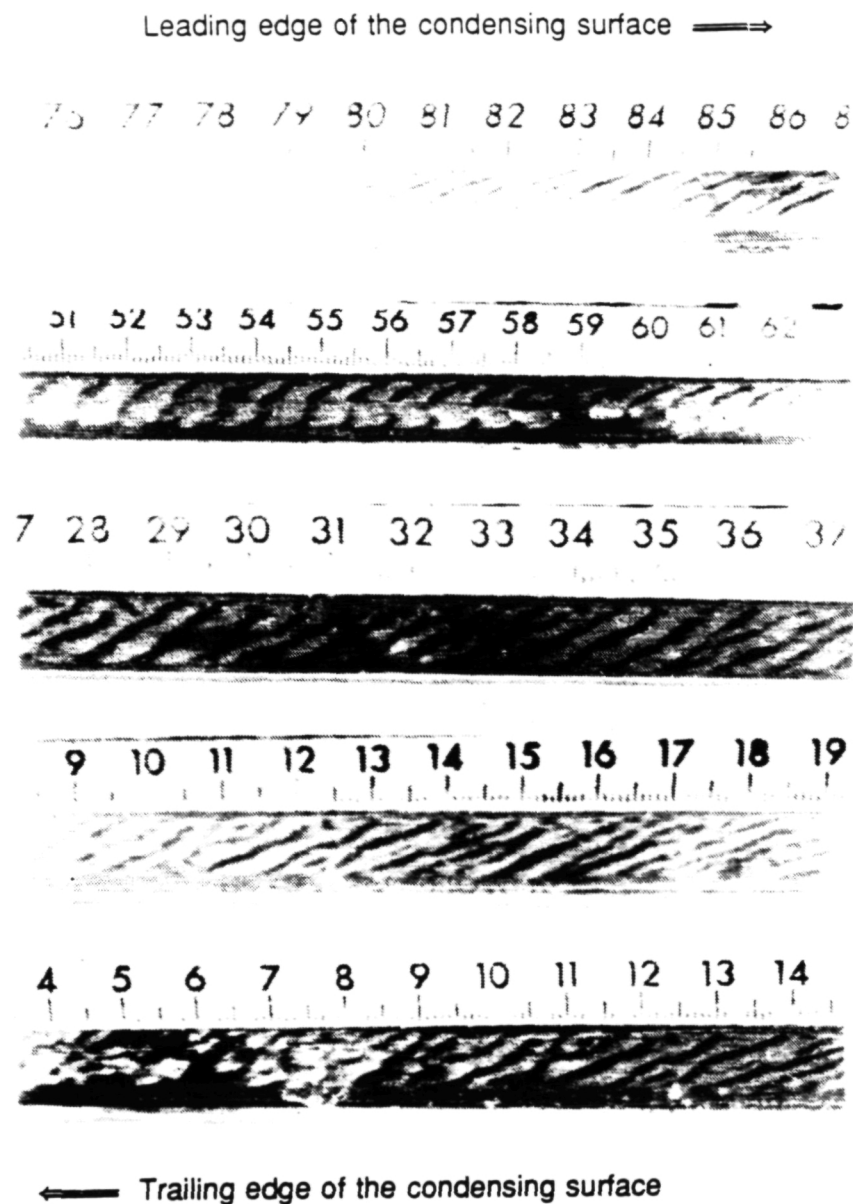


Fig. 6.2 Photograph of condensate flow patterns along condensing surface

FC-72; $\Delta T = 9.3^\circ\text{C}$; $v_{g1} = 1.5\text{ m/s}$; $Re_{gL} = 1,593,353$

6. Results and Discussion

waves along the condensing surface. When Re_{gL} was high, 3-D waves occurred all over the condensing surface. Table 6.4 gives the Re_{gL} at which the 3-D waves covered all the whole condensing surface. Before Re_{gL} reached the values listed in Table 6.4 at certain values of ΔT , all three flow patterns (smooth, wavy with 2-D waves, and wavy with 3-D waves) usually appeared on the condensing surface. It is seen in Fig. 6.2 that the surface of condensate was smooth at the beginning of the condensing surface, and gradually became wavy with 2-D waves, which changed into 3-D waves towards the end of the condensing surface.

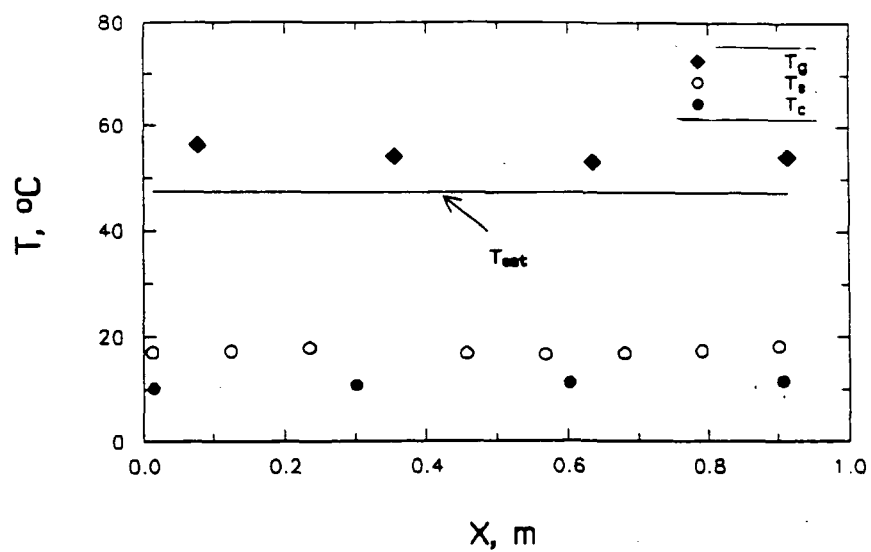
Table 6.4 Conditions at which 3-D waves covering the whole condensing surface

ΔT °C	R-113		FC-72	
	Re_{gL}	v_{gi} m/s	Re_{gL}	v_{gi} m/s
10	1,358,584	2.20	1,867,031	1.80
20	1,121,217	1.78	1,700,628	1.60
30	1,120,653	1.73	1,471,876	1.38
40	976,646	1.52	1,471,163	1.34
50	—	—	1,345,425	1.30

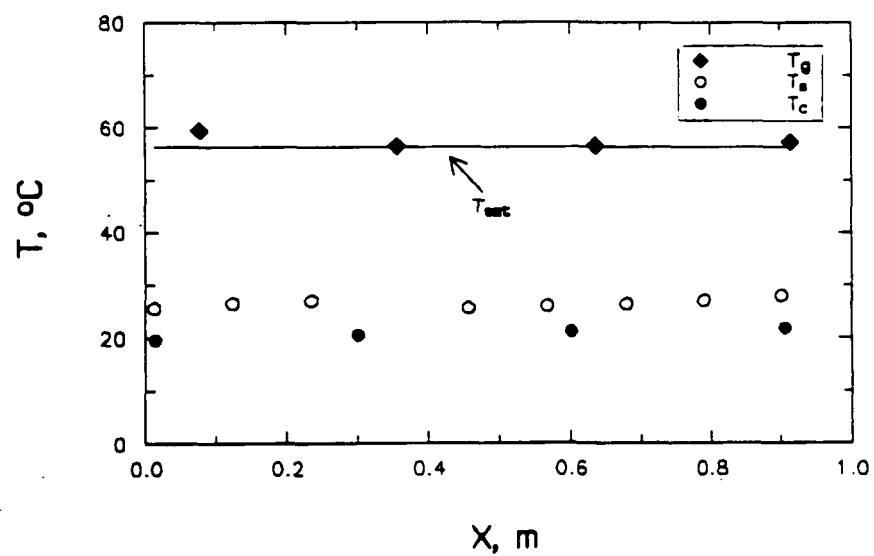
6.4. Temperature Distributions in the Test Section

Fig. 6.3a gives the typical distributions of vapor temperature (T_g), condensing surface temperature (T_s), and coolant temperature (T_c) in the test section when R-113 was used as the condensing fluid. Fig. 6.3b gives these measurements when FC-72 was used. It is seen in both the figures that the vapor temperature is nearly uniform, except near the inlet of the test section where it is slightly higher due to the heating of

6. Results and Discussion



a



b

Fig. 6.3 Various temperature distributions in the test section

a. R-113; $\Delta T = 30^{\circ}\text{C}$; $v_{gi} = 2.2 \text{ m/s}$

b. FC-72; $\Delta T = 30^{\circ}\text{C}$; $v_{gi} = 1.2 \text{ m/s}$

6. Results and Discussion

the vapor along the inlet tube. The maximum difference between the average vapor temperature and the saturation temperature was within 5 °C. The temperature of the condensing surface is seen to rise slightly along the condensing surface, but the overall variation of the surface temperature from its average value was less than ± 1.25 °C.

6.5. Condensate Film Thickness

The condensate film thickness of condensate with a smooth interface and a wavy interface with small amplitudes and speeds was measured. When more waves appeared on the interface and the interfacial wave speed was high, the measurement of the film thickness was not possible because of the difficulty in distinguishing the interface due to its rapid oscillation.

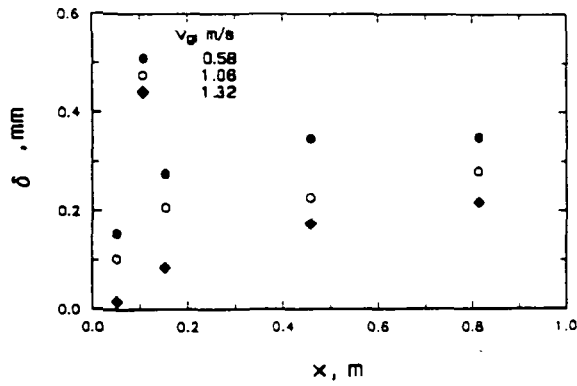
Fig. 6.4 illustrates the distributions of the film thickness (δ), along the length of the condensing surface (x), using R-113 and FC-72 as the condensing fluids at two different values of ΔT . The film thickness increases rapidly in the leading section of the condensing surface (high condensate rate); however, the rate of the increase of the film thickness decreases with distance from the leading edge of the condensing surface; with increasing v_{gi} , the film thickness decreases, but near the trailing edge of the condensing surface, especially for the cases with large ΔT (Fig. 6.4 b), the effect of v_{gi} on the film thickness is not significant.

6.6. Heat Transfer Rates and Heat Transfer Coefficients

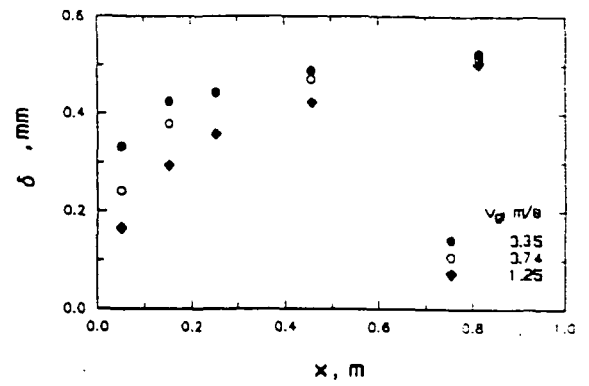
6.6.1. Total Heat Transfer Rates and Average Heat Transfer Coefficients

The variations of total heat transfer rate (q) with the inlet vapor velocity (v_{gi}) for four different values of ΔT and the two condensing fluids are plotted in Fig. 6.5. This figure shows that the heat transfer rate increases with increasing inlet vapor velocity. The rate of the increase is higher when the inlet vapor velocity is greater than 1.6 m/s.

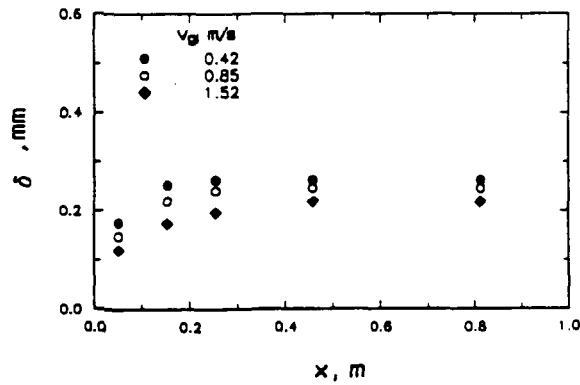
6. Results and Discussion



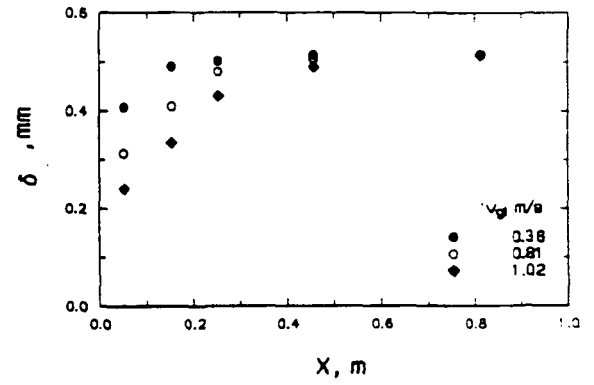
a. R-113; $\Delta T = 10^\circ\text{C}$



b. R-113; $\Delta T = 40^\circ\text{C}$

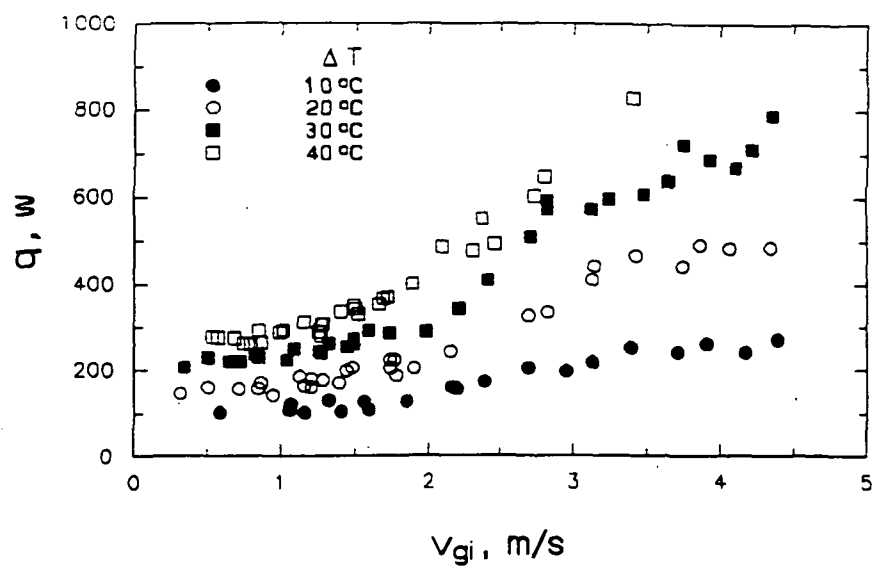


c. FC-72; $\Delta T = 10^\circ\text{C}$

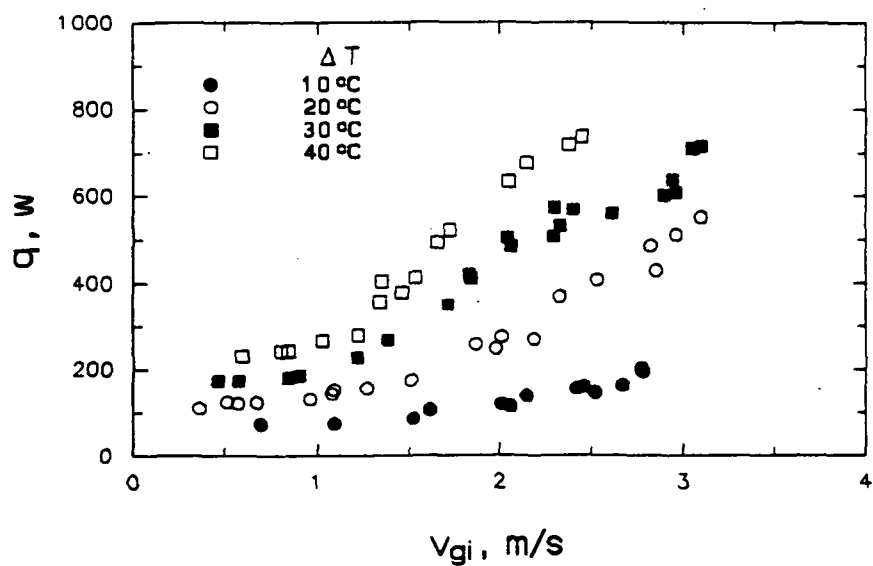


d. FC-72; $\Delta T = 40^\circ\text{C}$

Fig. 6.4 Distributions of condensate film thickness along the condensing surface



a. R-113



b. FC-72

Fig. 6.5 Total heat transfer rates

6. Results and Discussion

(Note: when the inlet vapor velocity is higher than approximate 1.6 m/s, interfacial waves developed on the condensate surface). However, the influence of the inlet vapor velocity on the total heat transfer rate at $\Delta T \approx 10^\circ\text{C}$ is not as significant as it is on the total heat transfer rates at other values of ΔT s.

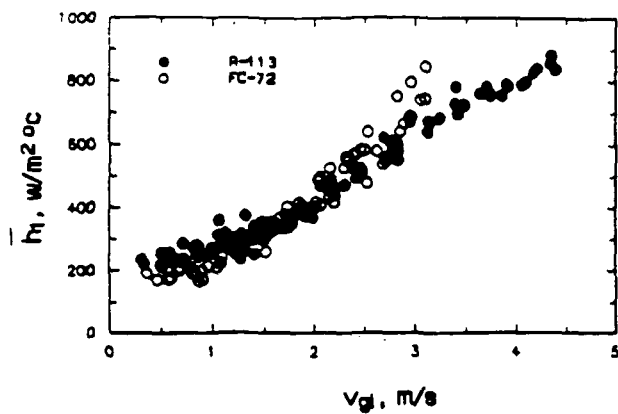
The average heat transfer coefficients are calculated using Eq. 4-13. The variation of the average heat transfer coefficient with inlet vapor velocity is shown in Fig. 6.6. In the figure, \bar{h}_1 denotes the value of the average heat transfer coefficient over the section 1; \bar{h}_2 is the value over section 1 and section 2; \bar{h}_t is the overall average heat transfer coefficient over the entire condensing surface. The three different average heat transfer coefficients display similar trends:

- the average heat transfer coefficient increases with an increase in the vapor velocity
- beyond a certain value of the vapor velocity, the average heat transfer coefficient increases nearly linearly with the vapor velocity

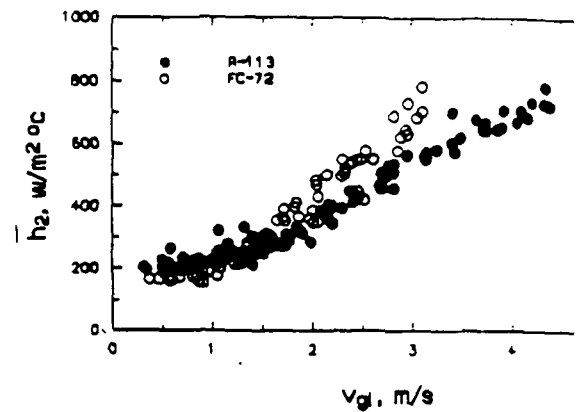
The total heat transfer coefficient can also be determined from the measurement of the measured film thickness using the equation (Eq. 4-21)

$$\bar{h}_t = \frac{k_f L^{-c_1}}{c_1(1-c_2)}$$

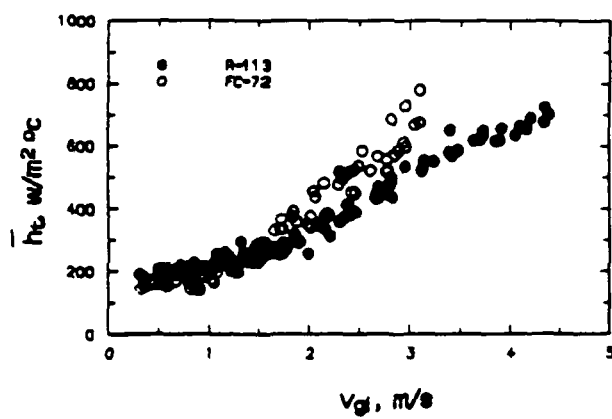
where c_1 and c_2 are the coefficients in the film thickness correlation ($\delta = c_1 x^{c_2}$) and are determined from a regression analysis of the experimental data. Fig. 6.7 shows a comparison between the total heat transfer coefficients obtained using the film thickness distribution (\bar{h}_{tr}) and those measured using the method of the heat balance of coolant through the test section (\bar{h}_t). Using the definition of the average deviation



a. \bar{h}_1



b. \bar{h}_2



c. \bar{h}_c

Fig. 6.6 Variation of average heat transfer coefficients with v_{g1}

6. Results and Discussion

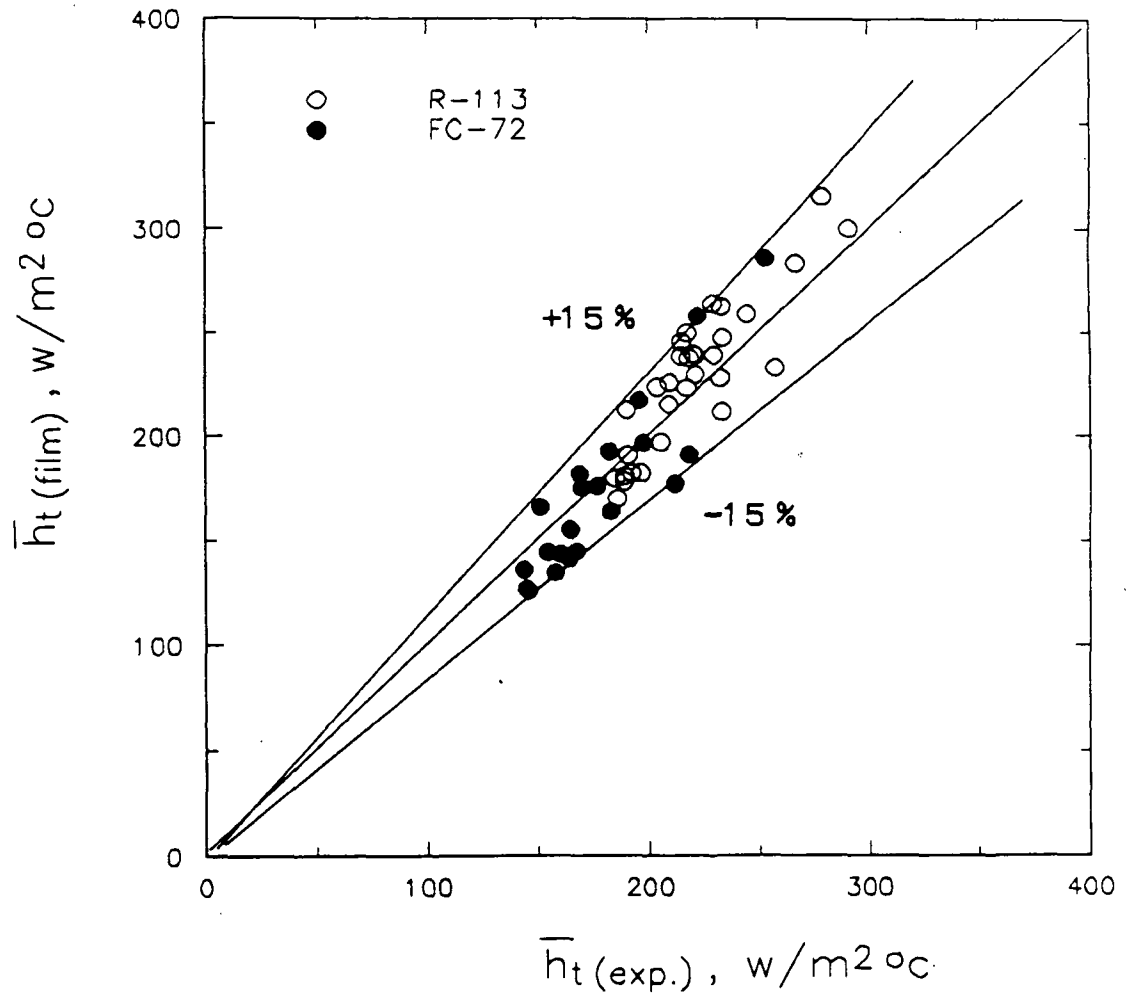


Fig. 6.7 Comparison of heat transfer coefficients measured from the heat balance method with the values obtained from the film thickness data

$$S = \sqrt{\frac{1}{N} \sum_{i=1}^N \left(\frac{\bar{h}_{if} - \bar{h}_t}{\bar{h}_t} \right)^2} \quad (6-0)$$

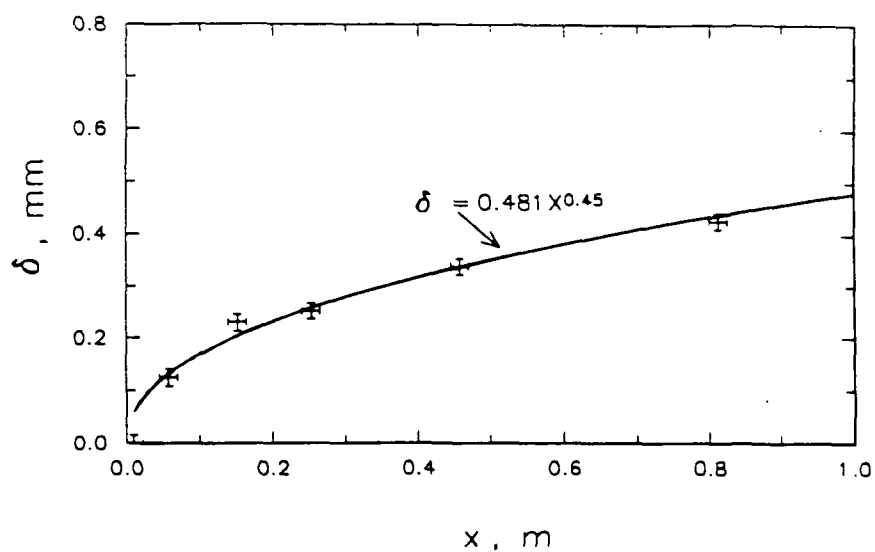
the average deviation between the two different values is found to be within 10 %. This comparison validates the technique of measuring the local condensate film thickness by the ultrasonic transducer. As a check of the validity of the power law correlation for the film thickness, two typical correlations ($\delta = 0.481x^{0.45}$ and $\delta = 0.483x^{0.24}$) are shown in Fig. 6.8. The average deviation between the calculated thickness using the correlation and the measured values is less than ± 6 % for both the correlations. As shown in Appendix G, the range of the values of the exponent (c_2) in all the correlations is 0.17 to 0.47 for R-113 and 0.15 to 0.50 for FC-72.

Fig. 6.9 shows the effect of the temperature difference (ΔT) on the total average heat transfer coefficients (\bar{h}_t). In the figure, \bar{h}_t is plotted against the mass velocity (G) to compare the trends of the present experimental results with those of Akers and et al. (1958). It is seen that:

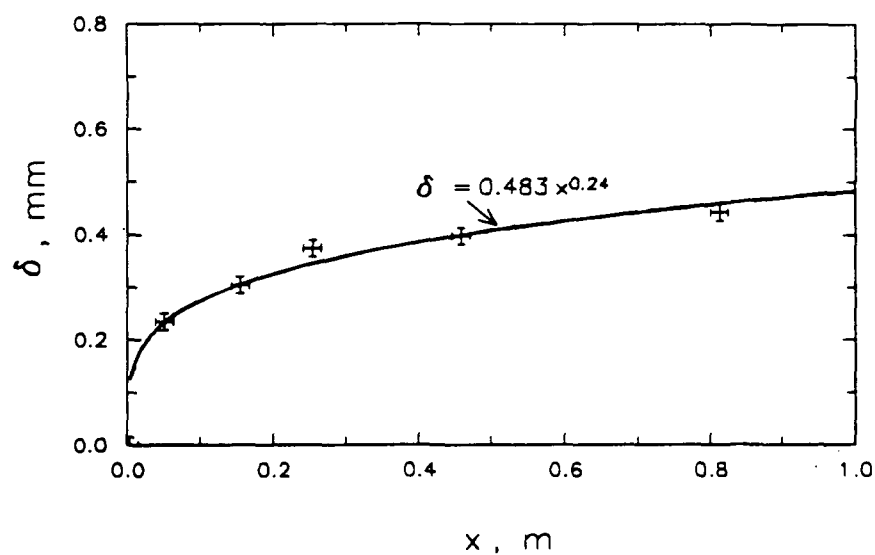
- the influence of ΔT on \bar{h}_t for R-113 is insignificant in the whole range of the mass velocity of vapor ($G < 33 \text{ kg/s m}^2$)
- the influence of ΔT on \bar{h}_t for FC-72 is also insignificant when G was less than or equal to 25 kg/s m^2
- for FC-72, when G is greater than 25 kg/s m^2 , \bar{h}_t with $\Delta T = 10^\circ \text{C}$ is smaller than the others
- for FC-72, when G is greater than 35 kg/s m^2 , \bar{h}_t with $\Delta T = 30^\circ \text{C}$ is less than \bar{h}_t with 20°C , but greater than \bar{h}_t with 10°C (The reason for this result is not clear and it needs further investigation)

Akers et al. (1958) measured the total average heat transfer coefficient for R-12

6. Results and Discussion



a

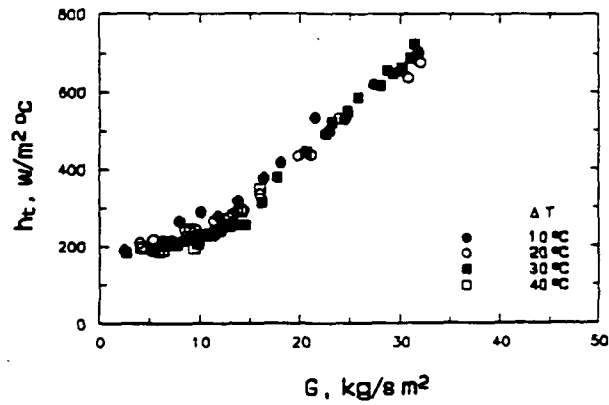


b

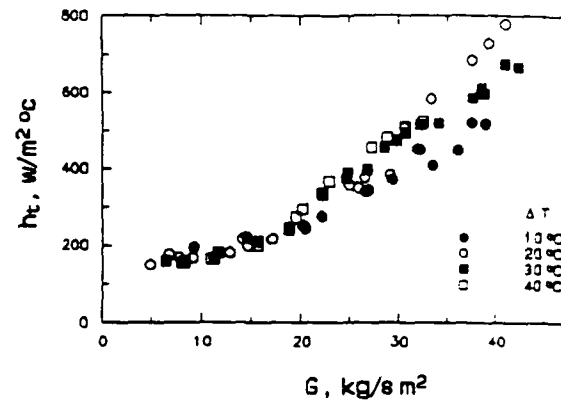
Fig. 6.8 Typical examples of film thickness correlations

a. R-113; $\Delta T = 22.8$ °C; $v_{g1} = 1.8$ m/s

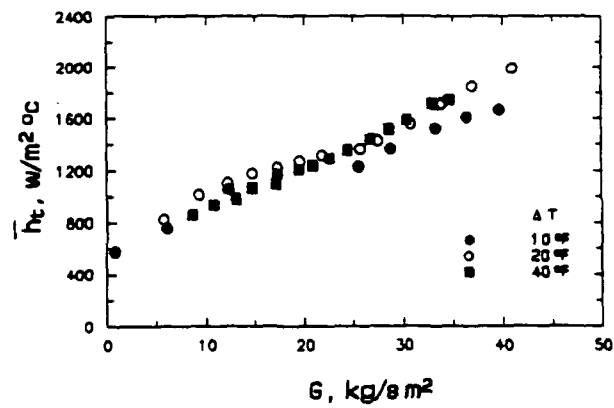
b. FC-72; $\Delta T = 30.8$ °C; $v_{g1} = 0.8$ m/s



a. R-113



b. FC-72



c. Akers, Dean, and Crosser (1958)

Fig. 6.9 Total average heat transfer coefficients as a function of vapor mass velocity to the inlet of the test section

6. Results and Discussion

flowing inside a horizontal condensing tube. Their results also showed that the heat transfer coefficient with a lower ΔT is smaller than that with a higher ΔT when the total vapor mass velocity was higher than 25 kg/s m^2 . Abis (1969) also studied the effect of ΔT on \bar{h}_t in a horizontal condensing tube. However, no conclusion about the relationship between ΔT and \bar{h}_t was drawn from his experiments.

6.6.2. Sectional Heat Transfer Rates and Sectional Heat Transfer Coefficients

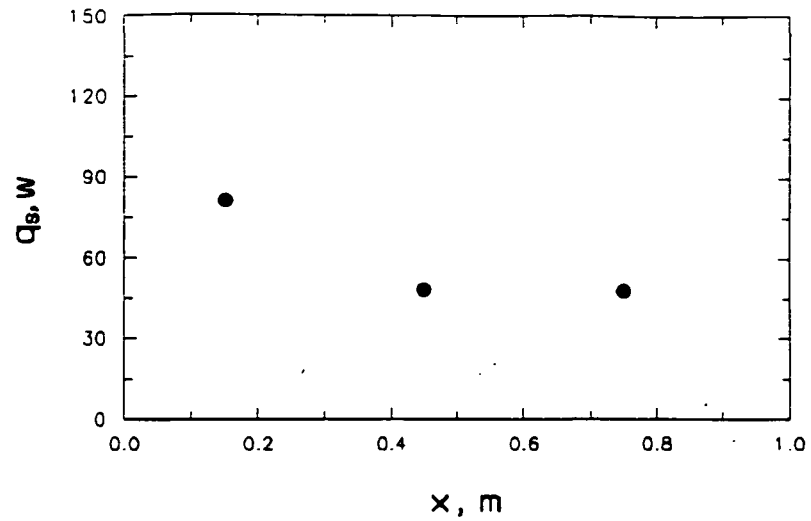
The condensing surface was divided into three equal sections; the heat transfer from the vapor to each section is the sectional heat transfer rate (q_s). The sectional heat transfer rate is obtained from an energy balance on the coolant in each section. Fig. 6.10 illustrates the variation of the three sectional heat transfer rates with the condensing surface. It is seen that the heat transfer rate at section 1 is higher than the heat transfer rates at sections 2 and 3, while the change of heat transfer rate from section 2 to section 3 is quite small.

The sectional heat transfer coefficient is an average heat transfer coefficient in the section and is evaluated using Eq. 4-15. Two typical distributions of the sectional heat transfer coefficients along the length of the condensing surface are shown in Fig. 6.11. Similar to the trend of the sectional heat transfer rates, the sectional heat transfer coefficients decrease from section to section along the length of the condensing surface.

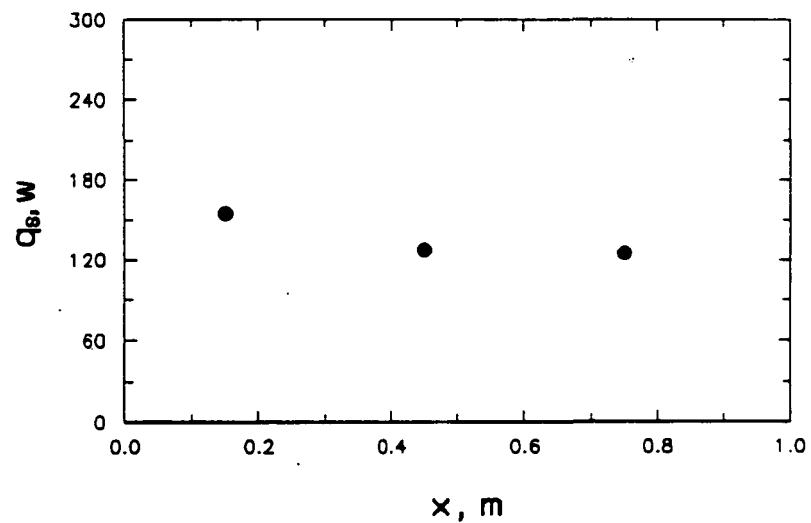
Fig. 6.12 compares the sectional heat transfer coefficients of R-113 with those of FC-72 at approximately the same values of ΔT and \dot{m}_t (one plot for lower \dot{m}_t and the other for higher \dot{m}_t). It is seen that when \dot{m}_t is lower, the sectional heat transfer coefficient of R-113 is larger than that of FC-72 (figure a). However, when \dot{m}_t is higher, the reverse happens except in the first section (figure b).

The phenomenon shown in Fig. 6.12a may be explained by comparing the film thickness of R-113 with that of FC-72 at a lower \dot{m}_t . At approximately the same \dot{m}_t and ΔT , the value of the film thickness of R-113 is smaller than that of FC-72

6. Results and Discussion



a



b

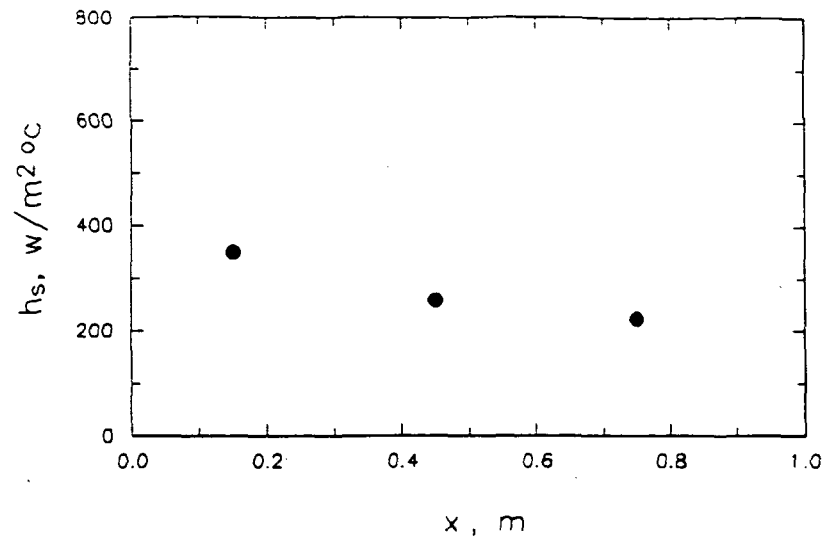
Fig. 6.10 Sectional heat transfer rates

a. R-113; $\Delta T = 21.7^\circ\text{C}$; $v_{g1} = 1.3\text{ m/s}$

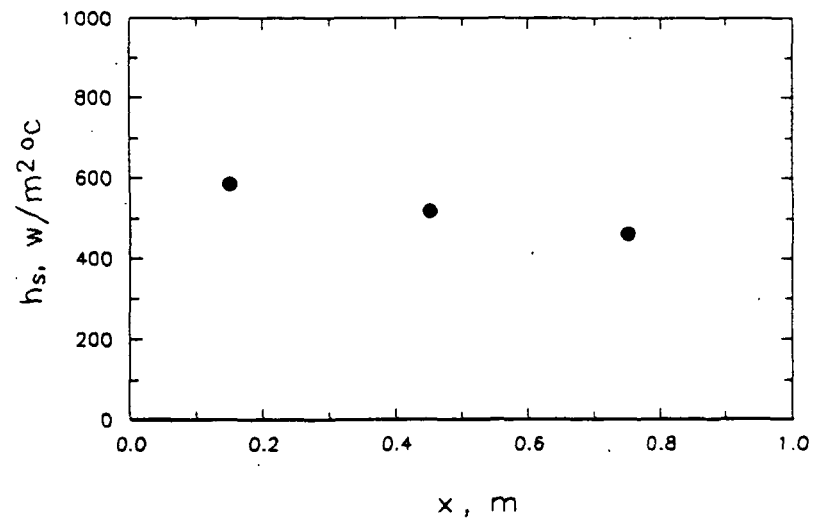
b. FC-72; $\Delta T = 19.4^\circ\text{C}$; $v_{g1} = 2.5\text{ m/s}$

Note: Each point represents the average heat transfer coefficient at a section whose midpoint corresponding to the x-value.

6. Results and Discussion



a



b

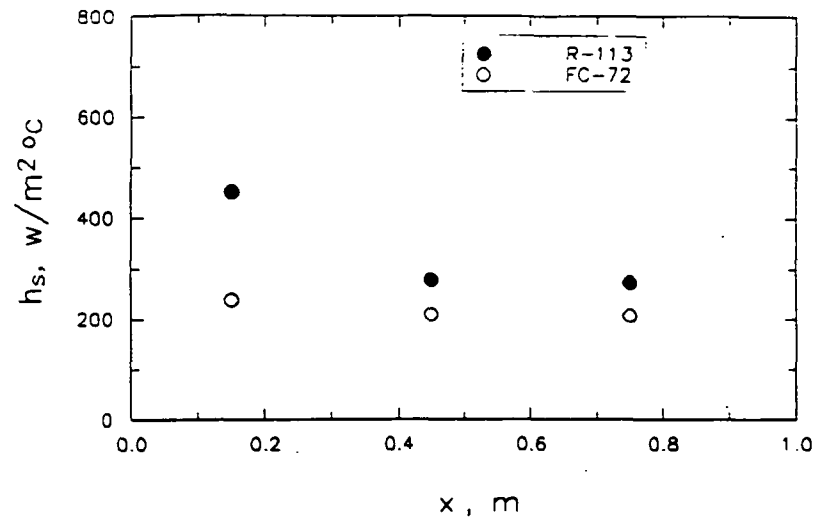
Fig. 6.11 Sectional heat transfer coefficients

a. R-113; $\Delta T = 10.8 \text{ } ^\circ C$; $v_{gl} = 1.6 \text{ m/s}$

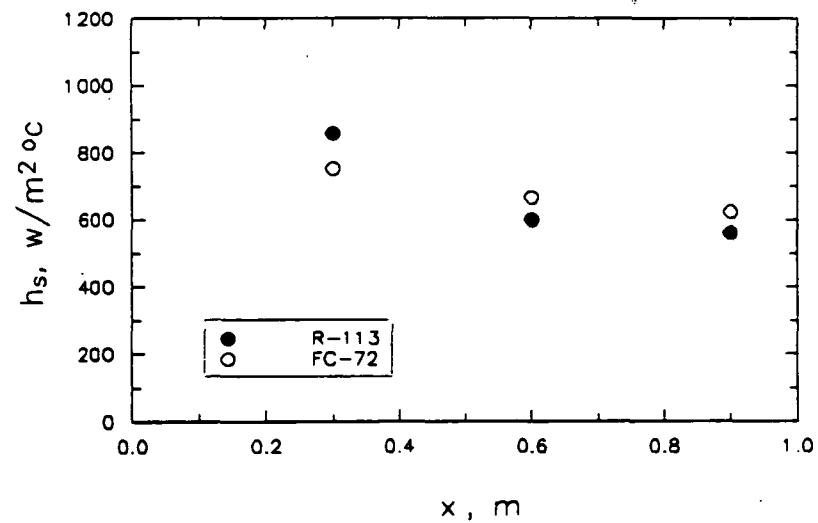
b. FC-72; $\Delta T = 39.1 \text{ } ^\circ C$; $v_{gl} = 2.5 \text{ m/s}$

Note: Each point represents the average heat transfer coefficient at a section whose midpoint corresponding to the x-value.

6. Results and Discussion



a. $\Delta T = 20\text{ }^\circ\text{C}$; $m_1 = 0.016\text{ kg/s}$



b. $\Delta T = 20\text{ }^\circ\text{C}$; $m_1 = 0.032\text{ kg/s}$

Fig. 6.12 Comparison of sectional heat transfer coefficients of R-113 with that of FC-72

Note: Each point represents the average heat transfer coefficient at a section whose midpoint corresponding to the x -value.

6. Results and Discussion

(Fig. 6.13a) and this is more obvious when ΔT is higher (Fig. 6.13b). Studying the thermal properties of the condensing fluids (Table 4.1), it is found that the thermal conductivity of liquid R-113 is about 1.3 times higher than that of FC-72. The thinner film thickness and higher thermal conductivity of R-113 results in a lower thermal resistance across the condensate film, and therefore leads to a higher heat transfer coefficient.

At higher \dot{m}_l (implying higher Re_{gl}), interfacial waves appear on the condensate film. The interfacial waves influence the heat transfer coefficients and the extent of the effect of the interfacial waves on the heat transfer coefficients may vary for different condensing fluids.

Based on the measured distribution of the film thickness along the condensing surface, the sectional heat transfer coefficients can also be calculated using the measured film thickness (Eq. 4-22). The sectional heat transfer coefficients obtained using the measured film thickness ($\bar{h}_{s,f}$) are compared with those measured using the method of the heat balance of the coolant flow (\bar{h}_s) and the results are shown in Fig. 6.14. The average deviation between $\bar{h}_{s,f}$ and \bar{h}_s in section 1 is within $\pm 10\%$; in section 2 and 3 the average deviation is between $\pm 10\%$ and $\pm 20\%$.

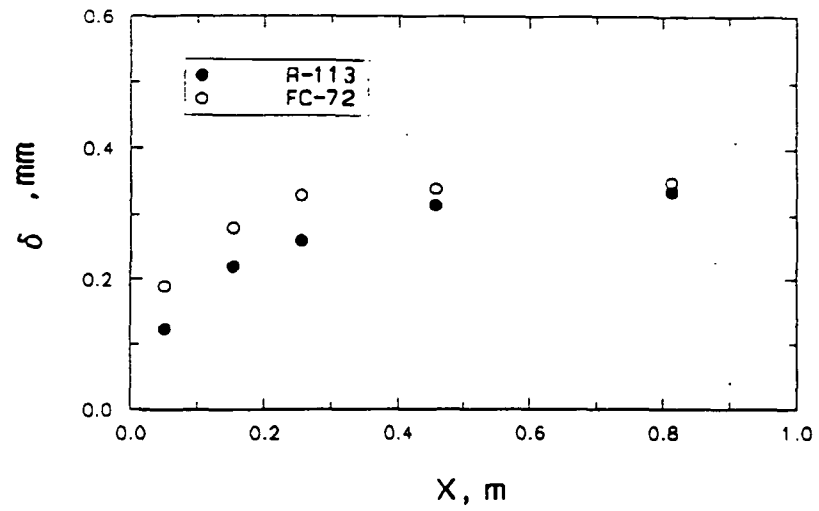
6.6.3. Local Heat Transfer Coefficients

The local heat transfer coefficients (h_x) are obtained from the measurement of the condensate film thickness along the condensing surface

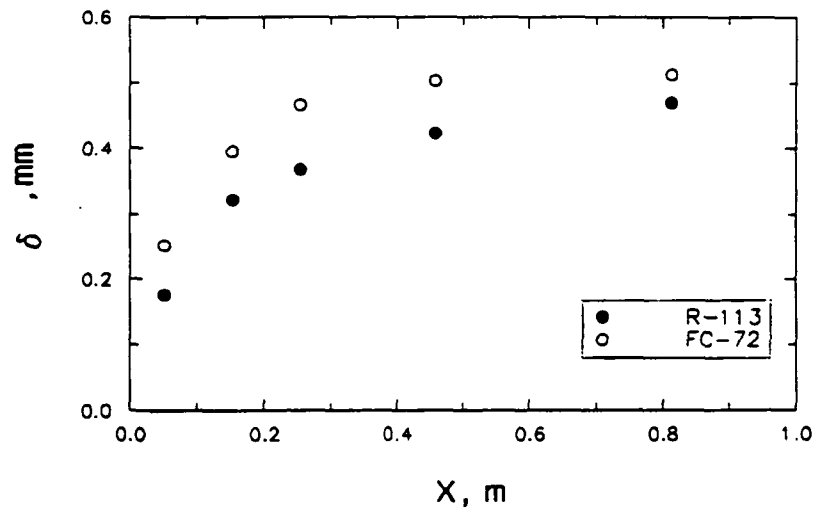
$$h_x = \frac{k_l}{c_1} x^{-c_2}$$

where c_1 and c_2 are the coefficients in the film thickness power correlation (Eq. 4-17). Fig. 6.15 shows some typical trends of local heat transfer coefficients (h_x) varying with the axial distance of the condensing surface (x). It is seen that with increasing inlet vapor velocity (v_{gi}), the local heat transfer coefficient increases; however, the effect

6. Results and Discussion



a



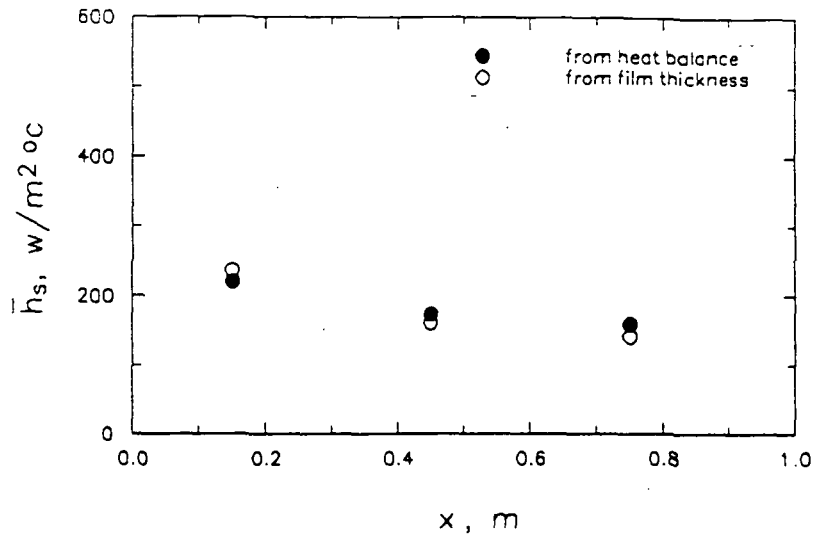
b

Fig. 6.13 Effect of condensing fluids on film thickness of condensate

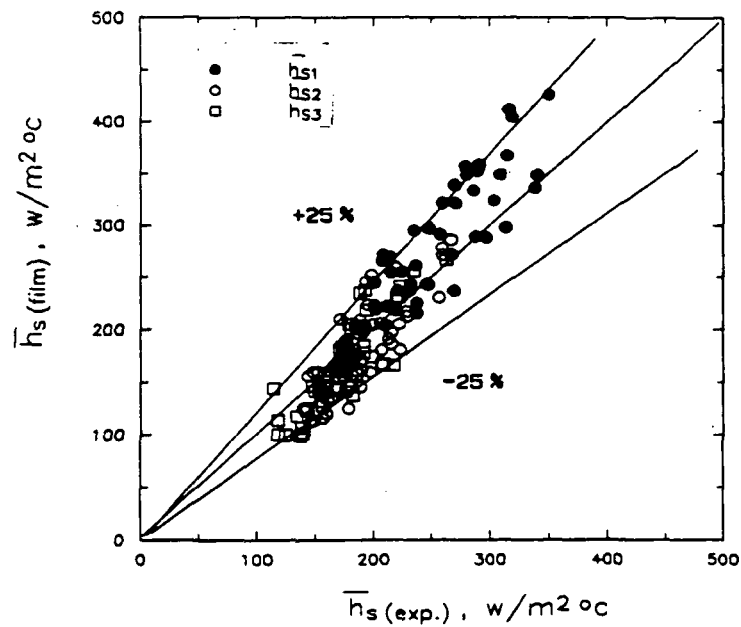
a. $\Delta T = 20^\circ\text{C}$; $\dot{m}_l \approx 0.008 \text{ kg/s}$

b. $\Delta T = 40^\circ\text{C}$; $\dot{m}_l \approx 0.008 \text{ kg/s}$

6. Results and Discussion



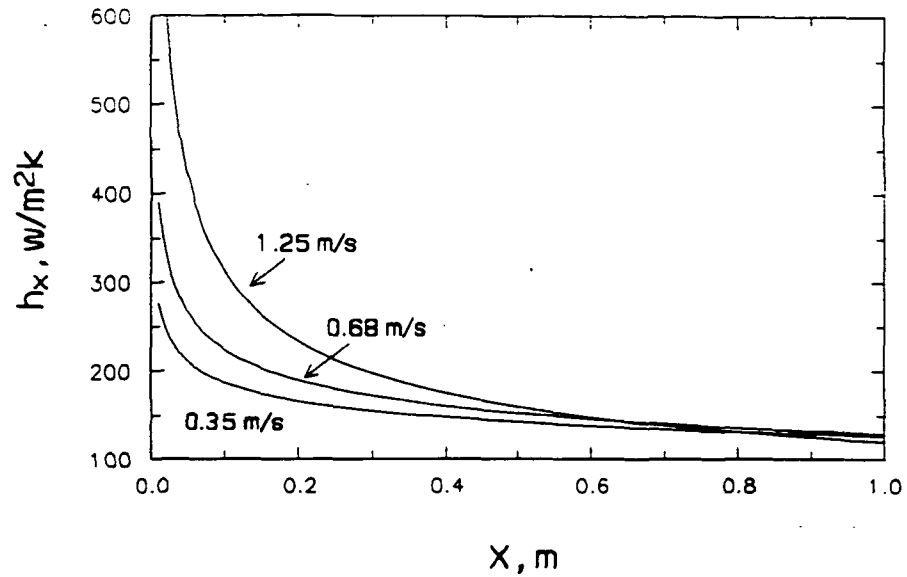
a. Typical comparison



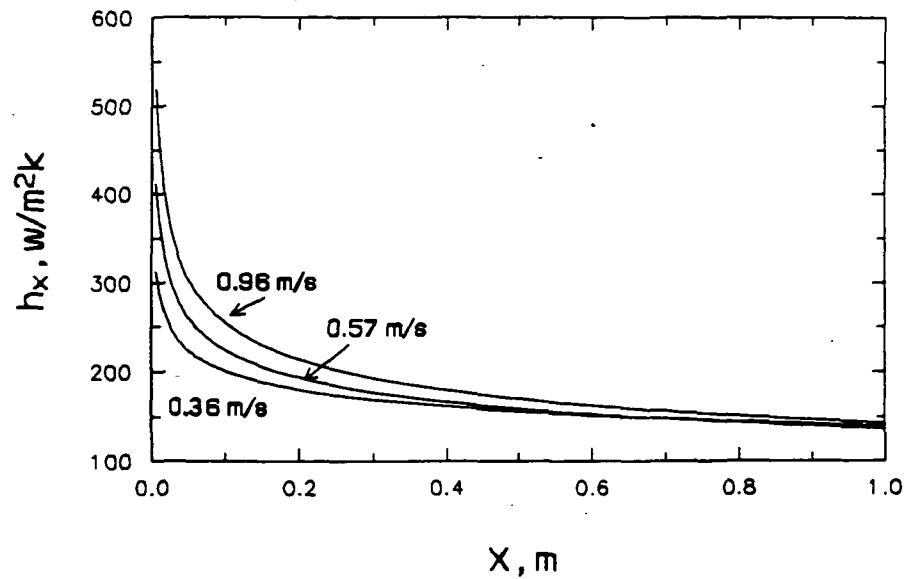
b. overall comparison

Fig. 6.14 Comparisons of sectional heat transfer coefficients measured from heat balance method with values obtained from film thickness data

6. Results and Discussion



a. $\Delta T = 40^\circ\text{C}$; R-113



b. $\Delta T = 20^\circ\text{C}$; FC-72

Fig. 6.15 Variation of local heat transfer coefficients along the condensing surface

6. Results and Discussion

due to the increase in the vapor velocity on the local heat transfer coefficient decreases with increasing axial distance from the leading edge; near the trailing edge of the surface, this effect is almost negligible.

In experiments of film condensation with steam-air mixture inside a horizontal square duct (0.1 m on each side and 1.8 m long), Barry and Corradini (1988) also found that the local heat transfer coefficients decrease along the condensing surface and increase when the velocity of the steam-air mixture increases. In their experiments, the local heat transfer coefficients were obtained from the local heat flux obtained by measuring the temperature gradient across the thickness of the condensing wall.

Azer et al. (1971) also report that the local heat transfer coefficients decrease along the condensing surface and increase with an increase in the vapor velocity. However, their results show that the local heat transfer coefficients vary nearly linearly with the axial distance. Their experiment was conducted inside a 12.7 mm I.D. and 2.4 m long horizontal tube using R-12 as the condensing fluid. The local heat transfer coefficients were obtained from the local heat transfer flux determined from the product of the measured temperature gradient of the coolant, the coolant flow rate, and the coolant specific heat.

Traviss et al. (1973) conducted experiments of condensation inside a horizontal tube using R-12 as the condensing fluid. The trends of their local heat transfer coefficients with the axial distance and the inlet vapor velocity are very similar to the trends of the present experiments.

6.7. Dimensionless Parameters

6.7.1. Derivation of Dimensionless Parameters

To reduce the numbers of variables in any correlation, dimensionless variables are employed. Dimensionless variables can be obtained from differential equations or

6. Results and Discussion

from empirical methods.

A differential equation for the film thickness of condensation of vapor flow inside a horizontal rectangular duct was derived in Chapter 5 and is reproduced below

$$\frac{d\delta^*}{dx^*} = \frac{\kappa + [\alpha(x^*)L\delta^* + A_1\rho_l](\xi L\delta^* + \eta) - \gamma(x^*)L^3\delta^{*3}}{\varepsilon[\alpha(x^*)L\delta^* + A_1\rho_l] + 2L\delta^*[\theta(x^*)L\delta^* + \beta(x^*)] - \beta(x^*)L\delta^*}$$

where

$$\alpha(x) = (2 + n_r)A_2x^{n_r-1}v^{1-n_r}, \quad \beta(x) = \rho_l A_1 v$$

$$\gamma(x) = n_r A_2 x^{n_r-1} v^{2-n_r}, \quad \varepsilon(x) = 2A_1 \rho_l \int_0^x \frac{dx}{\delta}$$

$$\xi = \frac{A_1 \rho_l}{H \rho_g}, \quad \eta = 2A_1$$

$$\theta(x) = A_2 v^{2-n_r} x^{n_r}, \quad \kappa = 2A_1 \mu_l$$

Rearranging the above equation

$$\frac{d\delta^*}{dx^*} = \frac{\Psi(x^*)}{\Omega(x^*)} \quad (6-1)$$

where

$$\begin{aligned} \Psi(x^*) = & 2 + \left[k_1 \left(\frac{\mu_g}{\mu_l} \right) \left(\frac{\rho_l}{\rho_g} \right) \text{Re}_{gL}^{k_1} x^{n_r} \delta^* + \left(\frac{\text{Ja}}{\text{Pr}_l} \right) \right] \left[\left(\frac{L}{H} \right) \left(\frac{\rho_l}{\rho_g} \right) \delta^* + 1 \right] \\ & + k_3 \text{Re}_{gL}^{k_3} \left(\frac{\text{Pr}_l}{\text{Ja}} \right) \left(\frac{\rho_l}{\rho_g} \right) \left(\frac{\mu_g}{\mu_l} \right)^2 x^{n_r} \delta^{*3} \end{aligned}$$

and

6. Results and Discussion

$$\Omega(x^*) = k_6 \int_0^{x^*} \frac{dx^*}{\delta^*} \left[k_7 \text{Re}_{gL}^{k_1} \left(\frac{\mu_g}{\mu_l} \right) - \left(\frac{\text{Ja}}{\text{Pr}_l} \right) - \left(\frac{\rho_l}{\rho_g} \right) \left(\frac{\mu_g}{\mu_l} \right) \text{Re}_{gL} \delta^* \right. \\ \left. + 2 \text{Re}_{gL} \left(\frac{\text{Pr}_l}{\text{Ja}} \right) \left(\frac{\rho_l}{\rho_g} \right) \left(\frac{\mu_g}{\mu_l} \right) \delta^* \left[k_9 \text{Re}_{gL}^{k_{10}} \left(\frac{\mu_g}{\mu_l} \right) x^{*n} \delta^* + \left(\frac{\text{Ja}}{\text{Pr}_l} \right) \right] \right]$$

where k_i ($i=1$ to 10) represent some constants. Eq. 6-1 implies that the film thickness is a function of Pr_l/Ja , ρ_l/ρ_g , μ_l/μ_g , and Re_{gL} . Therefore, the following relation is assumed

$$\delta^* = f_8 \left[\left(\frac{\text{Pr}_l}{\text{Ja}} \right), \text{Re}_{gL}, \left(\frac{\mu_g}{\mu_l} \right), \left(\frac{\rho_l}{\rho_g} \right), x^* \right] \quad (6-2)$$

Using Eq. 5-39, the average heat transfer coefficient (\bar{h}_i) over the condensing surface with a length (L_i) measured from the leading edge can be calculated

$$\bar{h}_i = \frac{k_i}{L_i} \int_0^{L_i} \frac{dx^*}{\delta^*}, \quad i = 1 \text{ to } 3 \quad (6-3)$$

Defining the Nusselt number (Nu_i)

$$\text{Nu}_i = \frac{\bar{h}_i L_i}{k_i}$$

Eq. 6-3 becomes

$$\text{Nu}_i = \int_0^{L_i} \frac{dx^*}{\delta^*} \quad (6-4)$$

If Eq. 6-4 is integrated by substituting Eq. 6-2 for the dimensionless film thickness, the parameter (x^*) in Eq. 6-2 will be replaced by L^* (L/L), while the parameters $[\text{Pr}_l/\text{Ja}, \text{Re}_{gL}, (\mu_g/\mu_l), \rho_g/\rho_l]$ will remain in the relation for the Nusselt number

6. Results and Discussion

$$Nu_i = f_h\left[\left(\frac{Pr_i}{Ja}\right), Re_{gL}, \left(\frac{\mu_g}{\mu_l}\right), \left(\frac{\rho_l}{\rho_g}\right), \frac{L_i}{L}\right] \quad (6-5)$$

These parameters in Eq. 6-5, in addition to quality, can also be found in the heat transfer correlations of some other researchers [for example: Akers et al. (1958), Azer et al. (1971), Shah (1979)]. The quality included in those correlations accounts for the change in the local vapor velocity along the duct.

In Eq. 6-5, both Nu_i and Re_{gL} involve a characteristic length. There are two possible choices for the characteristic length used for condensation of vapor flow inside a duct: one is the hydraulic diameter (D_H), which is suitable for fully developed velocity and temperature profiles; the other is the length of the condensing surface (x or L), which is appropriate for a boundary layer problem. In the present study, the vapor enters the test section with a uniform velocity with a boundary layer on the condensate. It is assumed that the boundary layer thickness is much less than the height (25 mm) of the test section. (It has been estimated that the boundary thickness is less than 5 mm.) With such a boundary layer, the distance from the leading edge is much appropriate to be used as the characteristic length.

6.7.2. Average Nusselt Numbers and Stanton Numbers

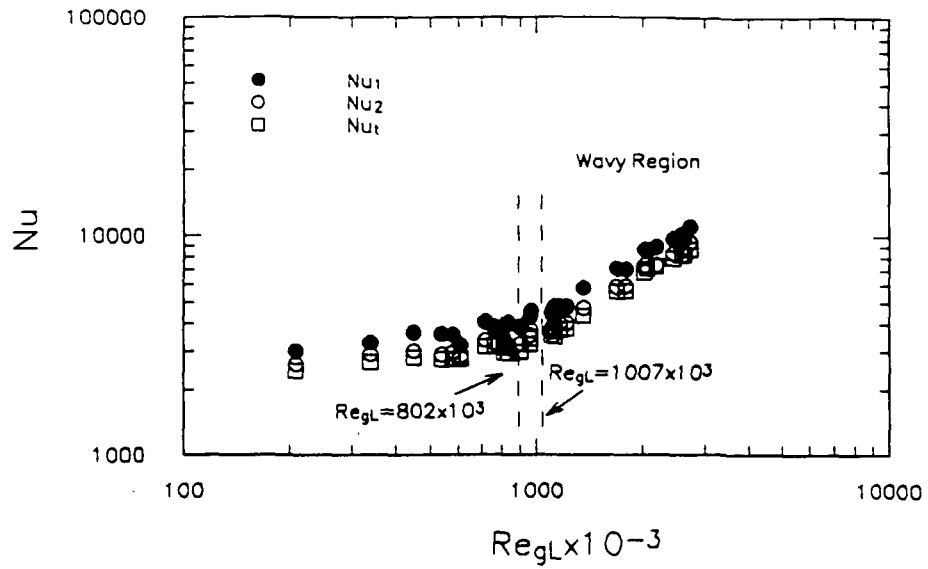
Average Nusselt Numbers

The variation of the average Nusselt numbers with the Reynolds number (Re_{gL}) based on the inlet vapor velocity for $\Delta T = 10^\circ\text{C}$ and $\Delta T = 40^\circ\text{C}$ is shown in Fig. 6.16, where Nu_1 , Nu_2 , and Nu_i are defined as the following

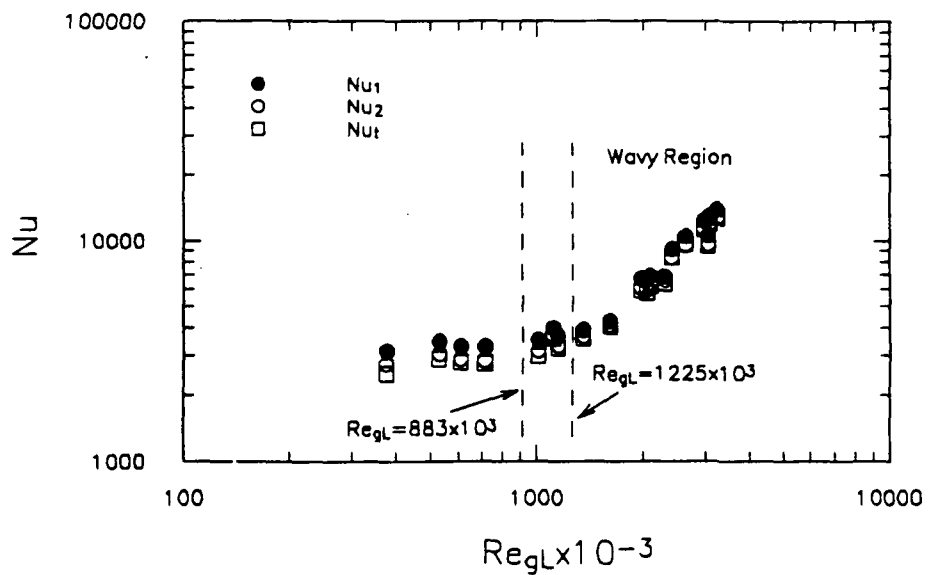
$$Nu_1 = \frac{\bar{h}_1 L_1}{k_l}, \quad Nu_2 = \frac{\bar{h}_2 L_2}{k_l}, \quad Nu_i = \frac{\bar{h}_i L_3}{k_l}$$

The Reynolds number at which the interfacial wave initiation was observed in the

6. Results and Discussion



a. R-113; $\Delta T = 20^\circ \text{C}$



b. FC-72; $\Delta T = 20^\circ \text{C}$

Fig. 6.16 Variation of average Nusselt numbers with Re_{gL}

6. Results and Discussion

experiments is denoted by the dashed lines. Before the initiation of the interfacial waves, the Nusselt numbers increase slightly with increasing the Reynolds number. However, after the interfacial waves appear, the Nusselt numbers increase rapidly. It can, therefore, be concluded that interfacial waves have a very significant effect on the condensation heat transfer rate.

Stanton numbers

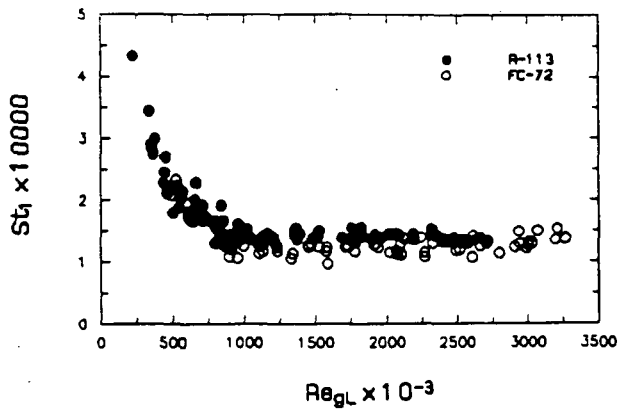
The Stanton number [$St_i = Nu_i / (Re_{g,i} Pr_i)$] can be expressed as $\bar{h}_i / (\rho_i c_{p,i} v_{g,i})$. The variation of the Stanton numbers with the inlet vapor Reynolds number is shown in Fig. 6.17, where St_1 is based on the average heat transfer coefficient (\bar{h}_1) in section 1; St_2 on the average heat transfer coefficient (\bar{h}_2) of section 1 and section 2 taken together; and St_t on the average heat transfer coefficients (\bar{h}_t) over the entire condensing surface. All the plots in the figure show that the Stanton numbers have the highest value at the leading edge of the condensing surface; they then decrease rapidly when the Reynolds number increases; beyond a certain value of the Reynolds number (about $Re_{g,L} > 800,000$), the Stanton numbers tend to be a constant. The Stanton numbers of both R-113 and FC-72 closely follow the same trend, varying with the Reynolds number and overlapping each other. The collapsing of all the experimental measurements opens the possibility of a correlation between St and $Re_{g,L}$.

6.8. Comparisons with Correlations and Data in Literature

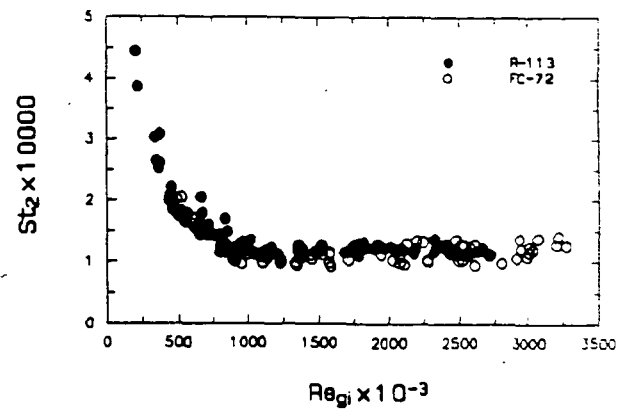
6.8.1. Comparison of Heat Transfer Correlations

There are a number of correlations predicting the heat transfer coefficient for condensation inside tubes. Some correlations are developed to predict the average heat transfer coefficients, while others can be used to predict both the local heat transfer coefficient and the average value. The latter correlations are more appropriate to compare the predictions of local, sectional, and average heat transfer coefficients with

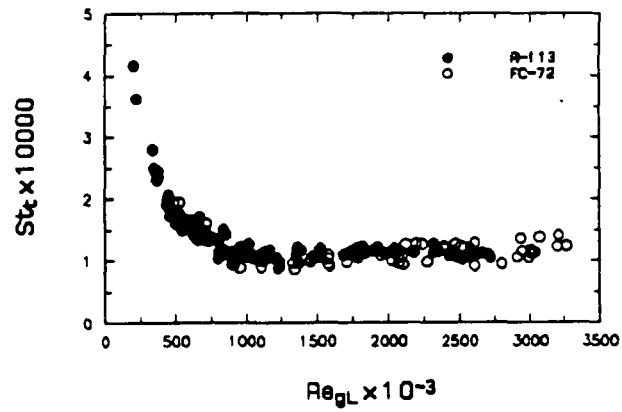
6. Results and Discussion



a. St_1



b. St_2



c. St_t

Fig. 6.17 Variation of Stanton numbers with Re_{GL}

6. Results and Discussion

the present experimental data. As a result, four correlations of Soliman et al. (1968), Azer et al. (1971), Traviss et al. (1973), and Shah (1979), predicting both the local and the average heat transfer coefficients of condensation inside a tube are chosen.

The backgrounds and techniques for developing those selected correlations are described in Chapter 1. A brief introduction for each correlation follows.

Correlation of Soliman, Schuster, and Berenson (1968)

Their correlation is derived based on a theory of an annular condensation and experimental data of condensation inside both horizontal and vertical tubes. The condensing fluids in the experiments were water, ethanol, methanol, toluene, trichloroethylene, R-113, and R-22. The correlation is

$$h_x = 0.036 \frac{k_l}{\mu_l} Pr_l^{0.65} \sqrt{(F_r + F_m) \rho_l} \quad (6-6)$$

where

$$\frac{F_r}{8\dot{m}_t^2/(\pi^2 \rho_g D_H^4)} = 0.045 Re_{gL}^{-0.2} [X^{1.8} + 5.7 \left(\frac{\mu_l}{\mu_g}\right)^{0.0523} (1 - X)^{0.47} X^{1.83}$$

$$\times \left(\frac{\rho_g}{\rho_l}\right)^{0.261} + 8.11 \left(\frac{\mu_l}{\mu_g}\right)^{0.105} (1 - X)^{0.94} X^{0.86} \left(\frac{\rho_g}{\rho_l}\right)^{0.522}]$$

$$\frac{F_m}{8\dot{m}_t^2/(\pi^2 \rho_g D_H^4)} = 0.5 D_H \left(\frac{dX}{dx}\right) [2(1 - X) \left(\frac{\rho_g}{\rho_l}\right)^{2/3} + \left(\frac{1}{X} - 3 + 2X\right) \left(\frac{\rho_g}{\rho_l}\right)^{4/3}$$

$$+ (2X - 1 - \beta X) \left(\frac{\rho_g}{\rho_l}\right)^{1/3} + \beta \left(\frac{\rho_g}{\rho_l}\right)^{5/3} \left(2 - \frac{1}{X} - X\right) + 2(1 - X - \beta + \beta X) \left(\frac{\rho_g}{\rho_l}\right)]$$

$\beta = 1.25$ for turbulent film; $\beta = 2.0$ for laminar condensate film. Since in the present

6. Results and Discussion

experiment, the flow of the condensate film is considered to be laminar, a value of 2.0 is chosen for β .

Correlation of Azer, Abis, and Swearingen (1971)

The correlation is derived based on an analytical model of condensation and their own experimental data of condensation inside a horizontal tube of 12.7 mm I.D. and 2.4 m long. In the experiment, R-12 was used as the condensing fluid; the range of the total vapor mass velocity varied from 137 to 448 kg/m² s; the quality (X) at the exit of the tube varied from 0.18 to 0.77. The correlation is

$$h_x = 0.153 \frac{k_i}{D_H} Pr_i Re_{gl}^{0.9} \left(\frac{\mu_g}{\mu_l} \right) \left(\frac{\rho_l}{\rho_g} \right)^{0.5} X^{0.9} \frac{\phi_g}{t_g^*} \quad (6-7)$$

where

$$\Phi_g = 1 + 1.0986 \chi_u^{0.039}$$

$$t_g^* = 3.88 Pr_i^{0.663} (4.67 - X) \quad \chi_u = \left(\frac{\mu_l}{\mu_g} \right)^{0.1} \left(\frac{\rho_g}{\rho_l} \right)^{0.5} \left(\frac{1-X}{X} \right)^{0.9}$$

Correlation of Traviss, Rohsenow, and Baron (1973)

The correlation is based on an annular flow model using the von Karman universal velocity distribution for the condensate film. The correlation is

$$h_x = 0.15 \frac{k_i}{D_H} \frac{Pr_i Re_i^{0.9}}{F_2} \left[\frac{1}{\chi_u} + 2.85 \chi_u^{-0.476} \right] \quad (6-8)$$

where

$$F_2 = 0.707 Pr_i Re_i^{0.5}, \quad Re_i \leq 50$$

$$F_2 = 5 Pr_i + 5 \ln[1 + Pr_i (0.09636 Re_i^{0.585} - 1)], \quad 50 < Re_i \leq 1125$$

6. Results and Discussion

$$F_2 = 5Pr_1 + 5\ln(1 + 5Pr_1) + 2.5\ln(0.00313Re_1^{0.812}), \quad Re_1 \geq 1125$$

$$\chi_u = \left(\frac{\mu_l}{\mu_g}\right)^{0.1} \left(\frac{\rho_g}{\rho_l}\right)^{0.5} \left(\frac{1-X}{X}\right)^{0.9}$$

$$Re_l = \frac{G(1-X)D_H}{\mu_l}$$

Correlation of Shah (1979)

Shah developed his correlation from a broad base of experimental data of condensation inside horizontal, vertical, and inclined tubes with diameters ranging from 7 to 40 mm. The condensing fluids involved in the experiments were water, R-11, R-12, R-22, R-113, methanol, ethanol, benzene, toluene, and trichloroethylene. The total vapor mass velocity varied from 10.83 to 211 kg/m²·s. His correlation is

$$h_x = h_L \left[(1-X)^{0.8} + \frac{3.8X^{0.76}(1-X)^{0.04}}{p_r^{0.38}} \right] \quad (6-9)$$

where h_L is the heat transfer coefficient for a single phase fluid in fully developed flow in a circular tube. From the Dittus-Boelter correlation

$$h_L = 0.023 \frac{k_l}{D_H} Re_{gL}^{0.8} Pr_l^{0.4}$$

and p_r represents the reduced pressure (actual pressure/critical pressure). Eq. 6-6 was further integrated to derive an expression for the average heat transfer coefficient over a certain length of a condensing surface.

$$\bar{h} = \frac{h_L}{X_2 - X_1} \left[-\frac{(1-X)^{1.8}}{1.8} + \frac{3.8}{p_r^{3.8}} \left(\frac{X^{1.76}}{1.76} - \frac{0.04X^{2.76}}{2.76} \right) \right]_{X_1}^{X_2} \quad (6-10)$$

6. Results and Discussion

where X_1 is the quality at the beginning of the condensing surface and X_2 is the quality at the end of the surface.

Shah's correlation appears to have the simplest form among the four selected correlations. However, his correlation predicts a zero value for the local heat transfer coefficient at the leading edge of the condensing surface where the quality (X) is 1, which is not acceptable. As a result, this correlation is used only to predict the average heat transfer coefficients, while the other three correlations are used to calculate both the local and the average heat transfer coefficients.

In using the above the correlations, the thermodynamic and physical properties of the vapor are evaluated at the saturation temperature, the properties of the condensate are determined at the arithmetic average of the saturation temperature and the condensing surface temperature. The quality (X) is calculated as follows.

The quality is defined as

$$X = 1 - \frac{\dot{m}_l}{\dot{m}_t} \quad (6-11)$$

The expression for the condensate flow rate (\dot{m}_l) is found by substituting Eq. 4-16 into Eq. 4-24

$$\dot{m}_l = \frac{Wk_l}{h_{fg}} \int_0^x \frac{\Delta T_x}{\delta} dx$$

Using the film thickness correlation (Eq. 4-17) and assuming ΔT_x to be constant, the above equation becomes

$$X = 1 - \frac{W}{c_1(1-c_2)} \frac{k_l \Delta T}{\dot{m}_l h_{fg}} x^{1-c_2} \quad (6-12)$$

Fig. 6.18 illustrates a typical distribution of the quality along the condensing duct. The maximum deviation between the calculated exit quality and the measured value

6. Results and Discussion

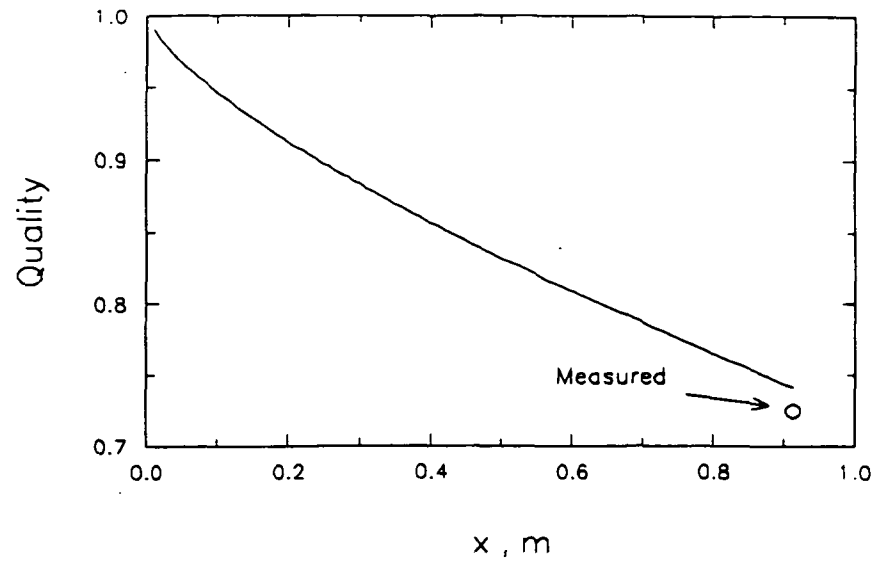


Fig. 6.18 Typical variation of quality along the condensing surface

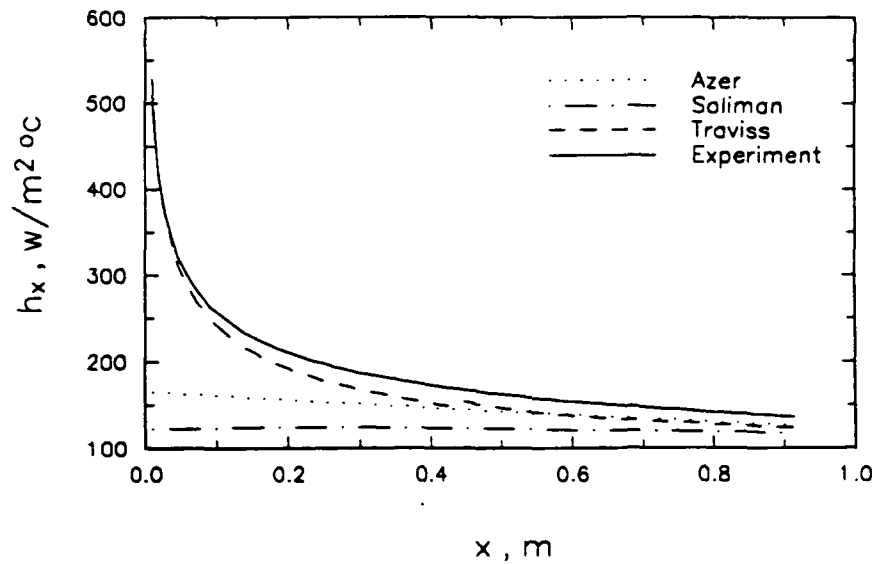


Fig. 6.19 Comparison of predictions for local heat transfer coefficients from correlations of Azer, Soliman, and Tranviss with experimental data

6. Results and Discussion

(which is determined using the expression: $X_e = 1 - \dot{m}_{lt} / \dot{m}_i$) is less than 3.5 % for all the 51 sets of experimental data with the film thickness measurement.

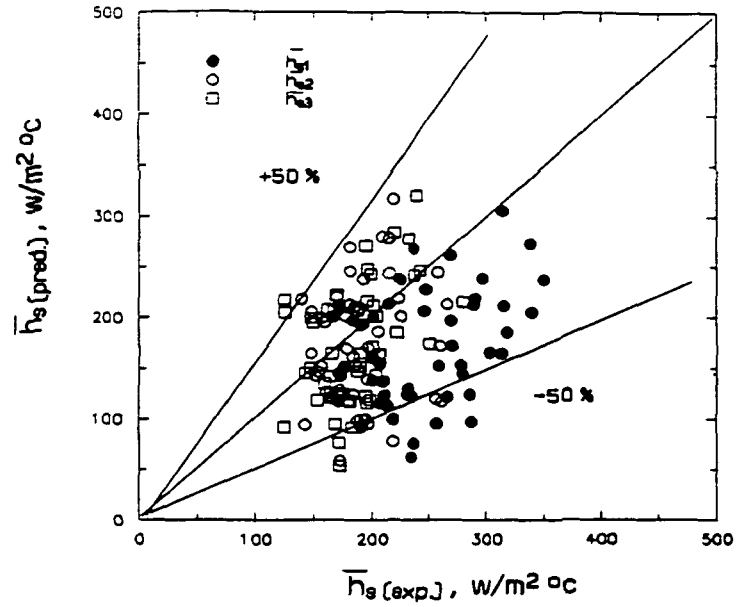
Fig. 6.19 shows a comparison of the predicted local heat transfer coefficient from correlations of Azer, Soliman, and Traviss with the present experimental data. The prediction from Traviss's correlation agrees well with the experimental data. Both Azer and Soliman's correlations give a nearly constant local heat transfer coefficients along the condensing surface. All the three correlations predict lower local heat transfer coefficients than the present experimental data. From a comparison of the results with predictions from the three correlations, it was found that the predictions are not good when the exit quality is less than about 0.5.

The four correlations of Soliman et al. (1968), Azer et al. (1971), Traviss et al. (1973), and Shah (1979) are used to calculate sectional heat transfer coefficients. Assuming constant ΔT , the following equation is employed to estimate the sectional heat transfer coefficients using the Azer, Soliman, and Traviss correlations

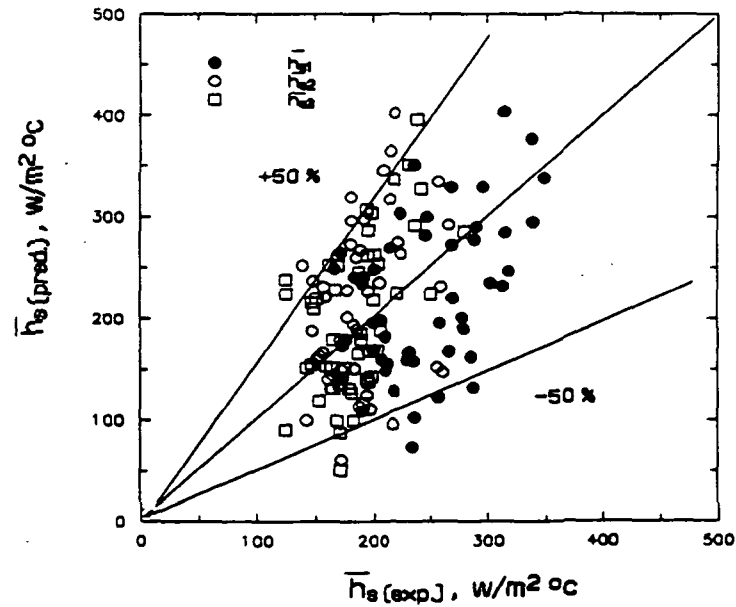
$$\bar{h}_{si} = \frac{1}{L_i - L_{i-1}} \sum_{i=1}^N h_{xi} \Delta x_i \quad (6-13)$$

while Shah's correlation (Eq. 6-10) for the average heat transfer coefficients can be used directly.

The comparison between the predicted sectional heat transfer coefficients and the present experimental data are shown in Fig. 6.20. The experimental data are about within ± 50 % of the predicted values. The average deviations are shown in Table 6.5. It is seen that Soliman's correlation has a fairly low deviation in section 1 but was higher deviations ($> \pm 30$ %) in sections 2 and 3; Azer's correlation leads to higher deviations ($> \pm 30$ %) in all the three sections; Traviss's correlation gives the highest deviation in section 1, but also produces the lowest deviations in sections 2 and 3; the deviations in all the three sections from Shah's correlation are nearly the same (around ± 29 %).



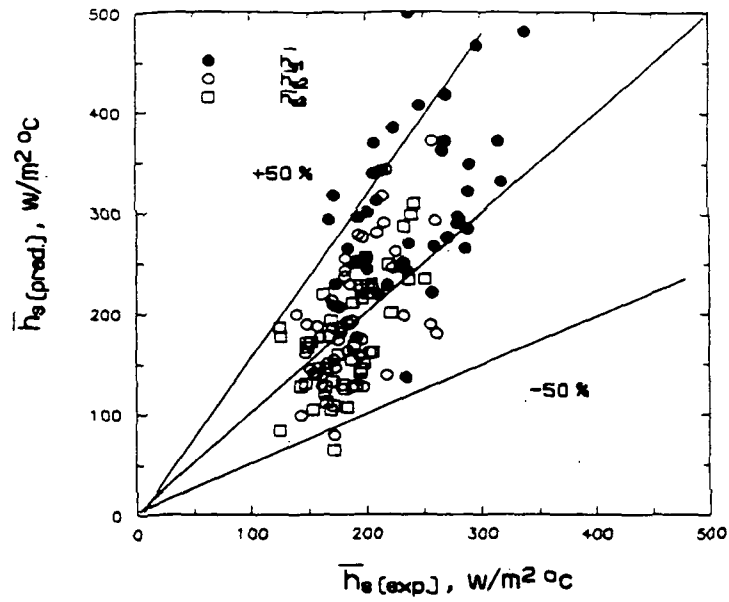
a. Comparison with the correlation of Sollman et. al (1968)



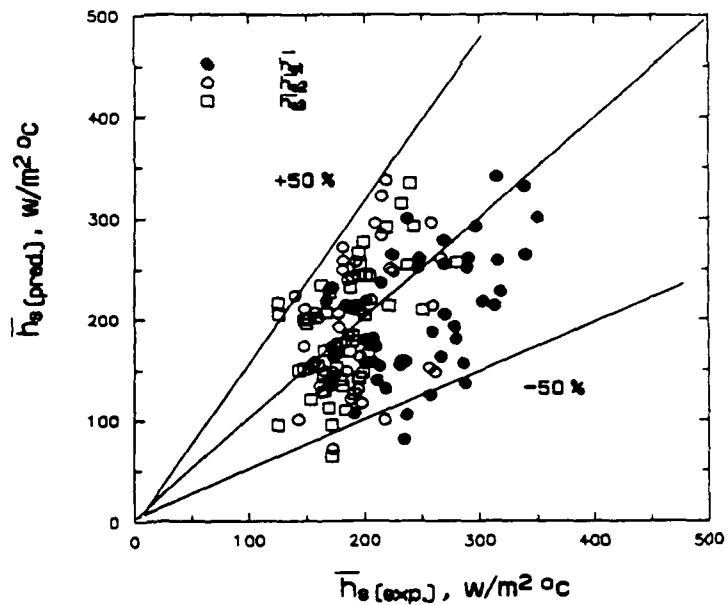
b. Comparison with the correlation of Azer et. al (1971)

Fig. 6.20 Predictions of sectional heat transfer coefficients from other researchers' correlations

6. Results and Discussion



c. Comparison with the correlation of Traviss (1973)



d. Comparison with the correlation of Shah (1979)

Fig. 6.20 Predictions of sectional heat transfer coefficients from other researchers' correlations

6. Results and Discussion

Table 6.5 Average deviations in comparison of sectional heat transfer coefficients

Correlations	Deviations (%)		
	Section 1	Section 2	Section 3
Soliman	22.2	37.0	31.9
Azer	30.3	39.9	37.8
Traviss	50.8	27.2	24.6
Shah	27.9	30.0	29.5

The four correlations are also used to predict the total average heat transfer coefficients (\bar{h}_t) over the whole range of the present experimental conditions. Since there is no film thickness measurement available when the vapor velocity is high, the quality can not be evaluated using Eq. 6-12. Instead, it is estimated by the following equation assuming a linear relation with the length (x) of the condensing surface

$$X = 1 - \frac{x}{L} \frac{\dot{m}_h}{\dot{m}_l} \quad (6-14)$$

Reviewing Fig. 6.18, it is seen that the quality changes nearly linearly along the length of the condensing surface except close to the leading edge. The distribution of the quality along the condensing tube was also studied by Shah (1979) based on a large amount of the experimental data. He showed that in estimating the heat transfer coefficient the error due to the assumption of a linear variation of quality is quite small if the change of the quality less than 40 %. Since the change of quality in the present experiment through the whole test section is less than 40 % for most of test runs, the use of Eq. 6-14 to estimate the quality distribution is appropriate.

Fig. 6.21 is a comparison of the predicted total average heat transfer coefficients

6. Results and Discussion

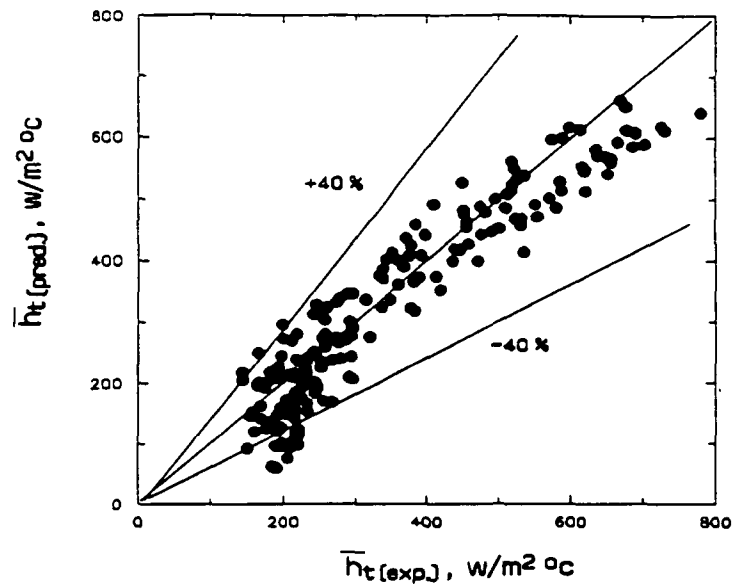
from the four correlations with the present experimental data. It is seen that the correlations of Azer and Traviss over-predict the heat transfer coefficients when the vapor velocity is high, while the correlations of Shah and Soliman generally give good predictions of the heat transfer coefficients. The over-prediction for the heat transfer coefficients from the correlations of Azer and Traviss were also observed by Luu (1980) after he compared the correlations with his experimental data. Also, those trends were found in the original works of Azer and Abis (1971) and Traviss et al (1973).

Table 6.6 lists the deviations as computed from Eq. 6-0 (where let $\bar{h}_{tr} = \bar{h}_{tr(pred)}$) between the predicted total average heat transfer coefficients from each of the four correlations and the present experimental data. Correlations of Shah and Soliman are the best of the four, with prediction that is within $\pm 22\%$ of the experimental value. The correlation of Traviss has the largest deviation. However, its prediction at lower vapor velocity is much better than the predictions from the other correlations (Fig. 6.21c).

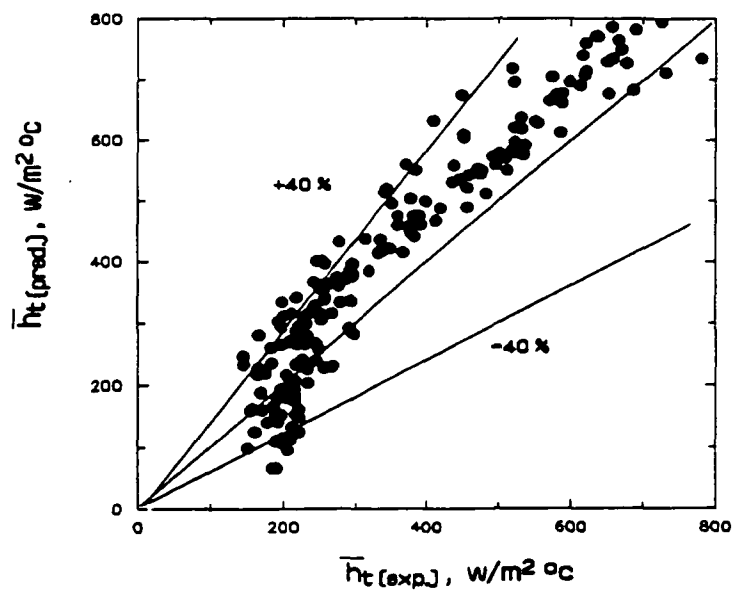
Table 6.6 Average deviations in comparison of the total average heat transfer coefficients

Correlations	Deviations (%)
Soliman	22.2
Azer	29.9
Traviss	36.7
Shah	20.7

6. Results and Discussion



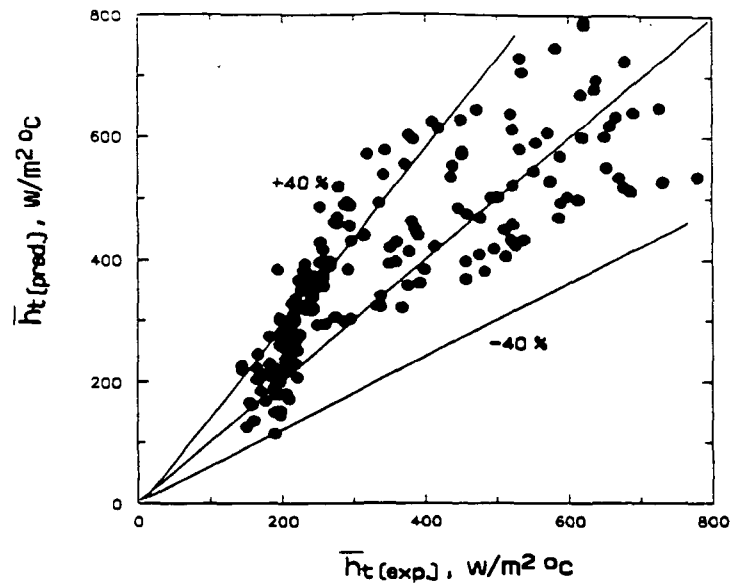
a. Comparison with the correlation of Soliman et. al (1968)



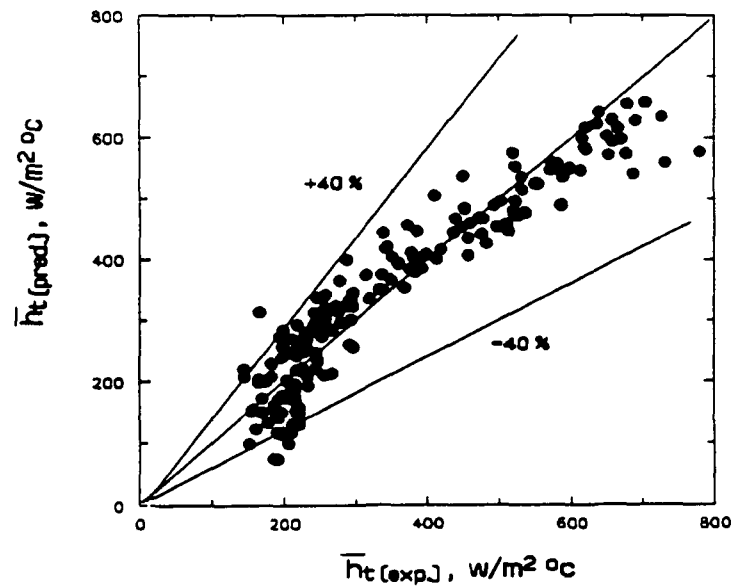
b. Comparison with the correlation of Azer et. al (1971)

Fig. 6.21 Predictions of overall average heat transfer coefficients from other researchers' correlations

6. Results and Discussion



c. Comparison with the correlation of Traviss et. al (1973)



d. Comparison with the correlation of Shah (1979)

Fig. 6.21 Predictions of overall average heat transfer coefficients from other researchers' correlations

6.8.2. Comparison with Experimental Data in the Literature

A comparison of the present experimental data with those of Akers and Rosson (1960) is shown in Fig. 6.22. The experimental data of Akers and Rosson was obtained with a 0.31 m horizontal condensing tube with a 9.5 mm I.D. Methanol, R-12, and propane were used as the condensing fluids. It is seen in the figure that the present experimental data display nearly the same trend as those of Akers and Rosson. There is an apparent difference between the two group of data when the parameter $[D_H G / \mu_l (\rho_l / \rho_g)^{1/4}]$ is low. However, this difference reduces when $D_H G / \mu_l (\rho_l / \rho_g)^{1/4}$ becomes larger. It is probably because the length of their condensing tube is similar to that of section 1 ($L_1 = 0.31$ m) of the present condensing surface, the value of the present Nu_1 appears closer to those of their Nusselt numbers (Fig. 6.22a) than Nu_2 and Nu_3 .

6.9. Predictions by Analysis

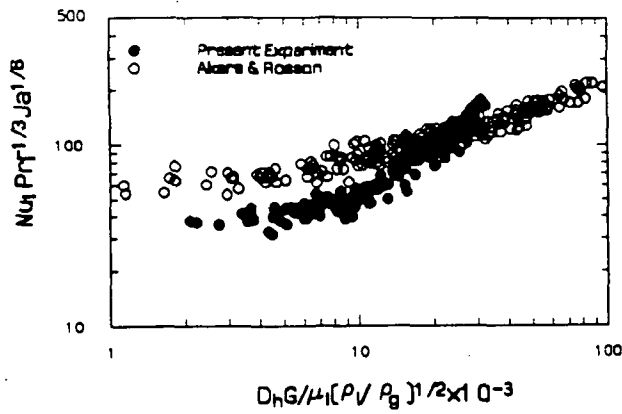
The analytical model described in Chapter 5 predicts the film thickness, the interfacial shear stress, and the local and the average heat transfer coefficients. The predicted values are compared with the present experimental data.

A key step in solving the analytical model is the determination of the interfacial shear stress. In the model, this shear stress is considered as the sum of an adiabatic shear stress and an equivalent shear stress due to the condensation of vapor on the vapor-condensate interface (See Eq. 5-16). The friction factor of the adiabatic shear stress is calculated in Eq. 5-18

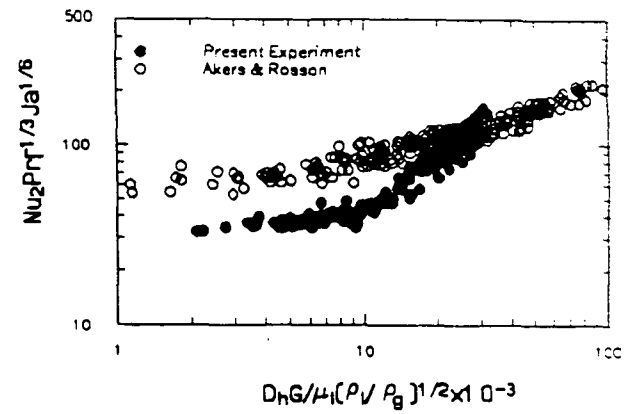
$$f_c = c_f Re_x^{n_f}$$

where the most appropriate values of the constants (c_f and n_f) are found from the available correlations for the local adiabatic friction factor and a trial procedure.

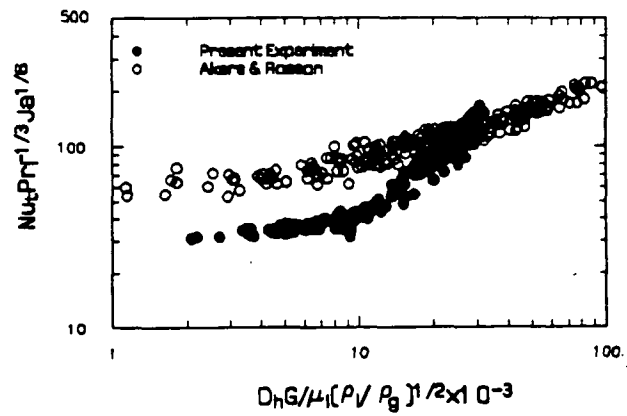
6. Results and Discussion



a. Comparison of \bar{h}_1



b. Comparison of \bar{h}_2



c. Comparison of \bar{h}_3

Fig. 6.22 Comparison of the present experimental data with that of Akers and Rosson (1960)

6. Results and Discussion

For a single phase turbulent boundary layer over a smooth flat plate, Schlichting (1979) proposed the following correlation for the local adiabatic friction factor

$$f_c = 0.0592 Re_x^{-0.2} \quad (6-15)$$

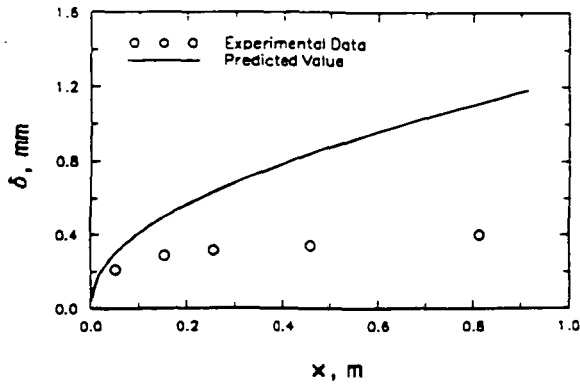
In the model, it is assumed that a vapor boundary layer exists over a flat condensate film. Although the vapor boundary layer may not be a turbulent one all along the condensate film, considering the difference between single-phase flows and two-phase flows, the uncertainty of the inlet conditions, and the idea of using a trial method to model the shear force, Eq. 6-15 is first chosen to evaluate the local adiabatic friction factor in Eq. 5-18.

Comparing Eq. 6-15 with Eq. 5-18, the constants, c_f and n_f , in Eq. 6-15 are found to be 0.0592 and -0.2 respectively. The model (Eq. 5-35) was solved with these values. The results from the initial calculation of the model are compared with the experimental values to evaluate the validity of Schlichting's friction equation in the model.

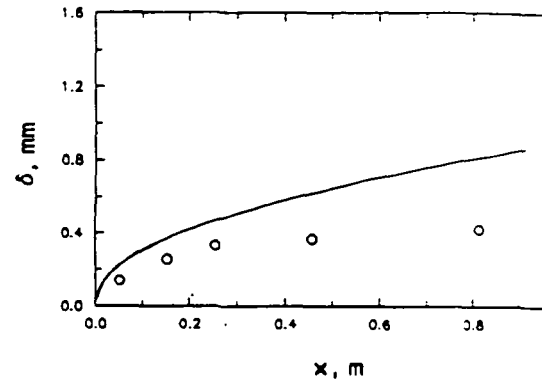
The film thickness predicted from the analytical model is compared with that measured in the experiment. This comparison is for $Re_{g,L} < 1,120,000$ for R-113 and $Re_{g,L} < 1,550,000$ for FC-72 in the experiment since for higher values of $Re_{g,L}$, interfacial waves set in and the film thickness measurement is not available. Fig. 6.23 shows some typical plots of the predicted film thickness and the experimental data for $\Delta T = 20^\circ C$. The predicted film thickness values are always larger than the experimental values. When the inlet vapor Reynolds number ($Re_{g,L}$) increases the difference between the predicted film thickness and the experimental value reduces.

Predicted sectional heat transfer coefficients are compared with the measured sectional heat transfer coefficients for the whole range of the experiment. Fig. 6.24 shows some typical comparisons. The experimental data used in this figure are the same as those used in Fig. 6.23. The deviation between the predicted value and the

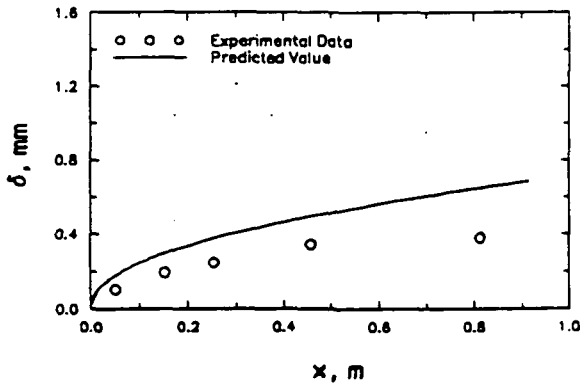
6. Results and Discussion



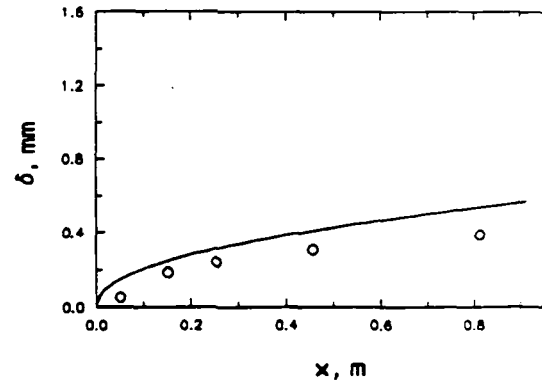
a. R-113; $\Delta T = 21.4\text{ }^{\circ}\text{C}$; $v_{gi} = 0.5\text{ m/s}$



b. R-113; $\Delta T = 22.3\text{ }^{\circ}\text{C}$; $v_{gi} = 0.9\text{ m/s}$



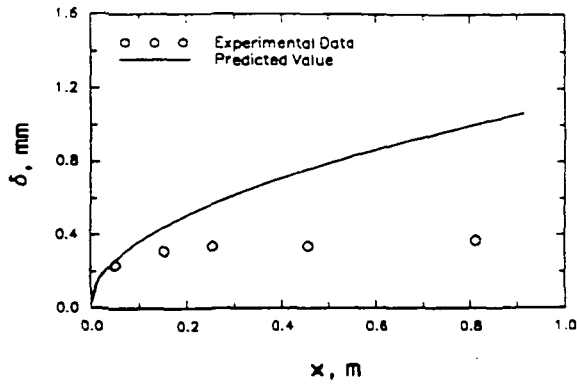
c. R-113; $\Delta T = 21.7\text{ }^{\circ}\text{C}$; $v_{gi} = 1.3\text{ m/s}$



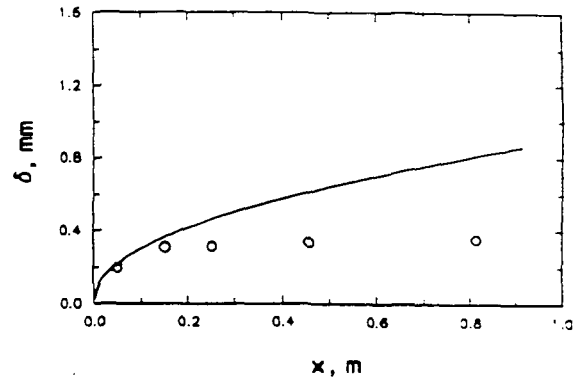
d. R-113; $\Delta T = 20.2\text{ }^{\circ}\text{C}$; $v_{gi} = 1.8\text{ m/s}$

Fig. 6.23 Comparisons of predicted film thickness with measured values ($c_1 = 0.0592$)

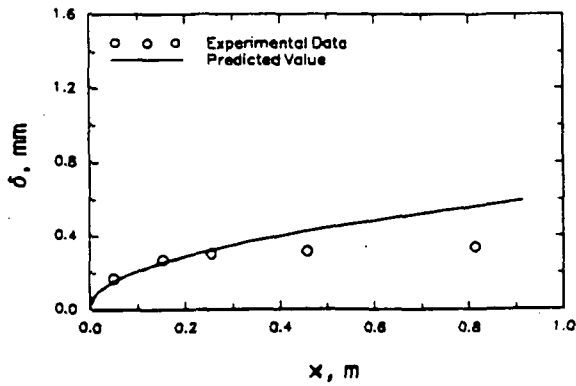
6. Results and Discussion



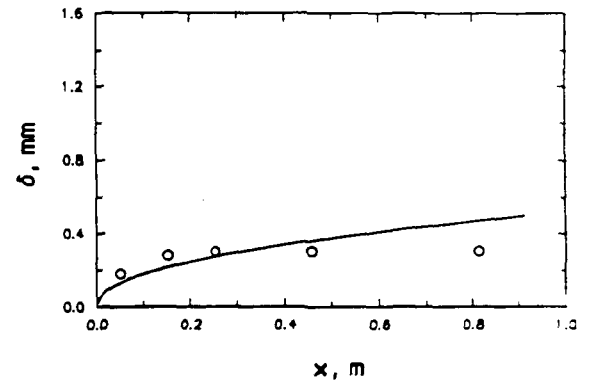
e. FC-72; $\Delta T = 20.3\text{ }^{\circ}\text{C}$; $v_{gi} = 0.4\text{ m/s}$



f. FC-72; $\Delta T = 19.7\text{ }^{\circ}\text{C}$; $v_{gi} = 0.5\text{ m/s}$



g. FC-72; $\Delta T = 20.1\text{ }^{\circ}\text{C}$; $v_{gi} = 1.0\text{ m/s}$



h. FC-72; $\Delta T = 20.0\text{ }^{\circ}\text{C}$; $v_{gi} = 1.3\text{ m/s}$

Fig. 6.23 Comparisons of predicted film thickness with measured values ($c_f = 0.0592$)

6. Results and Discussion

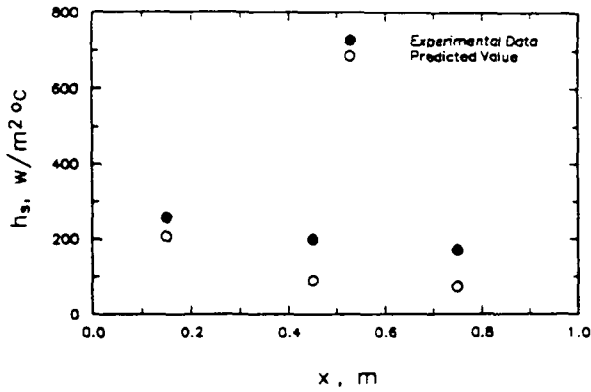
experimental data for each section is shown in the figure. When the inlet vapor Reynolds number is less than 600,000, the agreement of the predicted value with the experimental data is within $\pm 10\%$ in the first section; however, in the remaining two sections, the difference between the predicted value and the experimental data is large (Fig. 6.24 a, b, e, and f); with further increase in the inlet vapor Reynolds number, the difference reduces substantially (Fig. 6.24 c, d, g, and h); when the vapor Reynolds number increases beyond about 2,000,000, the difference again becomes large (Fig. 6.25).

Fig. 6.26 shows a comparison of the total average heat transfer coefficients predicted from the analytical model using Schlichting's correlation for the adiabatic friction factor with those measured in the present experiment. The predicted total heat transfer coefficient agrees quite well with the experimental data when the inlet vapor Reynolds number ($Re_{g,i}$) ranges from 500,000 to 1,500,000 for both R-113 and FC-72. However, at very low and high $Re_{g,i}$, the model under-predicts the heat transfer coefficients in most cases. The predicted heat transfer coefficients for $\Delta T = 10^\circ\text{C}$ are close to the experimental values.

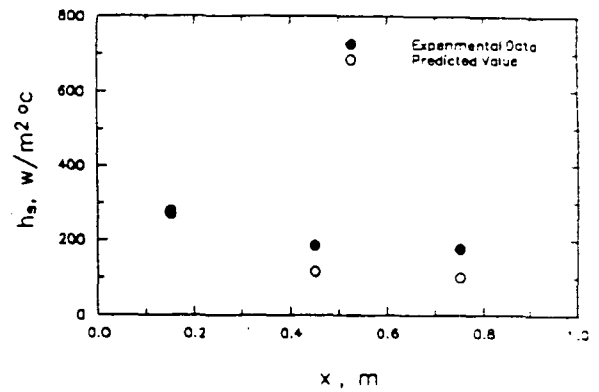
The prediction from the model with Schlichting's friction factor agrees with the experimental data within $\pm 30\%$ when $300,000 \leq Re_{g,i} \leq 1,750,000$. Beyond this range of $Re_{g,i}$, the model under-estimates the heat transfer coefficients. The reason for the underestimation of the heat transfer coefficients at very low $Re_{g,i}$ is not yet clear.

At high Reynolds number, interfacial waves set in. The waves affect the heat transfer rate in two ways. It has been shown by Suryanarayana (1972) that the rate of the heat transfer rate with a mean condensate film thickness ($\bar{\delta}$) with interfacial waves of amplitude (a) to the heat transfer rate without waves is $[1 - (a/\bar{\delta})^2]^{-1}$. The waves are likely to increase the turbulent shear stress as they act as surface roughness on the vapor boundary layer, leading to a thinner condensate film thickness. Thus the increase in heat transfer rate due to the interfacial waves may be the result of both the effects. As the amplitude of the waves is not available, only the effect of

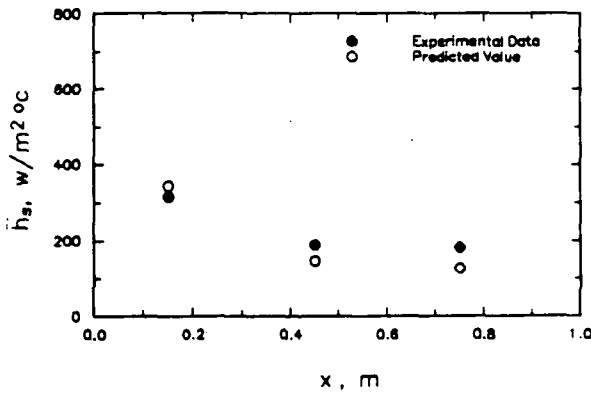
6. Results and Discussion



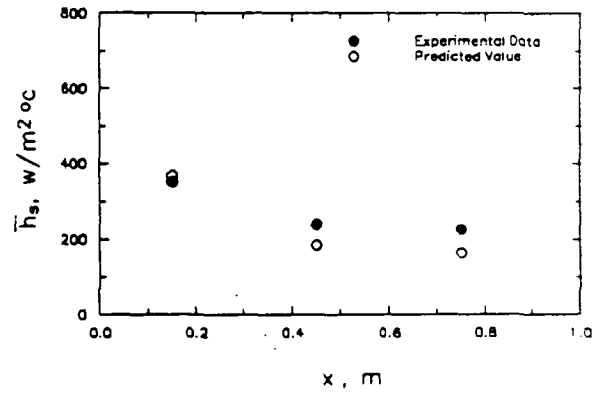
a. R-113; $\Delta T = 21.4\text{ }^{\circ}\text{C}$; $v_{gi} = 0.5\text{ m/s}$



b. R-113; $\Delta T = 22.3\text{ }^{\circ}\text{C}$; $v_{gi} = 0.9\text{ m/s}$



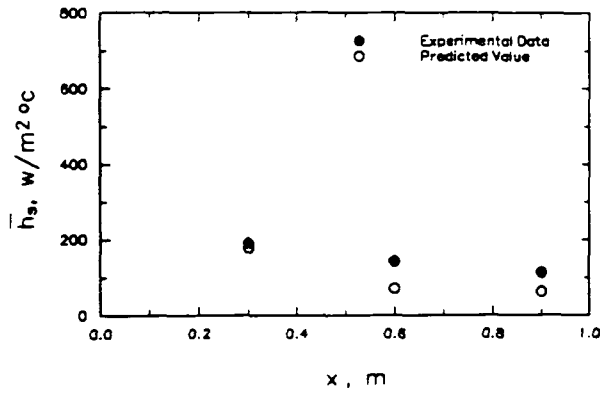
c. R-113; $\Delta T = 21.7\text{ }^{\circ}\text{C}$; $v_{gi} = 1.3\text{ m/s}$



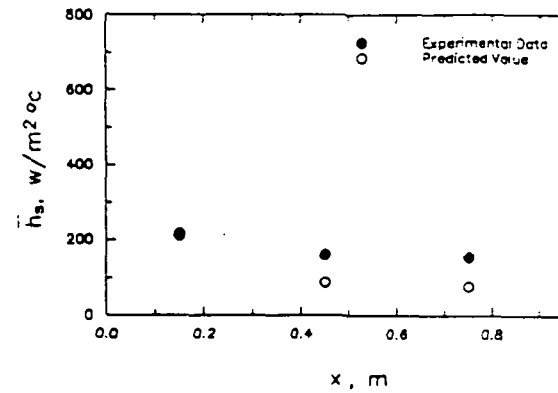
d. R-113; $\Delta T = 20.2\text{ }^{\circ}\text{C}$; $v_{gi} = 1.8\text{ m/s}$

Fig. 6.24 Comparisons of predicted sectional heat transfer coefficients with measured values ($c_f = 0.0592$)

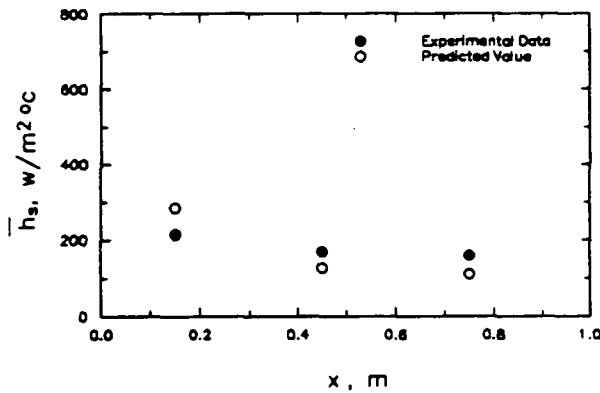
6. Results and Discussion



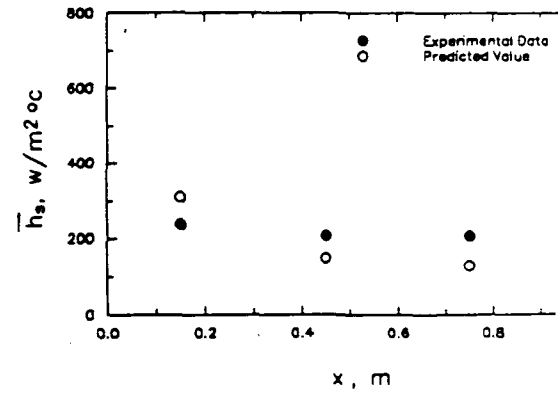
e. FC-72; $\Delta T = 20.3\text{ }^{\circ}\text{C}$; $v_{gi} = 0.4\text{ m/s}$



f. FC-72; $\Delta T = 19.7\text{ }^{\circ}\text{C}$; $v_{gi} = 0.5\text{ m/s}$



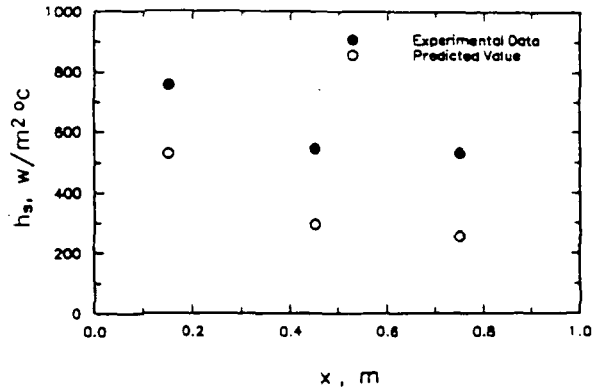
g. FC-72; $\Delta T = 20.1\text{ }^{\circ}\text{C}$; $v_{gi} = 1.0\text{ m/s}$



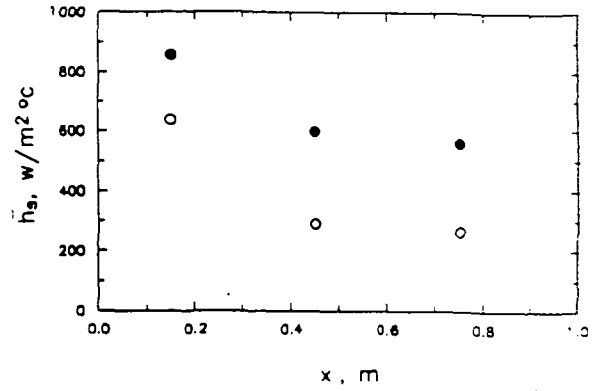
h. FC-72; $\Delta T = 20.0\text{ }^{\circ}\text{C}$; $v_{gi} = 1.3\text{ m/s}$

Fig. 6.24 Comparisons of predicted sectional heat transfer coefficients with measured values ($c_f = 0.0592$)

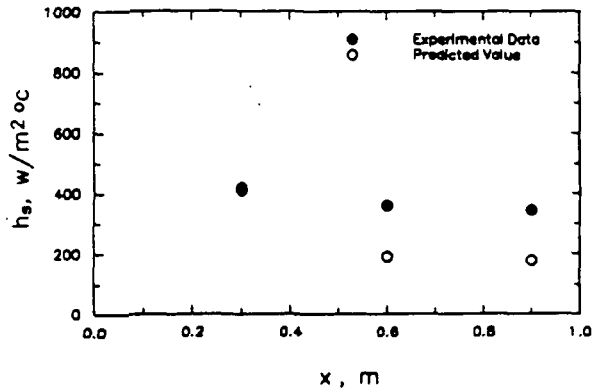
6. Results and Discussion



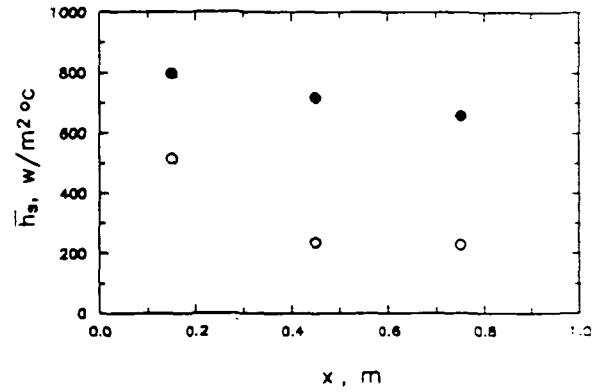
a. R-113; $\Delta T = 22.2\text{ }^{\circ}\text{C}$; $v_{gi} = 3.9\text{ m/s}$



b. R-113; $\Delta T = 20.0\text{ }^{\circ}\text{C}$; $v_{gi} = 4.3\text{ m/s}$



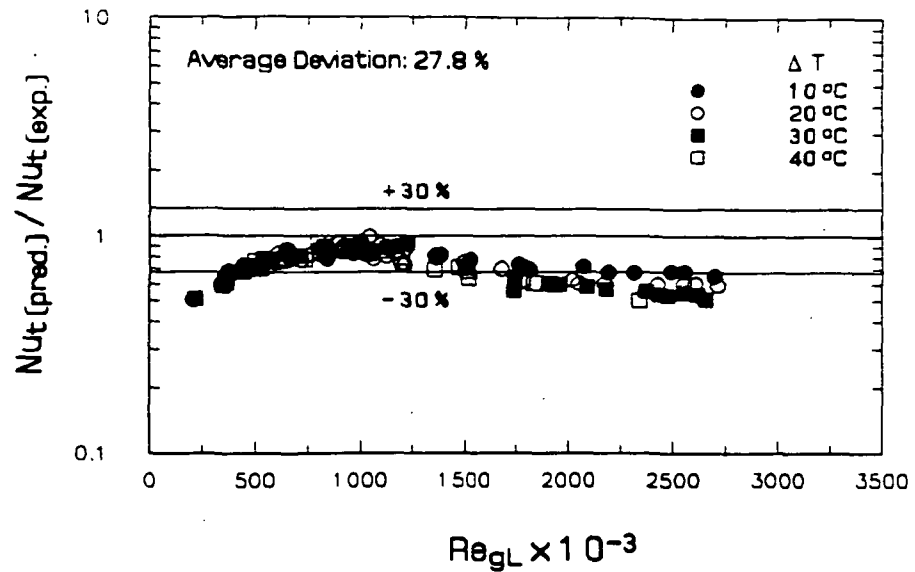
c. FC-72; $\Delta T = 20.3\text{ }^{\circ}\text{C}$; $v_{gi} = 2.0\text{ m/s}$



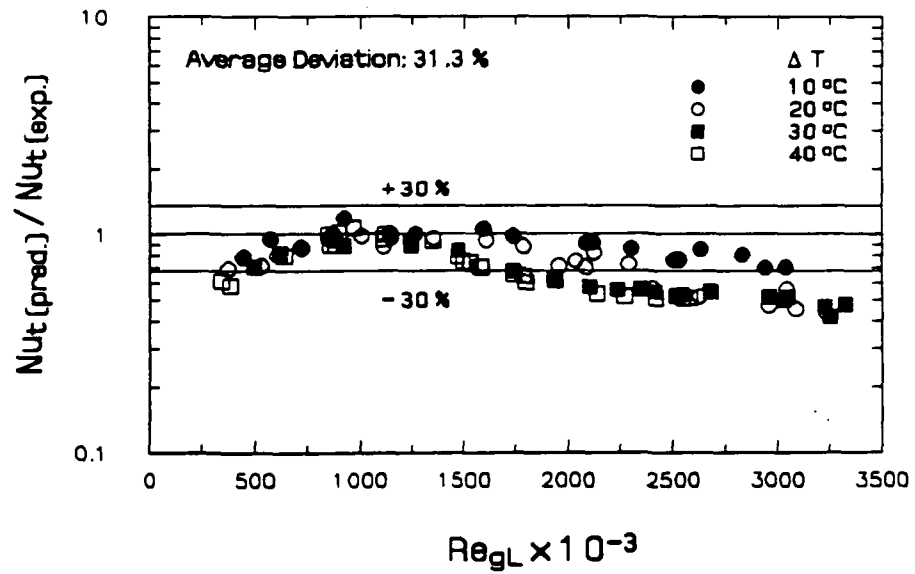
d. FC-72; $\Delta T = 19.5\text{ }^{\circ}\text{C}$; $v_{gi} = 3.0\text{ m/s}$

Fig. 6.25 Predicted sectional heat transfer coefficients at higher Re_{gL} ($c_i = 0.0592$)

6. Results and Discussion



a. R-113



b. FC-72

Fig. 6.26 Predicted total average heat transfer coefficients ($c_i = 0.0592$)

6. Results and Discussion

condensation on the shear stress can be accounted for. In Eq. 5-16, the interfacial shear stress is considered to be composed of a momentum shear stress (τ_m) due to condensation and an adiabatic shear stress (τ_a). A comparison of the values of the two components at higher inlet vapor Reynolds number is given in Fig. 6.27, where τ_a is estimated using Schlichting's expression for the friction factor. As seen from this figure, Near the leading edge of the condensing surface, the value of the equivalent shear stress due to momentum is much higher than that of the adiabatic shear stress; the difference between the two values decreases with increasing distance from the leading edge; beyond a certain distance, the adiabatic shear stress tends to be slightly higher than that of the equivalent shear stress. The figure shows that the contribution of both the adiabatic shear stress and the momentum shear stress should be considered. To determine an expression for τ_a that will better predict the condensation heat transfer, the shear stress (Eq. 5-16) needs to be modified.

Based on some available experimental data, Jensen and Yuen (1982) derived a correlation for adiabatic shear stress for two phase flows in a horizontal channel. For a smooth interface, the correlation is expressed as

$$\tau_a = 5 \times 10^{-3} \rho_g (v_g - v_l)^2 \quad (6-16a)$$

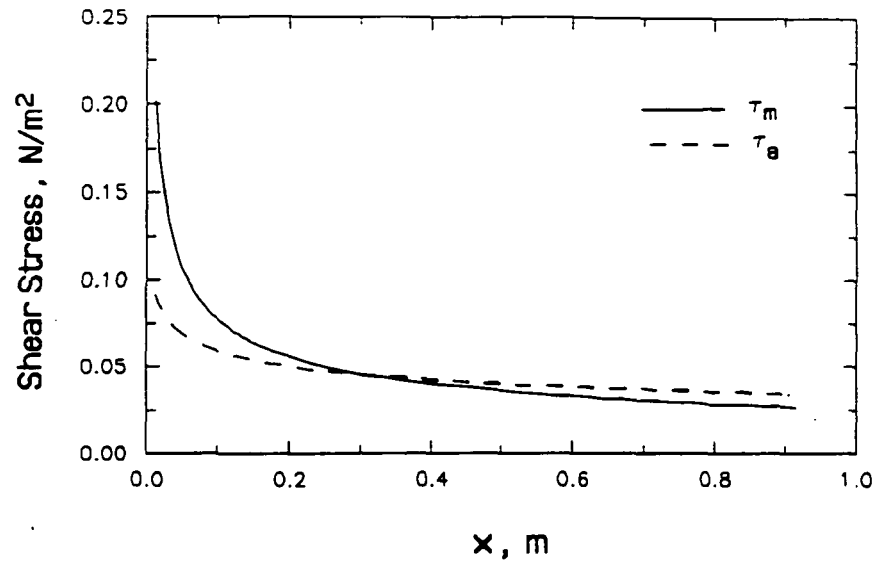
A different form of the correlation is given for a wavy interface with a developing flow [The definition for the fully developing flow is the distance $\geq 37/(H-\delta)$]

$$\tau_a = 6.02 \times 10^{-7} \rho_g \left[\frac{\rho_l}{\sigma g} \right]^{1.8} (v_g - v_l)^{3.8} \quad (6-16b)$$

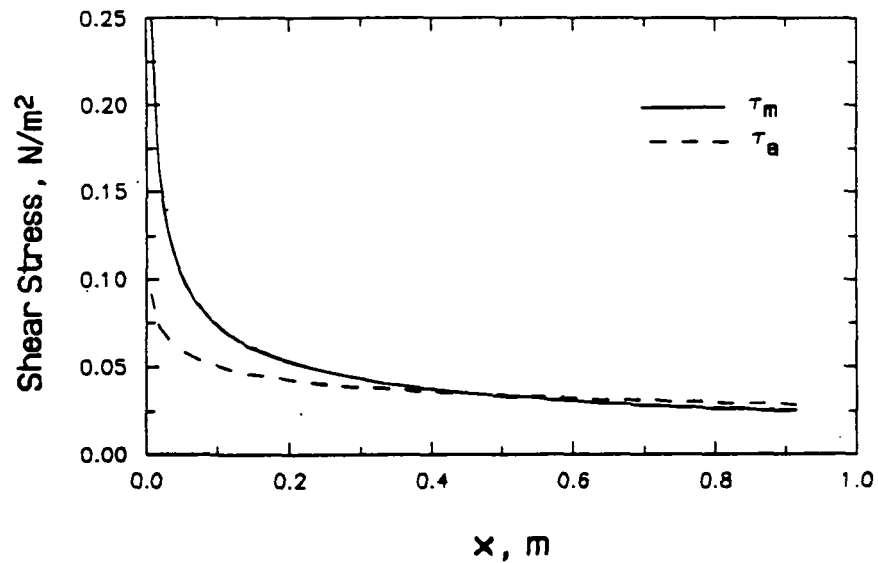
Wavy interface is assumed when the dimensionless parameter $(v_g - v_l)/(4\sigma g/\rho_l)^{1/4}$, is greater than 17.

Using Jensen and Yuen's correlation for the adiabatic shear stress, the analytical model was re-computed. Fig. 6.28 shows a comparison of the predicted total average

6. Results and Discussion



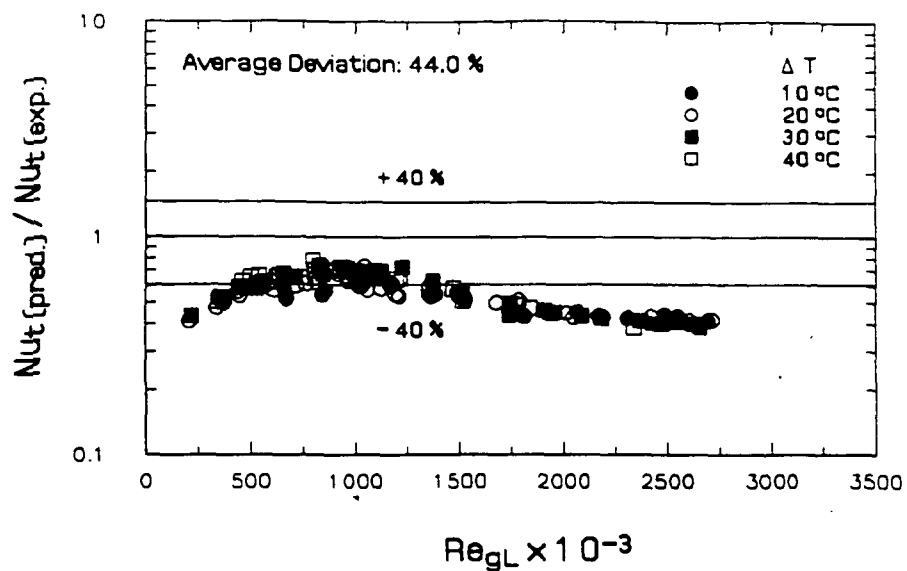
a. R-113; $\Delta T = 20.7$ °C; $v_{g1} = 1.8$ m/s; $Re_{gL} = 1,094,008$



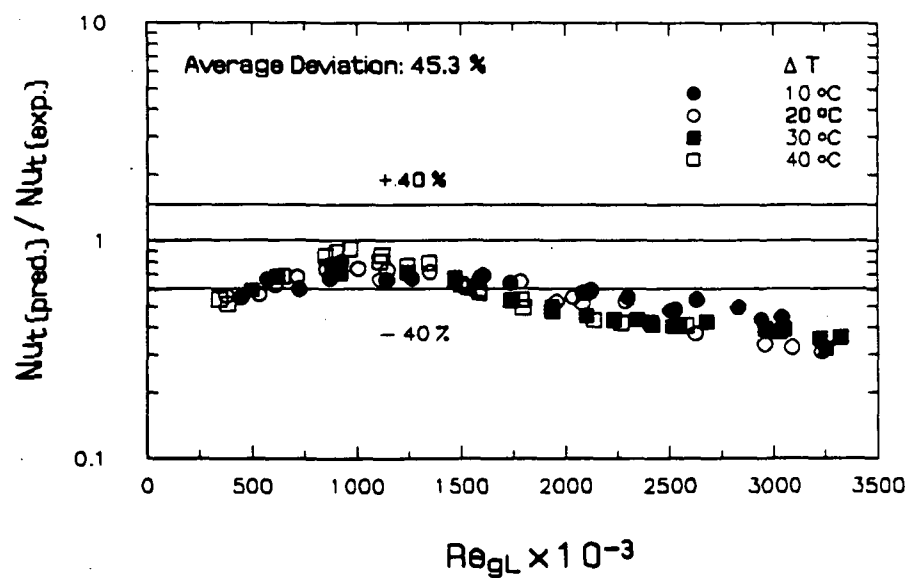
b. FC-72; $\Delta T = 20.0$ °C; $v_{g1} = 1.3$ m/s; $Re_{gL} = 1,347,494$

Fig. 6.27 Comparisons of adiabatic shear stress (τ_a) with momentum shear stress (τ_m)

($c_1 = 0.0592$)



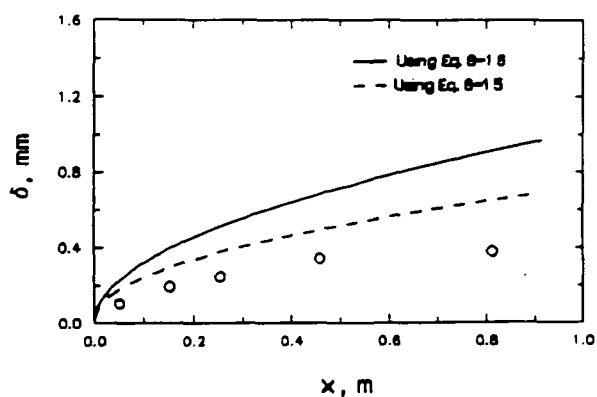
a. R-113



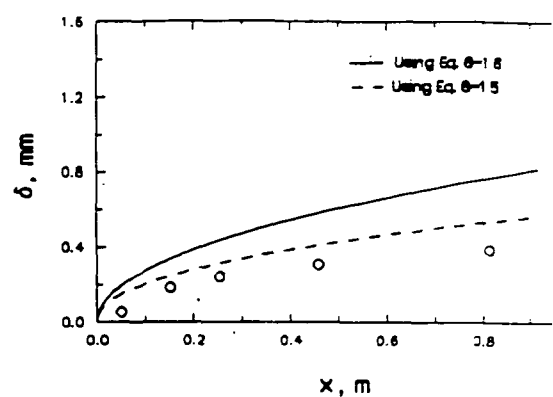
b. FC-72

Fig. 6.28 Predicted total average heat transfer coefficients using Jensen and Yuen's friction equation

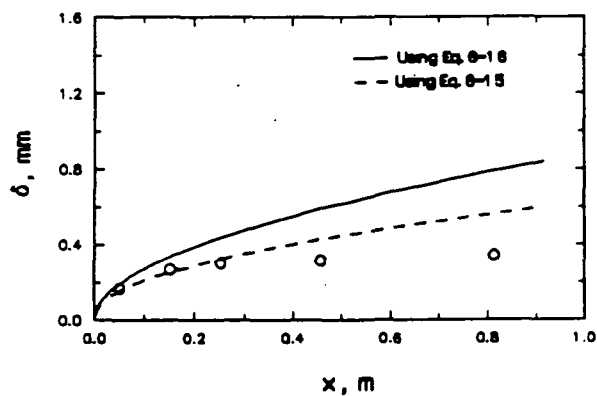
6. Results and Discussion



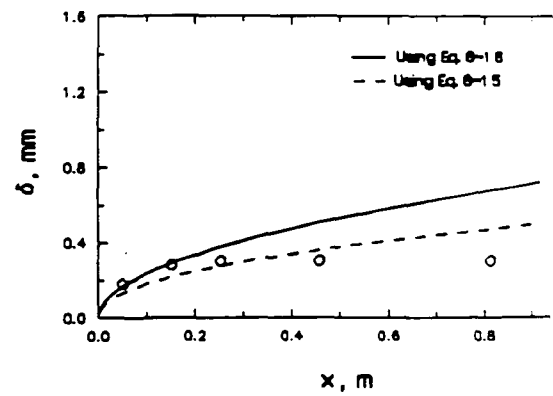
a. R-113; $\Delta T = 21.7^\circ\text{C}$; $v_{gi} = 1.3\text{ m/s}$



b. R-113; $\Delta T = 20.2^\circ\text{C}$; $v_{gi} = 1.8\text{ m/s}$



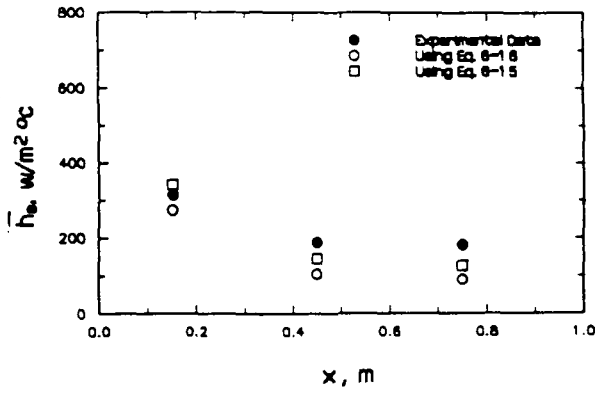
c. FC-72; $\Delta T = 20.1^\circ\text{C}$; $v_{gi} = 1.0\text{ m/s}$



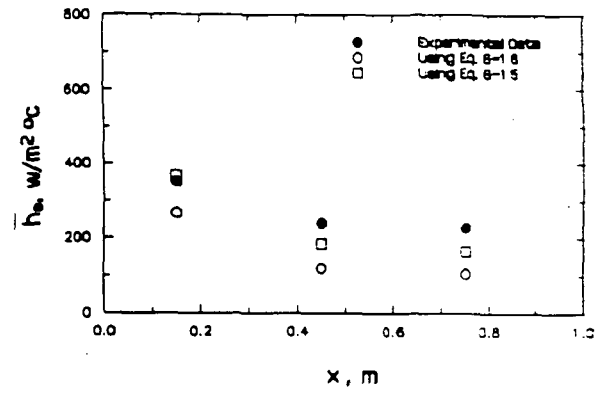
d. FC-72; $\Delta T = 20.0^\circ\text{C}$; $v_{gi} = 1.3\text{ m/s}$

Fig. 6.29 Predicted film thickness using Jensen and Yuen's friction equation

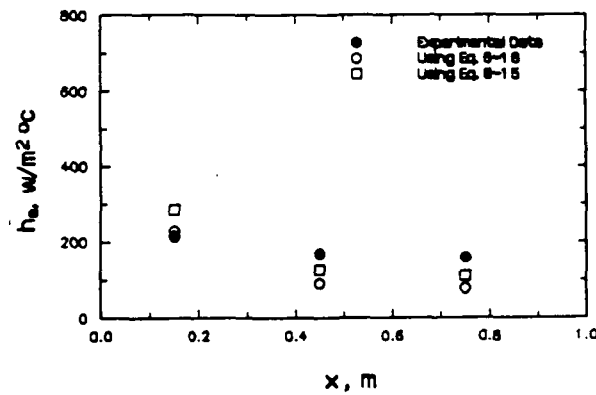
6. Results and Discussion



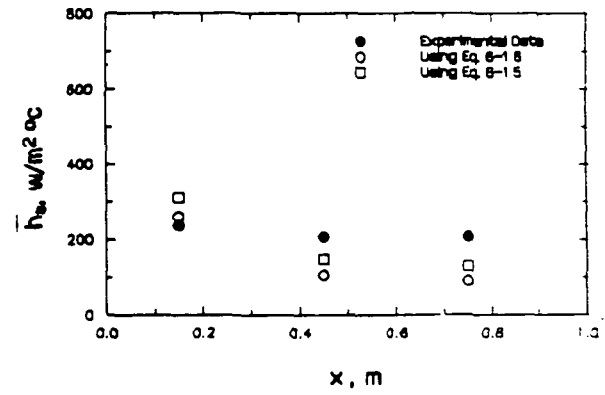
a. R-113; $\Delta T = 21.7\text{ }^{\circ}\text{C}$; $v_{gi} = 1.3\text{ m/s}$



b. R-113; $\Delta T = 20.2\text{ }^{\circ}\text{C}$; $v_{gi} = 1.8\text{ m/s}$



c. FC-72; $\Delta T = 20.1\text{ }^{\circ}\text{C}$; $v_{gi} = 1.0\text{ m/s}$



d. FC-72; $\Delta T = 20.0\text{ }^{\circ}\text{C}$; $v_{gi} = 1.3\text{ m/s}$

Fig. 6.30 Predicted sectional heat transfer coefficients using Jensen and Yuen's friction equation

6. Results and Discussion

Nusselt numbers from the model using Jensen and Yuen's friction correlation with the experimental data. The average deviation between the re-computed value and the measured value is 44.0 % for R-113 and 45.3 % for FC-72 in comparison with 27.8 % for R-113 and 31.3 for FC-72 (See Fig. 6.26) using Schlichting's friction equation. Comparing the newly computed film thickness (Fig. 6.29) and sectional heat transfer coefficients (Fig. 6.30) with the experimental data, it is further found the predictions of the model using Schlichting's friction equation are better than those using Jensen and Yuen's correlation.

Schlichting's friction equation applies to turbulent single phase flow over a smooth flat plate. But, the vapor-condensate interface may not be always smooth. When interfacial waves set in, the surface of the condensate become very rough, which increases the adiabatic shear stress. Once this occurs, the use of Schlichting's friction correlation may result in an underestimate of the interfacial shear stress and the heat transfer coefficients. One possible way to account for the effect of the interfacial waves on the shear stress is to modify the Schlichting friction correlation.

Schlichting friction correlation was modified by adjusting only the constant (c_f) in Eq. 5-18. The model was computed repeatedly, each time with a new value of c_f using 100 typical experimental runs. The variation of average deviation (S) between the predicted heat transfer coefficients and the experimental values with c_f is shown

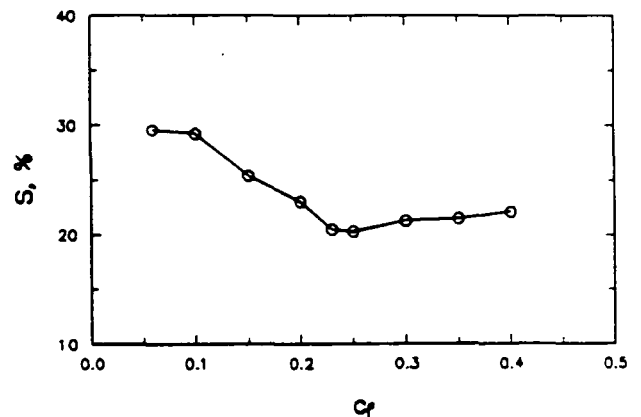


Fig. 6.31 Effect c_f on S

in Fig. 6.31. The average deviation decreases when c_f is increased from its original value ($c_f = 0.0592$); the deviation reaches a minimum value at $c_f = 0.245$; however, when c_f is further increased, the deviation increases again. Based on this comparison,

6. Results and Discussion

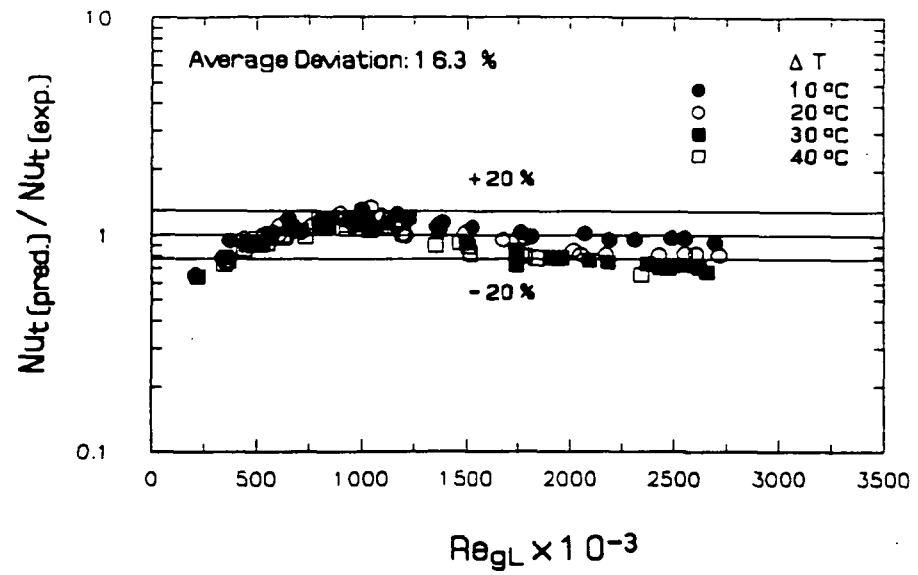
c_f was modified as 0.245, while n_f remains at its original value of -0.2.

Substituting $c_f = 0.245$ and $n_f = -0.2$ into Eq. 5-18 for the friction factor, the analytical model was re-computed. Fig. 6.32 shows a comparison of the total average Nusselt numbers predicted from the model with those measured in the present experiment. Examining Fig. 6.32 and Fig. 6.26, it is seen that the average deviation between the predicted Nu_t and the experimental data is reduced from 27.8 % to 16.3 % for R-113 and from 31.3 % to 21.2 % for FC-72. Also, the newly predicted film thickness is closer to the experimental value (Fig. 6.33). Fig. 6.34 shows comparisons between the predicted sectional heat transfer coefficients with the experimental data. It is seen in this figure that the predicted sectional heat transfer coefficients approach the experimental data in section 2 and section 3; however, in section 1, the model with $c_f = 0.245$ predicts a larger sectional heat transfer coefficients than the experimental values. At higher $Re_{g,L}$, the model still under-predicts the sectional heat transfer coefficients (Fig. 6.35), but the difference between the predicted value from the model using $c_f = 0.245$ and the experimental data is reduced in comparison with the prediction with $c_f = 0.0592$.

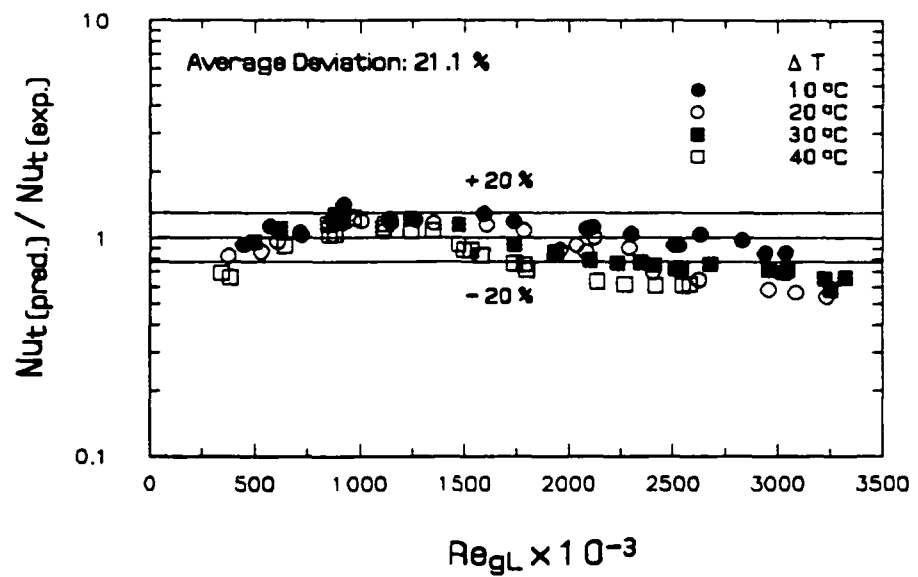
With $c_f = 0.245$, the performance of the model improves over the whole experimental range. For $500,000 \leq Re_{g,L} \leq 1,500,000$, the prediction of the model agrees well with the experimental data. For this range of $Re_{g,L}$, the average deviation between the predicted total average Nusselt number and the experimental value is less than ± 15 % for R-113 and less than ± 17 % for FC-72.

Narain and Kamath (1991) developed a model to simulate the process of condensation of a pure saturated vapor flow between two horizontal parallel plates. They identified the friction factor equation for the interface (with the help of the data collected in the present experiment) for both laminar and turbulent flows of vapor. Narain and Kamath further used their model to predict the film thickness of condensate in the present experiment. A comparison between the film thickness prediction of Narain's model and that of the present model (using $c_f = 0.245$) is given

6. Results and Discussion



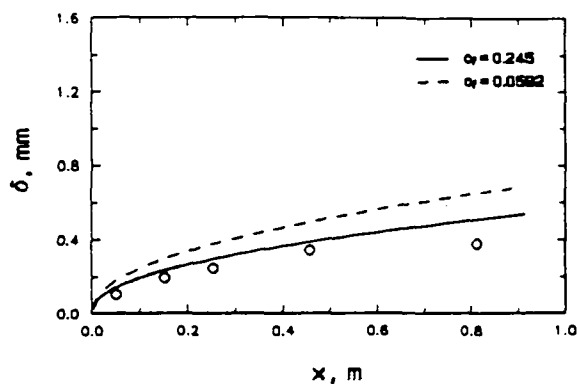
a. R-113



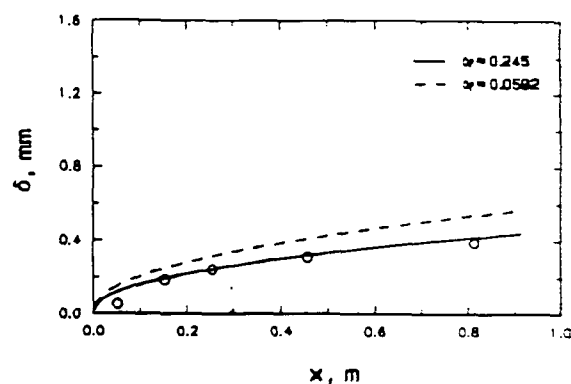
b. FC-72

Fig. 6.32 Predicted total average heat transfer coefficients ($c_1 = 0.245$)

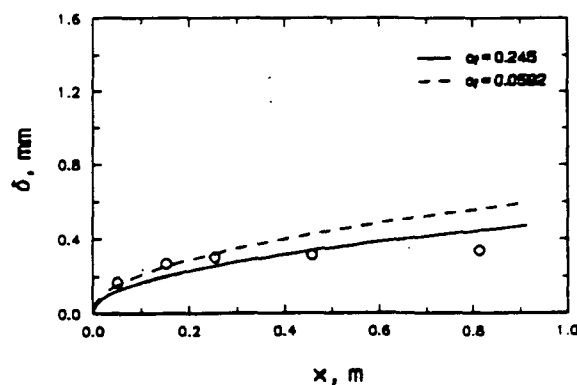
6. Results and Discussion



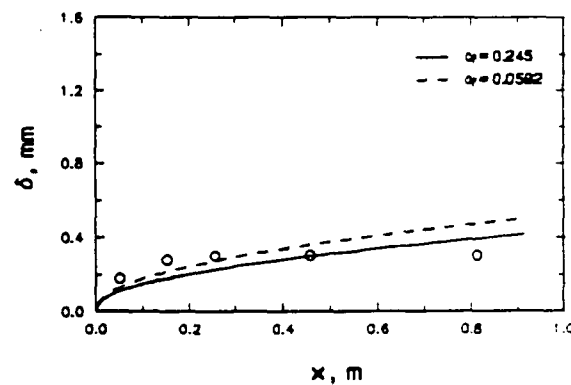
a. R-113; $\Delta T = 21.7$ °C; $v_{gi} = 1.3$ m/s



b. R-113; $\Delta T = 20.2$ °C; $v_{gi} = 1.8$ m/s

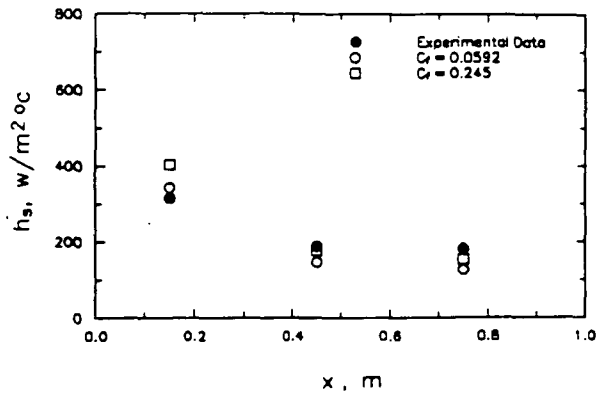
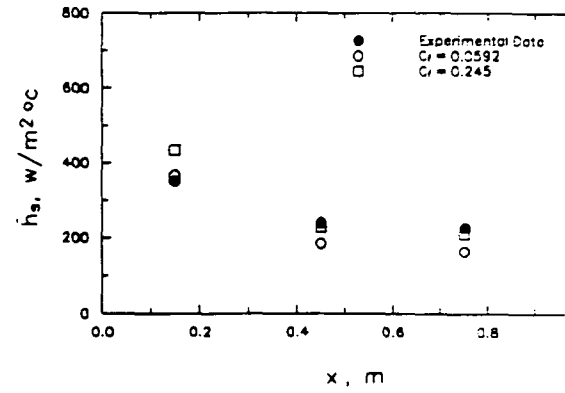
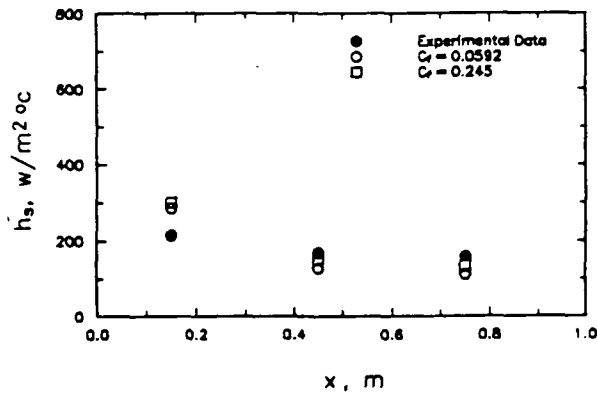
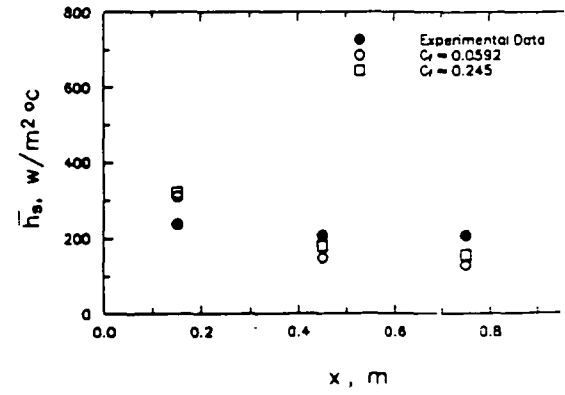


c. FC-72; $\Delta T = 20.1$ °C; $v_{gi} = 1.0$ m/s

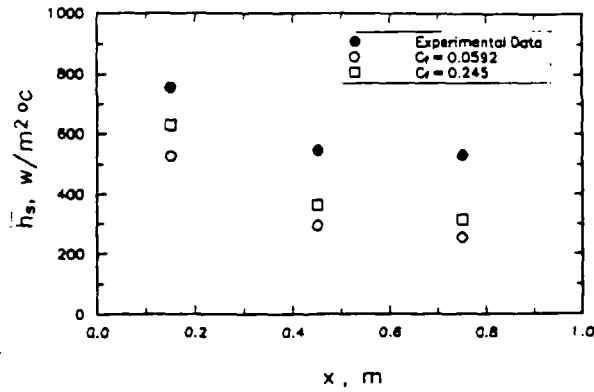


d. FC-72; $\Delta T = 20.0$ °C; $v_{gi} = 1.3$ m/s

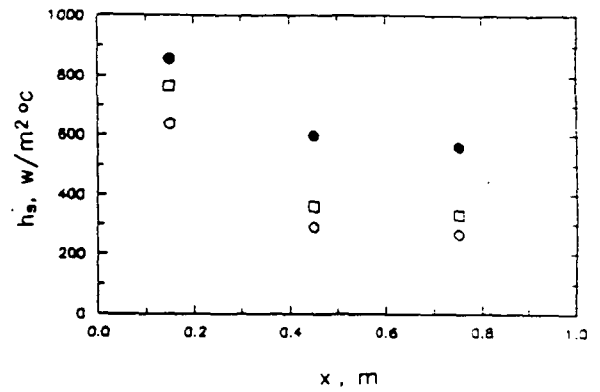
Fig. 6.33 Predicted film thickness ($c_f = 0.245$)

a. R-113; $\Delta T = 21.7^\circ\text{C}$; $v_{g1} = 1.3\text{ m/s}$ b. R-113; $\Delta T = 20.2^\circ\text{C}$; $v_{g1} = 1.8\text{ m/s}$ c. FC-72; $\Delta T = 20.1^\circ\text{C}$; $v_{g1} = 1.0\text{ m/s}$ d. FC-72; $\Delta T = 20.0^\circ\text{C}$; $v_{g1} = 1.3\text{ m/s}$ Fig. 6.34 Predicted sectional heat transfer coefficients ($C_f = 0.245$)

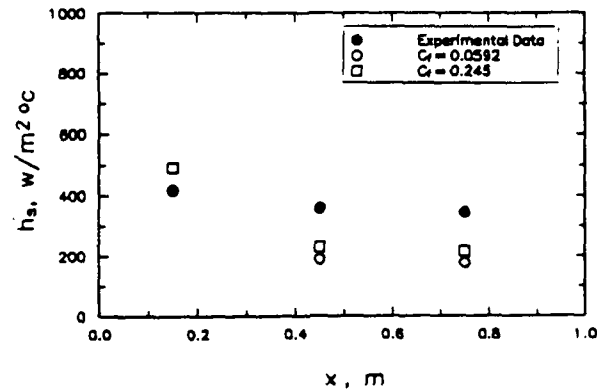
6. Results and Discussion



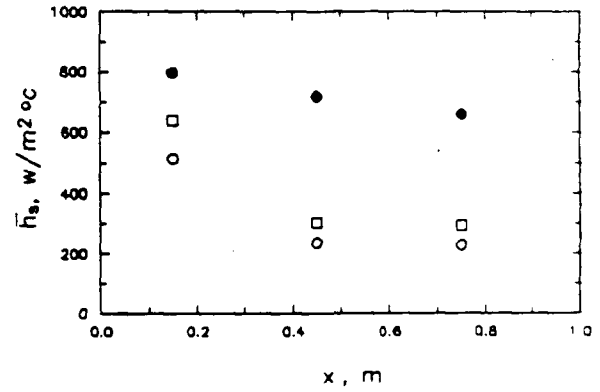
a. R-113; $\Delta T = 22.2^\circ\text{C}$; $v_{gi} = 3.9 \text{ m/s}$



b. R-113; $\Delta T = 20.0^\circ\text{C}$; $v_{gi} = 4.3 \text{ m/s}$



c. FC-72; $\Delta T = 20.3^\circ\text{C}$; $v_{gi} = 2.0 \text{ m/s}$



d. FC-72; $\Delta T = 19.5^\circ\text{C}$; $v_{gi} = 3.0 \text{ m/s}$

Fig. 6.35 Predicted sectional heat transfer coefficients at higher Re_{gL} ($c_i = 0.245$)

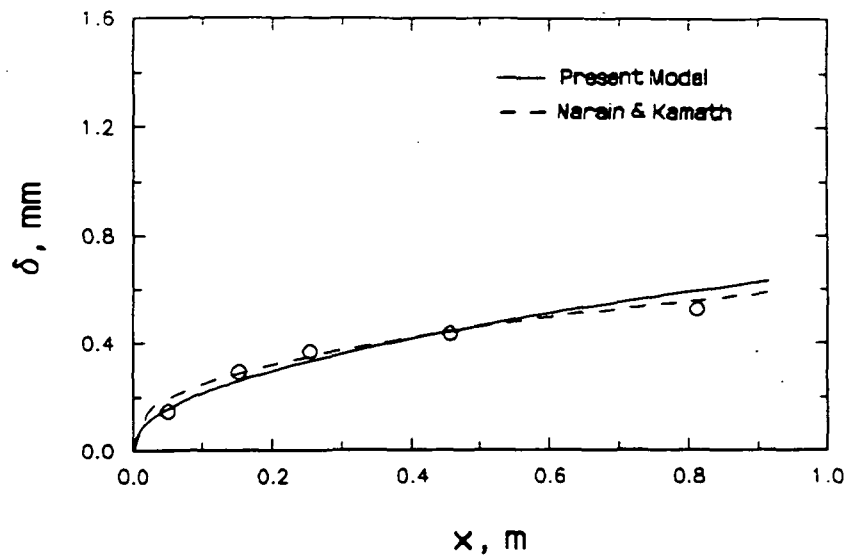


Fig. 6.36 Comparison between the present model and Narain's model

R-113; $\Delta T = 39.7^\circ\text{C}$; $v_{g1} = 1.28\text{ m/s}$

in Fig. 6-36. It is seen that the predictions from both the models are in good agreement with the experimental data. However, it should be noted that the experimental measurements of heat transfer were used to derive the friction factor.

Fig. 6.37 presents typical distributions of the predicted vapor velocity and the liquid velocity along the condensing surface. The vapor velocity and the liquid velocity are calculated using Eq. 5-6 and Eq. 5-22. It is seen from this figure that the vapor velocity decreases along the condensing surface from 1.28 m/s to 1.16 m/s, while the liquid velocity increases slightly from 0.05 m/s to 0.07 m/s.

Fig. 6.38 shows a typical distribution of the predicted interfacial shear stress along the test section. The interfacial shear stress decreases sharply near the leading edge of the condensing surface, and then reduces slowly along the test section.

6. Results and Discussion

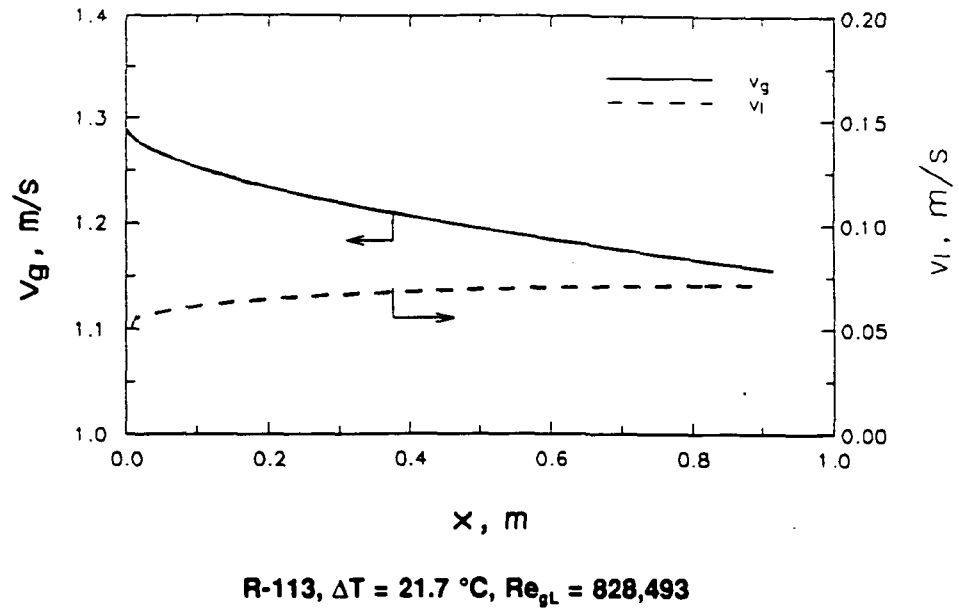


Fig. 6.37 Distributions of vapor and liquid velocities along the test section

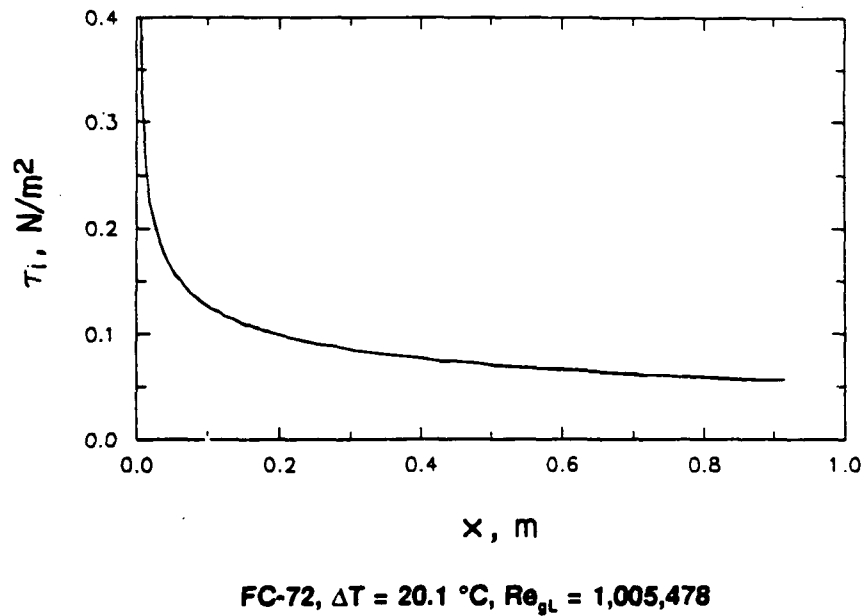


Fig. 6.38 Distribution of the interfacial shear stress along the test section

6.10. Heat Transfer Correlations

Two different correlations for calculating the average heat transfer coefficient in condensation inside a horizontal rectangular duct are derived. One is a semi-empirical correlation based on the condensation model and the present experimental data. The other is an empirical correlation based merely on the present experimental results and dimensionless parameters.

6.10.1. Semi-empirical Heat Transfer Correlation

Based on the analysis on the condensation model, the average Nusselt number (Nu_i) is found to be possibly a function of Re_{gL} , Pr_l/Ja , μ_g/μ_l , ρ/ρ_g , and L_i/L (Section 6.7.1). Hence, it is assumed that

$$Nu_i = a_0 \left(\frac{Pr_l}{Ja} \right)^{a_1} \left[Re_{gL} \frac{L_i}{L} \right]^{a_2} \left(\frac{\mu_g}{\mu_l} \right)^{a_3} \left(\frac{\rho_l}{\rho_g} \right)^{a_4} \quad (6-17)$$

where a_0 , a_1 , a_2 , a_3 , and a_4 are constants, which can be determined from the experimental results.

Since

$$Re_{gL} \frac{L_i}{L} = Re_{gL_i} \quad (6-18)$$

Eq. 6-17 is rearranged as

$$Nu_i = a_0 Re_{gL_i}^{a_2} \left(\frac{Pr_l}{Ja} \right)^{a_1} \left(\frac{\mu_g}{\mu_l} \right)^{a_3} \left(\frac{\rho_l}{\rho_g} \right)^{a_4} \quad (6-19)$$

Based on a regression analysis on Eq. 6-19 using the present experimental data, a correlation for the average Nusselt number is derived

6. Results and Discussion

$$Nu_i = 0.00292 Re_{gL_i}^{0.711} \left(\frac{Pr_i}{Ja} \right)^{0.0853} \left(\frac{\mu_i}{\mu_g} \right)^{2.537} \left(\frac{\rho_i}{\rho_g} \right)^{-1.105} \quad (6-20)$$

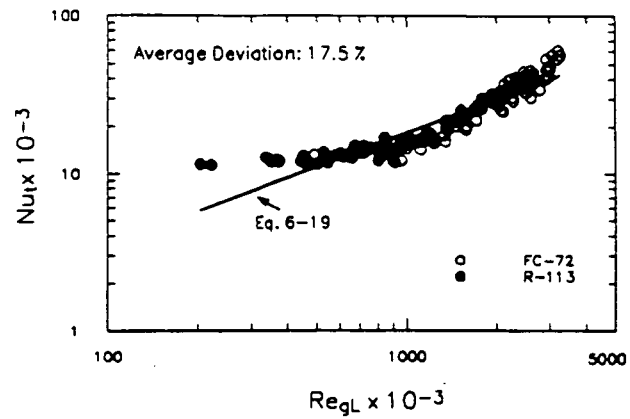
The range of the experimental data used in the regression analysis for Eq. 6.20 is listed in Table 6.7.

Table 6.7 Ranges of experimental data used in correlating Eq. 6-20

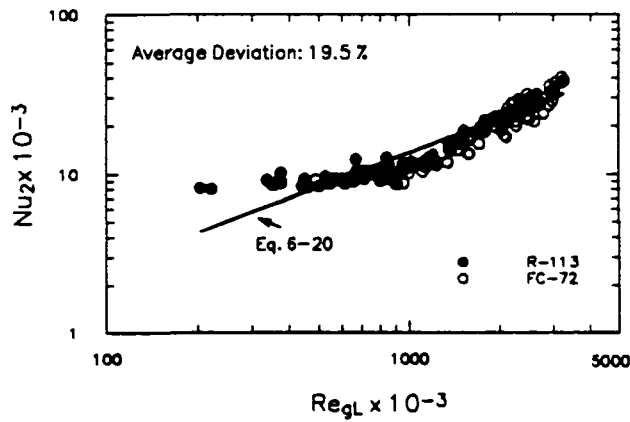
Fluids	$Re_{gL} \times 10^{-3}$	Pr_i/Ja	μ/μ_g	ρ/ρ_g
R-113	210 - 2,700	24.0 - 104.7	44.6 - 48.46	177.7 - 212.6
FC-72	380 - 3,322	13.7 - 79.4	36.1 - 39.8	112.7 - 129.7

Fig. 6.39a shows a comparison of the calculated average Nusselt numbers with the experimental values. The calculated Nusselt numbers agree fairly well with most of the experimental data. The average deviation between the calculated Nusselt numbers and the measured values is $\pm 17.5\%$ for the entire condensing surface. However, when the inlet vapor Reynolds number is very small (approximately when $Re_{gL} < 445,000$), the deviation is high. At the lowest Reynolds number ($Re_{gL} = 202,338$), the difference is the highest ($\sim \pm 50\%$).

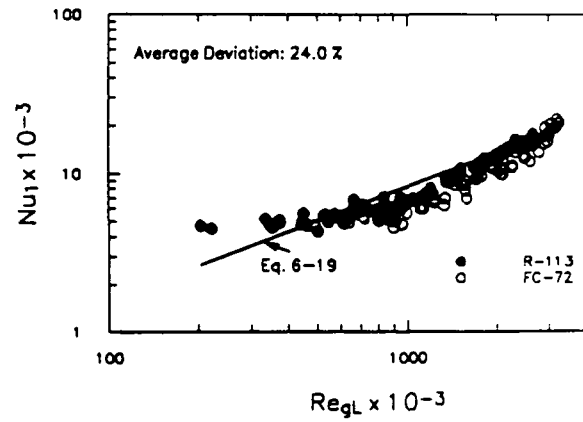
Eq. 6-20 can be used to predict the average Nusselt number over any specific length of the condensing surface from its leading edge by replacing L_i in Eq. 6-20 with that specific length. As a result, the average Nusselt number (Nu_2) over sections 1 and 2 ($L_1 = L_2$) and the average Nusselt number (Nu_1) over section 1 ($L_i = L$) are calculated. Comparisons of Nu_2 and Nu_1 with the experimental data are presented in Fig. 6.39b and Fig. 6.39c. The average deviation between the predicted Nusselt numbers and the experimental values increases with decreasing length of the



a. for entire condensing surface



b. for sections 1 and 2



c. for section 1

Fig. 6.39 Comparisons of the heat transfer correlation (Eq. 6-20) with experiment

6. Results and Discussion

condensing surface. Based on the whole length of the condensing surface, the average deviation is only $\pm 17.6\%$, while for the section 1, the deviation increases to $\pm 24\%$. The reason for increasing the deviation with decreasing the length of the condensing surface is not clear. Eq. 6-26 is probably more relevant for predicting the average Nusselt numbers with an appropriate longer length of condensing surface.

6.10.2. Empirical Heat Transfer Correlation

It has been shown previously in Fig. 6-17 that the Stanton number with an average heat transfer coefficient can be related to the inlet vapor Reynolds number. vapor. Therefore, it may be assumed that

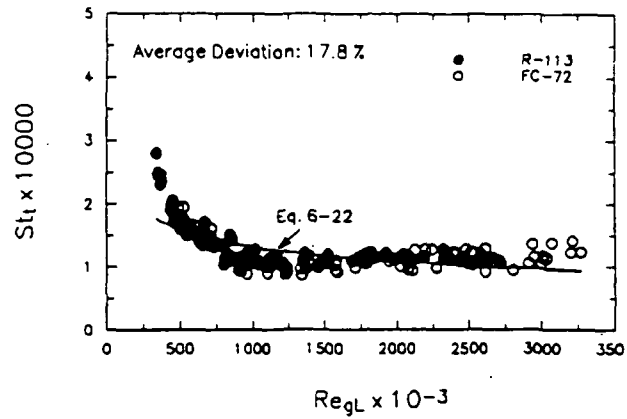
$$St_i = f_0 Re_{gL_i}^{f_1} \quad (6-21)$$

where the values of the constants, f_0 and f_1 , are determined using the present experimental data involving only the average heat transfer coefficient (\bar{h}_i) and the regression analysis. The correlation so obtained is

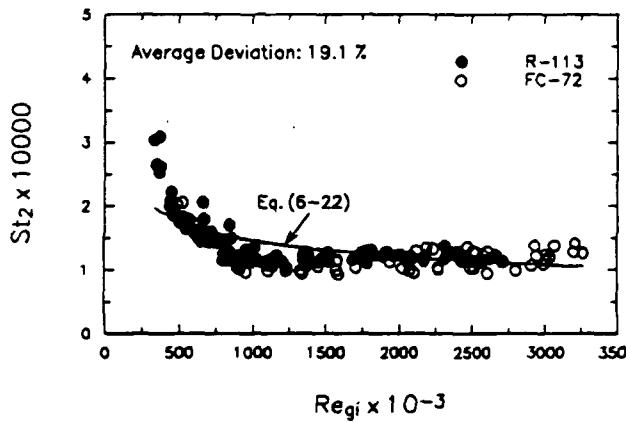
$$St_i = 0.00573 Re_{gL_i}^{-0.274} \quad (6-22)$$

The range of Re_{gL} used for the regression analysis of Eq. 6-22 is listed in Table 6.7.

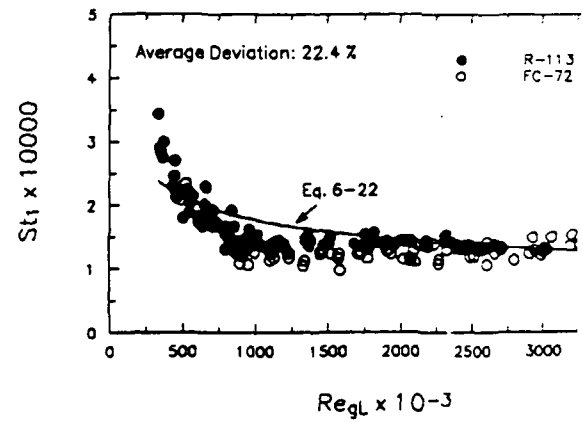
The Stanton number with the average heat transfer coefficient over the entire condensing surface ($L_1 = L$) is calculated from Eq. 6-22. Also, the Stanton number with the average heat transfer coefficient over section 1 and section 2 and the Stanton number with the average heat transfer coefficient over section I are calculated by replacing L_1 with L_2 and L_1 respectively. Predictions from Eq. 6-22 are compared with the experimental data (Fig. 6.40). The average deviation (Eq. 6-0) between the predicted and experimental values is $\pm 20\%$. However, as with Eq. 6-20, when Re_{gL} is approximately less than 445,000, the difference between the calculated Stanton number and the measured values is high. The maximum deviation at the lowest Re_{gL} ($Re_{gL} =$



a. for entire condensing surface



b. for sections 1 and 2



c. for section 1

Fig. 6.40 Comparison of the heat transfer correlation (Eq. 6-22) with experiment

202,338) is about 67.18 %.

6.10.3. Comparison between Heat Transfer Correlations

In Section 6.8, the heat transfer correlations of Soliman, Azer, Traviss, and Shah are discussed. Among the four correlations, it is found that the correlations of Shah (Eq. 6-10) and Soliman (Eq. 6-6) are better than the other two in predicting the total average heat transfer coefficients of the present experiment. The correlations of Shah and Soliman are compared with Eqs 6-20 and 6-22 on the basis of the present experiment. It appears that all the predictions for \bar{h}_l from all the four correlations are in good agreement with the experimental data except for low values of $Re_{g,L}$ (Fig. 6.41). At low values of $Re_{g,L}$, Shah's correlation greatly underestimates the heat transfer coefficients, while Soliman's correlation overestimates the heat transfer coefficients. Eqs. 6-20 and 6-22 also underestimate the heat transfer coefficients when $Re_{g,L}$ is low, but the difference between the experimental data and the predicted values from Eqs. 6-20 and 6-22 is small than that from the correlations of Shah and Soliman.

6.11. Interfacial Waves

6.11.1 Observation of the Interfacial Wave Initiation

The interfacial wave initiation was observed in two separated experiments: (1) condensation experiment; (2) adiabatic air-liquid flow experiment.

Interfacial Wave Initiation in Condensation

In the condensation experiment, the initiation of the interfacial waves on the condensate film (Fig. 6.42) depends on the inlet vapor Reynolds number ($Re_{g,L}$) and ΔT . As ΔT increases, the value of $Re_{g,L}$ initiating the waves decreases (Fig. 6.43). This may be because higher ΔT leads to a larger condensate film thickness (δ) and a larger δ is more likely to cause the instability of the condensate film than a smaller δ .

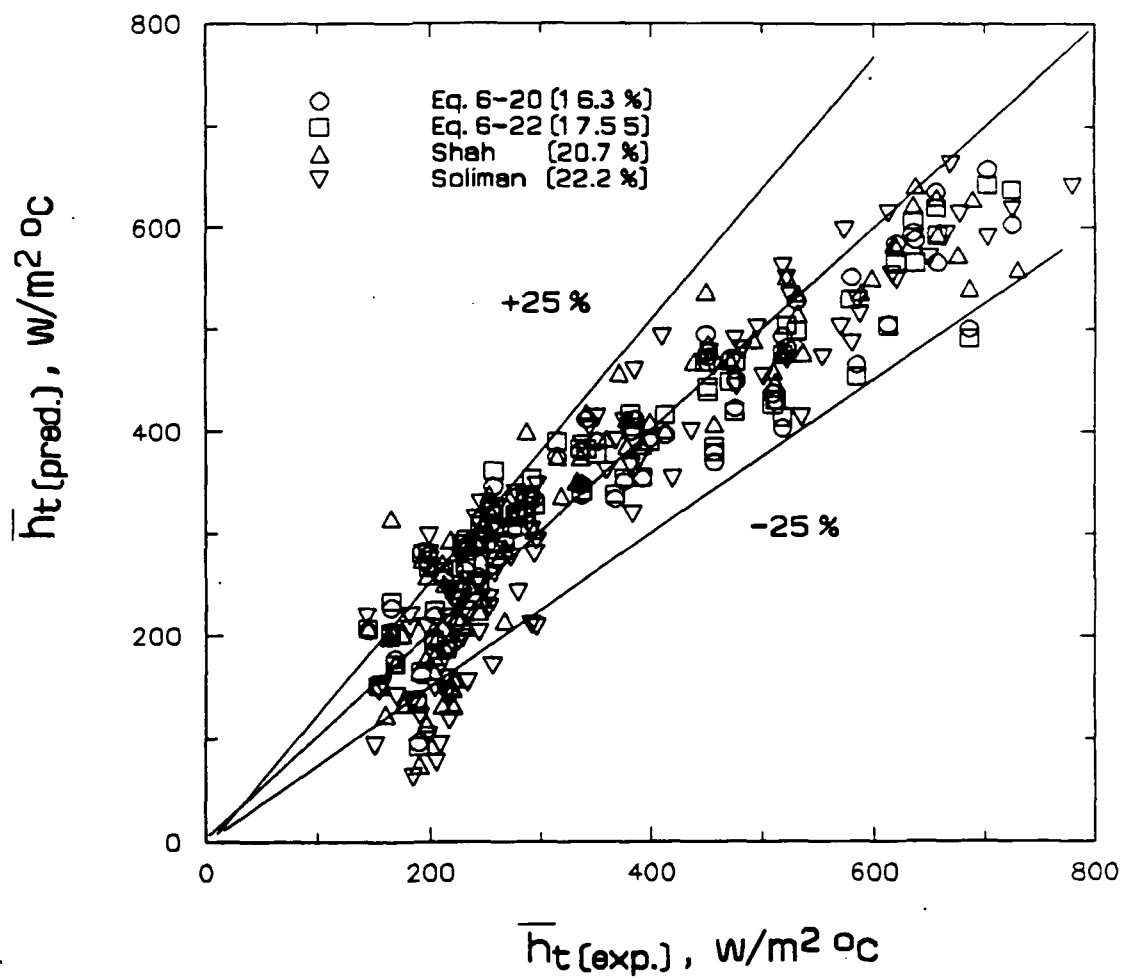


Fig. 6.41 Comparison of different heat transfer correlations

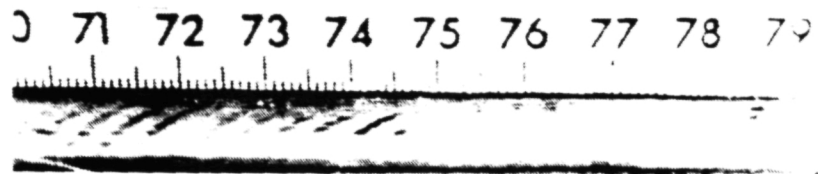


Fig. 6.42 Photograph of interfacial wave initiation in condensation

FC-72; $\Delta T = 9.7^\circ\text{C}$; $v_{g1} = 1.1 \text{ m/s}$; $Re_{gL} = 1,225,835$

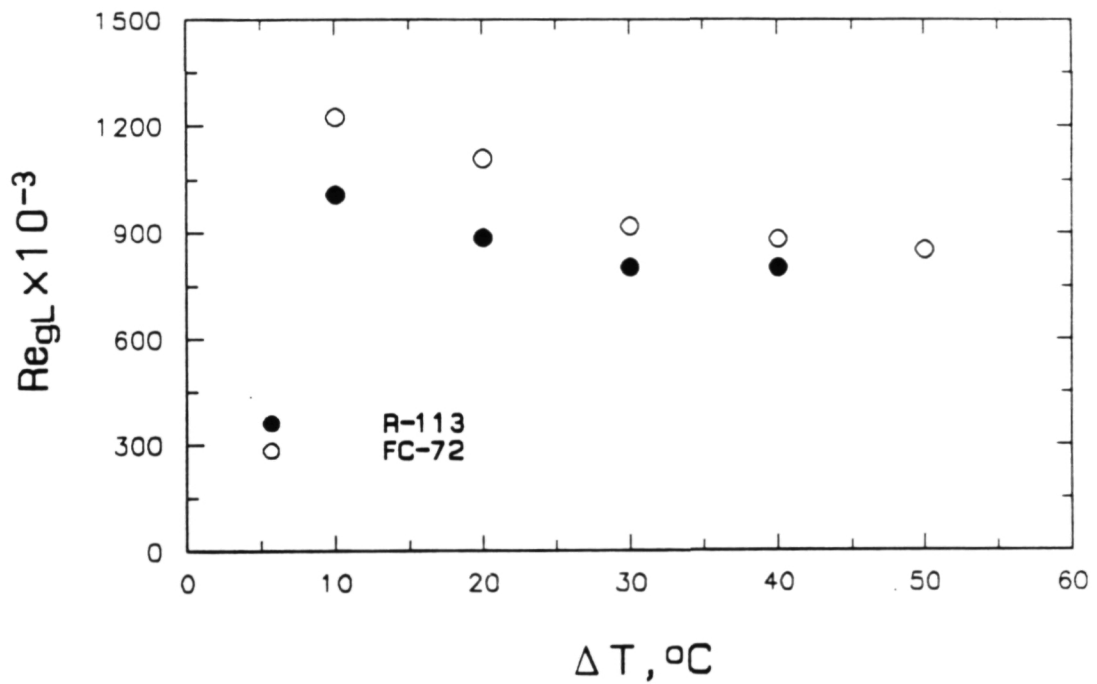
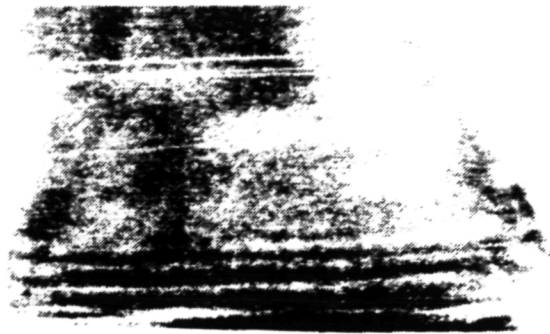


Fig. 6.43 Relationship between Re_{gL} causing the interfacial wave initiation and ΔT



a. Outlet view



b. Side view

Fig. 6.44 Photographs of interfacial wave initiation in air-liquid flow

a. $\mu_l = 5.2$ CP; $v_g = 3.2$ m/s; $\dot{m}_l = 1.8 \times 10^{-3}$ kg/s

b. $\mu_l = 4.5$ CP; $v_g = 6.0$ m/s; $\dot{m}_l = 6.1 \times 10^{-4}$ kg/s

6. Results and Discussion

Interfacial Wave Initiation in Adiabatic Air-liquid Flow

Typical photographs of the initiation of the interfacial waves in the experiment of the air-liquid flow are shown in Fig. 6.44. One of the photographs in the figure (Fig. 6.44 a) was taken at the outlet opening of the test section and the other (Fig. 6.44 b) was taken from the side of the test section. From a comparison between Fig. 6.44 and Fig. 6.42, it is seen that the structures of the interfacial waves in the condensation and those in the air-liquid flow are similar (both are two dimensional waves); the waves appear somewhere on the liquid film and then propagate towards the outlet of the test section. As illustrated in Fig. 6.45, the distance between the inlet of the test section and the first wave is defined as the onset length (L_{on}).

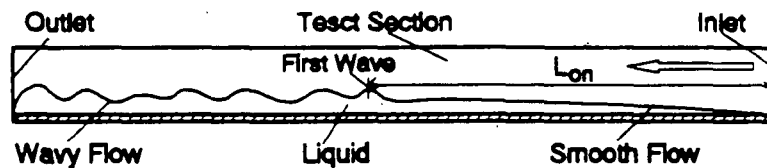
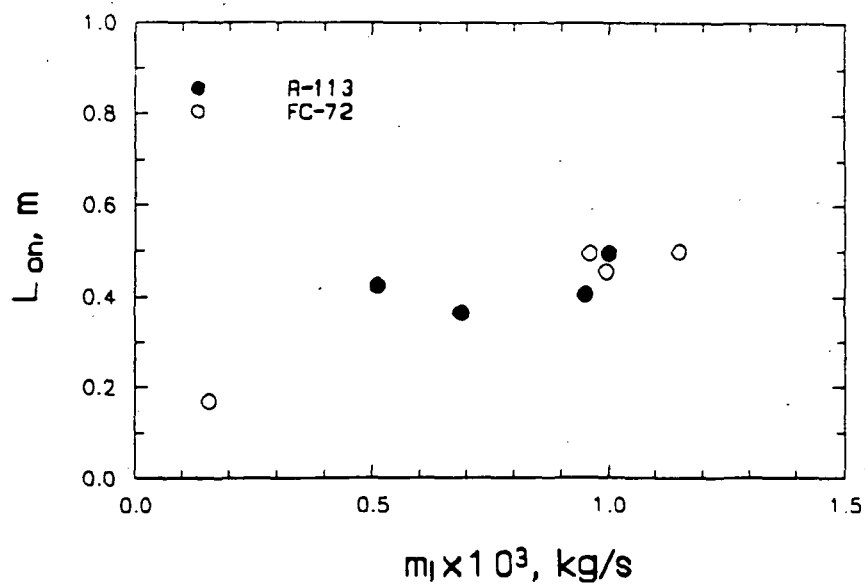
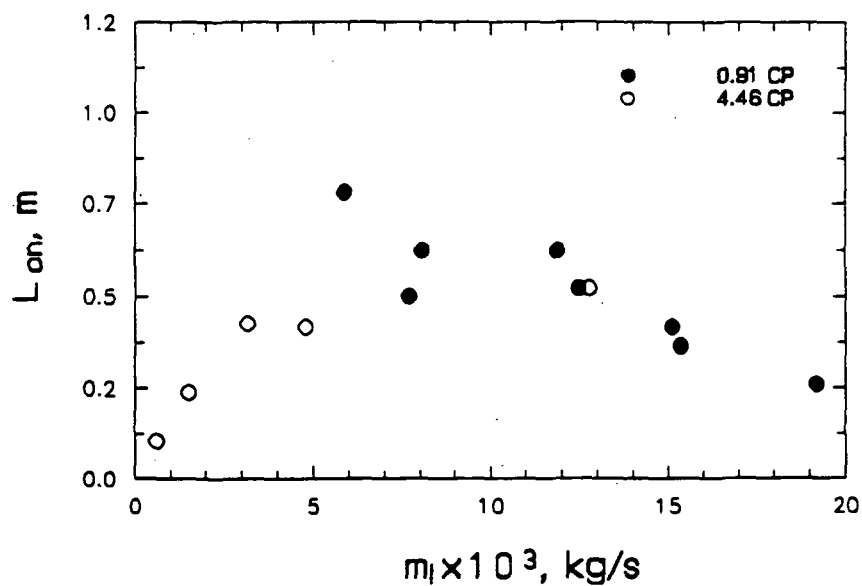


Fig. 6.45 Illustration of onset length

For both the condensation and the air-liquid experiments, the relationship between the onset-length and the liquid flow rate is shown in Fig. 6.46, where \dot{m}_l in figure a is the condensate rate at the point where the first wave (Fig. 6.45) appears and \dot{m}_l in figure b is the liquid flow rate. In the condensation experiment, the onset length does not change much with increasing \dot{m}_l ($L_{on} \approx 0.4$ m). In the air-liquid experiment, the onset-length varies from 0 to 0.75 m and the relationship between the onset length and the liquid flow rate displays two different trends: (1) L_{on} increases when $\mu_l = 0.91$ CP; (2) L_{on} decreases when $\mu_l = 4.46$ CP (figure b). Those conflicting trends of L_{on} with \dot{m}_l may indicate that L_{on} is influenced by other parameters besides the liquid flow rate.



a. Condensation



b. Air-liquid flow

Fig. 6.46 Variation of onset length with liquid flow rate

6. Results and Discussion

Fig. 6.47 shows some typical variations of the liquid film thickness in the air-liquid flow experiment. It is seen that the liquid film thickness decreases along the test section. This trend is different from that of the condensate film thickness in the condensation experiment (Fig. 6.4). This difference may be attributed to the different driving forces in the two separate experiments. In the condensation experiment, the condensate is mainly driven by the momentum of the condensate and the shear stress of the vapor flow; in the air-liquid flow experiment, the flow of the liquid is caused by the hydraulic gradient of the liquid and the shear stress at the interface.

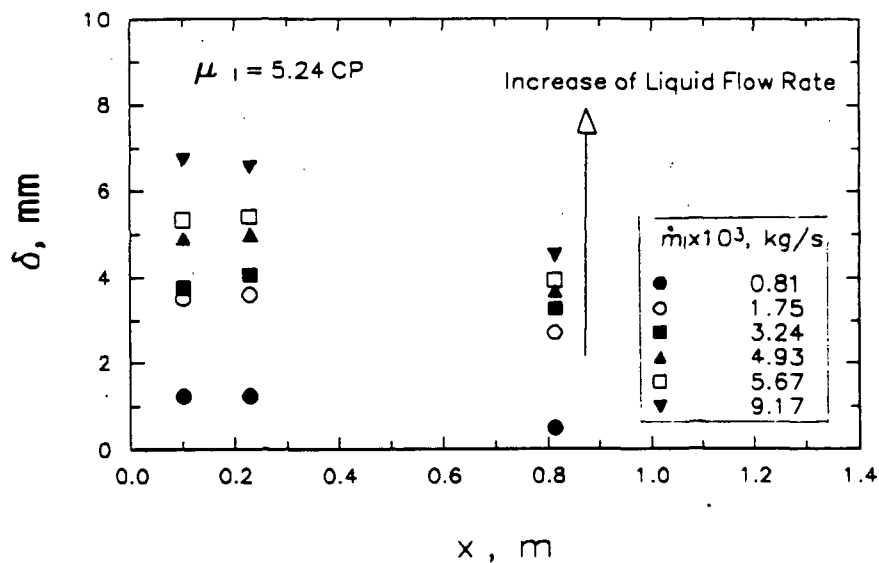


Fig. 6.47 Variation of liquid film thickness along the test section, air-liquid flow

Because the distributions of the liquid film thickness in condensation and the air-liquid flow experiments are different, the variations of the liquid velocity along the test section may differ. However, those differences do not affect the following discussion since only the liquid velocity at the point when the first wave appears is considered.

6. Results and Discussion

Fig. 6.48 shows the relationship between the air velocity (v_g), at which wave appears, and the liquid velocity (v_l) calculated using Eq. 4-23. The air velocity at which waves appear decreases with increasing liquid velocity. Fig. 6.49 shows the effect of the liquid viscosity (μ_l) on the air velocity for wave initiation. It is found that this air velocity increases with increasing liquid viscosity; when the liquid viscosity and the liquid flow rate are greater than 2.37 CP and 0.002 kg/s respectively, the increase of the liquid viscosity is insignificant for the wave initiation. However, when the liquid flow rate is less than 0.002 kg/s, the effect of the liquid viscosity on the initiation of interfacial waves is significant (Fig. 6.50) and the air velocity for wave initiation increases with increasing liquid viscosity. The liquid viscosity has a stabilizing effect on the initiation of the interfacial waves.

The trends of the vapor velocity for wave initiation in condensate film seem to be similar to those of the air velocity for wave initiation. It is seen from Fig. 6.51 that the vapor velocity (at which waves appear) decreases with increasing condensate rate. The vapor velocity of R-133 for initiating the waves is slightly higher than that of FC-72. This may be because the viscosity of liquid R-113 is greater than that of FC-72 (about 1.2 times).

The experimental results indicate that the initiation of the interfacial waves is influenced by the gas (vapor or air) velocity, the liquid velocity, and the liquid viscosity. The effect of liquid viscosity decreases gradually with increasing liquid velocity.

Fig. 6-52 shows a relationship between Re_g and Re_l at which waves appear, where Re_g and Re_l are defined as $v_g L / \nu_g$ and $v_g \delta / \mu_l$. For condensation v_g and \dot{m}_l are the vapor velocity and the condensate flow rate at the point where the first wave (Fig. 6.44) appears; for air-liquid flow, v_g and \dot{m}_l are the air velocity and the liquid flow rate. At similar values of Re_l , the vapor Reynolds number is apparently larger than the air Reynolds number. This may indicate that the condensate flow is more stable than the air-liquid flow. This damping effect of condensation on the initiation of the

6. Results and Discussion

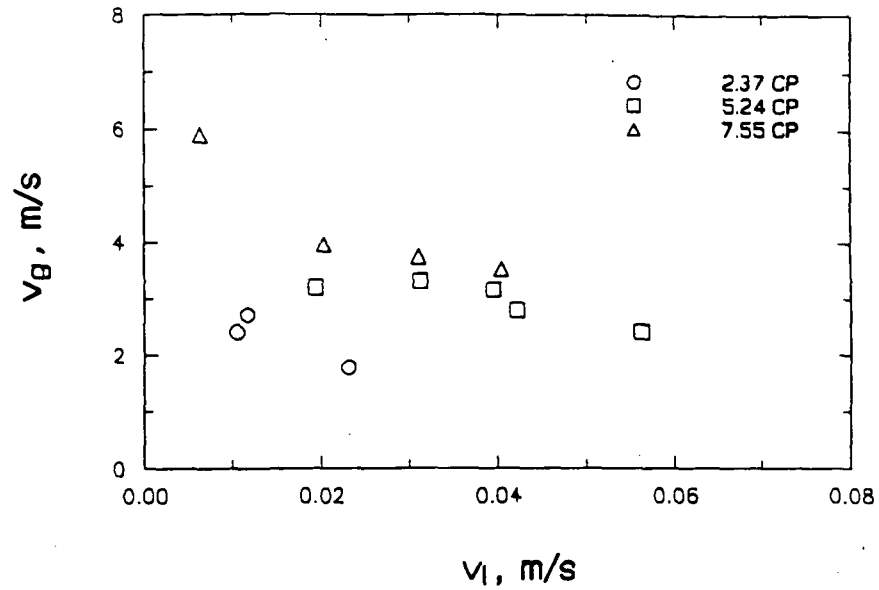


Fig. 6.48 Variation of v_g for wave initiation with v_l in air-liquid flow

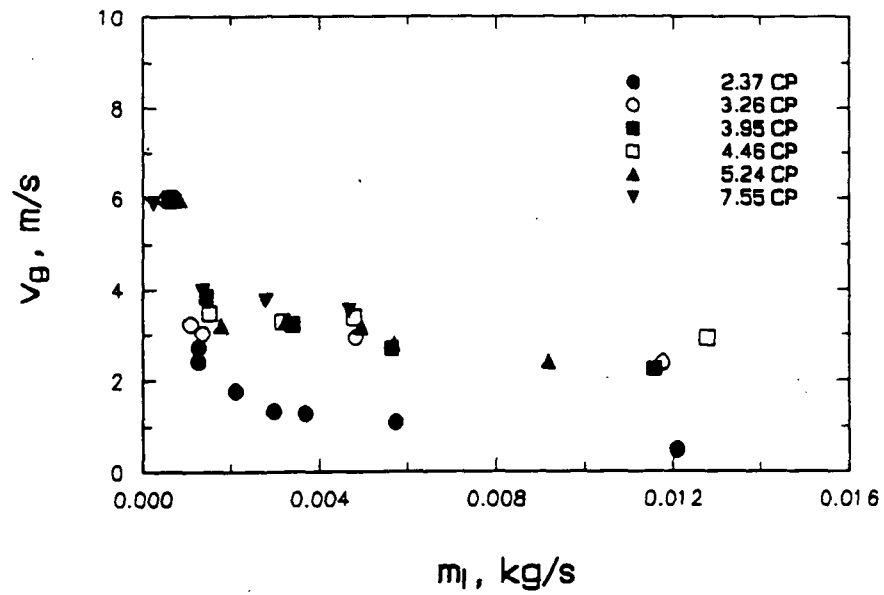


Fig. 6.49 Variation of v_g for wave initiation with m_l in air-liquid flow

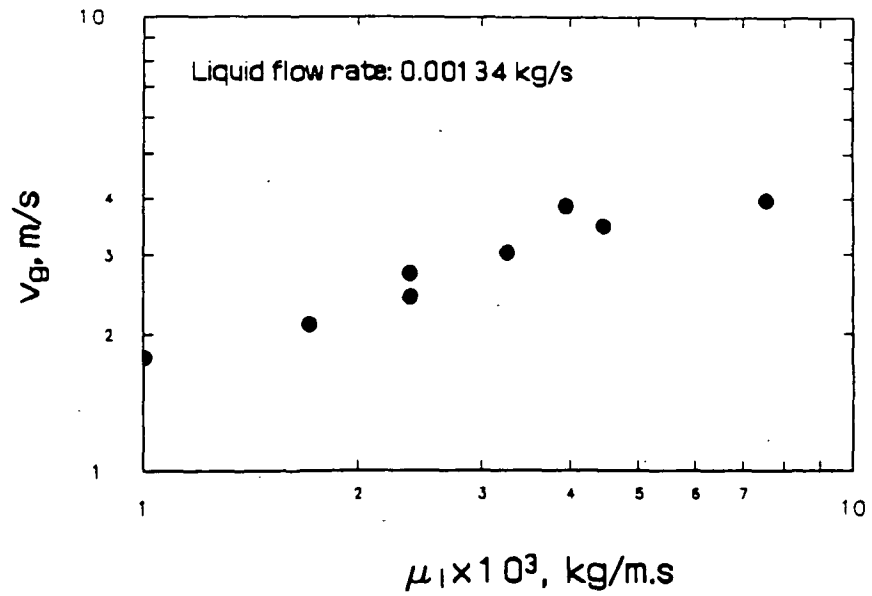


Fig. 6.50 Effect of liquid viscosity on wave initiation

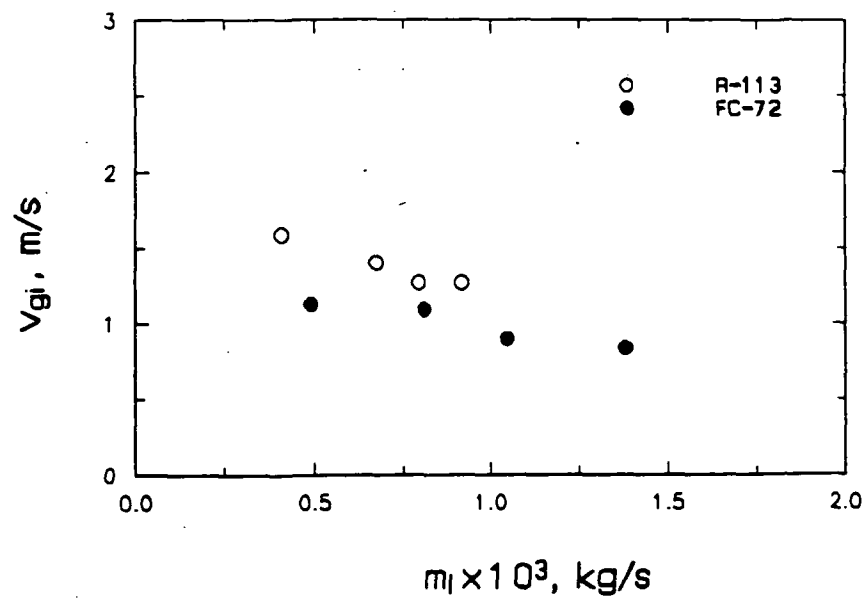


Fig. 6.51 Variation of v_{gi} for wave initiation with m_l in condensation

6. Results and Discussion

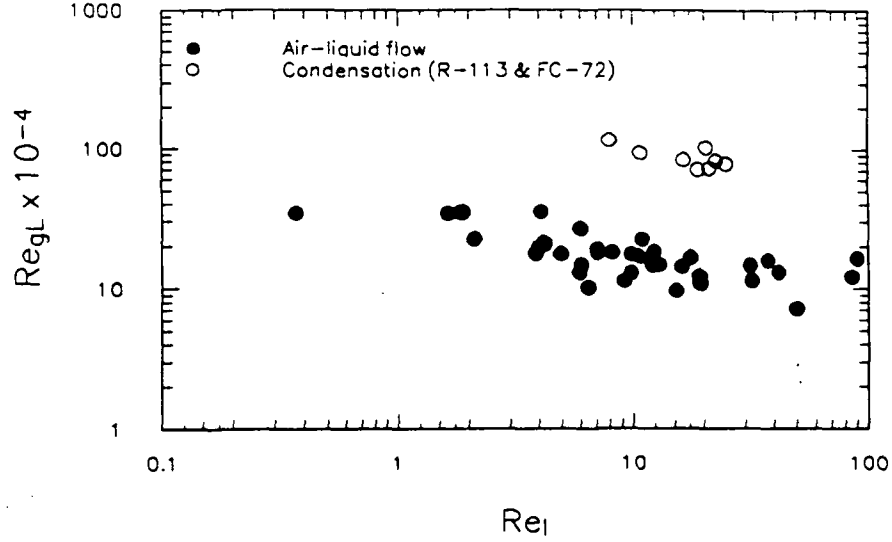


Fig. 6.52 Damping effect of condensation on wave initiation

interfacial waves was also reported by Barry and Corradini (1988)

6.11.2 Criteria Predicting the Instability of Liquid Flow

For gas and liquid flowing parallel and horizontally, the instability of the liquid flow is discussed by Chandrasekhar (1961) assuming that the domain of each of the fluids was semi-infinite. The condition for the onset of waves is given

$$(v_g - v_l)^2 > \frac{2}{\alpha_1 \alpha_2} \sqrt{\frac{\sigma g (\alpha_1 - \alpha_2)}{\rho_l + \rho_g}} \quad (6-23)$$

where

$$\alpha_1 = \frac{\rho_l}{\rho_l + \rho_g}, \quad \alpha_2 = \frac{\rho_g}{\rho_l + \rho_g}$$

Considering gas and liquid flowing horizontally between two horizontal plates, Milne-Thomson (1960) derived the instability condition of the liquid

6. Results and Discussion

$$(v_g - v_l)^2 > \frac{\rho_l \coth kH_l + \rho_g \coth kH_g}{\rho_l \rho_g \coth kH_l \coth kH_g} \left[\frac{g(\rho_l - \rho_g)}{k} + \sigma k \right] \quad (6-24)$$

where

H_l - depth of the liquid;

H_g - depth of the gas;

k - wave number ($2\pi/\lambda$);

λ - wave length.

For large values of the depths of the fluids making both kH_l , and kH_g much greater than 1; Eq. 6-24 becomes

$$(v_g - v_l)^2 > \frac{\rho_g + \rho_l}{\rho_g \rho_l} \left[\frac{g(\rho_l - \rho_g)}{k} + \sigma k \right] \quad (6-25)$$

To find a value of k to make the right hand side minimum

$$\frac{d}{dx} \left[\frac{g(\rho_l - \rho_g)}{k} + \sigma k \right] = 0 \rightarrow k = \left[\frac{g(\rho_l - \rho_g)}{\sigma} \right]$$

Substitution of the above equation into Eq. 6-25 yields

$$(v_g - v_l)^2 = 2 \frac{\rho_l + \rho_g}{\rho_l \rho_g} [\sigma g(\rho_l - \rho_g)]^{1/2} \quad (6-26)$$

It is seen that Eq. 6-26 is the same as Eq. 6-23.

For gas and liquid flowing inside a horizontal channel, Jensen and Yuen (1982) proposed a criterion to determine the transition of liquid flow from a smooth surface to a wavy surface

$$\frac{(v_g - v_l)}{w_J} > 17 \quad (6-27)$$

6. Results and Discussion

where

$$w_j = \left(\frac{4\sigma g}{\rho_l} \right)^{0.25}$$

The only criterion applied for predicting the stability of condensate flow appears to be the one given by Kocamustafaogullari (1985)

$$Ka\delta^*k^* - [g^*\delta^* + 2\rho^*\left(\frac{Ku}{Pr}\right)^2 + \frac{1}{3}\delta^*(1 + \frac{\tau^*}{\delta^*})]k^* - \frac{3}{\delta^*}\left[\frac{Ku}{Pr}\right] \geq 0 \quad (6-28)$$

where

$$Ka = \left(\frac{\sigma^3 \rho_l^2}{\mu_l^4 \Delta \rho g_x} \right)^{1/3} \quad Ku = -\frac{C_{pl} \Delta T}{h_{fg}}$$

$$\delta^* = \delta \left[\frac{\rho_l \Delta \rho g_x}{\mu_l^2} \right]^{1/3} \quad k^* = k \left(\frac{\mu_l^2}{\rho_l \Delta \rho g_x} \right)^{1/3}$$

$$\tau^* = \frac{\tau_i}{\Delta \rho \delta g_x} \quad g^* = \frac{g_y}{g_x} \quad \rho^* = \frac{\rho_l - \rho_g}{\rho_g}$$

For condensate flowing horizontally, the component of the gravity force in the x direction (g_x) is zero. In this case, Eq. 6-28 can be simplified as

$$\frac{3}{\delta^*} \left(\frac{Ku}{Pr} \right) \geq 0 \quad (6-29)$$

Eq. 6-29 predicts that for condensation inside a horizontal duct, the condensate flow is always stable. This prediction is contradicted with the present and other experimental results. Hence, the criterion of Kocamustafaogullari may not be appropriate for condensation on a horizontal surface.

Eqs. 6-23, 6-24, and 6-27 are used to predict the instability of the present experiments. Some typical comparisons of the predictions from those equations with

6. Results and Discussion

the experimental results of the air-liquid flow are shown in Table 6.8, where v_{gi}^2 represents $(v_g - v_l)^2$ and the values in a column with equation numbers are the right hand side values of the equations. It is seen that the right hand side values of both Eq. 6-23 and 6-24 are larger than the values of $(v_g - v_l)^2$ in the same row, especially when the air velocity (v_g) is small. The left hand side values of Eq. 6-27 is close to 17 (the criterion value in Eq. 6-23), but it is in a lower side. When Eqs. 6-23, 6-24, and 6-27 are used to predict the onset of the waves in condensation, it is found that none of these equations give satisfactory results (Table 6.9).

The present experimental results show that the instability of the liquid flow may also be a function of the liquid viscosity (Figs. 6.50 and 6.51). However, this viscosity influence is not taken into account in any of the three equations (Eqs. 6-23, 6-24, and 6-27). To include the viscosity effect in Eq. 6-27, it is assumed that

$$\left(\frac{v_{gi} - v_l}{w_j}\right)\left(\frac{\mu_l}{\mu_g}\right)^{a_j} > b_j, \quad w_j = \left(\frac{4\sigma g}{\rho_l}\right)^{0.25} \quad (6-30)$$

where a_j and b_j are constants and are determined only from the experimental data of the air-liquid flow and the regression analysis. As a result, Eq. 6-30 becomes

$$\left(\frac{v_g - v_l}{w_j}\right)\left(\frac{\mu_l}{\mu_g}\right)^{-0.328} > 2.0 \quad (6-31)$$

Using Eq. 6-31 to evaluate the instability in the condensation experiment, it is found that the predictions from the equation are in good agreement with the experimental data (Fig. 6.52). However, some predictions from Eq. 6-31 for the instability of the air-liquid flow fall inside the smooth flow region, which is in contradiction with the experimental observation. Hence, Eq. 6-31 still needs more improvement and experimental support.

6. Results and Discussion

Table 6.8 Comparison of the predictions from Eq.s 6-23, 6-24, and 6-27 with the experimental results of air-liquid flow

Run	μ_l	v_g	v_l	v_{gl}^2	Eq.6-23 ^a	Eq.6-24 ^b	Eq.6-27 ^c
26	1.00	1.78	0.01	3.13	43.75	50.22	7.66
69	1.12	3.08	0.02	9.36	43.48	50.00	13.23
27	1.71	1.94	0.00	3.76	44.43	50.39	8.51
31	2.37	1.78	0.01	3.13	44.55	49.80	7.88
29	2.37	2.73	0.01	7.40	44.55	49.81	12.11
40	2.67	1.44	0.05	1.93	44.38	49.70	6.18
36	2.67	5.94	0.04	34.81	44.38	49.67	26.23
41	3.26	2.38	0.09	5.24	44.51	49.62	10.23
43	3.26	3.92	0.03	15.13	44.51	49.62	17.38
46	3.26	5.99	0.01	35.76	44.51	49.60	26.72
47	3.95	2.26	0.05	4.88	44.42	49.41	9.90
50	3.95	3.85	0.01	14.75	44.42	49.41	17.20
51	3.95	5.97	0.02	35.40	44.42	49.39	26.66
52	4.46	2.91	0.05	8.18	44.93	49.73	12.89
55	4.46	3.48	0.01	12.04	44.93	49.73	15.63
56	4.46	6.00	0.01	35.88	44.93	49.72	26.99
62	5.24	2.41	0.04	5.62	44.97	49.75	10.68
60	5.24	3.21	0.01	10.24	44.97	49.75	14.42
64	7.55	3.53	0.03	12.25	45.36	49.94	15.87
67	7.55	5.90	0.00	34.81	45.36	49.92	26.75
59	5.24	5.98	0.02	35.52	44.97	49.73	26.86

a: right hand side values of Eq. 6-23

b: right hand side values of Eq. 6-24

c: left hand side values of Eq. 6-27

6. Results and Discussion

Table 6.9 Comparison of the predictions from Eqs. 6-23, 6-24, and 6-27 with the experimental results of condensation

Run	ΔT	v_g	v_l	v_{gl}^2	Eq.6-23	Eq.6-24	Eq.6-27
273	39.6	1.24	0.013	1.51	4.09	4.10	8.80
274	31.48	1.25	0.016	1.52	3.95	3.96	8.83
278	22.42	1.38	0.016	1.86	3.91	3.91	9.74
279	10.75	1.56	0.017	2.38	4.01	4.02	11.00
345	40.58	0.81	0.013	0.64	1.79	1.92	6.63
346	28.21	0.87	0.015	0.74	1.85	1.98	7.10
388	19.53	1.07	0.021	1.10	1.86	2.00	8.66
389	9.69	1.11	0.012	1.21	1.72	1.83	9.05

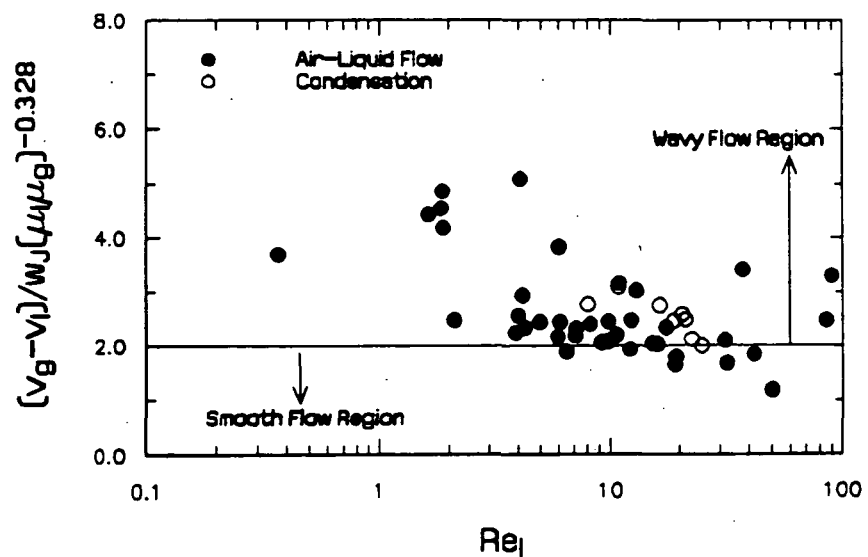


Fig. 6.53 Validity of the instability criterion (Eq. 6-31)

6.11.3 Interfacial Wave Length and Speed

To study the interfacial waves in condensation, the wave length and the wave speed were measured. The experimental data of the wave length include the local wave length measured along the condensing surface and the average wave length, which is the arithmetic mean of all the values of the local wave length. Since the measured wave speed is an average value over the length of the wave-speed measuring device (Fig. 4.19) and also no obvious change of the wave speed was found when moving the device along the test section, the data of the wave speed are considered as the average wave speed over the whole condensing surface.

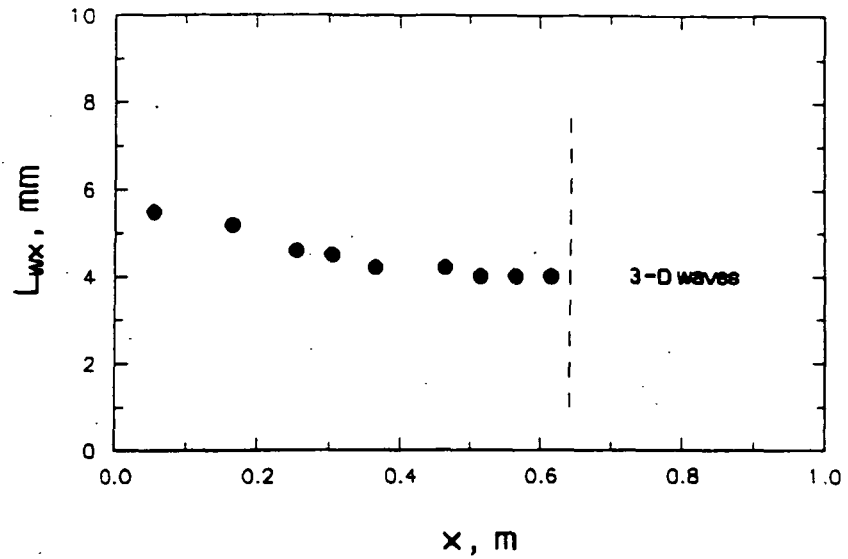
Fig. 6.54 presents two typical distributions of the two dimensional local wave length (L_{wx}) along the condensing surface. For both R-113 and FC-72 used as the condensing fluids, the largest wave length occurs near the leading edge of the condensing surface; the wave length decreases along the surface; at some distance down stream of the condensing surface, the two dimensional waves become three-dimensional waves.

For the average wave length (L_w), it is seen in Fig. 6.55 that the effect of ΔT on L_w is not quite significant and the influence of the inlet vapor velocity (v_{gi}) on L_w is not clear (for R-113, it shows that L_w decreases with increasing v_{gi} ; for FC-72 it shows that L_w does not change much with v_{gi}).

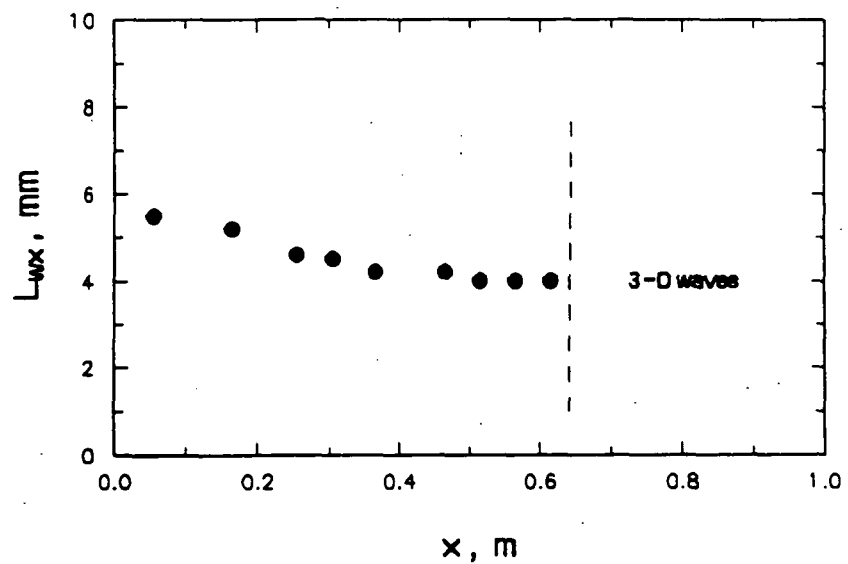
Fig. 6-56 shows the relationship between the average wave length and the liquid Reynolds number. The liquid Reynolds number varies approximately from 40 to 130 for R-113 and from 85 to 400 for FC-72. Within those ranges, the average wave length is approximately constant. This trend is similar to the experimental results summarized by Hishburg and Florschuetz (1982).

The variation of the wave speed with the inlet vapor velocity using R-113 and FC-72 as the condensing fluids is shown in Fig. 6.57. It is seen that with increasing vapor velocity, initially the wave speed is mainly constant; when the vapor velocity further increases, the wave speed increases; the temperature difference (ΔT) generally

6. Results and Discussion



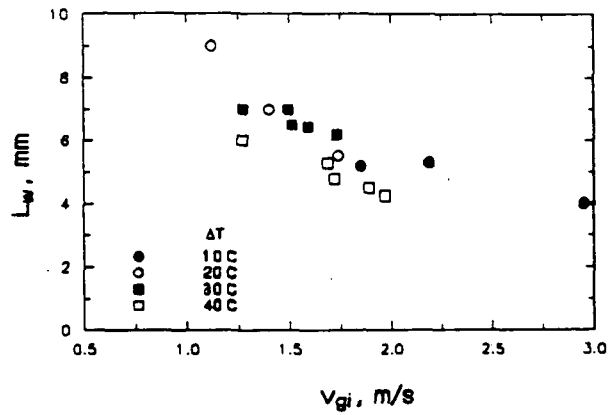
a. R-113; $\Delta T = 21.2$ °C; $v_{g1} = 1.7$ m/s



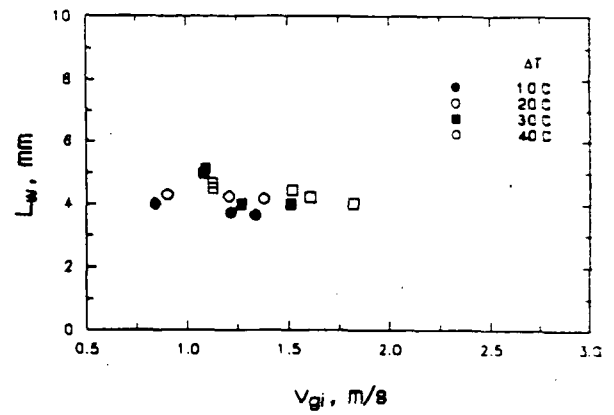
b. FC-72; $\Delta T = 10.6$ °C; $v_{g1} = 1.6$ m/s

Fig. 6.54 Distributions of local wave length along the condensing surface

6. Results and Discussion

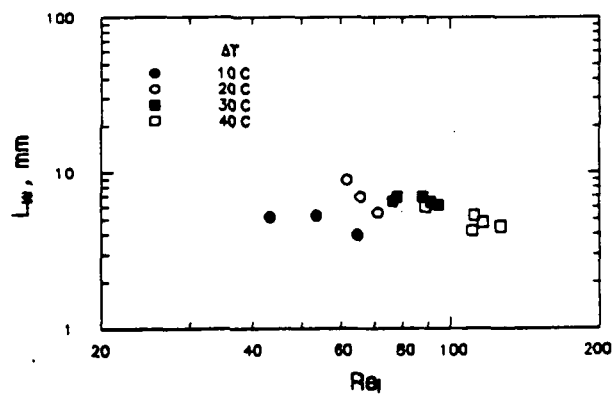


a. R-113

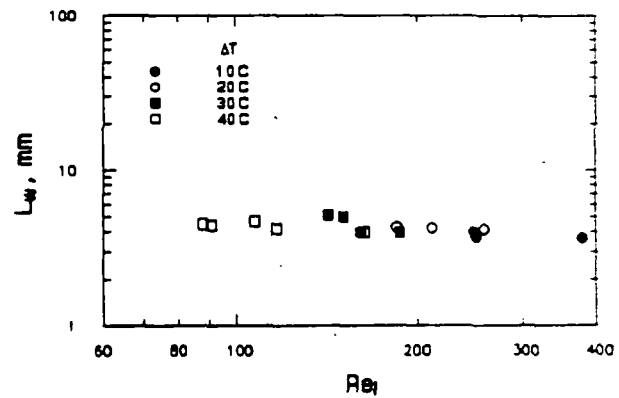


b. FC-72

Fig. 6.55 Variations of average wave length with Inlet vapor velocity



a. R-113



b. FC-72

Fig. 6.56 Variations of average wave length with Reynolds number of condensate

6. Results and Discussion

has no noticeable effect on the wave speed except for $\Delta T \approx 10^\circ\text{C}$, for which, the wave speed is lower.

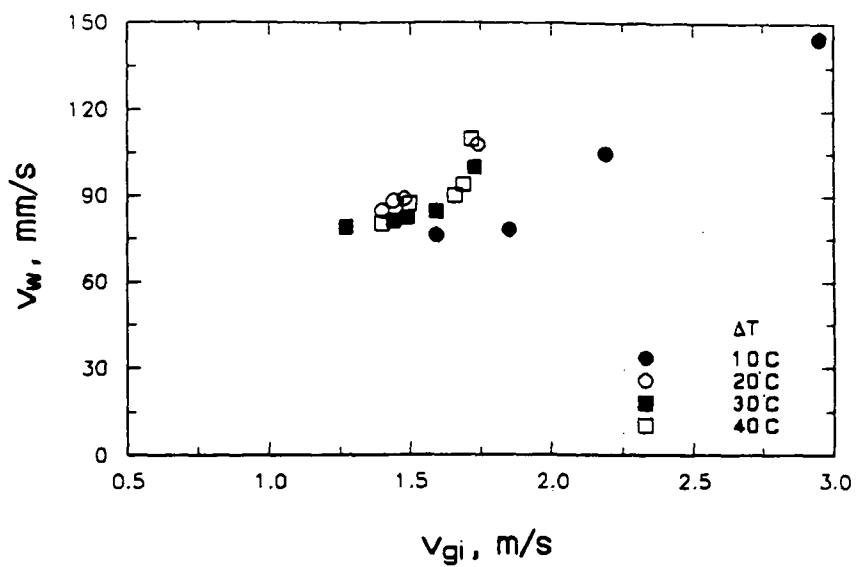
Fig. 6.58 shows comparisons of the wave length and wave speed of R-113 with those of FC-72. It is seen that the wave length of R-113 is always larger than that of FC-72 at the same vapor velocity; the wave speeds of both fluids are about the same.

From the above results, two main conclusions are drawn

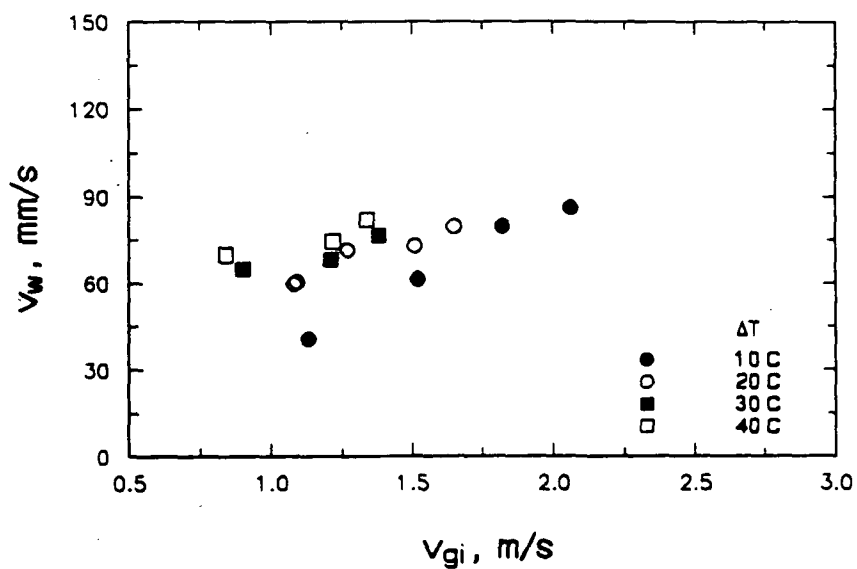
- the wave length reduces along the condensing surface and finally the two dimensional wave becomes the three dimensional wave;
- the wave speed increases with increasing the vapor velocity.

One unexpected feature that was observed was that the interfacial waves with condensation were not perpendicular to the side plates but made an angle of approximately 30° to 45° with the side plates, as shown in Fig. 6.2. A slight rotation of the duct about its axis had no influence on the orientation of the waves. However, with air-liquid adiabatic flows, the waves were perpendicular to the side plates even when the bottom surface was tilted by rotating the duct about its axis.

6. Results and Discussion



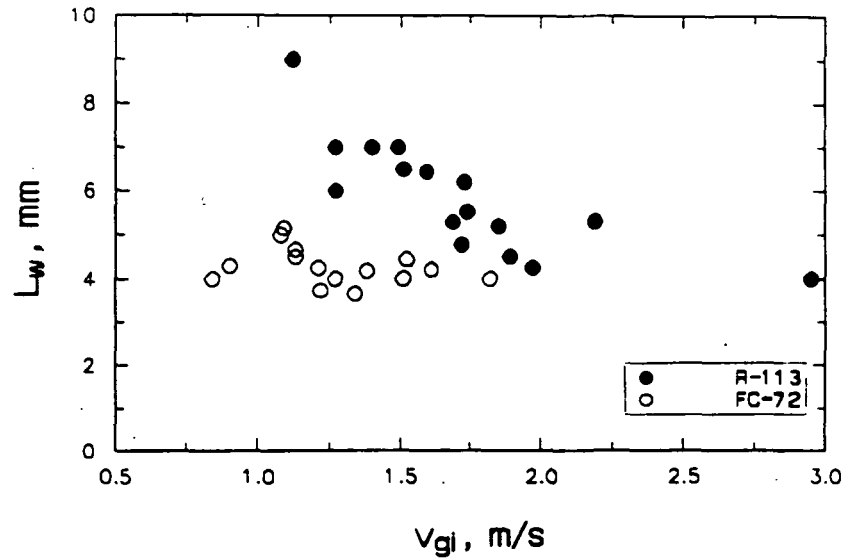
a. R-113



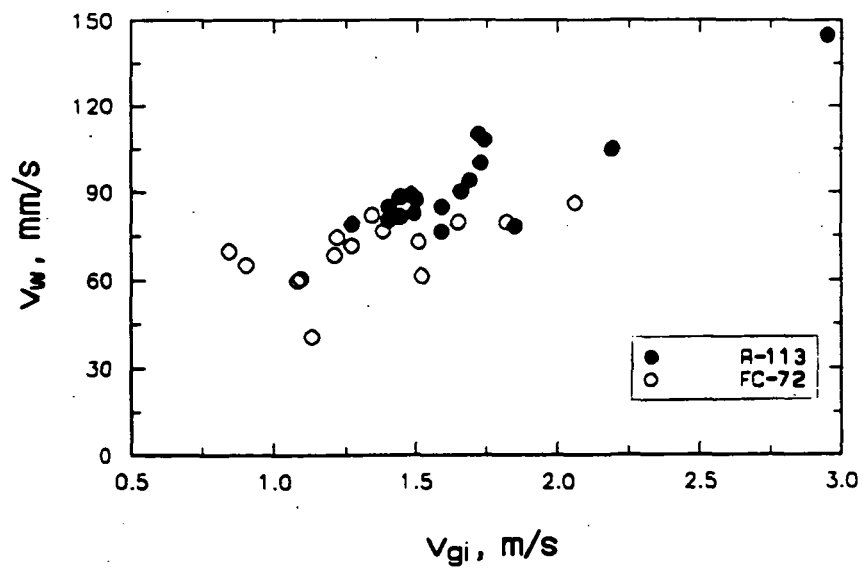
b. FC-72

Fig. 6.57 Variation of wave speed with Inlet vapor velocity

6. Results and Discussion



a. Comparison of wave length



b. Comparison of wave speed

Fig. 6.58 Comparison of wave length and wave speed of R-113 with those of FC-72

7. CONCLUSIONS AND RECOMMENDATIONS

7.1. Conclusions

Condensation heat transfer in an annular flow regime with and without interfacial waves was experimentally investigated. The study included measurements of heat transfer rate with condensation of vapor flowing inside a horizontal rectangular duct and experiments on the initiation of interfacial waves in condensation, and adiabatic air-liquid flow. An analytical model for the condensation was developed to predict condensate film thickness and heat transfer coefficients. The conclusions drawn from the study are as follows:

- 1. The condensate film thickness was very thin (< 0.6 mm). The film thickness, growing rapidly at the leading edge of the condensing surface, increased gradually along the surface. With increasing the inlet vapor velocity, the condensate film thickness decreased.
- 2. The average heat transfer coefficient increased with increasing the inlet vapor velocity. After the appearance of interfacial waves, the increasing rate of the heat transfer coefficient with the vapor velocity enhanced greatly (it appeared that the effect of interfacial waves became significant when $Re_{gl} > 1 \times 10^6$).
- 3. The local heat transfer coefficient decreased with the axial distance of the condensing surface, with the largest change at the leading edge of the test section.
- 4. The prediction of the average heat transfer coefficients from the present analytical model agreed within $\pm 17\%$ with the experimental data for $5 \times 10^5 \leq Re_{gl} \leq 1.5 \times 10^6$.

7. Conclusions and Recommendations

However, outside this range, the predicted average heat transfer coefficients were lower than the measured values with an average deviation of approximate -40 %.

- The interfacial shear stress, which consisted of the momentum shear stress and the adiabatic shear stress, appeared to have a significant effect on the heat transfer coefficients. In the analytical model, a modified Schlichting's friction equation (Eq. 6-15) was used in calculating the adiabatic shear stress.
- The heat transfer correlation based on the present analytical model and the experimental data (Eq. 6-20) and the correlation developed from the present experimental results (Eq. 6-22) were in good agreement with the experimental data. The average deviation between the calculated heat transfer coefficients and the experimental values was ± 18 %.
- In the experiment, the condensate flow along the condensing surface experienced a smooth flow, a two-dimensional wavy flow, and a three-dimensional wavy flow. The change of the flow patterns depended on the vapor velocity and the viscosity of liquid.
- In the condensation experiment, the local wave length decreased with the axial distance of the condensing surface and the average wave length decreased with increasing inlet vapor velocity, while the wave speed increased with increasing vapor velocity.
- The heat transfer measurements are reliable. The difference between the heat transfer rate obtained from a heat balance in the cooling channel and that obtained from a heat balance in the vapor duct was usually within ± 5 %.
- The ultrasonic technique was effective for measuring the condensate film thickness when the surface was smooth or had waves of small amplitude.

7. Conclusions and Recommendations

7.2. Recommendations for Further Study

Although a large amount of data and results were obtained in the present study, further work is still required for a clear understanding of the condensation process. Based on the present study, the following recommendations are proposed:

- Only two different condensing fluids were used in the present experiment. For investigating the effects of the parameters (Pr , Ja , ρ/ρ_g , μ/μ_g) on the condensation heat transfer, more fluids are needed. Also, for studying the geometric effect, experiment should be conducted inside different test sections with various height, width, and length dimensions.
- The present experiment showed that for R-113 the effect of ΔT on the heat transfer coefficients was not significant, but for FC-72 this effect was not quite clear. More experiments are needed to study the effect of changing ΔT on the heat transfer coefficients.
- A better analytical model may be achieved by obtaining experimental values of interfacial shear stress and including a vapor velocity profile inside the model. Also, since the heat transfer is influenced by the flow patterns (smooth flow or wavy flow), it is necessary to derive the different models according to the different flow patterns.
- More work is need to study interfacial waves, including the wave length and wave speed. To support the criterion (Eq. 6-31) predicting the initiation of interfacial waves, future work should provide more data on the instability in condensation, as well as in the air-liquid flow with a wider range of liquid viscosity and surface tension and, possibly, other parameters.

7. Conclusions and Recommendations

- Besides the ultrasonic technique, some other methods (such as, using capacitance probe, conductance, and optical glass) may be considered to measure the condensate film thickness.
- The average heat transfer coefficients were found to increase rapidly with increasing inlet vapor velocity after the appearance of the waves. However, when the vapor velocity was more than approximately 4 m/s, it seemed that the rate of the increase of the heat transfer coefficients started to decrease (Fig. 6.6). To verify this result, more experiments with higher vapor velocity are needed. To do this, two major modifications on the present experimental set-up of condensation are needed: (1) to add more heating power to the boiler; (2) to increase the cooling capacity of the auxiliary condenser.

APPENDIX A

UNCERTAINTY ANALYSES

A.1. Total Average Heat Transfer Coefficient

The total average heat transfer coefficient (\bar{h}_t) is expressed as

$$\bar{h}_t = \frac{q}{A(T_{sat} - T_s)} \quad (A-1)$$

The value of the total average heat transfer coefficient (\bar{h}_t) depends on the measurements of the heat transfer rate (q) the total area of the condensing surface (A), and the difference between the saturation temperature of vapor (T_{sat}) and the condensing surface temperature (T_s). The uncertainties in measuring q , A , $T_{sat} - T_s$ will propagate through the calculations to produce an uncertainty in determining \bar{h}_t . Based on the method given by Kline and McClintock (1953), the uncertainty of \bar{h}_t is estimated as flows.

The basic equation for the uncertainty of \bar{h}_t is derived according to Eq. A-1

$$\epsilon_{\bar{h}_t} = [(\frac{\partial \bar{h}_t}{\partial q} \epsilon_q)^2 + (\frac{\partial \bar{h}_t}{\partial A} \epsilon_A)^2 + (\frac{\partial \bar{h}_t}{\partial T_{sat}} \epsilon_{T_{sat}})^2 + (\frac{\partial \bar{h}_t}{\partial T_s} \epsilon_{T_s})^2]^{1/2} \quad (A-2)$$

where

$$\frac{\partial \bar{h}_t}{\partial q} = \frac{1}{A(T_{sat} - T_s)} \quad (A-3)$$

$$\frac{\partial \bar{h}_t}{\partial A} = -\frac{q}{A^2(T_{sat} - T_s)} \quad (A-4)$$

Appendix A: Uncertainty Analyses

$$\frac{\partial \bar{h}_i}{\partial T_{sat}} = -\frac{q}{A(T_{sat} - T_s)^2} \quad (A-5)$$

and

$$\frac{\partial \bar{h}_i}{\partial T_s} = \frac{q}{A(T_{sat} - T_s)^2} \quad (A-6)$$

Substituting Eqs A-3, A-4, A-5, and A-6 into Eq. A-2 and using Eq. A-1 yield

$$\epsilon_{\bar{h}_i} = \bar{h}_i \left[\left(\frac{\epsilon_q}{q} \right)^2 + \left(\frac{\epsilon_A}{A} \right)^2 + \frac{(\epsilon_{T_{sat}}^2 + \epsilon_{T_s}^2)}{(T_{sat} - T_s)^2} \right]^{1/2} \quad (A-7)$$

where ϵ_q , ϵ_A , $\epsilon_{T_{sat}}$, and ϵ_{T_s} represent the uncertainties of q , A , T_{sat} , and T_s and are estimated as follows.

(i) ϵ_q

The equation for the heat transfer rate (q) is expressed as

$$q = \dot{m}_w C_{pw} \Delta T_w \quad (A-8)$$

Based on Eq. A-8, the equation for ϵ_q is derived

$$\epsilon_q = \left[\left(\frac{\partial q}{\partial \dot{m}_w} \epsilon_{\dot{m}_w} \right)^2 + \left(\frac{\partial q}{\partial C_{pw}} \epsilon_{C_{pw}} \right)^2 + \left(\frac{\partial q}{\partial \Delta T_w} \epsilon_{\Delta T_w} \right)^2 \right]^{1/2} + \Delta_q \quad (A-9)$$

where \dot{m}_w is the mass flow rate of coolant; ΔT_w is the temperature difference of coolant across the entire cooling channel; Δ_q is the possible heat transfer between the test section and the environment.

Since the value of the specific heat of coolant (C_{pw}) has been well established, it is assumed that

$$\epsilon_{C_{pw}} \approx 0$$

Appendix A: Uncertainty Analyses

With this assumption, Eq. A-9 simplifies to

$$\epsilon_q = \left[\left(\frac{\partial q}{\partial \dot{m}_w} \epsilon_{\dot{m}_w} \right)^2 + \left(\frac{\partial q}{\partial \Delta T_w} \epsilon_{\Delta T_w} \right)^2 \right]^{1/2} + \Delta_q \quad (\text{A-10})$$

From Eq. A-8

$$\frac{\partial q}{\partial \dot{m}_w} = C_{pw} \Delta T_w \quad (\text{A-11})$$

$$\frac{\partial q}{\partial \Delta T_w} = C_{pw} \dot{m}_w \quad (\text{A-12})$$

Substitution of Eq.s A-11 and A-12 into Eq. A-10 yields

$$\epsilon_q = C_{pw} [(\Delta T_w \epsilon_{\dot{m}_w})^2 + (\dot{m}_w \epsilon_{\Delta T_w})^2]^{1/2} + \Delta_q \quad (\text{A-13})$$

The uncertainty of $\epsilon_{\dot{m}_w}$ is mainly due to the accuracy of the rotameter measuring the coolant flow rate. It is assumed that

$$\epsilon_{\dot{m}_w} = 0.02 \dot{m}_w \quad (\text{A-14})$$

The uncertainty of the temperature difference of coolant ($\epsilon_{\Delta T_w}$) is caused by the two uncertainties: (1) due to the inaccuracy of the thermocouple wire and junction (ϵ_{tc}) and (2) due to the uncertainty of the thermocouple readout (ϵ_{me}). It is estimated that

$$\epsilon_{tc} = 0.2 \text{ } ^\circ\text{C} \quad \text{and} \quad \epsilon_{me} = 0.1 \text{ } ^\circ\text{C}$$

therefore

$$\epsilon_{\Delta T_w} = 0.2 + 0.1 = 0.3 \text{ } ^\circ\text{C} \quad (\text{A-15})$$

Substitution of Eq.s (A-14) and (A-15) into Eq. (A-13) and using Eq. (A-8) yields

Appendix A: Uncertainty Analyses

$$\epsilon_q = 0.02q[1 + (\frac{15}{\Delta T_w})^2]^{\frac{1}{2}} + \Delta_q \quad (A-16)$$

The heat transfer between the test section and the environment (Δ_q) includes the heat transfer between the vapor duct of the test section and the environment (q_1) and the heat transfer between the cooling channel and the environment (q_2), i.e.

$$\Delta_q = q_1 + q_2 \quad (A-17)$$

Here, q_1 and q_2 are calculated using one-dimensional heat transfer analysis. The parameters and their values used in the calculation are listed below:

- A_1 area of the side wall of the vapor duct in the test section, 0.05 m^2 ;
- A_{21} area of the side wall of the cooling duct, 0.032 m^2 ;
- A_{22} area of the bottom wall of the cooling duct, 0.036 m^2 ;
- A_{23} area of the end wall of the cooling duct, $5.4 \times 10^{-4} \text{ m}^2$;
- k_b thermal conductivity of brass, $110 \text{ W/m}\cdot\text{K}$;
- k_g thermal conductivity of fiber glass, $0.036 \text{ W/m}\cdot\text{K}$;
- k_p thermal conductivity of polycarbonate, $0.19 \text{ W/m}\cdot\text{K}$;
- k_r thermal conductivity of rubber gasket, $0.36 \text{ W/m}\cdot\text{K}$;
- k_s thermal conductivity of styrofoam, $0.033 \text{ W/m}\cdot\text{K}$;
- h_w convective heat transfer coefficient of coolant, $600 \text{ W/m}^2\cdot\text{K}$;
- h_e convective heat transfer coefficient of environment (air), $10 \text{ W/m}^2\cdot\text{K}$;
- T_w temperature of coolant, $5 \text{ }^\circ\text{C}$;
- T_o surface temperature of the flange of converging section connecting to the the front end of the cooling channel, $40 \text{ }^\circ\text{C}$;
- T_e temperature of environment (air), $20 \text{ }^\circ\text{C}$.

Calculation of q_1

Due to the additional heating applied to the top wall of the vapor duct, it is assumed that the top wall is adiabatic and the heat transfer (q_1) occurs through the side wall of the duct. Fig. A.1 illustrates the side wall and the attached insulation involving the heat transfer. This figure shows that the temperature of the inner surface of the side wall is assumed to be the saturation temperature of vapor, T_{sat} . Referring to Fig. A.1, q_1 is calculated as

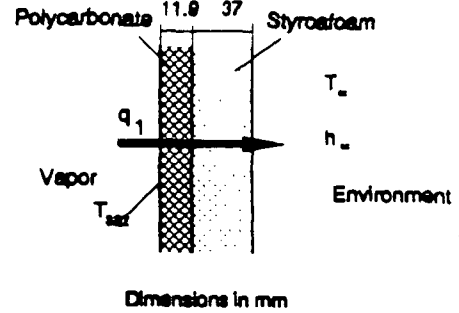


Fig. A.1 Illustration of heat transfer through the vapor duct

$$q_1 = A_1 \frac{T_\infty - T_{sat}}{\left(\frac{11.9}{k_p} + \frac{37}{k_s}\right) \times 10^{-3} + \frac{1}{h_\infty}}$$

$$= 0.05 \frac{20 - T_{sat}}{\left(\frac{11.9}{0.19} + \frac{37}{0.033}\right) \times 10^{-3} + \frac{1}{10}} = 0.04(20 - T_{sat}) \quad (A-18)$$

Calculation of q_2

The heat transfer between the environment and the cooling channel (q_2) consists of heat transfer through the sides of the channel (q_{21}), heat transfer through the bottom of the channel (q_{22}), heat transfer through the front end side of the channel (q_{23}), and heat transfer through the rear end side of the channel (q_{24}). Therefore

$$q_2 = q_{21} + q_{22} + q_{23} + q_{24} \quad (A-19)$$

Referring Figs. A.2 through A.4, q_{21} , q_{22} , q_{23} , and q_{24} are estimated in the following

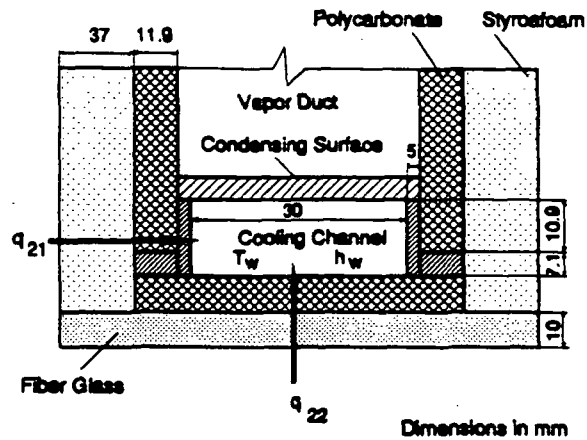


Fig. A.2 Heat transfer through the sides and the bottom of the cooling channel

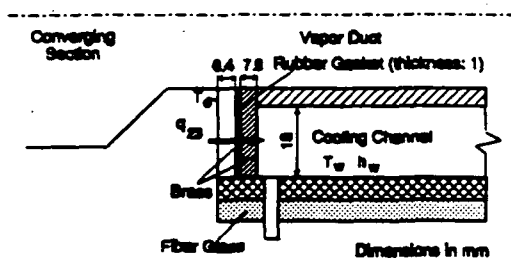


Fig. A.3 Heat transfer through the front side of the cooling channel

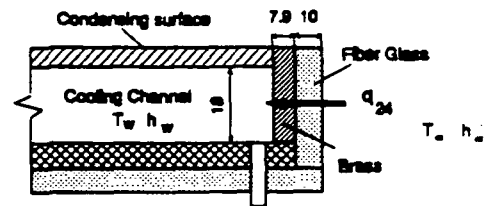


Fig. A.4 Heat transfer through the rear side of the cooling channel

Appendix A: Uncertainty Analyses

Estimate of q_{21}

$$q_{21} = A_{21} \frac{T_{\infty} - T_w}{\frac{1}{h_{\infty}} + \frac{1}{h_w} + \left(\frac{37}{k_s} + \frac{11.9}{k_p} + \frac{5}{k_b}\right) \times 10^{-3}} =$$

$$= 0.032 \frac{20 - 5}{\frac{1}{10} + \frac{1}{600} + \left(\frac{37}{0.033} + \frac{11.9}{0.19} + \frac{5}{110}\right) \times 10^{-3}} = 0.37 \text{ W}$$

Estimate of q_{22}

$$q_{22} = A_{22} \frac{T_{\infty} - T_w}{\frac{1}{h_{\infty}} + \frac{1}{h_w} + \left(\frac{10}{k_g} + \frac{11.9}{k_p}\right) \times 10^{-3}} = 0.027 \frac{20 - 5}{\frac{1}{10} + \frac{1}{600} + \left(\frac{10}{0.036} + \frac{11.9}{0.19}\right) \times 10^{-3}}$$

$$= 0.92 \text{ W}$$

Estimate of q_{23}

$$q_{23} = A_{23} \frac{T_o - T_w}{\left(\frac{1}{k_r} + \frac{14.3}{k_b}\right) \times 10^{-3} + \frac{1}{h_w}} = 5.4 \times 10^{-4} \frac{40 - 5}{\left(\frac{1}{0.39} + \frac{0.0143}{110}\right) \times 10^{-3} + \frac{1}{600}}$$

$$= 4.33 \text{ W}$$

Estimate of q_{24}

$$q_{24} = A_{23} \frac{T_{\infty} - T_w}{\frac{1}{h_{\infty}} + \frac{1}{h_w} + \left(\frac{7.9}{k_b} + \frac{10}{k_g}\right) \times 10^{-3}} = 5.4 \times 10^{-4} \frac{20 - 5}{\frac{1}{10} + \frac{1}{600} + \left(\frac{7.9}{110} + \frac{10}{0.036}\right) \times 10^{-3}}$$

$$= 0.02 \text{ W}$$

Substitution of the values of q_{21} , q_{22} , q_{23} , and q_{24} into Eq. A-19 yields

$$q_2 = 5.64 \text{ W} \quad (\text{A-20})$$

Appendix A: Uncertainty Analyses

Substitution of Eqs. A-18 and A-20 into Eq. A-17, the heat transfer from the environment to the test section is found to be

$$\Delta_q = 6.44 - 0.04T_{sat} \quad W \quad (A-21)$$

Substitution of Eq. A-21 into Eq. A-16 yields

$$\epsilon_q = 0.02q[1 + (\frac{15}{\Delta T_w})^2]^{\frac{1}{2}} - 0.04T_{sat} + 6.44 \quad (A-22)$$

(ii) ϵ_A

The total area of the condensing surface (A) is calculated by

$$A = WL \quad (A-23)$$

where W and L are the width and the entire length of the condensing surface.

From Eq. A-23

$$\epsilon_A = [(\frac{\partial A}{\partial W}\epsilon_w)^2 + (\frac{\partial A}{\partial L}\epsilon_L)^2]^{1/2} \quad (A-24)$$

where

$$\frac{\partial A}{\partial W} = L, \quad \frac{\partial A}{\partial L} = W \quad (A-25)$$

Substitution of Eq. A-25 into Eq. A-24 yields

$$\epsilon_A = [(L\epsilon_w)^2 + (W\epsilon_L)^2]^{1/2} \quad (A-26)$$

Both ϵ_w and ϵ_L are related to the accuracy of machining the condensing surface. By assuming $\epsilon_w = 0.001 W$ and $\epsilon_L = 0.001 L$ and using Eq. A-23, Eq. A-26 becomes

Appendix A: Uncertainty Analyses

$$\epsilon_A = 1.41 \times 10^{-3} \text{A} \quad (\text{A-27})$$

(iii) $\epsilon_{T_{\text{sat}}}$

The uncertainty of the measured saturation temperature of vapor (T_{sat}) results from the accuracies of the pressure gage measuring the vapor pressure in the test section and the barometer measuring the atmospheric pressure. It is estimated that the uncertainty of $\epsilon_{T_{\text{sat}}}$ is

$$\epsilon_{T_{\text{sat}}} = 0.5^\circ\text{C} \quad (\text{A-28})$$

(iv) ϵ_{T_s}

The uncertainty of the measured surface temperature (ϵ_{T_s}) is considered to be a summation of the following factors:

- uncertainty due to thermocouple wire and junction ($\epsilon_{tc} \approx 0.2^\circ\text{C}$);
- uncertainty due to the data acquisition system ($\epsilon_{ac} \approx 0.01^\circ\text{C}$);
- uncertainty in the location of the thermocouple junction inside the condensing surface (ϵ_{cm}).

Hence

$$\epsilon_{T_s} = \epsilon_{tc} + \epsilon_{ac} + \epsilon_{cm} \quad (\text{A-29})$$

The value of ϵ_{cm} is estimated as follows

It is shown in Fig. A.5 that the junction of the thermocouple is 7 mm deep inside the condensing surface. The junction of thermocouple may not coincide with the condensing surface, so that the temperature obtained by the thermocouple (T'_s) is not same as the surface temperature (T_s). The difference between T'_s and T_s is the uncertainty (ϵ_{cm}), which is estimated using one-dimensional heat conduction analysis

$$\epsilon_{em} = \frac{q_t'' \Delta}{k_t} \quad (A-30)$$

where Δ is the distance between the condensing surface and the junction of the thermocouple; k_t is the thermal conductivity of tin (See Fig. A.5); q_t'' is the heat transfer rate from the condensing surface to the junction of the thermocouple.

Substituting $\epsilon = 7$ mm and $k_t = 66.6$ W/m·K into Eq. A-30 yields

$$\epsilon_{em} = 1.05 \times 10^{-5} q_t'' \text{ } ^\circ\text{C}$$

Substitution of the expression for ϵ_{em} , the values of ϵ_{tc} (0.2 $^\circ\text{C}$) and ϵ_{ac} (0.01 $^\circ\text{C}$) into Eq. A-29 yields

$$\epsilon_{T_s} = 0.21 + 1.05 \times 10^{-5} q_t'' \text{ } ^\circ\text{C} \quad (A-31)$$

By substituting Eqs. A-22, A-27, A-28, and A-31 into Eq. A-7, an equation for estimating the uncertainty of \bar{h}_t is derived

$$\epsilon_{\bar{h}_t} = \bar{h}_t \sqrt{[0.02(1 + \frac{15^2}{\Delta T_w^2})^{1/2} + \frac{6.44 - 0.04 T_{sat}}{q}]^2 + \frac{0.5^2 + (0.51 + 1.05 \times 10^{-5} q_t'')^2}{\Delta T^2} + 1.99 \times 10^{-6}} \quad (A-32)$$

The uncertainty increases with decreasing temperature difference of coolant (ΔT_w), and decreasing temperature difference between temperatures of saturated vapor and the condensing surface (ΔT).

Sample Calculations

(1) Run 180 (R-113)

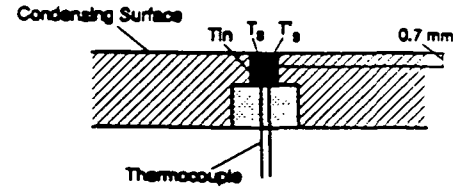


Fig. A.5 Illustration of the surface thermocouple

Appendix A: Uncertainty Analyses

$\bar{h}_t = 188.91 \text{ W/m}^2\cdot\text{k}$, $q = 229.83 \text{ W}$, $T_{sat} = 51 \text{ }^\circ\text{C}$, $\Delta T = 33.83 \text{ }^\circ\text{C}$, and $\Delta T_w = 2.68 \text{ }^\circ\text{C}$. Substituting these values into Eq. (A-33) and assuming $q_t'' = q/A = 6384.17 \text{ W/m}^2$ yields $\epsilon_{\bar{h}_t} = 25.48 \text{ W/m}^2\cdot\text{k}$. Hence

$$\bar{h}_{t(\text{actual})} = 188.91 \pm 25.48 \text{ W / m}^2\cdot\text{ }^\circ\text{C}$$

The percentage uncertainty of the total average heat transfer coefficient in Run 180 is 13.49 %.

(2) Run 360 (FC-72)

$\bar{h}_t = 585.27 \text{ W/m}^2\cdot\text{k}$, $q = 407.75 \text{ W}$, $T_{sat} = 56.66 \text{ }^\circ\text{C}$, $\Delta T = 19.37 \text{ }^\circ\text{C}$, and $\Delta T_w = 2.44 \text{ }^\circ\text{C}$. Substituting these values into Eq. A-32 and assuming $q_t'' = q/A = 11020.2 \text{ W/m}^2$ yields $\epsilon_{\bar{h}_t} = 82.54 \text{ W/m}^2\cdot\text{k}$. Hence

$$\bar{h}_{t(\text{actual})} = 585.27 \pm 82.54 \text{ W / m}^2\cdot\text{ }^\circ\text{C}$$

The percentage uncertainty of the total average heat transfer coefficient in Run 320 is 14.10 %.

A.2. Inlet Vapor Reynolds Number

The inlet vapor Reynolds number (Re_{gL}) is defined as

$$Re_{gL} = \frac{v_{gi} L}{v_g} \quad (\text{A-33})$$

The uncertainty equation associated with Eq. A-33 is expressed as

$$\epsilon_{Re_{gL}} = \left[\left(\frac{\partial Re_{gL}}{\partial v_{gi}} \epsilon_{v_{gi}} \right)^2 + \left(\frac{\partial Re_{gL}}{\partial L} \epsilon_L \right)^2 + \left(\frac{\partial Re_{gL}}{\partial v_g} \epsilon_{v_g} \right)^2 \right]^{1/2}$$

Expansion of the partial derivative terms in the above equation yields

Appendix A: Uncertainty Analyses

$$\epsilon_{Re_{\mu}} = Re_{gL} \left[\left(\frac{\epsilon_{v_g}}{v_{gi}} \right)^2 + \left(\frac{\epsilon_L}{L} \right)^2 + \left(\frac{\epsilon_{v_g}}{v_g} \right)^2 \right]^{1/2} \quad (A-34)$$

where ϵ_{v_g} , ϵ_L , and ϵ_{v_g} are the uncertainties of v_g , L , and v_{gi} .

The value of v_g is considered to be well established (v_g is taken from the thermodynamics property table in the ASHRAE Handbook of Fundamentals). It is assumed that $\epsilon_{v_g} \approx 0$. Also, similar to the consideration in deriving of Eq. A-27, ϵ_L is assumed to 0.001L. Hence Eq. A-34 becomes

$$\epsilon_{Re_{\mu}} = Re_{gL} \left[10^{-6} + \left(\frac{\epsilon_{v_g}}{v_g} \right)^2 \right]^{1/2} \quad (A-35)$$

The vapor velocity (v_{gi}) at the inlet to the test section is calculated by

$$v_{gi} = \frac{\dot{m}_t}{\rho_g W \cdot H} \quad (A-36)$$

The uncertainty equation for v_{gi} is expressed as

$$\epsilon_{v_g} = v_{gi} \left[\left(\frac{\epsilon_{\dot{m}_t}}{\dot{m}_t} \right)^2 + \left(\frac{\epsilon_{\rho_g}}{\rho_g} \right)^2 + \left(\frac{\epsilon_W}{W} \right)^2 + \left(\frac{\epsilon_H}{H} \right)^2 \right]^{1/2} \quad (A-37)$$

where $\epsilon_{\dot{m}_t}$ is the uncertainty in \dot{m}_t due to the inaccuracy of the vapor rotameter measuring \dot{m}_t ; ϵ_H and ϵ_W are the uncertainties of H and W due to the inaccuracy of machining and assembling the vapor duct of the test section; ϵ_{ρ_g} is the uncertainty in determining the value of ρ_g . It is assumed that

$$\epsilon_{\dot{m}_t} = 0.01\dot{m}_t, \quad \epsilon_W = 0.01W, \quad \epsilon_H = 0.01H \quad (A-38)$$

Substitution of Eq. A-38 into Eq. A-37 and considering $\epsilon_{\rho_g} = 0$ (ρ_g is considered to be well established) yields

Appendix A: Uncertainty Analyses

$$\epsilon_{v_g} = 0.0173 v_{gi} \quad (A-39)$$

Substitution Eq. A-39 into Eq. A-35 leads to

$$\epsilon_{Re_g} = 0.0173 Re_{gL} \quad (A-40)$$

The percentage uncertainty of Re_{gi} is 1.73 %.

A.3. Total Average Nusselt Number

The total average Nusselt Number (Nu_t) is defined as

$$Nu_t = \frac{\bar{h}_t L}{k_1} \quad (A-41)$$

Based on the above equation, the uncertainty equation of Nu_t is derived

$$\epsilon_{Nu_t} = \left[\left(\frac{\partial Nu_t}{\partial \bar{h}_t} \epsilon_{\bar{h}_t} \right)^2 + \left(\frac{\partial Nu_t}{\partial L} \epsilon_L \right)^2 + \left(\frac{\partial Nu_t}{\partial k_1} \epsilon_{k_1} \right)^2 \right]^{1/2}$$

Expansion of the partial derivative terms in the above equation using Eq. A-41 yields

$$\epsilon_{Nu_t} = Nu_t \left[\left(\frac{\epsilon_{\bar{h}_t}}{\bar{h}_t} \right)^2 + \left(\frac{\epsilon_L}{L} \right)^2 + \left(\frac{\epsilon_{k_1}}{k_1} \right)^2 \right]^{1/2} \quad (A-42)$$

Assuming $\epsilon_L = 0.001L$ (uncertainty of L) and $\epsilon_{k_1} = 0$ (uncertainty of k_1), Eq. (A-42) becomes

$$\epsilon_{Nu_t} = Nu_t \left[\left(\frac{\epsilon_{\bar{h}_t}}{\bar{h}_t} \right)^2 + 10^{-6} \right]^{1/2} \quad (A-43)$$

Sample Calculations

(1) Run 180 (R-113)

$$Nu_t = 2428.78; \bar{h}_t = 188.91 \text{ W/m}^2\cdot^\circ\text{C}; \epsilon_{\bar{h}_t} = 25.48 \text{ W/m}^2\cdot^\circ\text{C} \text{ (See page A-11).}$$

Substituting these values into Eq. A-43 yields $\epsilon_{Nu_t} = 327.64$. Hence

$$Nu_t = 2428.78 \pm 327.64$$

The percentage uncertainty of Nu_t in run 180 is 13.49 %.

(2) Run 360 (FC-72)

$$Nu_t = 9606.34; \bar{h}_t = 585.27 \text{ W/m}^2\cdot^\circ\text{C}; \epsilon_{\bar{h}_t} = 85.54 \text{ W/m}^2\cdot^\circ\text{C} \text{ (See page A-11).}$$

Substituting these values into Eq. A-43 yields $\epsilon_{Nu_t} = 1354.81$. Hence

$$Nu_t = 9606.34 \pm 1354.81$$

The percentage uncertainty of Nu_t in run 360 is 14.10 %.

A.4. Total Average Stanton Number

The total average stanton Number (St_t) is defined as

$$St_t = \frac{\bar{h}_t}{\rho_l C_{pl} v_{gi}}, \quad \text{or} \quad St_t = \frac{Nu_t}{Re_{gL} Pr_t} \quad (\text{A-44})$$

Based on the above equation, the uncertainty equation of St_t is derived

$$\epsilon_{St_t} = \left[\left(\frac{\partial St_t}{\partial Nu_t} \epsilon_{Nu_t} \right)^2 + \left(\frac{\partial St_t}{\partial Re_{gL}} \epsilon_{Re_{gL}} \right)^2 + \left(\frac{\partial St_t}{\partial Pr_t} \epsilon_{Pr_t} \right)^2 \right]^{1/2}$$

Expanding the partial derivative terms in the above equation using Eq. A-44

Appendix A: Uncertainty Analyses

$$\epsilon_{St_i} = St_i \left[\left(\frac{\epsilon_{Nu_i}}{Nu_i} \right)^2 + \left(\frac{\epsilon_{Re_{gl}}}{Re_{gl}} \right)^2 + \left(\frac{\epsilon_{Pr_i}}{Pr_i} \right)^2 \right]^{1/2} \quad (A-45)$$

where ϵ_{Pr_i} is the uncertainty of Pr_i . Assuming $\epsilon_{Pr_i} = 0$ and using Eq. A-40, Eq. A-45 becomes

$$\epsilon_{St_i} = St_i \left[\left(\frac{\epsilon_{Nu_i}}{Nu_i} \right)^2 + 2.99 \times 10^{-4} \right]^{1/2} \quad (A-46)$$

Sample Calculations

(1) Run 180 (R-113)

$St_i = 2.53 \times 10^{-4}$; $Nu_i = 2428.78$; $\epsilon_{Nu_i} = 327.64$ (See page A.14). Substituting these values into Eq. A-45 yields $\epsilon_{St_i} = 0.344 \times 10^{-4}$. Hence

$$St_i = 2.54 \times 10^{-4} \pm 0.344 \times 10^{-4}$$

The percentage uncertainty of St_i in run 180 is 13.60 %.

(2) Run 360 (FC-72)

$St_i = 1.32 \times 10^{-4}$; $Nu_i = 9606.34$; $\epsilon_{Nu_i} = 1354.81$ (See page A.14). Substituting these values into Eq. A-45 yields $\epsilon_{St_i} = 1.32 \times 10^{-4}$. Hence

$$St_i = 1.34 \times 10^{-4} \pm 0.188 \times 10^{-4}$$

The percentage uncertainty of St_i in run 320 is 14.21 %.

APPENDIX B

TEST OF CONVERGING UNIT

The purpose of the converging unit was to obtain a uniform velocity at the inlet of the test section. A deflector was installed inside the unit (Fig. 4.6). The deflector was selected among eight deflectors of different shapes.

The converging unit was tested with air as the working fluid. The air passed through the converging unit assembled with a deflector and packed with thin glass tubes. The air velocity was measured at 40 equally spaced locations at the outlet of the unit using an air velocity meter. The average deviation of the local velocities was evaluated for each testing deflector. The deflector corresponding to the lowest average deviation ($\pm 9.1\%$) was selected to be used in the experiment.

A schematic of this selected deflector is shown in Fig. B.1. The profile of the measured air velocity at the outlet of the converging unit is given in Fig. B.2, where each grid joint indicates each measured local velocity. It is seen that the velocity

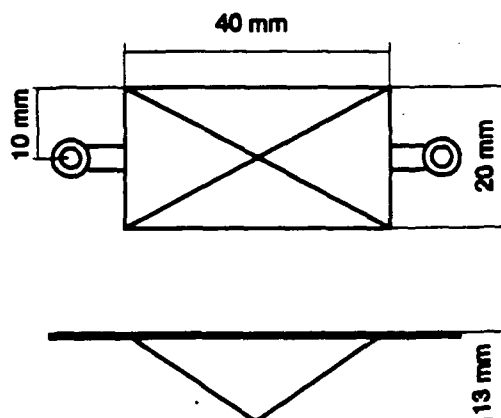


Fig. B.1 Schematic of the selected deflector

Appendix B: Test of Converging Section

profile is basically uniform except that at the two sides of the unit, the velocity is a little lower. The maximum difference between the local velocity and the average velocity is -23.0 %. The average difference is ± 9.1 %.

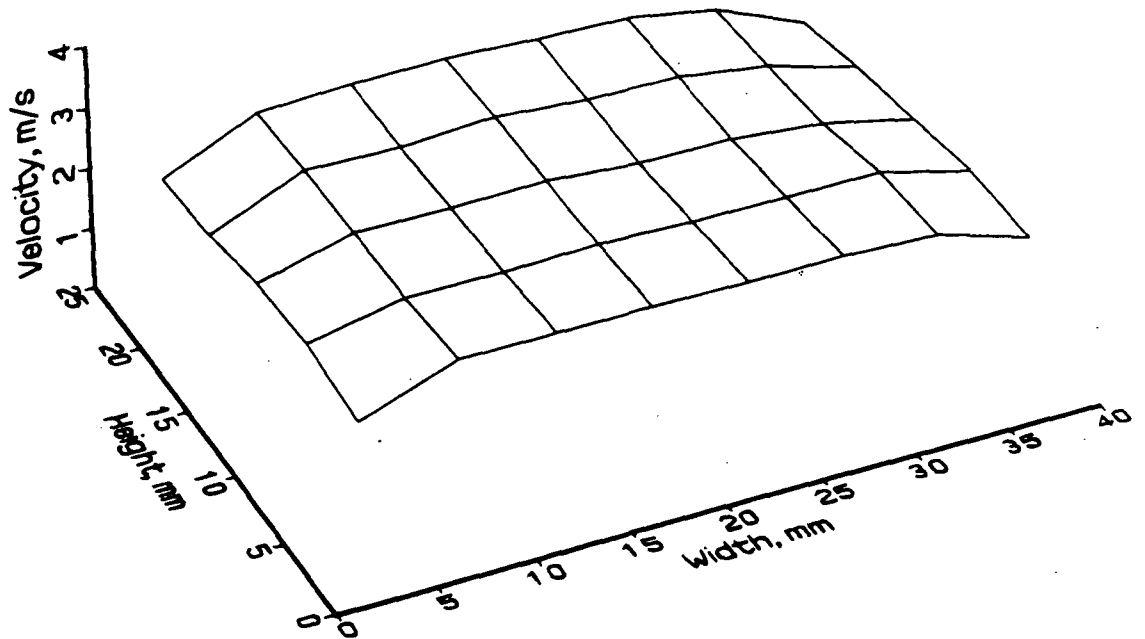


Fig. B.2 Air velocity profile at the outlet of the converging unit

APPENDIX C

CALIBRATION OF FLOW METERS

Vapor rotameter, venturimeters, and coolant flow meters were calibrated. The following describes the calibration and the calibration results.

Vapor Rotameter

The vapor rotameter was used to measure the inlet vapor flow rate to the test section of condensation. It was specially calibrated for use with R-113 by the manufacturer. It was also calibrated in the laboratory.

Fig. C.1 illustrates the system for the calibration of the rotameter. This system included the rotameter, a calibrated laminar flow meter, and two regulating valves, with air as the calibrating fluid. The rotameter was calibrated using air flow. The results of the present calibration (V_{lab}) were compared with the calibration data provided by the manufacture (V_{fac}) and are shown in Fig. C.2. The values presented in the figure are based on one of the experimental conditions with $T_{sat} = 55\text{ }^{\circ}\text{C}$, $P_{sat} = 1.14\text{ bar}$, and using R-113 as the condensing fluid. The maximum difference between the two different calibrations was $\pm 2.6\%$. The results of the calibration is given in Table C.1. In the table, the scale indicates the reading on the gage glass of the rotameter; the symbol SCMM means cubic meter of air per minute at the standard condition (the air pressure and temperature at 1 atm and $20\text{ }^{\circ}\text{C}$ respectively). Having the flow rate of air at the

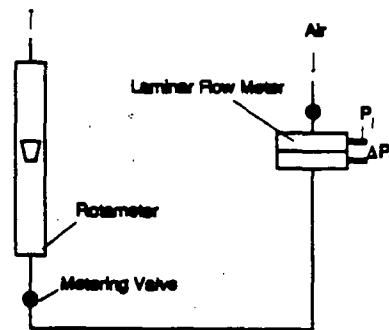


Fig. C.1 Rotameter calibration

Appendix C: Calibration of Flow Meters

standard condition, the flow rate of vapor in experiment was determined by

$$V_{\text{vap}} = V_{\text{air}} \sqrt{\frac{\rho_{\text{air}}}{\rho_{\text{vap}}}} \quad (\text{C-1})$$

where

V_{air} — volumetric flow rate of air at the standard condition, m^3/s

V_{vap} — volumetric flow rate of vapor in experiment, m^3/s

ρ_{air} — density of air at the standard conditions, kg/m^3

ρ_{vap} — density of vapor in experiment, kg/m^3

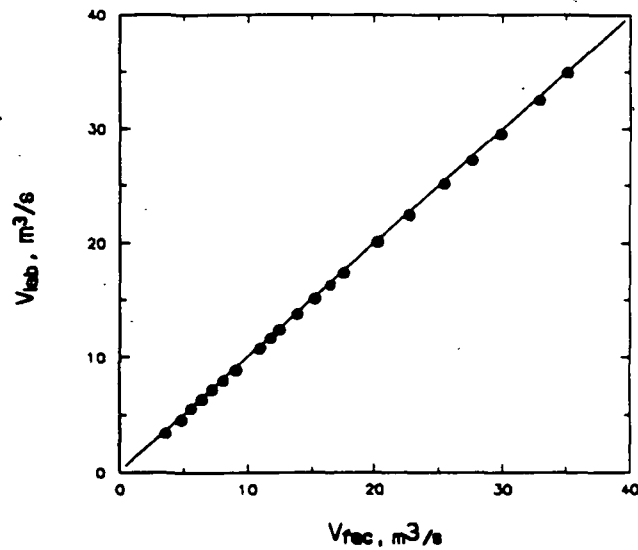


Fig. C.2 Comparison between the laboratory calibration results of the vapor rotameter and the manufacturer data

Appendix C: Calibration of Flow Meters

Table C.1 Calibration data of vapor rotameter

Vapor Rotameter			
Scale	SCMM ² ×10 ³	Scale	SCMM ² ×10 ³
3.54	3.36	15.22	64.60
4.80	6.00	16.50	75.09
5.55	8.79	17.58	85.44
6.40	11.51	20.25	114.50
7.20	14.65	22.75	142.31
8.10	18.22	25.45	175.57
9.10	22.36	27.60	209.19
10.93	32.89	29.85	245.55
12.45	43.23	32.90	297.76
13.85	53.68	35.10	344.01

Venturimeters

Venturimeters were used to measure the inlet and the outlet vapor flow rates of the test section in the condensation experiment and the air flow rate in the air-liquid flow experiment. All the venturimeters were made of brass and were calibrated using the laminar flow meter and air in the same calibration system as used for the rotameter

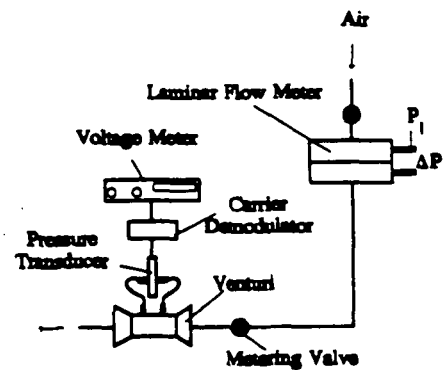


Fig. C.3 Venturimeter calibration

(Fig. C.3). During the calibrations, the pressure drop across the venturimeter was measured with a diaphragm type pressure transducer. The pressure drop was then transformed into a voltage output via a carrier demodulator. The pressure transducers for the venturimeters were calibrated by Christodoulou (1987). It was shown in his

Appendix C: Calibration of Flow Meters

results that the measured pressure drop was linear with the output voltage.

The calibration of the venturimeters was repeated several times. It was found that the results were quite repeatable (Fig. C.4). The results of the calibration of the venturimeters are listed in Table C.2, where venturi#1 and venturi#2 were those used for measuring the inlet and outlet vapor flow rate respectively, and venturi(air) was used for measuring the air flow rate in the air-liquid experiment.

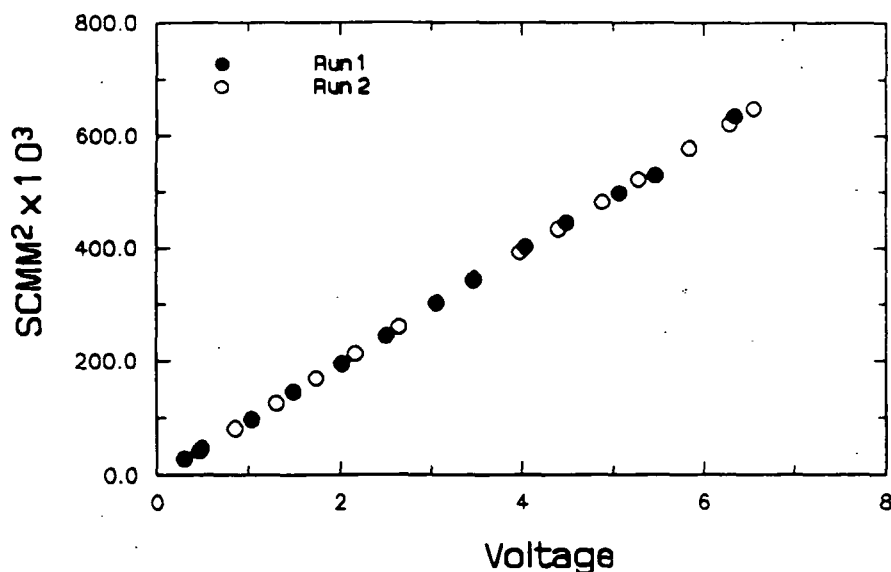


Fig. C.4 Repeatability of the calibration of venturimeter

Coolant Flow Meters

Four rotameters were used to measure the coolant flow rate. All the rotameters were calibrated using water and measuring the time taken for a certain amount of water to be collected. The results of the calibration are given in Table C.3.

Appendix C: Calibration of Flow Meters

Table C.2 Calibration data of venturimeters

Venturi#1		Venturi#2		Venturi(air)	
Vol.	SCMM ² ×10 ³	Vol.	SCMM ² ×10 ³	Vol.	SCMM ² ×10 ³
0.29	28.06	0.33	14.78	0.10	1.26
0.48	46.65	0.96	42.55	0.47	4.67
1.03	97.95	1.42	64.49	1.27	12.12
1.49	146.44	2.06	95.87	1.75	15.68
2.02	195.66	2.76	125.66	2.46	21.93
2.50	244.29	3.48	161.87	3.78	34.21
3.05	300.87	4.20	194.14	5.87	49.54
3.48	344.96	4.88	226.90	7.27	60.91
4.04	402.28	5.18	243.46	9.10	76.51
5.06	497.93	5.70	264.78	—	—
6.34	634.32	6.05	285.23	—	—

Appendix C: Calibration of Flow Meters

Table C.3 Calibration data of coolant rotameters (unit in kg/s)

Scale	No.1	No.2	No.3	No.4
10	0.0013	0.0013	0.0011	—
20	0.0034	0.0034	0.0032	0.0006
30	0.0059	0.0062	0.0061	0.0015
40	0.0080	0.0082	0.0074	0.0020
50	0.0102	0.0109	0.0100	0.0026
60	0.0122	0.0123	0.0115	0.0033
70	0.0143	0.0145	0.0140	0.0039
80	0.0169	0.0168	0.0163	0.0046
90	0.0188	0.0190	0.0185	0.0052
100	0.0212	0.0212	0.0209	0.0058
110	0.0234	0.0237	0.0228	0.0063
120	0.0258	0.0261	0.0251	0.0070
130	0.0279	0.0282	0.0274	0.0076
140	0.0304	0.0302	0.0301	0.0083
150	0.0318	0.0321	0.0316	0.0088

APPENDIX D

CALIBRATION OF THERMOCOUPLES

The thermocouples for measuring the vapor (condensate) temperature and the differential thermocouples for measuring the coolant temperature change in the cooling sections were calibrated in the laboratory.

Vapor and Condensate Thermocouple

Fig. D.1 shows the calibration system. The thermocouples were connected to the data acquisition system (also used in the condensation experiment); the measuring junction of the thermocouple was placed inside an insulated bath along with a high accuracy thermometer. The thermocouple was calibrated at three different temperatures: 1) ice-water; 2) room; 3) boiling water. The temperatures measured by the thermometer and the thermocouple (through the data acquisition system) were compared with each other. Table D.1 lists two typical calibration results.

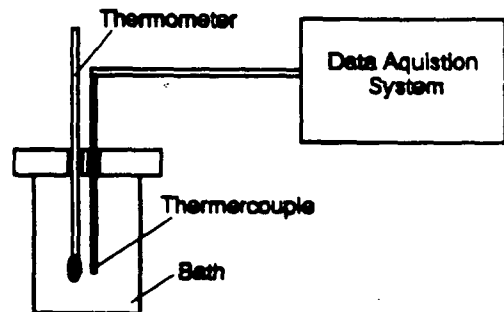


Fig. D.1 Thermocouple calibration

Differential Thermocouples

The calibration system for the differential thermocouples is shown in Fig. D.2. The junctions of one differential thermocouple were placed inside two baths with different temperatures. The voltage generated by the differential thermocouple (Vol_{th})

Appendix D: Calibration of Thermocouples

Table D.1 Sample results of the thermocouple calibrations

Condensate (°C)		Boiler (°C)	
Thermometer	Thermocouple	Thermometer	Thermocouple
0.19	0.20	0.12	0.13
22.62	22.48	23.63	23.89
94.87	94.91	93.67	93.60

was measured by a micro-voltmeter.

The difference (ΔT_1) of the temperatures in the two baths was measured by two thermometers was compared with the temperature difference (ΔT_2) determined by

$$\Delta T_2 = \frac{Vol_{th}}{0.039}$$

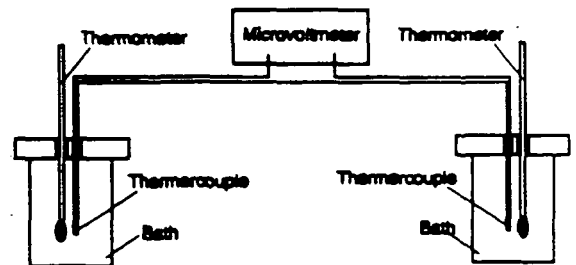


Fig. D.2 Differential thermocouple calibration

where 0.039 is the gradient of the linear curve of temperature-voltage for type T thermocouple with temperature ranging from 0 - 20 °C (See the general thermocouple table). The results of the comparison between ΔT_1 and ΔT_2 for three differential thermocouples are given in Table D.2, where S denotes the average deviation and the term — chamber means the coolant mixing chamber (See Fig. 4.17). As seen in Table D.2, the maximum average deviation is less than ± 4 %.

Appendix D: Calibration of Thermocouples

Table D.2 Results of calibration of differential thermocouples

Chamber 1-2 (°C)		Chamber 2-3 (°C)		Chamber 3-4 (°C)	
ΔT_1	ΔT_2	ΔT_1	ΔT_2	ΔT_1	ΔT_2
0.83	0.82	0.35	0.37	0.90	0.92
1.17	1.15	1.10	1.16	1.29	1.24
2.00	2.17	1.69	1.72	1.42	1.35
3.06	3.14	2.60	2.65	2.23	2.27
4.04	4.08	2.71	2.75	2.74	2.78
4.95	4.99	3.08	3.07	3.67	3.79
6.01	6.30	3.43	3.54	6.70	6.77
6.37	6.25	3.63	3.65	8.75	8.95
8.34	8.40	4.19	4.30	9.42	9.70
21.30	22.50	4.84	5.03	21.19	21.80
S:	3.8 %	S:	3.2 %	S:	2.9%

APPENDIX E

CALIBRATION OF THE ULTRASONIC TRANSDUCER

The ultrasonic transducer was calibrated prior to its use in the experiment. The calibration device consisted of a pointer attached to a micrometer traversing arrangement mounted on a small container (Fig. E.1). The transducer was placed underneath an aluminum plug inserted into the bottom copper plate of the container. The depth of the fluid in the container was determined by moving the pointer connected to the micrometer to the surface of the liquid. The time for the ultrasonic signal to pass through the liquid film was measured with an oscilloscope. Knowing the time and the thickness of the liquid film, the sonic velocity in the fluid was determined. The arithmetic average (which was within ± 0.8 % of the measured values for R-113 and within ± 1.3 % for FC-72) was taken as the sonic velocity at the measured temperature. The sonic velocity is function of the density of the fluid, which is temperature dependent. Reid and Sherwood (1958) suggested that the sonic velocity in a liquid be expressed as

$$a = c_m \rho_l^3 \quad (E-1)$$

where the constant c_m was obtained from the measured velocities. Table E.1 shows the sonic velocities computed by Eq. E-1 and the comparison with the values reported

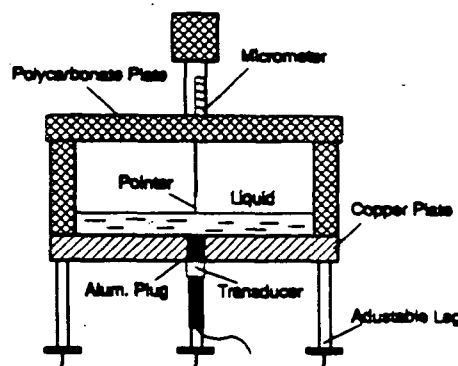
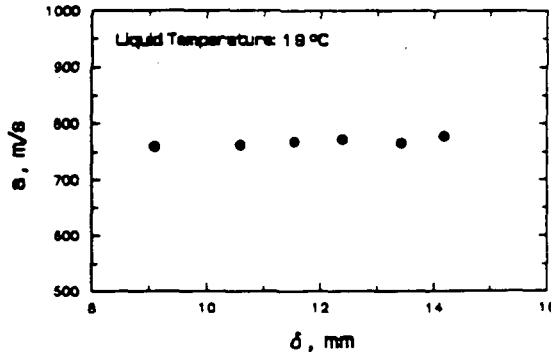


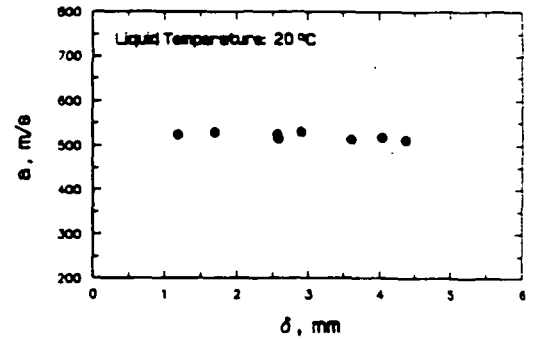
Fig. E.1 Schematic of calibration device of ultrasonic transducer

Appendix E: Calibration of the Ultrasonic Transducer

by Meyer (1969) for R-113 and by the 3M company (1989) for FC-72. The values of c_m in Eq. E-1 determined from the calibration is $1.97 \times 10^{-7} \text{ m}^{10}/\text{kg}^3 \text{ s}$ for R-113 and $1.08 \times 10^{-7} \text{ m}^{10}/\text{kg}^3 \text{ s}$ for FC-72.



a. R-113



b. FC-72

Fig. E.2 Sonic velocities of condensing liquids (R-113 and FC-72)

Table E.1 Comparison of measured and reported sonic velocities

R-113				FC-72			
Temp.	Meyer	Calib.	Diff.	Temp.	3M	Calib.	Diff.
°C	m/s	m/s	%	°C	m/s	m/s	%
20.1	714.5	767.1	6.9	10	555.0	548.02	1.3
14.9	732.4	784.8	6.7	20	527.5	521.5	1.2
10.2	748.2	801.0	6.6	30	498.0	501.0	0.6

APPENDIX F

COMPARISON BETWEEN EQ. 4-6 AND EQ.4-7

In Chapter 4, two equations (Eqs. 4-6 and 4-7) are introduced to calculate the condensate film thickness. Eq. 4-6 is expressed as

$$\delta_1 = \frac{2c_m(1+\beta)^2(1+\alpha T_s)^3\rho_o^3}{2+\beta}t_f$$

where

$$\beta = \frac{\alpha\Delta T}{1+\alpha T_s}$$

Eq. 4-7 is expressed as

$$\delta_2 = c_m\bar{\rho}_l^3t_f$$

The ratio of the values of δ given from these two different equations is

$$\frac{\delta_1}{\delta_2} = \frac{2(1+\beta)^2(1+\alpha T_s)^3\rho_o^3}{(2+\beta)\bar{\rho}_l^3} \quad (F-1)$$

Assuming that the equation for the mean liquid density ($\bar{\rho}_l$) is

$$\bar{\rho}_l = \rho_o(1 + \alpha T_{ref}) \quad (F-2)$$

where

$$T_{ref} = \frac{T_s + T_{sat}}{2}$$

Substitution of Eq. F-2 into F-1 yields

Appendix F: Comparison between Eq. 4-6 and Eq. 4-7

$$\frac{\delta_1}{\delta_2} = \frac{2(1+\beta)^2}{2+\beta} \left(\frac{1+\alpha T_s}{1+\alpha T_{ref}} \right)^3 \quad (F-3)$$

Sample Calculations

(1) condensing liquid: R-113; $T_s = 7^\circ\text{C}$; $T_{sat} = 47^\circ\text{C}$; ($\Delta T = 40^\circ\text{C}$ and $T_{ref} = 27^\circ\text{C}$);

$$\rho_l = 1619.48(1-1.45 \times 10^{-3}) \quad (\rho_o = 1619.48 \text{ and } \alpha = -1.45 \times 10^{-3})$$

$$\beta = \frac{-1.45 \times 10^{-3} \times (47-7)}{1-1.45 \times 10^{-3} \times 7} = -0.058$$

$$\frac{\delta_1}{\delta_2} = \frac{2(1-0.058)^2}{2-0.058} \left(\frac{1-1.45 \times 10^{-3} \times 7}{1-1.45 \times 10^{-3} \times 27} \right)^3 = 0.999$$

$$\frac{\delta_1}{\delta_2} = \left| 1 - \frac{\delta_2}{\delta_1} \right| = \left| 1 - \frac{1}{0.999} \right| = \pm 0.1 \%$$

(2) condensing liquid: FC-72; $T_s = 27^\circ\text{C}$; $T_{sat} = 57^\circ\text{C}$; ($\Delta T = 30^\circ\text{C}$ and $T_{ref} = 42^\circ\text{C}$);

$$\rho_l = 1737.86(1-1.26 \times 10^{-3}) \quad (\rho_o = 1737.86 \text{ and } \alpha = -1.26 \times 10^{-3})$$

$$\beta = \frac{-1.26 \times 10^{-3} \times (57-27)}{1-1.26 \times 10^{-3} \times 27} = -0.039$$

$$\frac{\delta_1}{\delta_2} = \frac{2(1-0.039)^2}{2-0.039} \left(\frac{1-1.26 \times 10^{-3} \times 27}{1-1.26 \times 10^{-3} \times 42} \right)^3 = 0.999$$

$$\frac{\delta_1}{\delta_2} = \left| 1 - \frac{\delta_2}{\delta_1} \right| = \left| 1 - \frac{1}{0.999} \right| = \pm 0.1 \%$$

The above two examples show that the difference between the value of film thickness evaluated from Eq. 4-6 and that from Eq. 4-7 is less than $\pm 0.1 \%$.

APPENDIX G

EXPERIMENTAL DATA

Table G.1 Heat transfer coefficients

Run#	Fluid	v_g m/s	$\dot{m}_c \times 10^3$ kg/s	$\dot{m}_h \times 10^3$ kg/s	T_{sat} °C	ΔT °C	q w	\bar{h}_1 w/m ² ·°C	\bar{h}_2 w/m ² ·°C	\bar{h}_i w/m ² ·°C
179	R-113	0.53	4.11	1.74	49.32	39.25	277.02	228.80	208.57	196.28
176	R-113	0.57	4.27	1.72	48.00	38.68	274.97	235.63	216.55	197.68
201	R-113	0.68	5.22	1.81	48.91	39.79	274.70	230.78	202.13	192.00
239	R-113	0.79	5.92	1.66	48.18	39.10	260.97	210.29	203.16	185.61
225	R-113	0.74	5.45	1.78	47.24	38.71	262.81	231.89	202.41	188.79
178	R-113	0.85	6.51	1.85	48.87	39.53	290.84	257.58	223.68	204.61
183	R-113	0.86	6.38	1.71	47.50	38.36	264.45	244.43	211.90	191.69
195	R-113	0.99	7.42	1.83	47.82	38.28	288.00	270.01	224.16	209.23
172	R-113	1.01	7.53	1.81	47.71	39.45	293.29	255.24	232.20	206.73
177	R-113	1.15	8.65	1.92	47.99	38.48	311.44	297.64	249.92	225.05
223	R-113	1.25	9.51	1.89	48.10	37.03	289.43	289.19	237.55	217.38
273	R-113	1.27	9.40	1.84	47.60	39.60	279.88	246.81	218.32	196.52

Table G.1 Heat transfer coefficients (continued)

Run#	Fluid	v_f m/s	$\dot{m}_c \times 10^3$ kg/s	$\dot{m}_h \times 10^3$ kg/s	T_{sat} °C	ΔT °C	q w	\bar{h}_1 $w/m^2 \cdot ^\circ C$	\bar{h}_2 $w/m^2 \cdot ^\circ C$	h_i $w/m^2 \cdot ^\circ C$
280	R-113	1.27	9.75	2.05	48.53	41.04	306.33	260.81	227.22	207.56
213	R-113	1.28	9.86	2.02	48.63	39.73	307.45	282.87	224.97	215.20
194	R-113	1.40	10.94	2.14	49.41	40.47	336.42	298.33	240.51	231.19
192	R-113	1.49	11.88	2.20	50.06	40.32	350.97	315.30	262.01	242.07
187	R-113	1.50	11.72	2.21	49.37	39.51	343.18	310.44	263.16	241.55
175	R-113	1.52	11.51	2.09	48.20	37.98	331.12	312.22	269.79	242.46
189	R-113	1.66	12.25	2.25	47.51	38.18	353.93	339.56	279.93	257.81
190	R-113	1.69	12.84	2.29	48.43	40.11	366.47	334.37	274.24	254.09
205	R-113	1.72	13.22	2.37	48.74	39.82	369.03	342.93	280.86	257.73
283	R-113	1.89	14.10	2.61	47.52	38.19	400.23	397.24	322.32	291.42
281	R-113	2.09	15.92	3.37	48.13	38.76	486.37	469.50	387.51	348.92
277	R-113	2.30	17.35	3.23	48.31	36.82	476.37	474.01	396.31	359.74
282	R-113	2.37	17.87	3.82	47.88	37.16	551.41	529.93	452.25	412.67
236	R-113	2.46	17.78	3.29	46.99	35.25	493.56	511.35	431.10	389.35
275	R-113	2.74	21.00	4.06	48.76	36.51	603.27	569.06	501.39	459.54
242	R-113	2.80	21.66	4.79	48.76	37.79	648.36	597.53	519.43	477.10
243	R-113	3.40	27.57	5.69	50.49	35.43	830.27	783.05	700.06	651.71
220	R-113	0.34	2.58	1.35	48.58	31.21	207.18	220.60	196.82	184.61

Table G.1 Heat transfer coefficients (continued)

Run#	Fluid	v_e m/s	$\dot{m}_p \times 10^3$ kg/s	$\dot{m}_c \times 10^3$ kg/s	T_{in} °C	ΔT °C	q w	\bar{h}_1 w/m ² ·°C	\bar{h}_2 w/m ² ·°C	h_i w/m ² ·°C
180	R-113	0.50	4.17	1.60	51.00	33.83	229.83	218.72	203.52	188.91
202	R-113	0.64	5.32	1.50	51.30	32.19	220.62	235.69	200.83	190.57
226	R-113	0.72	5.44	1.53	48.17	31.28	220.91	237.19	208.64	196.40
184	R-113	0.82	6.18	1.48	48.33	30.70	237.19	268.24	224.38	214.84
207	R-113	0.84	6.60	1.52	49.14	31.62	232.01	258.79	217.37	204.04
210	R-113	1.08	8.39	1.71	49.20	32.24	250.83	282.84	232.72	216.33
196	R-113	1.03	7.71	1.61	48.07	30.55	224.57	270.06	220.00	204.42
214	R-113	1.25	9.74	1.73	49.02	31.25	244.97	286.54	236.12	218.01
274	R-113	1.27	9.73	1.59	48.71	31.48	241.03	255.79	231.27	212.91
284	R-113	1.32	9.94	1.74	47.98	31.54	263.75	290.05	256.52	232.52
228	R-113	1.44	11.08	1.81	48.50	31.10	255.70	306.36	250.89	228.63
193	R-113	1.49	11.99	1.77	50.30	31.04	272.97	323.57	265.52	244.52
285	R-113	1.49	11.31	1.80	48.43	31.34	262.76	296.52	255.90	233.18
191	R-113	1.59	12.34	1.86	49.17	31.69	294.19	329.37	272.21	258.19
206	R-113	1.73	13.21	1.93	48.74	30.95	286.46	338.20	276.59	257.44
246	R-113	1.98	14.39	2.18	47.24	31.17	288.33	368.17	286.32	257.21
247	R-113	2.20	16.11	2.48	47.40	30.25	341.89	442.19	346.95	314.28
237	R-113	2.41	17.62	2.71	47.31	29.86	409.81	496.57	416.80	381.62

Table G.1 Heat transfer coefficients (continued)

Run#	Fluid	v_f m/s	$\dot{m}_f \times 10^3$ kg/s	$\dot{m}_g \times 10^3$ kg/s	T_{in} °C	ΔT °C	q w	\bar{h}_1 $w/m^2 \cdot ^\circ C$	\bar{h}_2 $w/m^2 \cdot ^\circ C$	h_i $w/m^2 \cdot ^\circ C$
276	R-113	2.70	20.53	3.54	48.51	31.76	510.03	548.77	481.42	446.58
233	R-113	2.82	22.83	4.11	50.48	32.96	594.53	605.52	539.68	501.64
240	R-113	2.82	22.47	3.98	50.00	32.47	574.83	581.21	511.59	492.24
291	R-113	3.12	23.09	4.08	47.58	30.51	573.59	642.17	563.97	522.81
257	R-113	3.24	24.64	4.13	48.64	30.23	599.12	685.88	583.85	551.13
254	R-113	3.48	25.73	4.18	47.74	28.82	609.27	725.69	622.79	587.80
230	R-113	3.64	27.94	4.27	49.11	28.72	639.12	762.00	676.88	618.92
241	R-113	3.74	29.16	4.94	49.36	30.94	722.91	762.58	667.69	649.70
234	R-113	3.92	28.65	4.36	47.41	29.18	689.57	785.63	707.75	657.27
293	R-113	4.10	30.07	4.73	47.37	28.01	669.84	799.13	707.89	664.98
292	R-113	4.21	30.90	5.01	47.48	28.79	713.57	842.17	735.20	689.35
231	R-113	4.35	31.31	5.09	46.99	30.33	790.78	883.89	783.21	725.08
221	R-113	0.31	2.45	1.02	49.47	21.42	146.46	234.64	203.78	190.18
181	R-113	0.50	3.99	1.10	50.19	21.37	160.87	257.12	227.47	209.36
203	R-113	0.71	5.29	1.07	47.82	20.11	157.78	285.69	235.06	218.14
185	R-113	0.84	6.34	1.09	48.10	20.46	157.98	279.48	225.58	214.78
208	R-113	0.86	6.82	1.19	49.53	22.28	171.79	278.14	232.15	214.40
126	R-113	0.94	7.16	0.97	48.57	18.48	143.43	249.32	220.17	215.81

Table G.1 Heat transfer coefficients (continued)

Run#	Fluid	v_f m/s	$\dot{m}_f \times 10^3$ kg/s	$\dot{m}_c \times 10^3$ kg/s	T_w °C	ΔT °C	q w	\bar{h}_1 w/m ² ·°C	\bar{h}_2 w/m ² ·°C	h_i w/m ² ·°C
211	R-113	1.12	8.43	1.26	48.30	21.20	186.40	318.29	262.03	244.53
62	R-113	1.15	9.50	1.00	51.07	19.96	164.65	269.37	247.37	229.44
127	R-113	1.20	8.94	1.02	47.54	18.15	161.49	300.17	255.95	247.43
125	R-113	1.20	9.51	1.23	49.78	20.70	181.55	299.58	256.39	243.92
215	R-113	1.28	9.76	1.28	48.39	21.65	178.21	315.38	248.41	228.93
286	R-113	1.39	10.57	1.24	48.18	20.60	171.61	299.50	252.82	231.63
229	R-113	1.44	11.26	1.35	49.20	22.08	200.16	334.36	275.82	252.11
217	R-113	1.48	11.33	1.43	48.80	21.61	207.53	355.07	290.08	267.05
218	R-113	1.74	13.68	1.44	49.58	21.21	224.36	375.10	314.29	294.16
142	R-113	1.74	12.80	1.30	47.19	20.72	205.79	350.84	295.29	276.24
134	R-113	1.77	13.28	1.37	47.86	22.83	224.00	351.04	292.75	272.81
136	R-113	1.78	13.21	1.18	47.45	18.25	188.09	371.10	310.80	286.59
128	R-113	1.90	14.30	1.37	48.27	19.23	204.50	374.68	314.59	295.76
248	R-113	2.15	15.92	1.72	47.76	20.09	243.06	453.60	366.18	336.42
262	R-113	2.69	19.79	2.36	47.37	20.75	325.39	555.20	458.73	436.04
263	R-113	2.82	21.02	2.45	47.99	21.19	334.05	552.71	461.68	438.47
256	R-113	3.14	24.18	2.84	49.02	22.14	441.43	669.93	555.03	554.48
287	R-113	3.13	23.76	2.91	48.53	21.39	409.53	675.01	575.62	532.41

Table G.1 Heat transfer coefficients (continued)

Run#	Fluid	v_f m/s	$\dot{m}_f \times 10^3$ kg/s	$\dot{m}_c \times 10^3$ kg/s	T_{in} °C	ΔT °C	q w	\bar{h}_1 w/m ² ·°C	\bar{h}_2 w/m ² ·°C	h_i w/m ² ·°C
255	R-113	3.42	25.63	3.16	48.20	22.76	466.79	698.53	574.89	570.39
245	R-113	3.74	30.73	3.16	50.90	19.28	442.34	754.52	644.63	638.00
235	R-113	3.86	28.59	3.16	47.83	22.19	491.95	755.71	648.15	616.44
294	R-113	4.06	30.10	3.56	47.79	21.18	484.03	790.12	672.99	635.52
288	R-113	4.34	32.00	3.43	47.52	19.97	486.43	858.82	729.68	677.48
269	R-113	1.15	7.88	0.69	47.99	10.64	102.11	302.72	281.33	266.86
268	R-113	1.40	10.06	0.69	47.16	9.97	104.28	339.95	303.32	290.83
290	R-113	1.56	12.02	0.95	49.07	12.02	126.70	353.77	311.45	293.14
279	R-113	1.59	11.78	0.82	47.86	10.75	107.84	349.84	303.95	278.91
267	R-113	1.85	13.74	0.89	47.89	11.17	127.87	396.75	336.58	318.48
249	R-113	2.16	16.01	1.09	47.92	11.62	160.27	490.71	407.26	383.55
266	R-113	2.19	16.30	1.10	47.94	11.51	156.35	468.09	395.84	377.78
265	R-113	2.39	17.96	1.27	48.29	11.52	173.48	529.74	445.43	418.84
289	R-113	2.69	20.75	1.51	48.97	12.09	205.19	621.56	511.06	471.81
264	R-113	2.95	21.37	1.34	47.16	10.22	196.62	674.08	566.85	534.79
258	R-113	3.13	24.39	1.56	49.38	11.36	217.04	675.24	552.80	531.54
259	R-113	3.39	25.81	1.71	48.64	12.03	251.11	728.89	604.15	580.39
272	R-113	3.71	27.24	1.74	47.58	10.83	241.74	782.57	646.38	620.58

Table G.1 Heat transfer coefficients (continued)

Run#	Fluid	v_g m/s	$\dot{m}_p \times 10^3$ kg/s	$\dot{m}_c \times 10^3$ kg/s	T_{sat} °C	ΔT °C	q w	\bar{h}_1 w/m ² ·°C	\bar{h}_2 w/m ² ·°C	h_i w/m ² ·°C
295	R-113	3.91	29.33	2.00	48.20	11.71	261.12	790.56	655.92	620.28
271	R-113	4.17	30.07	1.63	46.95	10.26	242.18	829.01	687.29	656.33
250	R-113	4.39	31.76	1.83	47.09	10.71	270.53	838.28	725.49	702.64
103	R-113	0.58	4.40	0.66	48.64	13.46	102.18	256.86	264.60	211.10
104	R-113	1.06	7.80	0.80	47.48	13.29	122.26	359.61	323.17	255.87
108	R-113	1.05	7.66	0.73	47.30	12.93	108.38	313.29	255.01	233.06
91	R-113	1.32	9.88	0.88	48.11	12.31	130.77	375.41	333.05	295.33
182	R-113	0.51	4.37	0.83	52.53	14.15	112.43	287.57	241.15	220.96
100	R-113	0.42	3.19	0.67	49.01	14.76	109.09	236.87	227.53	205.50
93	R-113	0.64	5.07	0.77	50.08	15.84	125.29	213.38	237.48	219.96
90	R-113	0.65	5.24	0.75	50.38	14.65	114.47	207.70	231.95	217.26
101	R-113	0.71	5.48	0.77	49.27	15.35	122.06	266.46	249.54	221.19
102	R-113	0.90	7.03	0.87	49.31	15.74	132.12	308.56	269.86	233.35
120	R-113	1.07	8.11	0.95	48.11	16.31	132.42	283.68	238.36	225.73
118	R-113	1.43	10.77	1.06	47.89	16.25	147.75	326.14	268.87	252.78
299	FC-72	0.86	11.45	2.36	57.07	47.38	246.71	167.00	157.96	144.80
301	FC-72	0.90	12.29	2.60	57.59	47.58	245.64	172.43	156.21	143.56
296	FC-72	1.04	14.25	3.21	58.17	48.02	285.21	209.50	180.09	165.17

Table G.1 Heat transfer coefficients (continued)

Run#	Fluid	v_i m/s	$\dot{m}_i \times 10^3$ kg/s	$\dot{m}_c \times 10^3$ kg/s	T_{sat} °C	ΔT °C	q w	\bar{h}_1 w/m ² ·°C	\bar{h}_2 w/m ² ·°C	h_i w/m ² ·°C
300	FC-72	1.30	17.05	3.48	56.54	46.33	331.43	263.19	220.13	198.96
297	FC-72	1.56	20.01	5.09	56.12	45.42	468.43	324.34	310.93	286.81
298	FC-72	1.73	22.68	5.97	56.80	44.80	543.75	359.22	356.50	337.56
308	FC-72	2.49	32.76	7.35	56.46	35.46	684.19	584.54	555.33	536.59
312	FC-72	0.59	8.15	2.43	57.89	40.86	231.43	176.60	166.55	157.52
311	FC-72	0.80	10.89	2.63	57.89	41.12	242.63	190.82	175.34	164.07
345	FC-72	0.84	11.23	2.76	57.60	40.58	243.98	183.99	180.99	167.19
304	FC-72	1.02	14.14	2.59	58.67	42.44	266.76	216.94	189.96	174.78
310	FC-72	1.22	15.70	2.86	56.21	38.91	279.50	254.32	215.67	199.76
306	FC-72	1.34	18.75	4.12	58.45	39.86	356.16	295.73	269.50	248.50
302	FC-72	1.35	19.08	4.31	58.67	43.24	404.24	310.54	283.61	259.99
307	FC-72	1.46	19.45	3.99	56.93	38.40	378.58	324.89	296.26	274.16
309	FC-72	1.53	20.15	4.82	56.99	38.84	412.34	334.92	313.84	295.22
303	FC-72	1.65	22.15	5.22	57.46	41.22	492.83	368.50	357.03	332.51
368	FC-72	1.72	22.86	6.35	57.35	39.40	520.59	403.41	393.82	367.42
385	FC-72	2.05	27.18	7.23	57.24	38.59	633.49	498.46	472.10	456.50
367	FC-72	2.15	28.84	7.88	57.56	39.08	677.38	526.66	504.68	482.04
369	FC-72	2.38	30.64	7.64	56.35	38.98	718.19	572.72	541.90	512.31

Table G.1 Heat transfer coefficients (continued)

Run#	Fluid	v_a m/s	$\dot{m}_c \times 10^3$ kg/s	$\dot{m}_h \times 10^3$ kg/s	T_{sat} °C	ΔT °C	q w	\bar{h}_1 w/m ² ·°C	\bar{h}_2 w/m ² ·°C	h_c w/m ² ·°C
370	FC-72	2.45	32.38	7.94	57.09	39.05	737.46	586.54	554.17	525.19
317	FC-72	0.46	6.29	1.96	57.78	30.23	174.10	171.10	167.41	160.15
313	FC-72	0.57	7.87	1.98	58.41	31.37	174.21	172.96	163.78	154.41
314	FC-72	0.84	11.21	2.07	57.26	30.81	182.51	192.37	174.98	164.71
346	FC-72	0.90	11.64	2.09	56.55	28.21	185.30	201.30	194.59	182.64
315	FC-72	1.21	15.68	2.33	56.31	29.88	227.39	268.92	225.15	211.63
316	FC-72	1.38	18.73	2.85	57.83	30.90	268.17	310.12	255.75	241.33
347	FC-72	1.71	22.00	4.04	56.24	28.88	350.23	378.31	364.68	337.23
372	FC-72	1.83	24.59	5.04	57.61	31.14	420.29	413.13	401.37	375.39
348	FC-72	1.84	24.65	4.78	57.55	29.13	410.79	419.00	416.23	392.13
349	FC-72	2.04	28.49	5.66	58.70	30.68	504.06	488.56	487.02	456.87
356	FC-72	2.06	26.67	5.14	56.47	30.87	484.76	469.72	434.90	398.70
373	FC-72	2.29	29.74	6.10	56.56	29.55	505.43	527.49	500.52	475.60
350	FC-72	2.30	32.05	6.41	58.65	30.83	574.57	562.16	553.08	518.20
374	FC-72	2.33	30.62	6.25	56.88	29.77	530.82	550.60	524.35	495.87
375	FC-72	2.40	32.34	6.73	57.66	30.45	568.65	571.73	546.39	519.33
352	FC-72	2.61	33.97	6.30	56.58	29.77	559.22	580.86	554.05	522.36
376	FC-72	2.89	37.48	6.82	56.46	28.50	602.77	667.37	624.12	588.11

Table G.1 Heat transfer coefficients (continued)

Run#	Fluid	v_{ai} m/s	$\dot{m}_a \times 10^3$ kg/s	$\dot{m}_c \times 10^3$ kg/s	T_{am} °C	ΔT °C	q w	\bar{h}_1 w/m ² °C	\bar{h}_2 w/m ² °C	\bar{h}_c w/m ² °C
354	FC-72	2.94	38.39	7.20	56.68	29.00	639.64	689.99	646.27	613.33
377	FC-72	2.96	38.68	7.12	56.67	28.34	609.77	686.97	632.99	598.34
378	FC-72	3.05	42.33	7.93	58.34	29.59	711.92	742.48	683.97	668.95
355	FC-72	3.10	40.92	8.07	56.89	29.48	716.64	747.67	703.11	676.12
322	FC-72	0.36	4.77	1.34	57.26	20.26	109.90	191.49	167.47	150.84
321	FC-72	0.51	6.73	1.33	56.84	19.67	124.83	211.14	186.25	176.47
320	FC-72	0.57	7.73	1.40	57.26	19.86	121.16	200.73	176.28	169.64
319	FC-72	0.67	9.06	1.48	57.47	20.47	124.09	200.62	174.16	168.60
323	FC-72	0.96	12.77	1.61	57.26	20.12	131.63	214.77	192.50	181.91
324	FC-72	1.08	14.57	1.66	57.79	20.32	144.33	224.06	202.85	197.49
388	FC-72	1.09	14.05	1.62	56.29	19.53	152.72	242.80	223.40	217.49
325	FC-72	1.27	17.13	1.78	57.58	19.99	156.74	236.87	222.91	218.08
326	FC-72	1.51	20.41	2.06	57.68	19.83	175.01	260.89	249.77	245.40
380	FC-72	1.87	24.86	3.17	57.30	20.01	258.34	408.32	370.58	359.00
358	FC-72	1.98	25.83	2.86	56.58	19.75	249.06	404.23	363.40	350.73
387	FC-72	2.01	26.46	3.35	57.03	20.28	275.35	419.89	390.21	377.64
329	FC-72	2.19	29.08	3.32	57.21	19.58	271.21	419.05	403.70	385.19
359	FC-72	2.33	30.50	4.12	56.63	20.09	368.21	561.36	510.55	509.74

Table G.1 Heat transfer coefficients (concluded)

Run#	Fluid	v_a m/s	$\dot{m}_c \times 10^3$ kg/s	$\dot{m}_h \times 10^3$ kg/s	T_{in} °C	ΔT °C	q w	\bar{h}_1 w/m ² ·°C	\bar{h}_2 w/m ² ·°C	h_i w/m ² ·°C
360	FC-72	2.53	33.28	4.86	56.66	19.37	407.75	641.36	581.11	585.27
362	FC-72	2.82	37.54	5.28	56.89	19.68	485.55	753.21	689.72	685.97
379	FC-72	2.85	38.72	5.14	57.71	20.80	429.04	643.36	582.67	573.61
363	FC-72	2.96	39.18	5.62	56.79	19.45	510.55	796.85	729.43	729.91
361	FC-72	3.10	41.00	6.51	56.79	19.67	551.68	847.97	781.68	780.14
331	FC-72	0.69	9.16	0.93	57.32	10.53	74.16	207.00	195.44	195.85
337	FC-72	1.52	20.24	1.01	57.32	9.34	84.96	313.96	266.26	253.04
338	FC-72	1.61	22.13	1.28	58.32	10.61	105.66	351.75	292.98	276.84
390	FC-72	2.01	26.45	1.39	56.82	9.72	119.36	403.07	351.22	341.62
339	FC-72	2.06	26.81	1.21	56.48	9.26	114.44	410.76	352.42	343.85
340	FC-72	2.15	29.26	1.61	57.90	10.39	138.74	437.91	384.08	371.47
382	FC-72	2.42	31.77	1.79	56.67	9.57	155.50	511.35	444.47	452.07
383	FC-72	2.46	32.05	1.94	56.56	9.85	159.85	524.55	452.97	451.45
341	FC-72	2.52	33.40	1.62	57.06	9.90	145.91	480.15	424.79	409.47
342	FC-72	2.67	35.97	1.85	57.48	10.12	163.56	539.66	468.90	449.64
343	FC-72	2.77	38.76	2.18	58.58	10.88	202.95	599.29	534.73	518.61
384	FC-72	2.78	37.37	2.30	57.56	10.35	194.35	611.20	525.27	522.44

Appendix G: Experimental Data

Note:

Based on the data of the average heat transfer coefficients provided in Table G.1, the sectional heat transfer coefficients can be evaluated using the following equations.

$$\bar{n}_{s1} = \bar{n}_1 \quad (G-1)$$

$$\bar{n}_{s2} = 2\bar{n}_2 - \bar{n}_1 \quad (G-2)$$

$$\bar{n}_{s3} = 3\bar{n}_3 - 2\bar{n}_2 \quad (G-3)$$

Table G.2 Film thickness

Run#	Fluid	v_d m/s	ΔT °C	δ , mm			$\delta = c_1 x^{c_2}$			
				$x^*=50.8$	$x=152.4$	$x=254.0$	$x=457.2$	$x=812.8$	c_1	c_2
201	R-113	0.68	39.79	0.259	0.368	0.424	0.442	0.496	0.545	0.239
239	R-113	0.79	39.10	0.315	0.400	0.452	—	0.487	0.529	0.165
225	R-113	0.74	38.71	0.241	0.379	0.444	0.472	0.517	0.594	0.283
195	R-113	0.99	38.28	0.176	0.322	0.368	0.424	0.470	0.559	0.364
223	R-113	1.25	37.03	0.165	0.294	0.358	0.423	0.504	0.589	0.416
213	R-113	1.28	39.73	0.148	0.295	0.368	0.436	0.525	0.634	0.470
220	R-113	0.34	31.21	0.254	0.380	0.397	0.461	0.505	0.557	0.253
180	R-113	0.50	33.83	0.296	0.360	0.412	0.430	0.466	0.495	0.172
202	R-113	0.64	32.19	0.224	0.340	0.412	0.440	0.476	0.551	0.287
207	R-113	0.84	31.62	0.181	0.289	0.342	0.397	0.432	0.501	0.329
284	R-113	1.32	31.54	0.140	0.341	0.360	—	0.440	0.564	0.411
285	R-113	1.49	31.34	0.208	0.326	0.325	—	0.450	0.490	0.279
206	R-113	1.73	30.95	0.170	0.280	0.340	0.375	0.412	0.484	0.333
221	R-113	0.31	21.42	0.194	0.317	0.352	0.387	0.439	0.498	0.298
181	R-113	0.50	21.42	0.194	0.288	0.316	0.342	0.402	0.423	0.230
203	R-113	0.71	20.11	0.174	0.283	0.313	0.344	0.410	0.454	0.308

* x is the distance between the leading edge of the condensing surface to the point where δ is measured. x is in mm.

Table G.2 Film thickness (continued)

Run#	Fluid	v_f m/s	ΔT °C	δ , mm			$\delta = c_1 x^{1/2}$		
				x=50.8	x=152.4	x=254.0	x=457.2	x=812.8	c_1 c_2
185	R-113	0.84	20.46	0.168	0.269	—	0.370	0.386	0.447 0.319
208	R-113	0.86	22.28	0.147	0.296	0.334	0.370	0.400	0.492 0.366
211	R-113	1.12	21.20	0.134	0.271	0.298	0.368	0.397	0.490 0.406
62	R-113	1.15	19.96	0.160	0.312	—	0.367	0.384	0.450 0.316
215	R-113	1.28	21.65	0.106	0.195	0.247	0.345	0.380	0.481 0.406
269	R-113	1.15	10.64	0.213	0.225	0.232	—	0.294	0.289 0.121
268	R-113	1.40	9.97	0.194	0.210	0.225	—	0.277	0.278 0.136
279	R-113	1.59	10.75	0.132	0.214	0.232	—	0.279	0.319 0.274
108	R-113	1.05	12.93	0.225	0.249	—	0.269	0.314	0.310 0.115
182	R-113	0.51	14.15	0.230	0.256	0.280	0.324	0.358	0.365 0.173
100	R-113	0.42	14.76	0.310	0.346	—	0.382	0.383	0.399 0.083
93	R-113	0.64	15.84	0.241	0.293	—	0.303	0.330	0.338 0.108
90	R-113	0.65	14.65	0.245	0.280	—	0.296	0.301	0.312 0.076
101	R-113	0.71	15.35	0.241	0.277	—	0.347	0.349	0.372 0.152
102	R-113	0.90	15.74	0.155	0.294	—	0.348	0.367	0.432 0.312
299	FC-72	0.86	47.38	0.288	0.393	0.551	0.552	0.551	0.604 0.247
301	FC-72	0.90	47.58	0.294	0.392	0.391	0.416	0.525	0.523 0.195
312	FC-72	0.59	40.86	0.220	0.396	0.460	0.484	0.513	0.619 0.311

Table G.2 Film thickness (concluded)

Run#	Fluid	V_{fi} m/s	ΔT °C	δ , mm			$\delta = c_1 x^{c_2}$		
				$x=50.8$	$x=152.4$	$x=254.0$	$x=457.2$	$x=812.8$	c_1 c_2
312	FC-72	0.59	40.86	0.220	0.396	0.460	0.484	0.513	0.619 0.311
311	FC-72	0.80	41.12	0.210	0.361	0.431	0.480	0.502	0.606 0.330
305	FC-72	0.81	41.84	0.270	0.410	0.481	0.506	0.516	0.603 0.246
345	FC-72	0.84	40.58	0.215	0.350	0.420	0.460	0.478	0.570 0.304
317	FC-72	0.46	30.23	0.268	0.396	0.395	0.407	0.417	0.462 0.154
313	FC-72	0.57	31.37	0.239	0.372	0.406	0.418	0.440	0.502 0.222
314	FC-72	0.84	30.81	0.234	0.304	0.373	0.397	0.442	0.483 0.244
346	FC-72	0.90	28.21	0.205	0.298	0.367	0.394	0.400	0.468 0.262
315	FC-72	1.21	29.88	0.190	0.280	0.330	0.367	0.374	0.435 0.263
322	FC-72	0.36	20.26	0.238	0.317	0.340	0.341	0.372	0.398 0.158
321	FC-72	0.51	19.67	0.199	0.311	0.317	0.340	0.356	0.401 0.209
320	FC-72	0.57	19.86	0.193	0.317	0.328	0.339	0.355	0.407 0.216
319	FC-72	0.67	20.47	0.176	0.289	0.316	0.339	0.372	0.425 0.272
323	FC-72	0.96	20.12	0.170	0.272	0.304	0.317	0.340	0.390 0.253
324	FC-72	1.08	20.32	0.170	0.282	0.281	0.293	0.338	0.371 0.234
325	FC-72	1.27	19.99	0.204	0.281	0.303	0.305	0.305	0.341 0.148
331	FC-72	0.69	10.53	0.168	0.244	0.260	0.270	0.275	0.310 0.181
335	FC-72	1.09	9.38	0.160	0.202	0.216	0.220	0.226	0.244 0.128

Table G.3 Interfacial wave initiation in air-liquid flow

RUN#	μ_1 CT	v_s m/s	v_l m/s	$m_l \times 10^3$ kg/s	L_{on} m	δ mm
26	1.00	1.78	0.01	1.34	0.50	4.19
68	1.12	3.02	0.06	8.73	0.45	3.55
69	1.12	3.08	0.02	3.76	—	5.27
70	1.12	2.72	0.01	1.26	—	3.82
71	1.12	2.28	0.05	8.43	—	4.34
27	1.71	1.94	0.00	0.99	0.55	5.20
28	1.71	2.11	0.01	1.38	0.40	4.29
29	2.37	2.73	0.01	1.25	0.46	4.04
30	2.37	2.42	0.01	1.24	0.46	4.45
31	2.37	1.78	0.01	2.09	0.46	3.40
36	2.67	5.94	0.04	0.88	0.00	0.60
37	2.67	4.46	0.02	1.29	0.41	2.00
38	2.67	2.43	0.01	2.32	0.29	4.53
39	2.67	2.12	0.02	4.67	0.16	5.60
40	2.67	1.44	0.05	12.28	0.25	6.19
41	3.26	2.38	0.09	11.76	0.60	3.39
42	3.26	2.94	0.05	4.82	0.45	2.51
43	3.26	3.92	0.03	2.99	0.45	2.27
45	3.26	3.03	0.02	1.33	—	1.60
46	3.26	5.99	0.01	0.50	—	0.93
47	3.95	2.26	0.05	11.55	0.42	6.08
48	3.95	2.70	0.03	5.62	0.57	4.67
49	3.95	3.22	0.02	3.38	0.54	3.83
50	3.95	3.85	0.01	1.41	0.50	3.32

Appendix G: Experimental Data

Table G.3 Interfacial wave initiation in air-liquid flow (concluded)

RUN#	μ_l CT	v_g m/s	v_l m/s	$\dot{m}_l \times 10^3$ kg/s	L_{on} m	δ mm
51	3.95	5.97	0.02	0.60	0.60	1.03
52	4.46	2.91	0.05	12.77	0.50	6.01
53	4.46	3.37	0.03	4.78	—	3.96
54	4.46	3.28	0.02	3.16	0.41	3.58
55	4.46	3.48	0.01	1.50	0.23	2.65
56	4.46	6.00	0.01	0.61	0.00	1.94
57	5.24	2.80	0.03	5.67	0.40	4.89
58	5.24	3.32	0.02	3.24	—	3.77
59	5.24	5.98	0.02	0.81	—	0.98
60	5.24	3.21	0.01	1.75	0.55	3.28
62	5.24	2.41	0.04	9.17	0.50	5.93
63	5.24	3.17	0.03	4.93	0.55	4.54
64	7.55	3.53	0.03	4.67	0.40	4.12
65	7.55	3.75	0.02	2.77	0.35	3.17
66	7.55	3.97	0.01	1.34	—	2.35
67	7.55	5.90	0.00	0.23	—	1.31

Table G.4 Interfacial wave initiation in condensation

Run#	Fluid	v_{gi} m/s	v_g m/s	v_l m/s	T_{sat} °C	ΔT °C	L_{on} m	δ mm
273	R-113	1.27	1.24	0.013	47.60	39.60	0.50	0.389
274	R-113	1.27	1.25	0.016	48.71	31.48	0.41	0.357
278	R-113	1.40	1.38	0.016	49.00	22.42	0.37	0.272
279	R-113	1.59	1.56	0.017	47.86	10.75	0.43	0.201
345	FC-72	0.84	0.81	0.013	57.60	40.58	0.50	0.408
346	FC-72	0.90	0.87	0.015	56.55	28.21	0.46	0.370
388	FC-72	1.09	1.07	0.021	56.29	19.53	0.50	0.256
389	FC-72	1.13	1.11	0.012	58.55	9.70	0.17	0.391

Appendix G: Experimental Data

Table G.5 Interfacial wave speed and length

Run#	Fluid	v_{gi} m/s	ΔT °C	v_w mm/s	L_w mm
273	R-113	1.27	39.60	—	6.00
194	R-113	1.40	40.47	80.50	—
192	R-113	1.49	40.32	82.66	—
187	R-113	1.50	39.51	87.41	—
189	R-113	1.66	38.18	90.22	—
190	R-113	1.69	40.11	94.10	5.29
205	R-113	1.72	39.82	110.20	4.78
283	R-113	1.89	38.19	—	4.50
188	R-113	1.97	38.99	—	4.25
274	R-113	1.27	31.48	79.00	7.00
228	R-113	1.44	31.10	81.50	—
193	R-113	1.49	31.04	82.66	—
285	R-113	1.49	31.34	82.84	7.00
147	R-113	1.51	31.34	—	6.50
191	R-113	1.59	31.69	85.00	6.45
206	R-113	1.73	30.95	100.14	6.20
211	R-113	1.12	21.20	—	9.00
278	R-113	1.40	22.42	84.93	7.00
229	R-113	1.44	22.08	88.48	—
217	R-113	1.48	21.61	89.19	—
218	R-113	1.74	21.21	108.20	5.52
279	R-113	1.59	10.75	51.52	—
267	R-113	1.85	11.17	53.20	5.20
266	R-113	2.19	11.51	54.87	5.30

Table G.5 Interfacial wave speed and length (concluded)

Run#	Fluid	v_{gi} m/s	ΔT °C	v_w mm/s	L_w mm
264	R-113	2.95	10.22	—	4.00
345	FC-72	0.84	40.58	69.84	4.00
310	FC-72	1.22	38.91	74.60	3.73
306	FC-72	1.34	39.86	82.00	3.65
346	FC-72	0.90	28.21	65.00	4.30
315	FC-72	1.21	29.88	68.30	4.25
316	FC-72	1.38	30.90	76.60	4.18
388	FC-72	1.09	19.53	60.36	5.15
324	FC-72	1.08	20.32	59.71	5.00
325	FC-72	1.27	19.99	71.61	4.00
326	FC-72	1.51	19.83	73.00	4.00
327	FC-72	1.65	19.93	79.72	—
336	FC-72	1.13	10.91	—	4.67
389	FC-72	1.13	9.69	40.63	4.50
337	FC-72	1.52	9.34	61.23	4.44
338	FC-72	1.61	10.61	—	4.20
381	FC-72	1.82	11.07	79.72	4.00
339	FC-72	2.06	9.26	86.22	—

BIBLIOGRAPHY

- 3M, (1989), *FluorinertTM Electronic Liquids*.
- Abis, L. V., (1969), *Forced Convection Condensation inside Horizontal Tubes*, Ph.D. Dissertation, Kansas State University.
- Altman, M., Norris, R. H., and Staub, F. W., (1960), *Local Heat Transfer and Pressure Drop for Refrigerants Evaporating in Horizontal Tubes*, Journal of Heat Transfer, August, 189-198
- Altman, M., Staub, F. W., and Norris, R. H., (1960), *Local Heat Transfer and Pressure Drop for Refrigerant-22 Condensing inside Horizontal Tubes*, Chem. Eng. Prog. Symp. Series, 56, 151-159.
- Akers, W. W., Akers, Dean, H. A., and Crosser, O. K., (1958), *Condensing Heat Transfer within Horizontal Tubes*, Chem. Engg. Prog., 54, 89-90.
- Akers, W. W. and Rosson, H. E., (1960), *Condensation inside a Horizontal Tube*, Chem. Eng. Prog. Symp. Series, Heat Transfer, Storrs, 56, 145-149.
- Andritsos, N. and Hanratty, T. J., (1987), *Interfacial Instabilities for Horizontal Gas-Liquid Flows in Pipelines*, Int. J. Multiphase Flow, 13, 583-603
- ASHRAE *Handbook of Fundamentals*, (1985), SI Edition, American Society of Heating Refrigerating and Air-Conditioning Engineers, Inc., Atlanta, GA.
- Azer, N. Z., Abis, L. V., and Swearingen, T. B., (1971), *Local Heat Transfer Coefficients during Forced Convection Condensation inside Horizontal Tubes*, Trans. ASHRAE, 77, 182-201.
- Bae, S., (1969), *Refrigerant Forced-condensation inside Horizontal Tubes*, Ph.D. Thesis, MIT.
- Bae, S., Maulbetsh, J. S. and Rohsenow, W. M., (1971), *Refrigerant Forced-convection Condensation inside Horizontal Tubes*, ASHRAE Trans, Part two, 104-116.
- Bell, K. J., Taborek, J., and Fenoglio, F., (1970), *Interpretation of Horizontal In-tube Condensation Heat Transfer Correlations with a Two-Phase Flow Regime Map*, Chem. Eng. Prog. Symp. Series, 66, 150-163.

Bibliography

- Barry, J. J. and Corradini, M. L., (1988), *Film condensation in the Presence of Interfacial Waves*, ASME Proceedings, Vol. 2, 1988 National Heat Transfer Conference, Houston, TX.
- Carpenter, F. G. and Colburn, A. C., (1951), *The Effect of Vapor Velocity on Condensation inside Tubes*, *Proceedings of the General Discussion of Heat Transfer*, The Institute of Mechanical Engineers and the ASME, July, 20-26.
- Cavallini, A. and Zecchin, R., (1974), *A Dimensionless Correlation for Heat Transfer in Forced Convection Condensation*, 5th Int. Heat Transfer Conference, Tokyo, 3, 309-313.
- Chaddock, J. B., (1957), *Film Condensation of Vapor in a Horizontal Tube*, *Refrigerating Engineering*, 65, 36-41 and 90-95.
- Chandrasekhar, S., (1961), *Hydrodynamic and Hydromagnetic Stability*, Oxford University Press.
- Chang, J. S., Ichikawa, Y., and Irons, G. A., (1982), *Flow Regime Characterization and Liquid Film Thickness Measurement in Horizontal Gas-Liquid Two-Phase Flow by an Ultrasonic Method*, AIAA/ASME, June, 7-12.
- Chato, J. C., (1962), *Laminar Condensation inside Horizontal and Inclined Tubes*, *Ashrae Journal*, 4, 52-60.
- Chen, C. J., (1962), *Condensing Heat Transfer in a Horizontal Tube*, M.S. Thesis, Kansas State University.
- Christodoulou, C., (1987), *Condensation in a Horizontal Rectangular Duct*, An Experimental Study, M.S. Thesis.
- Dittus, F. W. and Boelter, L. M. K., (1930), University of California, Berkeley, *Publications on Engineering*, 2, 443.
- Dukler, A. E., (1977), *The Role of Waves in Two Phase Flow: Some New Understandings*, *Chem. Eng. Education*, Summer, 108-117.
- Eckert, E. R. G., (1950) *Introduction to the Transfer of Heat and Mass*, p. 115, McGraw-Hill.
- Feldman, S., (1957), *On the Hydrodynamic Stability of Two Viscous Incompressible*

Bibliography

- Fluids in Parallel Uniform Shearing Motion*, J. Fluid Mech., 2, 343-370.
- Jacob, M., (1949), *Heat Transfer*, Vol. 1, John Wiley, New York.
- Goodykoontz, J. H. and Dorsch, R. G., (1966), *Local Heat Transfer Coefficients for Condensation of Steam in Vertical Downflow within a 5/8 Inch-diameter Tube*, NASA-TN-D-3326.
- Goodykoontz, J. H. and Brown, W. F., (1967a), *Local Heat-Transfer and Pressure Distributions for Freon-113 Condensing in Downward Flow in a Vertical Tube*, NASA TN D-3952.
- Goodykoontz, J. H. and Dorsch, R. G. (1967b), *Local Heat-transfer Coefficients and Static Pressures for Condensation of High-velocity Steam within a Tube*, NASA TND-3953.
- Hagiwara, Y., Esmailzadeh, E., Tsutsui, H., and Suzuki, K., (1989), *Simultaneous Measurement of Liquid Film Thickness, Wall Shear Stress and Gas Flow Turbulence of Horizontal Wavy Two-phase Flow*, Int. J. Multiphase Flow, 15, 421-431.
- Hanratty, T. J., (1982), *Interfacial Instabilities Caused by Air Flow over a Thin Liquid Layer, in Waves on Fluid Interface*, Proc. Symp. Math. Rec. Center, The University of Wisconsin, Madison, ed. Richard E. Meyer, Academic Press.
- Hirshburg, R. I. and Florschuetz, L. W., (1982), *Laminar Wavy-film Flow: Part II, Condensation and Evaporation*, Journal of Heat Transfer, 104, 459-464.
- Jensen, R. J. and Yuen, M. C., (1982), *Local Heat and Mass Transfer Correlation in Horizontal Stratified Concurrent Flow*, Proc. 7th Int. Heat Transfer Conference, Munichen, 95-100.
- Kao, T. W. and Park, C., (1972), *Experimental Investigation of the Stability of Channel Flows, Part 2, Two-layered Co-current Flow in a Rectangular Channel*, J. Fluid Mech., 52, Part 3, 505.
- Khabenskiy, V. B., Granovskiy, V. S., and Morozov, P. A., (1981), *Condensation in Stratified Two-Phase Flow inside Horizontal or Sloping Tubes*, Heat Transfer-Soviet Research, 13, 85-97.
- Kline, S. J. and McClintock, F. A., (1953), *The Description of Uncertainties in Single*

Bibliography

- Sample Experiments*, Mech. Eng., 75, 3-8.
- Kocamustafaogullari, G., (1985), *Two-fluid Modeling in Analyzing the Interfacial Stability of Liquid Film Flows*, Int. J. Multiphase Flow, 11, 63.
- Koh, J. C. Y., (1962), *Film condensation in a Forced-Convection Boundary-Layer Flow*, Int. J. Heat Mass Transfer, 5, 941-954.
- Kosky, P. G. and Jaster, H., (1976), *Condensation Heat Transfer in a Mixed Flow Regime*, Int. J. Heat Mass Transfer, 19, 95-99.
- Kutsuna, J., I., K. and Nakanishi, S., (1987), *Filmwise Condensation of Vapor Containing Non-condensable Gas in a Horizontal Duct*, Heat Transfer Science and Technology, Ed., Wang Bu-Xuan, Hemisphere Publishing Corporation, International Symposium on Heat Transfer, Beijing.
- Linehan, J. H., Petrick, M., and El-Wakil, M. M., (1969), *On the Interface Shear Stress in Annular Flow Condensation*, Journal of Heat Transfer, August, 450-452.
- Lockhart, R. W. and Martinelli, r. C. (1949), *Proposed Correlation of Data for Isothermal Two-phase Two-component Flow in Pipes*, Chemical Engineering Progress, 45, 39.
- Luu, M. , (1980), *Augmentation of Horizontal In-Tube condensation of R-113*, Ph.D. Dissertation, Department of Mechanical Engineering, Iowa State University, Ames, Iowa.
- Milne-Thomson, L. M., *Theoretical Hydrodynamics*, MacMillan, (1960).
- Miner, C. S. and Dalton, N. N., (1953), *Glycerol*, Reinhold Publishing Corporation.
- Moalem, D. and Sideman, S., (1976), *Theoretical Analysis of A Horizontal Condenser-Evaporator Tube*, Int. J. Heat Mass Transfer, 19, 259-270.
- Narain, A.(1991), *Condensing Vapor Flows and the Case of Flow between Parallel Plates*, Recent Advances in Mechanics of Structured Continua, ASME, AMD-Vol. 117.
- Narain, A. and Kizilyalli, Y., (1991), *Pressure Driven Flow of Pure Vapor Undergoing Laminar Film Condensation between Parallel Plates*, International Journal of Non-linear Mechanics, Vol. 26, 501-520.

Bibliography

- Narain, A. and Kamath, R., (1991), *Internal Flows of Vapor Undergoing Film Condensation*, Proceedings of the Twenty-second Midwestern Mechanical Conference, Development in Mechanics, Vol. 16, University of Missouri-Rolla, 411-412.
- Nusselt, W., (1916), *Die Oberflächenkondensation des Wasserdampfes*, Z. Ver. Dt. Ing. 60, 541-546.
- Reid, R. C. and Sherwood, T. K., (1958), *The Properties of Gases and Liquids*, McGraw-Hill.
- Rohsenow, W. M., *Film Condensation*, (1970), Applied Mechanics Review, 23, 487-495.
- Rohsenow, W. M., Webber, J. H., and Ling, A. T., (1956), *Effect of Vapor Velocity on Laminar and Turbulent-film Condensation*, Transactions of the ASME, November, 1637-1643.
- Rosson, H. E. and Myer, J. A., (1965), *Point Values of Condensing Film Coefficient inside a Horizontal Pipe*, Chem Engg. Prog. Symp. Series, 61, 190-199.
- Rufer, C. E. and Kezios, S. P., (1966), *Analysis of Two-phase, One-component Stratified Flow with Condensation*, Journal of Heat Transfer, 88, 265-275.
- Sardesai, R. G., Owen, R. G., and Pulling, D. J., (1981), *Flow Regimes for Condensation of a Vapor inside a Horizontal Tube*, Chemical Engineering Science, 36, 1173-1180.
- Schlichting, H. (1979), *Boundary Layer Theory*, Seventh Edition, McGraw-Hill.
- Shah, M. M., (1979), *A General Correlation for Heat Transfer during Film Condensation inside Pipes*, Int. J. Heat Mass Transfer, 22, 547-556.
- Shekriladze, I. G. and Gomelaury, V. I., (1966), *Theoretical Study of Laminar Film condensation of Flowing Vapor*, Int. J. Heat Mass Transfer, 9, 581-591.
- Soliman, M. and Berenson, P. J., (1970), *Flow Stability and Gravitational Effects in Condenser Tubes*, Proc. 4th Int. Heat Transfer Conf., Vol. 6, Paris.
- Soliman, M., Schuster, J. R., and Berenson, P. J., (1968), *A General Heat Transfer Correlation for Annular Flow Condensation*, Journal of Heat Transfer, 90, 267- 276.

Bibliography

- Sparrow, E. M. and Gregg, J. L., (1959), *A boundary Layer Treatment of Laminar Film Condensation*, J. Heat Transfer, 81, 13-18.
- Sparrow, E. M., Minkowycz, W. J., and Saddy, M., (1967), *Forced Convection Condensation in the Presence of Non-condensables and Interfacial Resistance*, Int. J. Heat Mass Transfer, 10, 1829-1845.
- Suryanarayana, N. V. and Merte, H., Jr., *Film Boiling on Vertical Surface*, J. of Heat Transfer, 94, 377-384.
- Traviss, D. P., Rohsenow, and Baron, A. B., (1973), *Forced-convection Condensation inside Tubes: A heat Transfer Equation for Condenser Design*, ASHRAE Trans. Vol 79, Part 1, 157-165.
- Uehara, H., Nakaoka, T., and Kurosaki, M., (1984), *Turbulent Film Condensation in a Forced-convection Boundary Layer Flow*, Heat Transfer-Japanese Research, 13, 89-104.
- Yih., C. S., (1967), *Instability due to Viscosity Stratification*, J. Fluid Mech. 27, Part 2, 337.